PSL UNIVERSITÉ PARIS

THÈSE DE DOCTORAT
DE L'UNIVERSITÉ PSL

Préparée à l'Institut de Mécanique Céleste et de Calcul des Éphémérides, Observatoire de Paris

Dynamique des planètes co-orbitales
Marées et chaînes de résonance

Dynamics of co-orbital planets
Tides and resonance chains

Soutenue par
Jérémy COUTURIER
Le 21 Octobre 2022

École doctorale n°127
Astronomie et Astrophysique d'Île de France

Spécialité
Mécanique Céleste

Composition du jury :

Françoise Roques Astronome, Observatoire de Paris	*Présidente*
Alessandra Celletti Professor, Univ. of Rome Tor Vergata	*Rapportrice*
Benoît Noyelles Associate Professor, Institut UTINAM	*Rapporteur*
Adrien Leleu Post-Doctorant, Université de Genève	*Examinateur*
Anne Lemaître Professor, Université de Namur	*Examinatrice*
Philippe Robutel Directeur de Recherche, IMCCE	*Directeur de thèse*
Alexandre C.M. Correia Associate Professor, Univ. de Coimbra	*Co-directeur de thèse*
Gwenaël Boué Maître de conférences, IMCCE	*Invité*

l'Observatoire de Paris — IMCCE
Institut de Mécanique Céleste et de Calcul des Éphémérides

Remerciements

Je tiens premièrement à remercier mes directeurs de thèse *Philippe Robutel* et *Alexandre C.M. Correia*. Ils ont su identifier un sujet de recherche digne de faire un beau travail de thèse, et leur encadrement optimal a permis à ces trois années de couler de source. Non seulement leurs conseils avisés m'ont permis d'élaborer une recherche de qualité, mais ils se sont aussi appliqués à rendre mes travaux visibles dans la communauté scientifique en mécanique céleste. *Philippe*, je te souhaite le meilleur en ta nouvelle qualité de directeur de l'IMCCE.

I deeply thank *Françoise Roques*, *Alessandra Celletti*, *Benoît Noyelles*, *Adrien Leleu*, *Anne Lemaitre* and *Gwenaël Boué* for being part of the jury of my oral defense. You will allow this work to officially end. *Alessandra* and *Benoît*, you deserve an additional thank for accepting to review this manuscript. *Alessandra*, I am grateful for the many opportunities you gave me to present my researches, be it at the CELMECH seminars, the symposium of the IAU, or even the soon-to-come CELMEC VIII at Tor Vergata. *Françoise* et *Gwenaël*, merci d'avoir géré aussi efficacement les comités de thèse.

I would like to thank *Miki Nakajima* and *Alice Quillen* for giving credit to my researches and offering me the opportunity to pursue them. I am excited to start working with you at Rochester University this fall.

Je remercie *Mickaël Gastineau* et *Stéphane Vaillant* pour leur aide sur le plan informatique. *Mickaël*, le numérique de cette thèse doit beaucoup à tes intégrateurs "dopri8" et "intpla", tandis que le bon déroulement de la soutenance doit à *Stéphane*. Merci à *Jacques Laskar* d'avoir développé l'outil Trip. De manière plus générale, merci aux membres de l'IMCCE qui permettent à ce formidable laboratoire de perdurer et d'évoluer. Merci à *Amélie Muslewski* et *Nevada Mendez* pour l'aide dans l'organisation des missions, et à *Lusiné Amirkhanyan* pour l'administratif.

Merci *Antoine Petit* pour ton template, la forme du manuscript te doit. Muchas gracias a *Andreas Reisenegger* por la calidad de sus clases de gravitación relativista en la PUC que me introducieron al mundo de la astrofísica. Merci à *Marie-Christine Angonin* d'avoir si habilement géré mes bêtises pendant l'année de M2. Merci à *Jacques Laskar* de m'avoir fait découvrir l'IMCCE en me proposant ce stage sur la théorie de la Lune, et à *Philippe Robutel*, *Gwenaël Boué* et *Hervé Manche* pour leur aide dans sa complétion. Merci à *Nam Hoàng Hoài*, *Federico Mogavero* et *Léo Bernus* pour les discussions entre deux portes. Je n'oublierai pas non plus de remercier mes professeurs de maths et de physique de MPSI et MP*, *Michel Renard*, *Fernand Canonico*, *Jean Dervieux* et *Benoît Gugger*. La qualité de l'enseignement scientifique en classe préparatoire est trop méconnue. Merci à *Jean-Marc Lefever* de m'avoir orienté vers la prépa.

Un merci considérable à *Cynthia*, *Martin*, *Mathis*, *Marième*, *Médérik* et *Mégane* de m'avoir accueilli si généreusement sur la glace à Iqaluit. Les résultats du Chapitre 6 vous doivent beaucoup, surtout les bottes en Figure 6.3. Thank you so much *Janine*, *Terry*, *Dion* and *Lucas* for such a warm welcome in your house in Tomar. I hope the construction of the new one is going on as planned. Muchísimas gracias a todos los miembros de la comunidad Santa Guillermina en Satipo, especialmente a *Felicia*, *Beatriz*, *Jose*, *Daniel*, *Josecito* y *Carmen*, por los momentos maravillosos que me hicieron pasar el la selva peruana. Gracias *William* por los tramites en Péru y *Charo* por el viaje a Lima. Gracias *Jesús* por tus talentos de fotógrafo y por hacerme descubrir Lobitos. *Boris*, merci pour ce voyage anticipé aux USA.

Merci à mes parents qui m'ont soutenu pendant mes études et avant, et à mes grands-parents paternels dont la maison à été propice au travail pendant deux années de classes préparatoires. Merci à mes grands parents maternels, à *Apolline*, à *Baptiste*, à *Elly* et à *Léticia* pour leur gentillesse. Finalement, merci à *Maxime* pour ces quelques mois formidables. J'ai hâte de voir tous les autres.

Contents

Chapter 1

Introduction

1.1 Definition of co-orbital motion

In order to provide a definition of co-orbital motion, we say that two planets are co-orbital if the difference of their mean longitude is a librating angle. More precisely, if λ_1 and λ_2 denote the mean longitudes of two planets of a planetary system, defining $\xi(t) = \lambda_1(t) - \lambda_2(t)$, these two planets are co-orbital if[1]

$$\forall t \in \mathbb{R} \quad \xi(t) \mod 2\pi \in]0, 2\pi[\,, \tag{1.1}$$

where the variable t is the time. In the framework of the three-body problem, co-orbital planets are in a $1:1$ mean motion resonance. The difference ξ of their mean longitudes generally librates around a value close to $\pm\pi/3$ or equal to π. Beyond the famous collinear and equilateral configurations described respectively by Euler (1764) and Lagrange (1772), other types of orbits are possible in this resonance, making the co-orbital dynamics very rich. While the Euler configurations, denoted by L_1, L_2 and L_3 in the restricted three-body problem, are unstable for all mass ranges, the Lagrangian equilibria are linearly stable, provided that the three masses satisfy the relation $27(m_0m_1 + m_0m_2 + m_1m_2) < (m_0 + m_1 + m_2)^2$ established by Gascheau (1843) for circular orbits. If we denote by m_0 the mass of the star, much larger than that of the planets m_1 and m_2, the Gascheau condition is satisfied when $(m_1 + m_2)/m_0 \lesssim 1/27$.

Therefore, in the planar case and for small eccentricities, when the sum of the planetary masses is smaller than about $1/27$ of the stellar mass, tadpole orbits arise, allowing the difference in the mean longitude to librate around $\pm 60°$. When $(m_1 + m_2)/m_0 \lesssim 3 \times 10^{-4}$, horseshoe-shaped orbits can arise (Laughlin and Chambers, 2002). They librate around $180°$ with a very large amplitude of at least $312°$. For small libration amplitudes, still in the planar case, the eccentric dynamics have been studied numerically by Giuppone *et al.* (2010) and analytically by Robutel and Pousse (2013), showing the existence of two proper modes called Lagrange and anti-Lagrange. For moderate to large eccentricities, quasi-satellite orbits are also possible, for which the planets appear to revolve around

[1] This definition excludes the quasi-satellite motion, that we do not study in this manuscript.

each other (Giuppone *et al.*, 2010; Pousse *et al.*, 2017). High eccentricities give rise to topological changes in the phase space, and thus to many more exotic trajectories (Leleu *et al.*, 2018), while the dynamics of the inclined problem is even more complex by allowing, among other things, transitions between these orbits and retrograde co-orbital motion (Namouni, 1999).

1.2 State of the art on co-orbital planets detection

An exoplanet is a planet orbiting a star other than the Sun. It is generally estimated that the Milky Way contains 10^{11} to 10^{12} planets, and all of them but eight are exoplanets. The era of exoplanet detection started 27 years ago, and as of August 26$^{\text{th}}$, 2022, 5154 were discovered[2], none co-orbital with another. Before reviewing the methods specifically used for the detection of hypothetical co-orbital exoplanets, we will focus on the detection of regular exoplanets.

Most exoplanets are located more than 10 light-years away from the Sun (only 8 out of 5154 are closer than that[3]), and most exoplanets have a radius less than that of Jupiter (63 % of the 5154 are smaller than Jupiter[2]). It is likely that the proportion of exoplanets smaller than Jupiter is higher than 63 %, but the detection is naturally biased towards larger exoplanets. Similarly, it is obvious that the proportion of exoplanets closer than 10 light-years is much smaller than 8/5154, since once again, the detection is strongly biased towards closer exoplanets. As a consequence, only a small minority of all exoplanets have an angular diameter larger than 0.3 milliarcseconds. Taking into account the small angular separation between the exoplanet and its host star, the feat of a direct detection is generally excluded, since the best-case scenario is equivalent to observe a fly circling a street light 14 800 km away[4].

As exoplanets can hardly be detected directly, their existence is generally highlighted from various kinds of perturbations they cause on their host star. If the exoplanet orbits its star in a plane almost parallel to our line of sight, then the luminosity of the star slightly decreases periodically due to eclipses caused by the planet passing in front of the star, called transits. When the radius of the planet is not too small with respect to that of the star, the S/N (signal over noise) ratio is high enough for the transit to be detected. The transit method gives the orbital period of the exoplanet with a good precision, and if the radius of the star is constrained, then that of the planet is estimated from the decrease in luminosity. Similarly, if the mass of the host star can be estimated, then the semimajor axis of the planet is deduced from Kepler's third law. However, the eccentricity and argument of pericentre generally cannot be constrained, unless the secondary eclipse, that occurs when the star passes in front of the planet, can be distinguished from the noise. The secondary eclipse is rarely detected though and only some tens of exoplanets are concerned. Some examples are given in Table A.3 of Lillo-Box *et al.* (2018).

Regardless of the ratio S/N, the transit method is bound to fail if the exoplanet orbits its star in a plane even slightly inclined with respect to our line of sight. In presence of an exoplanet, the star orbits the barycentre of the system star−exoplanet

[2] exoplanet.eu

[3] Namely, Proxima Centauri b,c,d; Wolf 359 b,c & Lalande 21185 b,c.

[4] 1 cm/14 800 km = 140 000 km/10 ly

periodically, and analyzing the radial velocity of the star can highlight the existence of an exoplanet. The main advantage of the radial velocity method is that it does not require the exoplanet to eclipse its host star . If the star is orbited by several exoplanets, its motion around the barycentre of the planetary system is quasiperiodic instead of periodic, and the radial velocity method is more adapted than the transit method to the detection of multi-planetary systems, as it can show the quasiperiodic motion of the star, and most planets of a planetary system might not transit. The amplitude of the motion of the star is related both to the mass m of the exoplanet and i, the inclination between its orbital plane and the plane of the sky. As a consequence, the method only allows the product $m \sin i$ to be constrained, but does not give these two quantities independently. Nevertheless, if the exoplanet detected with the radial velocity method happens to transit, then $i = \pi/2$ and its mass can be obtained. Contrarily to the transit method, the radial velocity method does not give constraints on the radius of the planet.

Some other techniques, still under development, can enable the detection of exoplanets, but transit and radial velocity are the two most successful. Both methods are a priori valid for the detection of co-orbital exoplanets, but difficulties inherent to the co-orbital motion arise. The transit method shows the presence of a co-orbital pair if both co-orbitals transit, but in case of moderate to large semimajor axes, even a tiny mutual inclination between the co-orbitals ensures that one of them passes above or below the star, and escapes detection. Because of the large orbital period induced by large semimajor axes, the transit method seems poorly adapted to detect pairs of co-orbital exoplanets with moderate to large semimajor axes. Small semimajor axes can allow both transits to happen despite a small mutual inclination, but as we investigate in this manuscript, close-in co-orbital pairs are subject to strong tidal dissipation that can disrupt the system.

For these reasons, the radial velocity technique seems more adapted than the transit method to locate co-orbital exoplanets. However, Leleu *et al.* (2017) have shown that at first order in eccentricity, a pair of co-orbital exoplanets yields the same radial velocity signature as a single exoplanet with well chosen parameters. In practice, it is hence very difficult to distinguish a pair of co-orbital exoplanets from a single exoplanet using only the radial velocity method. If both co-orbital exoplanets of masses m_1 and m_2 are at an equilateral Lagrangian equilibria, then they provoke the same perturbations on the radial velocity of the star as a single exoplanet of mass m located in front of m_2 by an angle φ (*resp.* behind m_1 by an angle $\pi/3 - \varphi$), where (Leleu *et al.*, 2017, Eq. (9))

$$m = \sqrt{m_1^2 + m_2^2 + m_1 m_2} \quad \text{and} \quad \varphi = \arctan \frac{\sqrt{3}\, m_1}{m_1 + 2\, m_2}. \tag{1.2}$$

As a consequence, it is impossible to differentiate the two black co-orbital exoplanets from their fictitious blue equivalent on Fig. 1.1 with the radial velocity method.

By themselves, the transit and radial velocity techniques are rather helpless on detecting co-orbital exoplanets. Combining both can nevertheless help the detection. Indeed, in the case of a single exoplanet, the transit occurs at the same time as the radial velocity reaches its mean value. In the co-orbital case though, there exists a time-shift Δt between these two events. The time Δt depends on the angular separation $\xi = \lambda_1 - \lambda_2$ between the co-orbitals, and denoting η their common mean-motion, it reads (Ford and Gaudi,

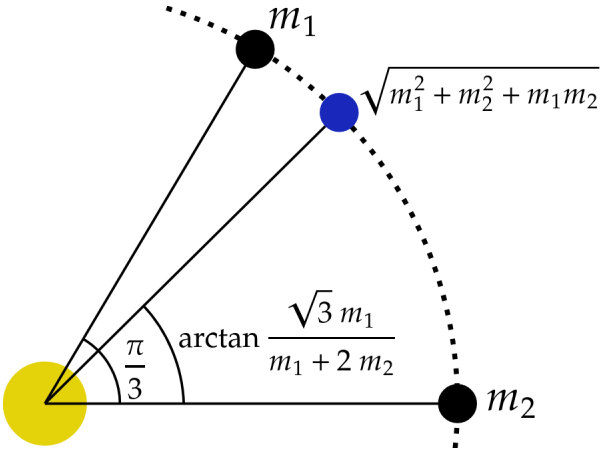

Fig. 1.1 — The two black co-orbital exoplanets of masses m_1 and m_2, located at an equilateral Lagrangian equilibrium, yield on the radial velocity of the central star the same signature as the fictitious blue exoplanet. Analyzing the radial velocity of the star is thus not enough to highlight the presence of the two distinct exoplanets. If $m_1 = m_2 = m$, then the blue exoplanet of mass $\sqrt{3}\, m$ is at mid-distance between the co-orbitals.

2006; Leleu *et al.*, 2017)

$$\Delta t = \eta^{-1} \left(\frac{\xi}{2} + \arctan \left[\frac{m_1 - m_2}{m_1 + m_2} \tan \frac{\xi}{2} \right] \right). \tag{1.3}$$

If one of the co-orbital exoplanets transits, analyzing the radial velocity of the star can highlight the presence of its companion, even if it does not transit, if such a time-shift is measured. However, even a single exoplanet features a time-shift $\Delta t = -\eta^{-1} e \cos\omega$ as soon as it is eccentric with eccentricity e and argument of pericentre ω. Unless the quantity $e \cos\omega$ can be constrained by means of the secondary eclipse, the time-shift method is useless on detecting co-orbital exoplanets.

When the star is orbited by a single exoplanet, transits occur periodically and plotting the light curve as a function of time, with a fold at every period $T = 2\pi/\eta$, draws a vertical line, corresponding to the luminosity decrease. If the lines of pixels of the subsequent image are added, the transiting exoplanet can be detected even with a poor S/N ratio. In the case of a multi-planetary system though, the motion of each exoplanet is no longer periodic and planet−planet gravitational interactions are responsible for transit timing variations (TTV). In the presence of TTV, the line corresponding to the luminosity decrease is no longer straight but can curve according to the TTV value, giving it a river shape such as the one presented in Fig. 2 of Leleu *et al.* (2021). The rivers caused by the TTV induced by a co-orbital companion are very characteristic (Vokrouhlický and Nesvorný, 2014, Fig. 3) and their observation would be enough to prove the existence of a co-orbital pair. Nevertheless, in presence of large TTV, adding the lines of the river diagram does not improve the S/N ratio, and such method is not suitable to detect co-orbital exoplanets. Recently, neural networks have been shown capable of efficiently detect exoplanets in river diagrams with high TTV and low S/N (Leleu *et al.*, 2021; Leleu *et al.*, 2022) and could yield to the detection of a co-orbital pair of exoplanets in the future.

1.3 State of the art on co-orbital planets formation

The discovery of exoplanets raised the question of the existence of co-orbital planets, which are absent from the Solar System. Despite the large number of exoplanet detection, no pair or co-orbital exoplanet has been discovered so far. However, the theories of planetary formation do not prohibit the existence of co-orbital planets. Indeed, Laughlin and Chambers (2002) introduced two possible processes that can form such systems : accretion in situ or capture at a stable Lagrangian point of an already existing planet. Depending on the physical characteristics of the gas disc, the capturing process can lead to systems with a high diversity of mass ratios (Cresswell and Nelson, 2008), but also to equal-mass co-orbitals (Giuppone *et al.*, 2012). In the in-situ scenario, different models lead to various upper limits for the mass that can form at a Lagrangian equilibrium of a giant planet. A maximum of about 0.6 Earth mass is found by Beaugé *et al.* (2007), while Lyra *et al.* (2009) obtain 5 to 15 Earth mass planets at the same location.

Once formed in the disc, the stability of the co-orbital system is not necessarily guaranteed. Beaugé *et al.* (2007) found that inward migration tends to slightly increase the libration amplitude of the co-orbital system, and instability during the late migrating stages with low gas friction may lead to the destruction of the system. Another study from Pierens and Raymond (2014) shows that equal-mass co-orbitals (from super-Earths to Saturns) are heavily disturbed during the gap-opening phase of their evolution. Leleu *et al.* (2019) studied the dynamics of a pair of migrating co-orbital planets and showed that, depending on the mass ratio, the eccentricities of the planets and the type of dissipative forces, the two planets may evolve towards the stable Lagrangian points or scatter out of the system. In the same work, Leleu *et al.* (2019) studied the formation of exoplanets around low mass star. They showed that when co-orbital pairs of exoplanets are formed, they are often part of a chain of mean motion resonance (see their Fig. 12)

1.4 Tidal effects and motivations

For systems with orbital periods less than 10 days, the planets undergo strong tidal interactions from the parent star (*e.g.* Correia *et al.*, 2020), which arise from differential and inelastic deformations of the planet. In the two-body problem, the ultimate stage for tidal evolution is the synchronization of the rotational and orbital periods, alignment of the planet spin axis with the normal to the orbit, and circularization of the orbit (*e.g.* Hut, 1980; Adams and Bloch, 2015).

In the full N-body problem, Moeckel (2017) proved that a relative equilibrium (solid rotation of the whole configuration) is never a minimum of energy of the phase space at a given total angular momentum. Thus, applied to the three-body problem with tidal dissipation, this result implies that the Lagrangian equilibria are made unstable by tides. However, we know neither the timescale of such instability nor if the phenomenon expands to the whole phase space, and we even less know what are the consequences to the dynamics of the co-orbital configuration. Indeed, although the spin of close-in planets quickly evolves into an equilibrium configuration, the orbital evolution is much slower (*e.g.* Correia and Laskar, 2010), and the co-orbital configuration may survive the whole age of the system.

The absence of co-orbital exoplanet detection could be explained by the challenge that such detection represents, as we justified in Sect. 1.2. Nevertheless, in this manuscript, we rather investigate the hypothesis that tidal effects are responsible for the disruption of the co-orbital motion. Rodríguez *et al.* (2013) provided a numerical study of the co-orbital motion under tidal dissipation and showed that identical co-orbitals (same masses, radii and tidal parameters) are always destroyed by tides, but before Couturier *et al.* (2021), no analytical work had been undertaken to investigate this hypothesis. Resonance chains are at the core of current researches in celestial mechanics, and since formation models predict that co-orbital planets are often formed within one, we investigate the behaviour and stability of the co-orbital motion as part of a resonance chain.

1.5 Organization of the manuscript and notations

In this thesis manuscript, we provide an in-depth study of the co-orbital motion, perturbed by tides and resonance chains. The different models that we elaborate take into account effects such as the gravitational interactions between the co-orbital bodies, dissipation due to tides, secular (*i.e.* long-term) perturbations due to interactions with a third planet, and general relativity. The main secular effect that we are interested in is tidal dissipation. Indeed, tides do not preserve the total energy of the system and have a high potential for long-term modifications of the orbits. However, it is important that the point-mass (*i.e.* tideless) dynamics are well described and understood before we can properly introduce tidal dissipation. For this reason, we do not treat the case of tides before Chap. 5. In the whole manuscript, we restrict ourselves to the planar case.

The theoretical work that we perform throughout the manuscript is often analytical and sometimes semi-analytical. Numerical simulations are generally bounded to the verification of the analytical results and their domain of validity. Our work makes use of the general theory on celestial mechanics and dynamical and Hamiltonian systems. In Chap. 2, we expose the main parts of this theory, and we rederive some important results that we frequently use later in the manuscript. For convenience to the reader, we gather in Table 1.1 the notations used throughout the manuscript.

In Chap. 3, we study the dynamics of two point-mass co-orbital bodies affected by their gravitational interaction with the central body, and perturbed by their mutual interaction, that is, we study the $1:1$ mean-motion resonance. Most results of Chap. 3 were first published in Robutel and Pousse (2013) and are recalled in Sect. 2 of Couturier *et al.* (2021). The end of Sect. 3.2.2 was first published in Couturier *et al.* (2021) and Sect. 3.3, where we study the perturbations due to general relativity on the co-orbital motion, is original.

Since it is not uncommon for exoplanets to be formed within a resonance chain, we expand our work in Chap. 4 by considering the case where the pair of co-orbital planets interacts with an outer third planet, in a first-order mean-motion resonance with the pair. In other words, we study the point-mass resonance chain $p:p:p+1$, where p is a small integer. The results of Chap. 4 were first published in Couturier *et al.* (2022).

The theory of tidal dissipation could be the scope of an entire thesis manuscript, and before we introduce tides in Chaps. 6 & 7, we dedicate Chap. 5 to the main theory on tidal dissipation. We redefine there some tidal parameters that the literature often makes

use of, namely, the Love numbers and the quality factor. We also give some examples of rheologies and their associated tidal models. In order to include tides in our model as smoothly as possible, we explain in Sect. 5.3 how a pseudo-Hamiltonian formalism can be developed that allows the equations of motion with tides to be derived from the Hamilton equations.

In Chaps. 6 & 7, we include tidal dissipation to the co-orbital $1:1$ mean-motion resonance, and to the $p:p:p+1$ resonance chain, respectively. We prove in Chap. 6 that the co-orbital motion is made unstable by tides, but that the third planet in the chain $p:p:p+1$ often makes the co-orbital pair much more stable. We give analytical expressions of the co-orbital lifetime depending on the parameters of the system. Our work is the first analytical proof of the instability of the Lagrangian equilibria under tides, and the results of Chap. 6 were published in Couturier *et al.* (2021), while those of Chap. 7 were published in Couturier *et al.* (2022). Section 6.4 treats the case of tides raised on the central body and is not yet published.

Notation	Definition	Notation	Definition	Notation	Definition
${}^t.$	transposition	bold	vector	t	time
$\dot{.}$	d/dt	$\circ$	composition	∇f	Eq. (2.2)
∇F	Eq. (2.4)	$\nabla^2 f$	Eq. (2.5)	$\mathcal{L}$	Lagrangian
$\mathcal{H}$	Hamiltonian	$\mathcal{G}$	grav. constant	m_j	mass
$\boldsymbol{q}$	coordinates	$\boldsymbol{p}$	momenta	$\mathbb{I}$	Identity matrix
$\mathbb{J}$	Eq. (2.19)	$\Phi_{\mathcal{H}}$	flow of $\mathcal{H}$ (2.23)	β_j	$m_0 m_j/(m_0+m_j)$
μ_j	$\mathcal{G}\,(m_0+m_j)$	ϖ_j	long. of periapsis	e_j	eccentricity
a_j	semimajor axis	λ_j	mean longitude	Λ_j	(2.49) & (4.10)
D_j	(2.49) & (4.10)	x_j	Eq. (2.50)	X_j	$\sqrt{2/\Lambda_j}\,x_j$
ι	$(m_1+m_2)\,/m_0$	L_χ	Eq. (2.64)	$\{\chi,\cdot\}$	L_χ
$\mathfrak{Re}$	real part	$\mathfrak{Im}$	imaginary part	$\digamma$	Eq. (3.7)
$\bar{a}$	Eq. (3.5)	η	Eq. (3.5)	$\Lambda_j^\star$	(3.6) & (4.5)
ξ	$\lambda_1-\lambda_2$	δ	Eq. (3.14)	δ	Eq. (4.34)
J	(3.18) & (3.20)	J_2	(3.18) & (3.20)	$\mathcal{R}_j$	Eq. (3.20)
f_j	Eq. (3.21)	m	$\sqrt{m_1 m_2}$	Δ	$\sqrt{2-2\cos\xi}$
A_h	Eq. (3.30)	B_h	Eq. (3.30)	ν	Eq. (3.32)
g_1	Eq. (3.42)	g_2	Eq. (3.42)	c	speed of light
$n_j^{(0)}$	Eq. (4.4)	$\xi_{2,3}$	Eq. (4.7)	σ_j	Eq. (4.7)
L,G,Γ	below Eq. (4.7)	$\Gamma^\star$	Eq. (4.9)	C_j	Eq. (4.14)
p	small integer	$C_{p,m}^{(n)}$	Append. (B.2)	F_0	below Eq. (4.21)
ν_2	Eq. (4.24)	ν_3	Eq. (4.30)	ΔG	Eq. (4.35)
$\mathbb{B}$	perturbed body	W	perturbing pot.	V	perturbed pot.
ζ	Eq. (5.16)	k_{lm}	Love number	h	Eq. (5.16)
μ	shear modulus	ρ	density	g	surface gravity
κ_2	Eq. (5.36)	Q	Sect. 5.2.4	Δt	time lag
$.^\star$	Eq. (6.5)	R_j	radius	$\Delta\varsigma$	$\varsigma-\varsigma^\star$
$\qoppa_j$	(6.7) & (7.2)	q_j	$\kappa_2^{(j)}\qoppa_j^5$	Ω	$q_1/Q_1+q_2/Q_2$
$\mathcal{C}_j$	mom. of inertia	α_j	$\mathcal{C}_j/\left(m_j R_j^2\right)$	ϑ_j	Eq. (6.14)
$A_t^{(j)}$	Eq. (6.10)	$B_t^{(j)}$	Eq. (6.10)	$C_t^{(j)}$	Eq. (6.10)
$\sampi_j$	Eq. (6.28)	λ	Eq. (6.28)	λ_{L}	Eq. (6.28)
λ_{AL}	Eq. (6.28)	τ_{L}	Eq. (6.29)	τ_{AL}	Eq. (6.29)
x	m_1/m_2	y	$q_2Q_1/\left(q_1Q_2\right)$	τ_{lib}	Eq. (6.35)
$\Delta\xi$	above Eq. (6.37)	τ_{hs}	Eq. (6.40)	$M_\oplus$	Earth mass
$M_\odot$	Solar mass	$R_\oplus$	Earth radius	$\aleph_p^q$	Eq. (6.59)
$\sampi$	Eq. (6.61)	$\bar{a}_c$	Eq. (6.62)	$\bar{a}_s$	Eq. (6.63)
F	Sect. 7.1.2	ω_j	below Eq. (7.8)	δ_0	$\delta(t=0)$

Table 1.1 — List of the notations used in this manuscript, ordered roughly by first apparition. A subscripted j means *of body number j*. Notations used right after their definition only are not included here. There exists a conflict of notation between δ defined by Eq. (3.14) and δ defined by Eq. (4.34). The conflict does not exist within a same chapter and we believe that no confusion is possible. $\digamma$ (varstigma), $\qoppa$ (qoppa) and $\sampi$ (sampi) are archaic Greek letters.

Chapter 2

Main theory on celestial mechanics and dynamical systems

This chapter establishes the main mathematical framework on celestial mechanics and dynamical systems, that we use throughout the rest of this manuscript.

2.1 Framework

We consider for this chapter a system of $n+1$ point masses m_j $(0 \leq j \leq n)$, moving under the effect of their mutual gravitational interactions. Their positions and speeds in an inertial reference frame are given by $\boldsymbol{r_j}$ and $\dot{\boldsymbol{r}}_{\boldsymbol{j}}$, respectively. In this manuscript, ${}^t\cdot$ denotes the transpose operator and an upper dot denotes d/dt. If p is an integer and f a differentiable scalar field

$$\begin{aligned} f : \mathbb{R}^p &\to \mathbb{R} \\ {}^t(x_1, \cdots, x_p) &\mapsto f({}^t(x_1, \cdots, x_p)), \end{aligned} \tag{2.1}$$

then $\nabla f : \mathbb{R}^p \to \mathbb{R}^p$ is defined as

$$\nabla f = {}^t\left(\frac{\partial f}{\partial x_1}, \cdots, \frac{\partial f}{\partial x_p}\right). \tag{2.2}$$

Writing $\boldsymbol{x}$ for ${}^t(x_1, \cdots, x_p)$, we will also use the notation $\nabla f = \partial f / \partial \boldsymbol{x}$. If $\boldsymbol{x_k}$ represents the subvector ${}^t(x_1, \cdots, x_k)$, where $k \leq p$, then $\nabla_{\boldsymbol{x_k}} f : \mathbb{R}^p \to \mathbb{R}^k$ is defined as

$$\nabla_{\boldsymbol{x_k}} f = {}^t\left(\frac{\partial f}{\partial x_1}, \cdots, \frac{\partial f}{\partial x_k}\right), \tag{2.3}$$

and once again, we will use the notation $\nabla_{\boldsymbol{x_k}} f = \partial f / \partial \boldsymbol{x_k}$. If $F : \mathbb{R}^p \to \mathbb{R}^p$ denotes a differentiable vector field, then, writing $F = (F_1, \cdots, F_p)$, where the F_i are scalar fields

like in Eq. (2.1), the notation ∇F is the Jacobian matrix of F

$$\nabla F = \begin{pmatrix} \dfrac{\partial F_1}{\partial x_1} & \cdots & \dfrac{\partial F_1}{\partial x_p} \\ \vdots & & \vdots \\ \dfrac{\partial F_p}{\partial x_1} & \cdots & \dfrac{\partial F_p}{\partial x_p} \end{pmatrix}. \tag{2.4}$$

Finally, if f is twice differentiable, we denote $\nabla^2 f$ the Hessian matrix of f, that is

$$\nabla^2 f = \begin{pmatrix} \dfrac{\partial^2 f}{\partial x_1 \partial x_1} & \cdots & \dfrac{\partial^2 f}{\partial x_1 \partial x_p} \\ \vdots & & \vdots \\ \dfrac{\partial^2 f}{\partial x_p \partial x_1} & \cdots & \dfrac{\partial^2 f}{\partial x_p \partial x_p} \end{pmatrix}. \tag{2.5}$$

2.1.1 Lagrangian formalism

We denote $\boldsymbol{q} = {}^t(\boldsymbol{r_0}, ..., \boldsymbol{r_n})$ and $\dot{\boldsymbol{q}} = {}^t(\dot{\boldsymbol{r}}_{\boldsymbol{0}}, ..., \dot{\boldsymbol{r}}_{\boldsymbol{n}})$. The Lagrangian of the system is defined as $\mathcal{L} = \mathcal{T} - \mathcal{U}$, where $\mathcal{T}$ and $\mathcal{U}$ are the kinetic and potential energies, respectively. They read

$$\mathcal{T} = \sum_{j=0}^{n} \frac{1}{2} m_j \dot{\boldsymbol{r}}_{\boldsymbol{j}} \cdot \dot{\boldsymbol{r}}_{\boldsymbol{j}} \quad \text{and} \quad \mathcal{U} = -\sum_{i=0}^{n} \sum_{j=i+1}^{n} \frac{\mathcal{G} m_i m_j}{|\boldsymbol{r_i} - \boldsymbol{r_j}|}, \tag{2.6}$$

where $\mathcal{G}$ is the gravitational constant. We define $\boldsymbol{x} = {}^t(\boldsymbol{q}, \dot{\boldsymbol{q}})$. The state $\boldsymbol{x}(t)$ of the system at time t is given by a point in $\mathbb{R}^{6n+6}$, and its evolution from $t = t_0$ to $t = t_1$ is a path

$$\begin{aligned} \gamma : [t_0, t_1] &\to \mathbb{R}^{6n+6} \\ t &\mapsto \boldsymbol{x}(t). \end{aligned} \tag{2.7}$$

The action $\mathcal{S}(\gamma)$ of the path γ is defined as

$$\mathcal{S}(\gamma) = \int_{t_0}^{t_1} \mathcal{L}(\boldsymbol{q}, \dot{\boldsymbol{q}}) dt, \tag{2.8}$$

and, according to the least action principle, the path actually followed by the system extremizes $\mathcal{S}$, that is

$$\frac{\delta \mathcal{S}}{\delta \gamma}(\boldsymbol{h}) := \lim_{\varepsilon \to 0} \frac{\mathcal{S}(\gamma + \varepsilon \boldsymbol{h}) - \mathcal{S}(\gamma)}{\varepsilon} = 0, \tag{2.9}$$

for every loop $\boldsymbol{h} : [t_0, t_1] \to \mathbb{R}^{6n+6}$ such that $\boldsymbol{h}(t_0) = \boldsymbol{h}(t_1) = 0$. Writing $\boldsymbol{h} = \left(h, \dot{h}\right) \in ([t_0, t_1] \to \mathbb{R}^{3n+3})^2$, we obtain

$$\frac{\delta \mathcal{S}}{\delta \gamma}(\boldsymbol{h}) = \int_{t_0}^{t_1} \frac{\partial \mathcal{L}}{\partial \boldsymbol{q}} \cdot h(t) + \frac{\partial \mathcal{L}}{\partial \dot{\boldsymbol{q}}} \cdot \dot{h}(t)\, dt, \tag{2.10}$$

and taking advantage of $h(t_0) = h(t_1) = 0$, an integration by part yields

$$\frac{\delta \mathcal{S}}{\delta \gamma}(\boldsymbol{h}) = \int_{t_0}^{t_1} \left(\frac{\partial \mathcal{L}}{\partial \boldsymbol{q}} - \frac{d}{dt} \frac{\partial \mathcal{L}}{\partial \dot{\boldsymbol{q}}} \right) \cdot h(t)\, dt = 0. \tag{2.11}$$

Since Eq. (2.11) is verified for any choice of the loop $\boldsymbol{h}$, the least action principle is equivalent to the Euler-Lagrange equation

$$\frac{\partial \mathcal{L}}{\partial \boldsymbol{q}} - \frac{d}{dt}\frac{\partial \mathcal{L}}{\partial \dot{\boldsymbol{q}}} = 0. \tag{2.12}$$

Substituting Eq. (2.6) into Eq. (2.12) yields Newton's law of gravitation

$$\ddot{\boldsymbol{r}}_{\boldsymbol{k}} = -\sum_{j \neq k} \frac{\mathcal{G} m_j}{|\boldsymbol{r}_{\boldsymbol{k}} - \boldsymbol{r}_{\boldsymbol{j}}|^3} \left(\boldsymbol{r}_{\boldsymbol{k}} - \boldsymbol{r}_{\boldsymbol{j}}\right), \tag{2.13}$$

but the Euler-Lagrange equation applies to many domains. As an example, the equation of geodesics in general relativity can be retrieved from Eq. (2.12) using[1] $\mathcal{L} = {}^t\boldsymbol{u}\boldsymbol{g}\boldsymbol{u}$, where $\boldsymbol{g}$ is the spacetime metric.

2.1.2 Hamiltonian formalism

Given a Lagrangian $\mathcal{L}(\boldsymbol{q}, \dot{\boldsymbol{q}})$, the generalized momenta $\boldsymbol{p}_j$ are defined as

$$\boldsymbol{p} = {}^t\left(\boldsymbol{p}_0, ..., \boldsymbol{p}_n\right) = \frac{\partial \mathcal{L}}{\partial \dot{\boldsymbol{q}}}, \tag{2.14}$$

while the Hamiltonian $\mathcal{H}$ is given by the Legendre transformation

$$\mathcal{H} = \boldsymbol{p} \cdot \dot{\boldsymbol{q}} - \mathcal{L}. \tag{2.15}$$

Substituting Eq. (2.14) into the differential of Eq. (2.15) yields

$$d\mathcal{H} = \dot{\boldsymbol{q}} \cdot d\boldsymbol{p} - \frac{\partial \mathcal{L}}{\partial \boldsymbol{q}} \cdot d\boldsymbol{q}, \tag{2.16}$$

showing that $\mathcal{H}(\boldsymbol{p}, \boldsymbol{q})$ depends only on $\boldsymbol{p}$ and $\boldsymbol{q}$, and giving

$$\dot{\boldsymbol{q}} = \frac{\partial \mathcal{H}}{\partial \boldsymbol{p}} \quad \text{and} \quad \frac{\partial \mathcal{H}}{\partial \boldsymbol{q}} = -\frac{\partial \mathcal{L}}{\partial \boldsymbol{q}}. \tag{2.17}$$

Combining together Eqs. (2.12), (2.14) & (2.17), we obtain the Hamilton equations

$$\dot{\boldsymbol{q}} = \frac{\partial \mathcal{H}}{\partial \boldsymbol{p}} \quad \text{and} \quad \dot{\boldsymbol{p}} = -\frac{\partial \mathcal{H}}{\partial \boldsymbol{q}}. \tag{2.18}$$

The vector $X = {}^t\left(\boldsymbol{p}, \boldsymbol{q}\right)$ belongs to a $6\left(n+1\right)$ dimensional space, called phase space of the system. The number of degrees of freedom of the system, that we denote N, is defined as half the dimension of the phase space. The Hamilton equations are often written under the compact form

$$\dot{X} = \mathbb{J}\nabla\mathcal{H}(X) = \left(\begin{array}{c|c} 0 & -\mathbb{I}_N \\ \hline \mathbb{I}_N & 0 \end{array}\right) \begin{pmatrix} \partial\mathcal{H}/\partial\boldsymbol{p} \\ \partial\mathcal{H}/\partial\boldsymbol{q} \end{pmatrix}. \tag{2.19}$$

[1] with $\boldsymbol{u} = {}^t\left(\frac{dt}{d\tau}, \frac{dx}{d\tau}, \frac{dy}{d\tau}, \frac{dz}{d\tau}\right)$, τ the proper time and $d/d\tau$ instead of d/dt in Eq. (2.12).

2.1.3 Canonical transformation

When studying the dynamics of a planetary system, arbitrary changes of variables do not preserve, a priori, the form of the Hamilton equations. A transformation

$$\begin{aligned} \Psi : \mathbb{R}^{2N} &\to \mathbb{R}^{2N} \\ X &\mapsto Y \end{aligned} \tag{2.20}$$

is said to be canonical if it verifies

$$\dot{X} = \mathbb{J}\nabla\mathcal{H}(X) \quad \Rightarrow \quad \dot{Y} = \mathbb{J}\nabla\tilde{\mathcal{H}}(Y), \tag{2.21}$$

where $\tilde{\mathcal{H}} = \mathcal{H} \circ \Psi^{-1}$. That is, Ψ is canonical if it preserves the form of Eqs. (2.18). We denote $\mathcal{M} = \nabla\Psi = (\partial Y_i/\partial X_j)_{1\leq i,j\leq 2N}$ the Jacobian matrix of Ψ. Verifying that $\dot{Y} = \mathcal{M}\dot{X}$ and $\nabla\mathcal{H}(X) = {}^t\mathcal{M}\nabla\tilde{\mathcal{H}}(Y)$, and combining with Eq. (2.19), we obtain

$$\dot{Y} = \mathcal{M}\mathbb{J}\,{}^t\mathcal{M}\nabla\tilde{\mathcal{H}}(Y). \tag{2.22}$$

A matrix $\mathcal{Q}$ is said to be symplectic if[2] $\mathcal{Q}\mathbb{J}\,{}^t\mathcal{Q} = \mathbb{J}$. As a consequence, a transformation is canonical if, and only if, its Jacobian is symplectic.

The flow of $\mathcal{H}(X)$ is defined as the application

$$\begin{aligned} \Phi_{\mathcal{H}} : \mathbb{R} \times \mathbb{R}^{2N} &\to \mathbb{R}^{2N} \\ (t, X_0) &\mapsto X(t), \end{aligned} \tag{2.23}$$

where $X(t)$ is the unique solution to the Cauchy problem $\dot{X} = \mathbb{J}\nabla\mathcal{H}(X)$ with initial condition $X(0) = X_0$. We can give a sufficient condition of canonicity using the notion of flow. A transformation $\Psi : \mathbb{R}^{2N} \to \mathbb{R}^{2N}$ is canonical if there exists a scalar $t \in \mathbb{R}$ and a Hamiltonian $\chi : \mathbb{R}^{2N} \to \mathbb{R}$, called generator of Ψ, such that (Morbidelli, 2002, Sect. 1.6)

$$\Psi = \Phi_\chi(t, \cdot). \tag{2.24}$$

This result can be proven in two steps :

- We first prove that the Jacobian matrix $\mathcal{M}(t) = \nabla\Phi_\chi(t, X)$ of the transformation verifies the differential equation $\dot{\mathcal{M}} = \mathbb{J}S\mathcal{M}$, where S is a symmetrical matrix.
- We then prove that $\mathcal{M}$ is symplectic, which ends the demonstration, since we already proved that a transformation is canonical if, and only if, its Jacobian is symplectic.

First step

The new set of variables $Y(t) = \Psi(X(t)) = \Phi_\chi(t, X)$ is given by the flow of χ, thus we have

$$\frac{d}{dt}\Phi_\chi(t, X) = \mathbb{J}\nabla\chi(\Phi_\chi(t, X)). \tag{2.25}$$

If we evaluate Eq. (2.25) at $X + dX$, where dX is a small displacement of the initial condition, a first-order Taylor expansion gives

$$\frac{d}{dt}\left(\Phi_\chi(t, X) + \mathcal{M}(t)dX\right) = \mathbb{J}\nabla\chi\left(\Phi_\chi(t, X) + \mathcal{M}(t)dX\right). \tag{2.26}$$

[2] Or equivalently, if ${}^t\mathcal{Q}\mathbb{J}\mathcal{Q} = \mathbb{J}$, since $\mathbb{J}^2 = -\mathbb{I}_{2N}$.

Another Taylor expansion in the right-hand side yields $\dot{\mathcal{M}}(t)dX = \mathbb{J}S(t)\mathcal{M}(t)dX$, where

$$S(t) = \nabla^2\chi\left(\Phi_\chi(t, X)\right) \tag{2.27}$$

is the Hessian of χ (Eq. (2.5)), evaluated at $\Phi_\chi(t, X)$, which is a symmetrical matrix. This last equation being valid for any value of dX, we obtain

$$\dot{\mathcal{M}}(t) = \mathbb{J}S(t)\mathcal{M}(t). \tag{2.28}$$

Second step

The condition stating that $\mathcal{M}$ is symplectic is ${}^t\mathcal{M}\mathbb{J}\mathcal{M} = \mathbb{J}$. We have

$$\frac{d}{dt}\left({}^t\mathcal{M}\mathbb{J}\mathcal{M}\right) = {}^t\dot{\mathcal{M}}\mathbb{J}\mathcal{M} + {}^t\mathcal{M}\mathbb{J}\dot{\mathcal{M}} = {}^t\mathcal{M}\left({}^tS\,{}^t\mathbb{J}\mathbb{J} + \mathbb{J}^2S\right)\mathcal{M} = 0, \tag{2.29}$$

where we used Eq. (2.28) for the second equality and ${}^t\mathbb{J}\mathbb{J} = \mathbb{I} = -\mathbb{J}^2$ for the third one. Integrating both sides of Eq. (2.29) with respect to time and using $\mathcal{M}(0) = \mathbb{I}$, we obtain

$${}^t\mathcal{M}\mathbb{J}\mathcal{M} = \mathbb{J}, \tag{2.30}$$

and $\mathcal{M}(t)$ is symplectic, and $X \mapsto \Phi_\chi(t, X)$ is canonical.

This sufficient condition for canonicity will be very useful in Sect. 2.2.2, where we introduce Lie series. We can give another sufficient condition for canonicity, very useful in practice. If $\Psi : \mathbb{R}^{2N} \mapsto \mathbb{R}^{2N}$ is linear and takes the form

$$\Psi : \begin{pmatrix}\boldsymbol{p}\\ \boldsymbol{q}\end{pmatrix} \mapsto \left(\begin{array}{c|c} \mathcal{A} & 0 \\ \hline 0 & {}^t\mathcal{A}^{-1}\end{array}\right)\begin{pmatrix}\boldsymbol{p}\\ \boldsymbol{q}\end{pmatrix} = \nabla\Psi\begin{pmatrix}\boldsymbol{p}\\ \boldsymbol{q}\end{pmatrix}, \tag{2.31}$$

where $\mathcal{A}$ is any $N \times N$ non-degenerate matrix, then it is canonical. This is readily seen by checking that the Jacobian $\nabla\Psi$ is symplectic. We end this section by showing that a Hamiltonian $\mathcal{H}(\boldsymbol{p}, \boldsymbol{q})$ is conserved along its own flow. Indeed, we have

$$\frac{d\mathcal{H}}{dt} = \frac{\partial\mathcal{H}}{\partial\boldsymbol{p}}\cdot\dot{\boldsymbol{p}} + \frac{\partial\mathcal{H}}{\partial\boldsymbol{q}}\cdot\dot{\boldsymbol{q}} = \dot{\boldsymbol{q}}\cdot\dot{\boldsymbol{p}} - \dot{\boldsymbol{p}}\cdot\dot{\boldsymbol{q}} = 0. \tag{2.32}$$

2.1.4 Two-body problem & Poincaré variables

The two-body problem

Combining Eqs. (2.6), (2.14) & (2.15), the Hamiltonian of the two-body problem can be written

$$\mathcal{H}_{2BP}(\boldsymbol{p}, \boldsymbol{q}) = \frac{\boldsymbol{p_0}\cdot\boldsymbol{p_0}}{2m_0} + \frac{\boldsymbol{p_1}\cdot\boldsymbol{p_1}}{2m_1} - \frac{\mathcal{G}m_0m_1}{|\boldsymbol{q_0} - \boldsymbol{q_1}|}. \tag{2.33}$$

This Hamiltonian has 6 degrees of freedom, and 3 of them can be eliminated by performing the canonical[3] transformation

$$(\boldsymbol{q_0}, \boldsymbol{q_1}; \boldsymbol{p_0}, \boldsymbol{p_1}) \mapsto (\boldsymbol{r_0}, \boldsymbol{r}; \tilde{\boldsymbol{r}}_0, \tilde{\boldsymbol{r}}) = (\boldsymbol{q_0}, \boldsymbol{q_1} - \boldsymbol{q_0}; \boldsymbol{p_0} + \boldsymbol{p_1}, \boldsymbol{p_1}). \tag{2.34}$$

[3] It has the form (2.31).

The new Hamiltonian does not depend on $\boldsymbol{r_0}$, and given Eqs. (2.18), this means that $\tilde{\boldsymbol{r}}_{\boldsymbol{0}} = \boldsymbol{p_0} + \boldsymbol{p_1}$ is constant. Terms depending only on $\tilde{\boldsymbol{r}}_{\boldsymbol{0}}$ can therefore be removed from the Hamiltonian, since their gradient is zero. We obtain

$$\mathcal{H}_{2BP}(\tilde{\boldsymbol{r}}, \boldsymbol{r}) = \frac{\tilde{\boldsymbol{r}}^2}{2\beta} - \frac{\tilde{\boldsymbol{r}}_{\boldsymbol{0}} \cdot \tilde{\boldsymbol{r}}}{m_0} - \frac{\mathcal{G} m_0 m_1}{r}, \tag{2.35}$$

where $\beta = m_0 m_1 / (m_0 + m_1)$. The Hamiltonian can be further simplified by the translation[4] $\hat{\boldsymbol{r}} = \tilde{\boldsymbol{r}} - \beta \tilde{\boldsymbol{r}}_{\boldsymbol{0}} / m_0$. This yields

$$\mathcal{H}_{2BP}(\hat{\boldsymbol{r}}, \boldsymbol{r}) = \frac{\hat{\boldsymbol{r}}^2}{2\beta} - \frac{\mathcal{G} m_0 m_1}{r}. \tag{2.36}$$

The Hamiltonian $\mathcal{H}_{2BP}$ in Eq. (2.36) still has 3 degrees of freedom, but we can additionally eliminate two of them. We first notice that the angular momentum $\boldsymbol{G} = \boldsymbol{r} \times \hat{\boldsymbol{r}}$ is conserved

$$\frac{d\boldsymbol{G}}{dt} = \dot{\boldsymbol{r}} \times \hat{\boldsymbol{r}} + \boldsymbol{r} \times \frac{d\hat{\boldsymbol{r}}}{dt} = \frac{1}{\beta} \hat{\boldsymbol{r}} \times \hat{\boldsymbol{r}} - \frac{\mathcal{G} m_0 m_1}{r^3} \boldsymbol{r} \times \boldsymbol{r} = 0. \tag{2.37}$$

By definition of the cross product, $\boldsymbol{G}$ is perpendicular to both $\boldsymbol{r}$ and $\hat{\boldsymbol{r}}$. As a consequence, the motion occurs in a plane perpendicular to $\boldsymbol{G}$ containing the origin, and the Hamiltonian $\mathcal{H}_{2BP}$ is thus reduced to two degrees of freedom. We write

$$\boldsymbol{r} = {}^t(u, v) \quad \text{and} \quad \hat{\boldsymbol{r}} = {}^t(\hat{u}, \hat{v}), \tag{2.38}$$

where u and v (*resp.* $\hat{u}$ and $\hat{v}$) are the cartesian coordinates of $\boldsymbol{r}$ (*resp.* $\hat{\boldsymbol{r}}$) in the orbital plane. The transformation to the polar coordinates $(u, v; \hat{u}, \hat{v}) \mapsto (r, \varphi; \tilde{r}, \Phi)$, where

$$u = r\cos\varphi, \quad v = r\sin\varphi; \quad \tilde{r} = \frac{u\hat{u} + v\hat{v}}{r} \quad \text{and} \quad \Phi = u\hat{v} - v\hat{u}, \tag{2.39}$$

is canonical (Meyer and Hall, 2009, Sect. 7.4). By definition of the cross product, Φ is the norm of the total angular momentum

$$\Phi = |\boldsymbol{r} \times \hat{\boldsymbol{r}}| = |\boldsymbol{G}| = G. \tag{2.40}$$

Since $G = \Phi$ is conserved, the Hamiltonian $\mathcal{H}_{2BP}$ (Eq. (2.36)) in the new coordinates does not depend on φ and reads

$$\mathcal{H}_{2BP}(\tilde{r}, r) = \frac{1}{2\beta}\left(\tilde{r}^2 + \frac{G^2}{r^2}\right) - \frac{\mathcal{G} m_0 m_1}{r}. \tag{2.41}$$

We are reduced to one degree of freedom. The canonical coordinates $(r, \varphi; \tilde{r}, G)$, where φ is the true anomaly, are the Hill coordinates (Hill, 1913; Laskar, 2017).

[4] The Jacobian is identity, and the identity is symplectic, so it is a canonical transformation.

Poincaré variables

The form of Hamilton Eqs. (2.18) shows that the flow of a Hamiltonian $\mathcal{H} = \mathcal{H}(\boldsymbol{p})$ depending only on the momenta is trivial. It is given by

$$\boldsymbol{p}(t) = \boldsymbol{p}(0) \quad \text{and} \quad \boldsymbol{q}(t) = \boldsymbol{q}(0) + t\boldsymbol{\omega_0} = \boldsymbol{q}(0) + t\frac{\partial \mathcal{H}}{\partial \boldsymbol{p}}. \tag{2.42}$$

We now transform the Hamiltonian of the two-body problem so that it only depends on the momentum. We know since Newton that the orbit is a conic[5]

$$r(\varphi) = \frac{a\,(1-e)\,(1+e)}{1+e\cos\varphi}, \tag{2.43}$$

where a is the semimajor axis of the conic and e its eccentricity. At the periapsis ($\varphi = 0$) and apoapsis ($\varphi = \pi$), the value of r is

$$r_p = a\,(1-e) \quad \text{and} \quad r_a = a\,(1+e)\,. \tag{2.44}$$

Furthermore, at these points in the trajectory, r reaches an extremum and $\tilde{r} = \beta\dot{r}$ is zero. The conservation of the Hamiltonian along the trajectory (Eq. (2.32)) allows us to write $\mathcal{H}_{2BP}(0, r_p) = \mathcal{H}_{2BP}(0, r_a)$, which yields

$$G = \beta\sqrt{\mu a\,(1-e^2)}, \quad \text{where} \quad \mu = \mathcal{G}\,(m_0 + m_1)\,. \tag{2.45}$$

Evaluating the Hamiltonian at the periapsis, or at the apoapsis, gives

$$\mathcal{H}_{2BP}(a) = -\frac{\mu\beta}{2a}, \tag{2.46}$$

and $\mathcal{H}_{2BP}$ depends only on a. However, the transformation to the elliptic elements $(\hat{\boldsymbol{r}}; \boldsymbol{r}) \mapsto (a, e, i; M, \omega, \Omega)$, where M is the mean anomaly[6], i the inclination of the orbit, ω the argument of the pericentre and Ω the longitude of the ascending node, is not canonical. Delaunay (1861) & Andoyer (1923) solve the problem by introducing the canonical transformation $(\hat{\boldsymbol{r}}; \boldsymbol{r}) \mapsto (L, G, H; M, \omega, \Omega)$, where Delaunay variables read

$$\left.\begin{aligned} \Lambda &= \beta\sqrt{\mu a} \\ G &= \beta\sqrt{\mu a\,(1-e^2)} \\ H &= G\cos i \end{aligned}\right| \begin{aligned} &M, \\ &\omega, \\ &\Omega. \end{aligned} \tag{2.47}$$

See Laskar (2017) for a proof of canonicity. In Delaunay coordinates, the Hamiltonian takes the expression

$$\mathcal{H}_{2BP}(\Lambda) = -\frac{\mu^2\beta^3}{2\Lambda^2}. \tag{2.48}$$

This Hamiltonian has one degree of freedom and depends only on the momenta. All the Delaunay coordinates are thus constant, except $M(t) = nt = t\partial\mathcal{H}_{2BP}/\partial\Lambda = \mu^2\beta^3 t/\Lambda^3$ which evolves linearly with time. To avoid the equality of momenta when either e or i

[5] This comes from the conservation of the eccentricity vector $\boldsymbol{e} = (m_0 + m_1)\,\hat{\boldsymbol{r}} \times \boldsymbol{G}/\left(\mathcal{G}m_0^2 m_1^2\right) - \boldsymbol{r}/r$.
[6] Defined as $M(t) = 2\pi t/T$, where T is the period of the orbit.

is zero, we introduce Poincaré polar coordinates through a canonical linear change of variable of the form (2.31)

$$\left|\begin{array}{l} \Lambda = \beta\sqrt{\mu a} \\ D = \Lambda - G = \Lambda\left(1-\sqrt{1-e^2}\right) \\ \mathfrak{V} = G - H = G\left(1-\cos i\right) \end{array}\right| \left|\begin{array}{l} \lambda = M + \varpi, \\ -\varpi = -\omega - \Omega, \\ -\Omega, \end{array}\right. \tag{2.49}$$

where λ and ϖ are the mean longitude and longitude of the pericentre, respectively. In the rest of this manuscript, we only consider the planar case, and we do not use the variables $\mathfrak{V}$ and Ω. We can also adopt complex Poincaré variables with the canonical transformation

$$(D; -\varpi) \mapsto \left(x = \sqrt{D}\exp(i\varpi); -i\bar{x}\right), \tag{2.50}$$

where the upper bar denotes the complex conjugated. In Chap. 3, we start from Poincaré complex variables, while we rather use the polar Poincaré variables in Chap. 4.

2.2 The $(n+1)$-body problem

2.2.1 Decomposition of the Hamiltonian

We combine Eqs (2.6), (2.14) & (2.15) to give the Hamiltonian of the $(n+1)$-body problem under the form

$$\mathcal{H}(\tilde{\boldsymbol{u}}, \boldsymbol{u}) = \sum_{j=0}^{n} \frac{\tilde{\boldsymbol{u}}_{\boldsymbol{j}} \cdot \tilde{\boldsymbol{u}}_{\boldsymbol{j}}}{2m_j} - \sum_{j=0}^{n}\sum_{i=j+1}^{n} \frac{\mathcal{G}m_i m_j}{|\boldsymbol{u}_{\boldsymbol{i}} - \boldsymbol{u}_{\boldsymbol{j}}|}. \tag{2.51}$$

As for the two-body problem, three degrees of freedom can be eliminated by identifying body j with respect to body 0, for $j \neq 0$. We thus perform the transformation

$$\boldsymbol{u}_{\boldsymbol{j}} \mapsto \boldsymbol{r}_{\boldsymbol{j}} = \boldsymbol{u}_{\boldsymbol{j}} - \boldsymbol{u}_{\boldsymbol{0}} \text{ if } j \neq 0, \quad \text{and} \quad \boldsymbol{u}_{\boldsymbol{0}} \mapsto \boldsymbol{r}_{\boldsymbol{0}} = \boldsymbol{u}_{\boldsymbol{0}}. \tag{2.52}$$

The transformation is made canonical by transforming the momenta $\tilde{\boldsymbol{u}}_{\boldsymbol{j}} \mapsto \tilde{\boldsymbol{r}}_{\boldsymbol{j}}$ according to Eq. (2.31). The resulting Hamiltonian does not depend on $\boldsymbol{r}_{\boldsymbol{0}}$ and $\tilde{\boldsymbol{r}}_{\boldsymbol{0}}$ is constant. It contains terms of the form $\tilde{\boldsymbol{r}}_{\boldsymbol{0}} \cdot \tilde{\boldsymbol{r}}_{\boldsymbol{j}}$, and those can be eliminated by an extension of the translation of momenta that we performed for the two body problem. We obtain the $3n$ degrees of freedom Hamiltonian (Laskar and Robutel, 1995)

$$\mathcal{H}(\tilde{\boldsymbol{r}}, \boldsymbol{r}) = \sum_{j=1}^{n}\left(\frac{\tilde{\boldsymbol{r}}_{\boldsymbol{j}}^{\,2}}{2\beta_j} - \frac{\mathcal{G}m_0 m_j}{r_j}\right) + \sum_{j=1}^{n}\sum_{i=j+1}^{n}\left(\frac{\tilde{\boldsymbol{r}}_{\boldsymbol{i}} \cdot \tilde{\boldsymbol{r}}_{\boldsymbol{j}}}{m_0} - \frac{\mathcal{G}m_i m_j}{|\boldsymbol{r}_{\boldsymbol{i}} - \boldsymbol{r}_{\boldsymbol{j}}|}\right), \tag{2.53}$$

where $\beta_j = m_0 m_j / (m_0 + m_j)$. The first term of the Hamiltonian is a sum of two-body Hamiltonians like (2.36), and according to Eq. (2.48), Eq. (2.53) can be written in Poincaré polar coordinates as

$$\mathcal{H}(\boldsymbol{\Lambda}, \boldsymbol{D}; \boldsymbol{\lambda}, -\boldsymbol{\varpi}) = \mathcal{H}_K(\boldsymbol{\Lambda}) + \iota\mathcal{H}_P(\boldsymbol{\Lambda}, \boldsymbol{D}; \boldsymbol{\lambda}, -\boldsymbol{\varpi}), \tag{2.54}$$

where we restricted ourselves to the planar case[7],

$$\mathcal{H}_K(\boldsymbol{\Lambda}) = -\sum_{j=1}^{n} \frac{\beta_j^3 \mu_j^2}{2\Lambda_j^2}, \tag{2.55}$$

[7] And so, the Hamiltonian (2.54) has only $2n$ degrees of freedom.

and $\mu_j = \mathcal{G}(m_0 + m_j)$. In most practical problems of planetary dynamics, one body is much more massive than the others, and $m_j \ll m_0$, for $j \neq 0$. The Hamiltonian (2.54) is thus a sum of Kepler problems, perturbed by $\iota\mathcal{H}_P$. The Keplerian Hamiltonian $\mathcal{H}_K$ contains, for instance, star−planet interactions while $\iota\mathcal{H}_P$ contains the planet−planet interactions. The dimensionless parameter ι is defined as

$$\iota = \frac{m_1 + m_2 + ... + m_n}{m_0}, \tag{2.56}$$

and is introduced to emphasize the fact that the perturbation is much smaller than the sum of Kepler problems. Contrary to the Keplerian part, the perturbation $\iota\mathcal{H}_P$ cannot be given analytically as a function of the Poincaré coordinates, but Laskar and Robutel (1995) give the expansion

$$\iota\mathcal{H}_P = \sum_{i=1}^{n} \sum_{j=i+1}^{n} \iota\mathcal{H}_{i,j}, \tag{2.57}$$

where

$$\iota\mathcal{H}_{i,j} = \sum_{\boldsymbol{k}\in\mathbb{Z}^2} \left(\sum_{\boldsymbol{q}\in\mathbb{N}^4} \Xi(\Lambda_i, \Lambda_j) X_i^{q_1} X_j^{q_2} \bar{X}_i^{q_3} \bar{X}_j^{q_4} \right) e^{i(k_1\lambda_i + k_2\lambda_j)} \tag{2.58}$$

corresponds to the interaction between planet i and planet j. In this expression, $X_j = \sqrt{2/\Lambda_j}\, x_j = e_j e^{i\varpi_j} + \mathcal{O}(e_j^3)$, where x_j is the complex Poincaré coordinate introduced by Eq. (2.50). Most of the coefficients $\Xi(\Lambda_i, \Lambda_j)$ are zero. Indeed, the conservation of the total angular momentum implies that the Hamiltonian is invariant by the transformation[8] $(\lambda_i, \lambda_j, \varpi_i, \varpi_j) \mapsto (\lambda_i + \vartheta, \lambda_j + \vartheta, \varpi_i + \vartheta, \varpi_j + \vartheta)$, where ϑ is any constant angle. Injecting this transformation into Eq. (2.58) shows that, for a non-zero Ξ, the tuples $\boldsymbol{k} = (k_1, k_2) \in \mathbb{Z}^2$ and $\boldsymbol{q} = (q_1, q_2, q_3, q_4) \in \mathbb{N}^4$ comply with the d'Alembert rule

$$k_1 + k_2 + q_1 + q_2 - q_3 - q_4 = 0. \tag{2.59}$$

2.2.2 Perturbation theory : Lie serie expansion

We suppose in this subsection that we are facing a N degrees of freedom Hamiltonian similar to that of Eq. (2.54)

$$\mathcal{H}(\boldsymbol{I}, \boldsymbol{\theta}) = \mathcal{H}_0(\boldsymbol{I}) + \iota\mathcal{H}_1(\boldsymbol{I}, \boldsymbol{\theta}), \tag{2.60}$$

where $\boldsymbol{I} = (I_1, ..., I_N)$ is the vector of momenta (also called actions), while $\boldsymbol{\theta} = (\theta_1, ..., \theta_N)$ are the associated angular coordinates. Since ι is much smaller than unity, this Hamiltonian depends almost only on the momenta, and if $\iota\mathcal{H}_1$ were to be neglected, it would be trivially integrated by Eq. (2.42). We assume that among the angles of $\boldsymbol{\theta}$, one of them, say θ_1, is circulating at high frequency and we would like to lose one degree of freedom and simplify the dynamics by averaging[9] the Hamiltonian over it. In other words, we want to find a canonical transformation

$$\begin{aligned} \Psi : \mathbb{R}^{2N} &\to \mathbb{R}^{2N} \\ (\boldsymbol{I}, \boldsymbol{\theta}) &\mapsto (\boldsymbol{J}, \boldsymbol{\varphi}), \end{aligned} \tag{2.61}$$

[8] This is an occurence of Noether's theorem.

[9] The procedure is readily generalized when several (or all) angles are averaged.

close to the identity, such that

$$\check{\mathcal{H}}(\boldsymbol{J},\boldsymbol{\varphi}) = \mathcal{H}(\boldsymbol{I},\boldsymbol{\theta}) = \check{\mathcal{H}}_0(\boldsymbol{J}) + \iota\check{\mathcal{H}}_1(\boldsymbol{J},\varphi_2,..,\varphi_N) + \iota^2\check{\mathcal{H}}_2(\boldsymbol{J},\boldsymbol{\varphi}), \tag{2.62}$$

where $\check{\mathcal{H}} = \mathcal{H}\circ\Psi^{-1}$. The dependency on φ_1 is thus pushed at the second order in ι, and at first order, the subsequent Hamiltonian has only $N-1$ degrees of freedom left. To ensure a canonical transformation, we choose (Eq. (2.24))

$$\Psi = \Phi_{\iota\chi}(-1,\cdot), \quad \text{or equivalently} \quad \Psi^{-1} = \Phi_{\iota\chi}(1,\cdot), \tag{2.63}$$

where $\iota\chi$ is a generator that we will constrain to achieve the form (2.62). Once again, ι is written to emphasize the order of magnitude of the generator. Such an order of magnitude makes sure that Ψ is ι-close to the identity. We define the Lie derivative of $\chi(\boldsymbol{J},\boldsymbol{\varphi})$ as the time derivative along the flow generated by χ

$$L_\chi := \frac{\partial\chi}{\partial\boldsymbol{J}}\cdot\frac{\partial}{\partial\boldsymbol{\varphi}} - \frac{\partial\chi}{\partial\boldsymbol{\varphi}}\cdot\frac{\partial}{\partial\boldsymbol{J}} = \dot{\boldsymbol{\varphi}}\cdot\frac{\partial}{\partial\boldsymbol{\varphi}} + \dot{\boldsymbol{J}}\cdot\frac{\partial}{\partial\boldsymbol{J}} = \left.\frac{d}{dt}\right|_\chi. \tag{2.64}$$

The Lie derivative often appears written $L_\chi = \{\chi,\cdot\}$ in the literature[10]. We can now give for $\check{\mathcal{H}}$ the expression

$$\check{\mathcal{H}} = \mathcal{H}\circ\Psi^{-1} = \mathcal{H}\circ\Phi_{\iota\chi}(1,\cdot) = \sum_{j=0}^{+\infty}\frac{L_{\iota\chi}^{(j)}}{j!}(\mathcal{H}) = e^{\iota L_\chi}(\mathcal{H}), \tag{2.65}$$

where $L_{\iota\chi}^{(j)}$ denotes the j^{th} iteration of the Lie derivative, or the j^{th} time-derivative along the flow of $\iota\chi$. Let us expand Eq. (2.65) at second order in ι. We obtain

$$\check{\mathcal{H}}_0 + \iota\check{\mathcal{H}}_1 + \iota^2\check{\mathcal{H}}_2 = \mathcal{H}_0 + \iota\left(\mathcal{H}_1 + \{\chi,\mathcal{H}_0\}\right) + \iota^2\left(\{\chi,\mathcal{H}_1\} + \frac{1}{2}\{\chi,\{\chi,\mathcal{H}_0\}\}\right), \tag{2.66}$$

where, given Eq. (2.65), the different Poisson brackets are evaluated in the new variables. This yields the following equation, said cohomological, to constrain the generator

$$\mathcal{H}_1 - \check{\mathcal{H}}_1 = \{\mathcal{H}_0,\chi\}, \tag{2.67}$$

where we impose on $\check{\mathcal{H}}_1$ to be the average of $\mathcal{H}_1$ over φ_1

$$\check{\mathcal{H}}_1 = \frac{1}{2\pi}\int_0^{2\pi}\mathcal{H}_1(\boldsymbol{J},\boldsymbol{\varphi})d\varphi_1. \tag{2.68}$$

The cohomological Eq. (2.67) allows χ to be constrained, and $\check{\mathcal{H}}_2$ to be subsequently determined with Eq. (2.66). The dependency on φ_1 can be pushed to even larger orders of ι by repeating the procedure. The Hamiltonian $\check{\mathcal{H}}_0 + \iota\check{\mathcal{H}}_1$ becomes the new principal part (formerly $\mathcal{H}_0$), while $\iota^2\check{\mathcal{H}}_2$ becomes the new perturbative part (formerly $\iota\mathcal{H}_1$), and a new iteration of the method is performed to push the dependency on φ_1 to the third order on ι. The process could, a priori, be pushed up to infinity in order to find a canonical transformation that completely removes the dependency on φ_1, but in general, the sequence of remainders $\iota^n\check{\mathcal{H}}_n$ diverges beyond a certain order and there exists an optimal order on ι.

[10]Where the operator $\{\cdot,\cdot\}$ is called Poisson bracket.

Often enough in practice, one will only be interested in pushing the dependency on φ_1 up to ι^2 and to consider $\iota^2\check{\mathcal{H}}_2$ as a negligible remainder. In that case, the knowlegde of χ is only useful to retrieve the old variables as a function of the new ones, a transformation seldomly performed since the new variables are more desirable that the old ones. Indeed, the canonical transformation induced by the method is quasiperiodic and close to identity, and the new variables give the tendency of the trajectory, where the fast oscillations due to φ_1 have been removed. This means that in most cases, a first-order Lie serie expansion reduces to a mere average of the Hamiltonian over the fast-circulating angles.

When needed, the cohomological Eq. (2.67) is solved in the Fourier domain. We write

$$\chi = \sum_{\boldsymbol{k}\in\mathbb{Z}^N\setminus\{0\}} \chi_{\boldsymbol{k}} e^{i\boldsymbol{k}\cdot\boldsymbol{\varphi}}, \quad \text{and} \quad \mathcal{H}_1 - \check{\mathcal{H}}_1 = \sum_{\boldsymbol{k}\in\mathbb{Z}^N\setminus\{0\}} h_{\boldsymbol{k}} e^{i\boldsymbol{k}\cdot\boldsymbol{\varphi}}, \tag{2.69}$$

and denoting $\boldsymbol{\omega_0} = \partial\mathcal{H}_0/\partial\boldsymbol{J}$ the frequency vector, the solutions of Eq. (2.67) are

$$\chi_{\boldsymbol{k}} = \frac{h_{\boldsymbol{k}}}{i\boldsymbol{k}\cdot\boldsymbol{\omega_0}}. \tag{2.70}$$

For a non-zero $h_{\boldsymbol{k}}$, it is important that $\boldsymbol{\omega_0}$ respects the Diophantine-like condition $\boldsymbol{k}\cdot\boldsymbol{\omega_0} > \iota$, so that the order of magnitude of $\iota\chi$ is ι and the transformation is ι-close to the identity. If, for instance, the system features a mean-motion resonance $\xi_{i,j} = p_i\lambda_i + p_j\lambda_j \approx 0$, where p_i and p_j are small integers, then a linear canonical transformation has first to be applied to the Hamiltonian in order for $\xi_{i,j}$ to appear explicitly. Then, the Lie expansion is performed without averaging upon $\xi_{i,j}$. We use the results of this section at several occasions throughout the manuscript, and especially in Sect. 4.2.1 where we explain the notion of *libration centre*.

2.3 Secular evolution of a planar non-resonant two-planet system

The remaining chapters of this work will focus on the dynamics of planetary systems where mean motion resonances between planets exist. The $1:1$ resonance will be the core of Chaps. 3 & 6, while the chain of resonance $1:1:2$, and more generally $p:p:p+1$, will be studied in Chaps. 4 & 7. In this section, we focus on the simple case of a planar two-planet system, far from any mean motion resonance, limiting ourselves to the second order in eccentricity. This is known as the Laplace-Lagrange approximation. The star and two planets have masses m_0, m_1 and m_2, respectively. According to Eq. (2.54), the Hamiltonian of the problem in Poincaré canonical complex variables (Eq. (2.50)) reads

$$\mathcal{H} = -\sum_{j\in\{1,2\}} \frac{\mu_j^2\beta_j^3}{2\Lambda_j^2} + \iota\mathcal{H}_P(X_1, X_2, \bar{X}_1, \bar{X}_2, \boldsymbol{\lambda}, \boldsymbol{\Lambda}), \tag{2.71}$$

where $X_j = \sqrt{2/\Lambda_j}\, x_j$. We are mostly interested in the secular (*i.e.* long-term) evolution of the system, and so, we can eliminate two out of the four degrees of freedom by averaging over the mean longitudes λ_1 and λ_2. As we proved in Sect. 2.2.2, this amounts in performing a canonical transformation on the Hamiltonian that sends the dependency on

these variables in a remainder of order ι^2, that we neglect. For convenience, and as we do not plan to perform the inverse transformation[11], we do not change the name of the variables. In Eq. (2.58), averaging over λ_1 and λ_2 is equivalent to discarding every terms such that $\boldsymbol{k} \neq 0$. Taking into account the d'Alembert rule (2.59), we can deduce that the expansion of the perturbative part, truncated at second order in eccentricity, only features terms of the form $X_j\bar{X}_j$ or $X_j\bar{X}_k$, for $j,k \in \{1,2\}$, and we obtain the decomposition

$$\mathcal{H} = -\sum_{j\in\{1,2\}} \frac{\mu_j^2\beta_j^3}{2\Lambda_j^2} + \frac{m_1 n_2 \Lambda_2}{m_0}\left(B_0 + B_1\left(X_1\bar{X}_1 + X_2\bar{X}_2\right) + B_2\left(X_1\bar{X}_2 + X_2\bar{X}_1\right)\right), \quad (2.72)$$

where n_2 is the mean motion of the second planet, defined just below Eq. (2.48). The dimensionless coefficients B_0, B_1 and B_2 depend on the Λ_j, that are now constant, since the dependency on the λ_j has been lost. As a consequence, the Keplerian part and the factor B_0 are now constant, their gradient is zero and they can be removed from the Hamiltonian without changing the equations of motion. We thus have the final form of the two-degrees of freedom Laplace-Lagrange Hamiltonian

$$\mathcal{H}_{\mathrm{LL}}(X_1, X_2, \bar{X}_1, \bar{X}_2) = \frac{m_1 n_2 \Lambda_2}{m_0}\left(B_1\left(X_1\bar{X}_1 + X_2\bar{X}_2\right) + B_2\left(X_1\bar{X}_2 + X_2\bar{X}_1\right)\right). \quad (2.73)$$

Laskar and Robutel (1995) (top of page 216) give the coefficients B_1 and B_2 as a function of the Laplace coefficients

$$\begin{aligned} B_1 &= -\frac{1}{8}\alpha b_{3/2}^{(1)}(\alpha), \\ B_2 &= \frac{1}{4}\left(1+\alpha^2\right) b_{3/2}^{(1)}(\alpha) - \frac{3}{8}\alpha b_{3/2}^{(0)}(\alpha), \end{aligned} \quad (2.74)$$

where $\alpha = a_1/a_2$ and the Laplace coefficients are the coefficients of the Laurent expansion (*e.g.* Laskar, 2005)

$$\left(1-\alpha z\right)^{-s}\left(1-\alpha z^{-1}\right)^{-s} = \frac{1}{2}\sum_{k\in\mathbb{Z}} b_s^{(k)}(\alpha) z^k. \quad (2.75)$$

The variables X_j and $\bar{X}_j$ are not pairs of canonical variables and the equations of motion are not given by Eqs. (2.18). Nevertheless, $(x_j; -i\bar{x}_j)$ is a pair of canonical variables and we can obtain the equations of motion for X_j from those for x_j. We have

$$\dot{X}_j = -\frac{2i}{\Lambda_j}\frac{\partial \mathcal{H}_{\mathrm{LL}}}{\partial \bar{X}_j}, \quad (2.76)$$

and the complete equations of motion take the form

$$\begin{pmatrix}\dot{X}_1 \\ \dot{X}_2\end{pmatrix} = \mathcal{A}\begin{pmatrix}X_1 \\ X_2\end{pmatrix} = -\frac{2in_2}{m_0}\begin{pmatrix} m_2\alpha^{-1/2}B_1 & m_2\alpha^{-1/2}B_2 \\ m_1 B_2 & m_1 B_1\end{pmatrix}\begin{pmatrix}X_1 \\ X_2\end{pmatrix}. \quad (2.77)$$

This is a constant linear differential system, whose eigenvalues are the roots of the characteristic polynomial

$$\det\left(\mathcal{A} - \lambda\mathbb{I}\right) = \lambda^2 + \frac{2iB_1 n_2\left(m_1 + \alpha^{-1/2}m_2\right)}{m_0}\lambda + \frac{4\left(B_2 - B_1\right)\left(B_2 + B_1\right)m_1 m_2 n_2^2}{m_0^2\alpha^{1/2}}. \quad (2.78)$$

[11] See the paragraph before Eq. (2.69) in Sect. 2.2.2, for an explanation.

For any reasonable choice of masses and semimajor axes, the roots of Eq. (2.78) are pure imaginary. This means that all the trajectories of an averaged, planar, non-resonant two-planet system at second order in eccentricity are such that the semimajor axes are fixed while the eccentricity vectors $e_j e^{i\varpi_j}$ behave quasiperiodically (Sect. 2.4.1). Their fundamental frequencies are given by the eigenvalues. For the planetary system Sun−Earth−Jupiter, with the current masses and semimajor axes and assumed planar, a numerical evaluation gives, in arcseconds per year

$$\lambda_1 = i\,7.0758\,''/\mathrm{yr}, \quad \text{and} \quad \lambda_2 = i\,0.009198\,''/\mathrm{yr}. \tag{2.79}$$

2.4 The differential system $\dot{X} = F(X)$

We review in this section some methods to study differential systems of the form $\dot{X} = F(X)$, where $F : \mathbb{R}^n \to \mathbb{R}^n$ is a differentiable vector field.

2.4.1 Fixed points, linearization and eigenvalues

Unless F has a very particular form, the solutions of the Cauchy system

$$\dot{X} = F(X), \tag{2.80}$$

where $X(t = 0)$ is given, cannot be written analytically. Nevertheless, if the equation $F(X) = 0$ has solutions on the set of definition of F, then these solutions are called fixed points (or equilibria), and in their vicinity, the system (2.80) reduces to a linear system. Let $X_0 \in \mathbb{R}^n$ be such that $F(X_0) = 0$, and we write $X = X_0 + \delta X$. A first-order Taylor expansion in Eq. (2.80) gives

$$\frac{d\delta X}{dt} = \nabla F(X_0)\delta X + \mathcal{O}\left(|\delta X|^2\right), \tag{2.81}$$

and in the vicinity of X_0, the Cauchy system (2.80) is studied by diagonalizing (or reducing to a Jordan form) the matrix $\nabla F(X_0)$. Let $(\lambda_j)_{1\leq j\leq n}$ be the eigenvalues of $\nabla F(X_0)$. We call, *the linear system*, the system (2.81) without $\mathcal{O}(|\delta X|^2)$. If the matrix $\nabla F(X_0)$ is diagonalizable, then the following holds true[12]

- If $\forall j \leq n \quad \mathfrak{Re}\,\lambda_j \leq 0$, then for any initial condition, the flow of *the linear system* is bounded and the system is stable.
- If $\forall j \leq n \quad \mathfrak{Re}\,\lambda_j < 0$, then for all initial conditions, *the linear system* converges towards X_0 at exponential speed. The system is asymptotically stable.
- If $\forall j \leq n \quad \mathfrak{Re}\,\lambda_j = 0$, then all initial conditions lead to a quasiperiodic orbit. If furthermore $\forall i, j \leq n \quad \mathfrak{Im}\,\lambda_i/\mathfrak{Im}\,\lambda_j \in \mathbb{Q}$, then the trajectories are periodic.
- If $\exists j \leq n \quad \mathfrak{Re}\,\lambda_j > 0$, then for all initial conditions, but those in a set of measure zero, *the linear system* diverges away from the fixed point X_0 at exponential speed, and its flow is unbounded. The system is unstable.

[12] And is easily proven by diagonalizing the system.

The condition that $\nabla F(X_0)$ be diagonalizable is necessary. Consider for instance the case where this matrix is nilpotent and non-zero. Then all its eigenvalues are zero but the trajectories are unbounded for almost all initial conditions. We use the results of this section in Sect. 6.2.1 to study the stability, with tides, of a pair of co-orbital planets. We use them again in Sect. 7.2.1 to study the stability, with tides, of the resonance chain $p : p : p + 1$.

2.4.2 Eigenvalues of a perturbed matrix

The behaviour of a differential system in the vicinity of its equilibria is described by the knowledge of its eigenvalues. We consider in this subsection the case where the matrix of the linearized differential system takes the form

$$\mathcal{M} = \mathcal{M}_0 + \varepsilon \mathcal{M}_1, \tag{2.82}$$

where ε is a small quantity with respect with unity, written to emphasize the fact that $\mathcal{M}$ is ε-close to $\mathcal{M}_0$. The matrix $\mathcal{M}$ is too complicated for its eigenvalues to be computed directly in an analytical manner, but the perturbative approach we present here, briefly mentioned by Laskar *et al.* (2012), gives the eigenvalues and eigenvectors very easily. Assume that we know a diagonal basis for $\mathcal{M}_0$

$$\mathcal{D}_0 = P_0^{-1} \mathcal{M}_0 P_0 = \mathrm{diag}\left(\lambda_i\right), \tag{2.83}$$

where the columns of P_0 are the eigenvectors of $\mathcal{M}_0$ and the λ_i its eigenvalues, which are not assumed to be of multiplicity one but which are assumed to be sorted by value, that is, equal eigenvalues are consecutive. This does not restrict the generality, as any permutation can be applied on the columns of P_0 to achieve that. We now define

$$\mathcal{Q}_1 = P_0^{-1} \mathcal{M}_1 P_0. \tag{2.84}$$

Let P denote the matrix of the eigenvectors of $\mathcal{D}_0 + \varepsilon \mathcal{Q}_1$. Since $\mathcal{D}_0 + \varepsilon \mathcal{Q}_1$ is near diagonal, we write

$$P = \mathbb{I}_n + \varepsilon P_1 + \mathcal{O}\left(\varepsilon^2\right). \tag{2.85}$$

We have

$$P^{-1} \left(\mathcal{D}_0 + \varepsilon \mathcal{Q}_1\right) P = \mathcal{D}_0 + \varepsilon \left(\mathcal{Q}_1 + \left[\mathcal{D}_0, P_1\right]\right) + \mathcal{O}\left(\varepsilon^2\right), \tag{2.86}$$

where $\left[\mathcal{D}_0, P_1\right] = \mathcal{D}_0 P_1 - P_1 \mathcal{D}_0$. Denoting $\mathcal{D}_1 = \mathrm{diag}\left(q_{i,i}\right)$ the diagonal matrix composed of the diagonal terms of $\mathcal{Q}_1$, we obtain the cohomological equation

$$\mathcal{Q}_1 + \left[\mathcal{D}_0, P_1\right] = \mathcal{D}_1. \tag{2.87}$$

The solution of the cohomological equation is

$$p_{i,j} = \begin{cases} \dfrac{q_{i,j}}{\lambda_j - \lambda_i} & \text{if } \left|\lambda_i - \lambda_j\right| \gg \varepsilon, \\ 0 & \text{else,} \end{cases} \tag{2.88}$$

where $\varepsilon \mathcal{Q}_1 = \left(q_{i,j}\right)_{1 \leq i,j \leq n}$ and $\varepsilon P_1 = \left(p_{i,j}\right)_{1 \leq i,j \leq n}$. The matrix $\mathcal{M}_0 + \varepsilon \mathcal{M}_1$ is now block diagonal, that is

$$P^{-1} P_0^{-1} \left(\mathcal{M}_0 + \varepsilon \mathcal{M}_1\right) P_0 P = \mathrm{diag}\left(\mathcal{B}_0^1 + \varepsilon \mathcal{B}_1^1, \ldots, \mathcal{B}_0^r + \varepsilon \mathcal{B}_1^r\right), \qquad r \leq n \tag{2.89}$$

where the principal matrix of each block is an homothety

$$\forall i \leq r \quad \exists k \leq n \quad \mathcal{B}_0^i = \lambda_k \mathbb{I}_{m(k)}, \tag{2.90}$$

and $m(k)$ denotes the multiplicity of λ_k and thus the size of the block. The computation of the eigenvalues of $\mathcal{M}_0 + \varepsilon\mathcal{M}_1$ is reduced to the computation of the eigenvalues of the blocks $\mathcal{B}_0^i + \varepsilon\mathcal{B}_1^i$ which are hopefully all of small size and whose eigenvalues are then analytically easily found.

If the eigenvalues of $\mathcal{M}_0$ all have multiplicity one and we are only interested in computing the eigenvalues of $\mathcal{M}$, then the cohomological Eq. (2.87) does not need to be solved. At first order in ε, the eigenvalues of $\mathcal{M}$ can be read on the diagonal of $\mathcal{D}_0 + \varepsilon\mathcal{Q}_1$. This perturbative method was exposed in appendix E of Couturier *et al.* (2021). We use it in Sects. 6.2.1 & 6.4.3 to compute the eigenvalues of the differential system describing the motion of two co-orbital planets perturbed by tidal dissipation, in the vicinity of the Lagrangian equilateral equilibria. We also use it in Sect. 3.3.3.

2.4.3 Case where F is Hamiltonian

In the case where the vector field F derives from a Hamiltonian function, the differential system linearized in the vicinity of the equilibria has a particular form and this gives constraints on the eigenvalues. Assume that there exists a real Hamiltonian $\mathcal{H} : \mathbb{R}^{2n} \to \mathbb{R}$ such that $F = \mathbb{J}\nabla\mathcal{H}$. In the neighbourhood of a fixed point X_0 of the differential system, we note $X = X_0 + \delta X$ and the linearized system reads

$$\frac{d\delta X}{dt} = \mathbb{J}\nabla^2\mathcal{H}(X_0)\delta X = \mathbb{J}\mathcal{S}\delta X, \tag{2.91}$$

where $\mathcal{S} = \nabla^2\mathcal{H}(X_0)$ is the Hessian of $\mathcal{H}$ evaluated at X_0 (Eq. (2.5)). We now prove that[13] (Meyer and Hall, 2009, Sect. 3.3)

- If λ is eigenvalue of $\mathbb{J}\mathcal{S}$, then so are $-\lambda$, $\bar{\lambda}$ and $-\bar{\lambda}$.

A consequence of this result is that, in the complex plane, the eigenvalues of a linear and real Hamiltonian system are the vertices of rectangles centered at the origin and whose edges are parallel to the axes. Another consequence, in virtue of Sect. 2.4.1, is that a linear and real Hamiltonian system is either unstable or quasiperiodic. In the case $n = 1$, we can also deduce that the two eigenvalues of the system are either $\lambda = \pm\lambda$, or $\lambda = \pm i\lambda$, where λ is some positive real number.

We first prove that the matrix $\mathcal{A} = \mathbb{J}\mathcal{S}$ verifies[14] $\mathcal{A} = \mathbb{J}\,{}^t\mathcal{A}\mathbb{J}$. Indeed we have

$$\mathbb{J}\,{}^t\mathcal{A}\mathbb{J} = \mathbb{J}\,{}^t(\mathbb{J}\mathcal{S})\,\mathbb{J} = \mathbb{J}\mathcal{S}\,{}^t\mathbb{J}\mathbb{J} = \mathbb{J}\mathcal{S} = \mathcal{A}, \tag{2.92}$$

where we used the fact that $\mathcal{S}$ is symmetric for the second equality and ${}^t\mathbb{J}\mathbb{J} = \mathbb{I}$ for the third. Because $\mathcal{H}$ is real, $\mathcal{A}$ is a real matrix and its characteristic polynomial $P(\lambda) = \det(\mathcal{A} - \lambda\mathbb{I})$ is also real. It is thus clear that if λ is eigenvalue, so is $\bar{\lambda}$. Proving that $-\lambda$ is eigenvalue

[13] The upper bar denotes the complex conjugated.
[14] Such matrices are called Hamiltonian matrices.

if λ is, will also prove that $-\bar{\lambda}$ is eigenvalue if $\bar{\lambda}$ is. To do that we can show that $\det(\mathcal{A} - \lambda\mathbb{I}) = \det(\mathcal{A} + \lambda\mathbb{I})$. Using $\det\mathbb{J} = 1$, we have

$$\begin{aligned}\det(\mathcal{A} - \lambda\mathbb{I}) &= \det\left(\mathbb{J}\,{}^t\mathcal{A}\mathbb{J} - \lambda\mathbb{I}\right) = \det\left(\mathbb{J}\,{}^t\mathcal{A}\mathbb{J} + \lambda\mathbb{J}\mathbb{J}\right)\\ &= \det\mathbb{J}\det\left({}^t\mathcal{A} + \lambda\mathbb{I}\right)\det\mathbb{J} = \det(\mathcal{A} + \lambda\mathbb{I}),\end{aligned} \tag{2.93}$$

which ends the demonstration.

Protection against destabilization

Another consequence of the previous result is that one degree of freedom Hamiltonians are protected against destabilization by a Hamiltonian perturbation. Assume that a dynamical system is governed by a one degree of freedom Hamiltonian $\mathcal{H}_0(p,q)$, and that $X_0 = (p_0, q_0)$ is a stable equilibrium of that Hamiltonian. According to what was just proven, the eigenvalues in the vicinity of X_0 are $\lambda_0 = \pm i\lambda_0$, where we suppose $\lambda_0 > 0$ to prevent trivial dynamics. Assume now that this system is perturbed by a tiny Hamiltonian perturbation

$$\mathcal{H}(p,q) = \mathcal{H}_0(p,q) + \varepsilon\mathcal{H}_1(p,q), \tag{2.94}$$

where $\varepsilon \ll 1$ is written to emphasize the smallness of the perturbation. The fixed point is displaced at the position $X = X_0 + \varepsilon X_1$ by the perturbation and the eigenvalues, now given by the spectrum of $\mathbb{J}\nabla^2\mathcal{H}(X)$, are also perturbed to their new values[15]

$$\lambda^{(1)} = i\lambda_0 + \varepsilon\lambda^{(1)}, \quad \text{and} \quad \lambda^{(2)} = -i\lambda_0 + \varepsilon\lambda^{(2)}, \tag{2.95}$$

where $\lambda^{(1)}, \lambda^{(2)} \in \mathbb{C}$ are of the same order of magnitude than λ_0. Since the new differential system is still Hamiltonian, there exists $\lambda \in \mathbb{R}$ such that either $(\lambda^{(1)}, \lambda^{(2)}) = (i\lambda, -i\lambda)$ or $(\lambda^{(1)}, \lambda^{(2)}) = (\lambda, -\lambda)$. Given the small size of ε, the latter possibility is excluded, and we must have $(\lambda^{(1)}, \lambda^{(2)}) = (i\lambda, -i\lambda)$. The new equilibrium is still stable, and one degree of freedom Hamiltonian are protected against destabilization by a Hamiltonian perturbation.

We can use this result to prove that the perturbations due to general relativity (second order in the Post-Newtonian expansion) cannot destabilize a co-orbital system in the same way that tides do. See Sect. 3.3.1 for details.

[15] Which are conveniently computed in practice using the results of Sect. 2.4.2

Chapter 3

The co-orbital motion

Most results of this chapter were first published in Robutel and Pousse (2013) and are recalled in Sect. 2 of Couturier et al. *(2021). Section 3.3 is original, while the end of Sect. 3.2.2 was first published in Couturier* et al. *(2021).*

3.1 Hamiltonian of two planar co-orbital planets

In this chapter, we consider the point-mass, planar, three-body problem, where a star of mass m_0 is orbited by two planets of masses m_1 and m_2. We introduce the small parameter $\iota = (m_1 + m_2)/m_0$ and the quantities $\beta_j = m_0 m_j/(m_0 + m_j)$ and $\mu_j = \mathcal{G}(m_0 + m_j)$, where $\mathcal{G}$ is the gravitational constant.

3.1.1 Expansion in the neighbourhood of the resonance

In order to define a canonical coordinate system related to the semi-major axis a_j, the eccentricity e_j, the mean longitude λ_j and the longitude of the pericentre ϖ_j, we use Poincaré cartesian heliocentric canonical coordinates $(\lambda_j, \tilde{x}_j; \Lambda_j, x_j)$, defined as (Eq. (2.49), Sect. 2.1.4)

$$\Lambda_j = \beta_j \sqrt{\mu_j a_j}, \quad x_j = \sqrt{\Lambda_j}\sqrt{1 - \sqrt{1 - e_j^2}}\exp(i\varpi_j), \quad \tilde{x}_j = -i\bar{x}_j. \tag{3.1}$$

With this set of coordinates, the Hamiltonian derives from the symplectic form

$$\sum_{j\in\{1,2\}} \left(d\lambda_j \wedge d\Lambda_j + d\tilde{x}_j \wedge dx_j\right), \tag{3.2}$$

and according to Eq. (2.54), we write (Robutel and Pousse, 2013)

$$H = H_K(\Lambda_1, \Lambda_2) + \iota H_P(\Lambda_1, \Lambda_2, \lambda_1, \lambda_2, x_1, x_2, \tilde{x}_1, \tilde{x}_2), \tag{3.3}$$

where the Keplerian part H_K, due to star−planet interactions, reads (Eq. (2.55))

$$H_K(\Lambda_1, \Lambda_2) = -\sum_{j\in\{1,2\}} \frac{\beta_j^3 \mu_j^2}{2\Lambda_j^2}, \tag{3.4}$$

while the perturbation ιH_P is due to planet−planet interactions. If the system is at the co-orbital resonance 1 : 1, then the nominal mean motions of both planets comply with $n_1 = n_2 := \eta$. In that case, the semi-major axes a_j of the planets are close to their nominal value $\bar{a}$, defined as

$$\bar{a} = \mu_0^{1/3}\eta^{-2/3} \quad \text{and} \quad \mu_0 = \mathcal{G}m_0. \tag{3.5}$$

This also means that the circular angular momenta Λ_j are close to their nominal value $\Lambda_j^\star$ given by

$$\Lambda_j^\star = m_j\sqrt{\mu_0\bar{a}}. \tag{3.6}$$

At the exact mean motion resonance (also called Keplerian resonance), when $n_1 = n_2 = \eta$, the semi-major axes are not equal, but rather verify $a_j = \bar{a}\,(1 + \mathcal{O}(\iota))$. Considering that the exact co-orbital resonance occurs at $a_1 = a_2 = \bar{a}$ hence generates an error of size $\mathcal{O}(\iota)$, as does substituting m_j for β_j or μ_0 for μ_j, in Eqs. (3.5) and (3.6). However, Niederman *et al.* (2020) have shown that the planets are still in the co-orbital resonance if[1]

$$\frac{\Lambda_j}{\Lambda_j^\star} = 1 + \mathcal{O}(\iota^{\mathfrak{s}}), \quad \text{where} \quad \frac{1}{3} < \mathfrak{s} \leq \frac{1}{2}. \tag{3.7}$$

In other words, the resonance has a width at least $\mathcal{O}(\iota^{1/2})$ and errors of size $\mathcal{O}(\iota)$ have no consequences. Since we are interested in a study of the dynamics in the vicinity of the resonance, we expand the Hamiltonian in the neighbourhood of $\Lambda_j = \Lambda_j^\star$, assuming that $\Lambda_j^\star$ is the value of Λ_j at the exact resonance.

In the co-orbital resonance, the librating angle $\lambda_1 - \lambda_2$ plays an important role and in order for it to appear explicitly, we perform the canonical transformation (see Eq. (2.31))

$$\Phi_1(\Lambda_1, \Lambda_2, \lambda_1, \lambda_2) = (Z, Z_2, \phi, \phi_2) = (\Lambda_1 - \Lambda_1^\star, \Lambda_1 + \Lambda_2 - \Lambda_1^\star - \Lambda_2^\star, \lambda_1 - \lambda_2, \lambda_2)\,. \tag{3.8}$$

At second order in (Z, Z_2), the Keplerian part of the Hamiltonian reads

$$\hat{H}_K(Z, Z_2) = H_K(\Lambda_1, \Lambda_2) = \eta Z_2 - \frac{3}{2}\eta\left(\frac{Z^2}{\Lambda_1^\star} + \frac{(Z_2 - Z)^2}{\Lambda_2^\star}\right) + \hat{R}_K^{(2)}, \tag{3.9}$$

where $\hat{H}_K = H_K \circ \Phi_1^{-1}$ and a constant term $-\eta\,(\Lambda_1^\star + \Lambda_2^\star)\,/2$, corresponding to the order 0, has been removed. The remainder $\hat{R}_K^{(2)}$ has a size relative to the expansion $\hat{R}_K^{(2)}/\hat{H}_K = \mathcal{O}(\iota^{2\mathfrak{s}})$, or equivalently[2]

$$\hat{R}_K^{(2)} = \mathcal{O}(\iota^{3\mathfrak{s}})H_K. \tag{3.10}$$

Since the perturbation is small with respect to the Keplerian part, it is not necessary to expand it up to the second order in the vicinity of $\Lambda_j^\star$. If we limit ourselves to the zeroth order, that is

$$H_P(\Lambda_1, \Lambda_2, \lambda_1, \lambda_2, x_1, x_2, \tilde{x}_1, \tilde{x}_2) = H_P(\Lambda_1^\star, \Lambda_2^\star, \lambda_1, \lambda_2, x_1, x_2, \tilde{x}_1, \tilde{x}_2) + R_P^{(0)}, \tag{3.11}$$

then the size of the remainder relative to the expansion is $R_P^{(0)}/H_P = \mathcal{O}(\iota^{\mathfrak{s}})$, that is

$$R_P^{(0)} = \mathcal{O}(\iota^{1+\mathfrak{s}})H_K. \tag{3.12}$$

[1] This domain for $\mathfrak{s}$ corresponds to the horseshoe-shaped orbits (Sect. 3.2.1).

[2] The removal of the constant $-\eta\,(\Lambda_1^\star + \Lambda_2^\star)\,/2$ from $\hat{H}_K$ yields $\hat{H}_K/H_K = \mathcal{O}(\iota^{\mathfrak{s}})$.

Combining the estimates (3.10) and (3.12), we obtain

$$\frac{R_P^{(0)}}{\hat{R}_K^{(2)}} = \mathcal{O}(\iota^{1-2\mathfrak{s}}). \tag{3.13}$$

We can verify that truncating the expansion (3.11) at order zero in the vicinity of the Keplerian resonance is enough. When $\mathfrak{s} \leq 1/2$, Eq. (3.13) shows that $R_P^{(0)}$ is negligible with respect to $\hat{R}_K^{(2)}$, whereas when $\mathfrak{s} > 1/2$ (this corresponds to tadpole orbits, see Sect. 3.2.1), the estimates (3.10) and (3.12) show that both remainders quickly tend to 0 with increasing $\mathfrak{s}$. In both cases, the order 0 is enough and we simply evaluate the perturbation H_P at $\Lambda_j = \Lambda_j^\star$.

Lastly, for the expansion (3.9) to be valid, it is important that $\hat{R}_K^{(2)}$ is negligible with respect to H_P. Combining $R_P^{(0)}/H_P = \mathcal{O}(\iota^{\mathfrak{s}})$ with Eq. (3.13), we can write $\hat{R}_K^{(2)}/H_P = \mathcal{O}(\iota^{3\mathfrak{s}-1})$, and we must have $\mathfrak{s} > 1/3$. This is the lower bound of Niederman *et al.* (2020).

3.1.2 Averaged Hamiltonian

The timescales of evolution can be established by uncoupling the action variables in the Keplerian Hamiltonian. We perform the canonical transformation (Eq. (2.31))

$$\Phi_2(Z, Z_2, \phi, \phi_2) = (I, I_2, \xi, \xi_2) = (Z - \delta Z_2, Z_2, \phi, \delta\phi + \phi_2)\,, \quad \text{with} \quad \delta = \frac{m_1}{m_1 + m_2}, \tag{3.14}$$

where x_j and $\tilde{x}_j$ are unchanged. The Keplerian part of the Hamiltonian takes the form

$$\check{H}_K(I, I_2) = \hat{H}_K(Z, Z_2) = \eta I_2 - \frac{3}{2}\eta\frac{I_2^2}{\Lambda_1^\star + \Lambda_2^\star} - \frac{3}{2}\eta\frac{\Lambda_1^\star + \Lambda_2^\star}{\Lambda_1^\star\Lambda_2^\star} I^2, \tag{3.15}$$

where $\check{H}_K = \hat{H}_K \circ \Phi_2^{-1}$. This decoupling emphasizes the timescales involved in the dynamics. The Hamilton Eqs. (2.18) give

$$\dot{\xi}_2 = \frac{\partial \check{H}_K}{\partial I_2} = \eta\left(1 + \mathcal{O}(\iota^{\mathfrak{s}})\right) \quad \text{and} \quad \dot{\xi} = \frac{\partial \check{H}_K}{\partial I} = \eta\,\mathcal{O}(\iota^{\mathfrak{s}}), \tag{3.16}$$

and so, the angle ξ_2 evolves much more quickly than $\xi = \lambda_1 - \lambda_2$. As we will show in Sect. 3.2.2, the eccentricities x_j evolves on timescales much longer than the timescale of evolution of ξ. This means that the co-orbital dynamics takes place on three distinct timescales. The fast one, of frequency $\eta\,\mathcal{O}(1)$ is associated with ξ_2 (or either of the λ_j), the semi-fast one, of frequency $\eta\,\mathcal{O}(\iota^{\mathfrak{s}})$, is associated with the libration of ξ, while the secular (or slow) one has a frequency $\eta\,\mathcal{O}(\iota)$ and is associated with the x_j. This will be further detailed in Sects. 3.2.1 & 3.2.2.

Since the angle ξ_2 evolves at the orbital frequency, it is natural to average the Hamiltonian over it; that is, we perform a first-order Lie serie expansion (Sect. 2.2.2) and write[3]

$$\check{H}(I, I_2, \xi, x_1, x_2, \tilde{x}_1, \tilde{x}_2) = \check{H}_K(I, I_2) + \frac{1}{2\pi}\int_0^{2\pi} \iota\check{H}_P(\xi, \xi_2, x_1, x_2, \tilde{x}_1, \tilde{x}_2)d\xi_2 + \check{R}^{(2)}, \tag{3.17}$$

[3]The Lie expansion performs on the Hamiltonian a canonical transformation ι-close to the identity, but for convenience, we do not change the name of the variables.

where $\check{H}_P = H_P \circ \Phi_1^{-1} \circ \Phi_2^{-1}$ and $\check{R}^{(2)}$ is the remainder of the Lie expansion. Requesting that $\check{R}^{(2)} \ll \check{H}_P$ yields once again $\mathfrak{s} > 1/3$ (Niederman *et al.*, 2020). After the averaging process, the Hamiltonian no longer depends on ξ_2 and its conjugated momentum I_2 is a first integrale. That is, the total circular angular momentum $\Lambda_1 + \Lambda_2$ is conserved in the averaged problem. In the co-orbital resonance $1:1$, this quantity corresponds, for other resonances, to what various authors call the scaling parameter (Michtchenko *et al.*, 2008; Delisle, 2017; Petit *et al.*, 2020). In the averaged problem, the conservation of $\Lambda_1 + \Lambda_2$ allows us to lose one degree of freedom, and we are left with the three degrees of freedom $(\xi, \tilde{x}_1, \tilde{x}_2; I, x_1, x_2)$.

While the total circular angular momentum $\Lambda_1 + \Lambda_2$ is conserved in the averaged problem, it is well known that the total angular momentum $\sum_j \Lambda_j - |x_j|^2$ is also conserved[4], even in the complete (non-averaged) problem. Hence, there exists a transformation allowing one more degree of freedom to be lost, and the averaged planar co-orbital problem has two degrees of freedom. More generally, an averaged, resonant, two-planet planar system has two degrees of freedom[5]. The transformation to two degrees of freedom is performed by Giuppone *et al.* (2010) in their numerical study of the co-orbital motion. However, the subsequent set of coordinates is singular at zero eccentricity, which is not adapted for an analytical work. Hence we stick here with three degrees of freedom.

In order to work with dimensionless quantities, we normalise the action variables by

$$J = \frac{I}{m\bar{a}^2\eta}, \quad J_2 = \frac{I_2}{m\bar{a}^2\eta}, \quad X_j = \sqrt{\frac{2}{m_j\bar{a}^2\eta}}\, x_j, \quad \bar{X}_j = i\sqrt{\frac{2}{m_j\bar{a}^2\eta}}\, \tilde{x}_j, \tag{3.18}$$

where $m = \sqrt{m_1 m_2}$ and the upper bar denotes the complex conjugated. These new eccentricity variables comply with

$$X_j = e_j \exp(i\varpi_j)\left(1 + \mathcal{O}(\iota^{\mathfrak{s}}) + \mathcal{O}(e_j^2)\right). \tag{3.19}$$

The order of magnitude of J and J_2 is $\mathcal{O}(\iota^{\mathfrak{s}})$ and these variables are linked to the semi-major axes a_j by

$$a_j = \bar{a}\mathcal{R}_j^2, \tag{3.20}$$

with

$$\mathcal{R}_j = 1 + f_j, \qquad f_1 = \frac{m}{m_1 + m_2} J_2 + \frac{m}{m_1} J, \qquad f_2 = \frac{m}{m_1 + m_2} J_2 - \frac{m}{m_2} J. \tag{3.21}$$

The transformations Φ_1 and Φ_2 are canonical (Sect. 2.1.3), but the normalization (3.18) is not. We can nevertheless have equations of motion close to their canonical form (2.18) by rescaling the Hamiltonian by

$$\mathcal{H} = \frac{\check{H}}{m\bar{a}^2\eta}, \tag{3.22}$$

and we obtain, for the equations of motion (see Eq. (2.76))

$$\dot{J} = -\frac{\partial \mathcal{H}}{\partial \xi}, \quad \dot{J}_2 = -\frac{\partial \mathcal{H}}{\partial \xi_2}, \quad \dot{\xi} = \frac{\partial \mathcal{H}}{\partial J}, \quad \dot{\xi}_2 = \frac{\partial \mathcal{H}}{\partial J_2}, \quad \dot{X}_j = -2i\frac{m}{m_j}\frac{\partial \mathcal{H}}{\partial \bar{X}_j}, \quad \dot{\bar{X}}_j = \bar{\dot{X}}_j. \tag{3.23}$$

[4]The total AMD $\sum_j |x_j|^2$ (Laskar, 2000) is thus conserved in the averaged $1:1$ resonance.

[5]Henrard and Lemaitre (1983) even showed that at first order in eccentricity, the system has only one degree of freedom.

With this last transformation, the Keplerian part of the Hamiltonian reads

$$\mathcal{H}_K(J) = -\frac{3}{2}\eta\frac{m_1+m_2}{m}J^2, \tag{3.24}$$

where the constant terms depending only on the first integral J_2 have been ignored. In Chap. 6, due to tidal dissipation, J_2 is no longer a first integral and $\mathcal{H}_K$ includes more terms (see Eq. (6.12)).

3.1.3 Expansion of the perturbative part

In the set of canonical coordinates $(\tilde{\boldsymbol{r}}_j; \boldsymbol{r}_j)$, where $\boldsymbol{r}_j$ and $\tilde{\boldsymbol{r}}_j$ are respectively the heliocentric positions and barycentric momenta, the perturbation to the Hamiltonian takes the form given by Eq. (2.53)

$$\iota H_P(\boldsymbol{r}_j, \tilde{\boldsymbol{r}}_j) = \frac{\tilde{\boldsymbol{r}}_\mathbf{1}\cdot\tilde{\boldsymbol{r}}_\mathbf{2}}{m_0} - \frac{\mathcal{G}m_1m_2}{|\boldsymbol{r}_\mathbf{1}-\boldsymbol{r}_\mathbf{2}|}. \tag{3.25}$$

We write[6]

$$|\boldsymbol{r}_\mathbf{1}-\boldsymbol{r}_\mathbf{2}|^2 = r_1^2+r_2^2-2r_1r_2\cos(\boldsymbol{r}_\mathbf{1},\boldsymbol{r}_\mathbf{2}) = \bar{a}^2\Delta^2\left(1+\mathcal{O}(e_j^2)\right), \tag{3.26}$$

where $\Delta = \sqrt{2-2\cos\xi}$, and we expand H_P in power series of the eccentricities. The expansion takes the form (Robutel and Pousse, 2013; Couturier *et al.*, 2021)

$$\iota\mathcal{H}_P = \sum_{n=0}^{+\infty}\mathcal{H}^{(2n)}, \quad \text{with} \quad \mathcal{H}^{(2n)} = \sum_{|\boldsymbol{p}|=2n}\Psi_{\boldsymbol{p}}(\Delta^{-1}, e^{i\xi}, e^{-i\xi})\, X_1^{p_1}X_2^{p_2}\bar{X}_1^{p_3}\bar{X}_2^{p_4}, \tag{3.27}$$

where the norm of the tuple $\boldsymbol{p} = (p_1,p_2,p_3,p_4) \in \mathbb{N}^4$ is defined by $|\boldsymbol{p}| = p_1+p_2+p_3+p_4$ and $\Psi_{\boldsymbol{p}}$ is polynomial in its arguments. The d'Alembert rule (Eq. (2.59))

$$p_1+p_2 = p_3+p_4, \tag{3.28}$$

equivalent to the conservation of the total angular momentum, justifies that the expansion has no terms of odd order in eccentricity. In practice, the expansion (3.27) can be explicitly computed from the results of Laskar and Robutel (1995). We apply the transformations Φ_1 and Φ_2 to H_P, as well as the normalisation (3.18) and the rescaling (3.22). We use the algebraic manipulator *Trip* (Gastineau and Laskar, 2011), and up to the fourth order in eccentricity, we obtain (Couturier *et al.*, 2021)

$$\begin{aligned}
\mathcal{H}^{(0)} &= \frac{m}{m_0}\eta\left(\cos\xi-\Delta^{-1}\right),\\
\mathcal{H}^{(2)} &= \frac{1}{2}\frac{m}{m_0}\eta\left\{A_h\left(X_1\bar{X}_1+X_2\bar{X}_2\right)+B_hX_1\bar{X}_2+\bar{B}_h\bar{X}_1X_2\right\},\\
\mathcal{H}^{(4)} &= \frac{1}{4}\frac{m}{m_0}\eta\left\{D_h\left(X_1^2\bar{X}_1^2+X_2^2\bar{X}_2^2\right)+E_hX_1^2\bar{X}_2^2+\bar{E}_hX_2^2\bar{X}_1^2\right.\\
&\left.+F_h\left(X_1X_2\bar{X}_1^2+\bar{X}_1\bar{X}_2X_2^2\right)+\bar{F}_h\left(\bar{X}_1\bar{X}_2X_1^2+X_1X_2\bar{X}_2^2\right)+G_hX_1X_2\bar{X}_1\bar{X}_2\right\},
\end{aligned} \tag{3.29}$$

[6] This is because we expand at the zeroth order in Λ_j, see Sect. 3.1.1.

where the coefficients of the second order are

$$\begin{aligned} A_h &= \frac{5\cos 2\xi - 13 + 8\cos\xi}{4\Delta^5} - \cos\xi \quad \text{and} \\ B_h &= e^{-2i\xi} - \frac{e^{-3i\xi} + 16e^{-2i\xi} - 26e^{-i\xi} + 9e^{i\xi}}{8\Delta^5}. \end{aligned} \tag{3.30}$$

The coefficients D_h, E_h, F_h and G_h of the fourth order in eccentricity are given in Eqs. (B.1) of appendix B.

3.2 Lagrangian equilibria and linearization

3.2.1 Circular dynamics

The expansion of the perturbative part of the Hamiltonian has no terms of odd degree in the variables X_j (Eq. (3.29)). As a consequence, the form of dX_j/dt in Eqs. (3.23) implies that the manifold $X_1 = X_2 = 0$ is stable by the flow of the averaged Hamiltonian. In other words, initially circular orbits remain circular. The dynamics on this stable manifold is driven by the one-degree-of-freedom Hamiltonian $\mathcal{H}_K + \mathcal{H}^{(0)}$, whose phase space we plot in Fig. 3.1. This Hamiltonian has three fixed points at $(J = 0, \xi = \pi/3)$, $(J = 0, \xi = 5\pi/3)$ and $(J = 0, \xi = \pi)$, corresponding to the famous Lagrangian equilibria. The two elliptic points L_4 and L_5, located on energy maximizers, correspond to configurations where the three bodies are at the vertices of an equilateral triangle, while the hyperbolic configuration L_3 is a saddle point, where the bodies are aligned. The separatrix emanating from L_3

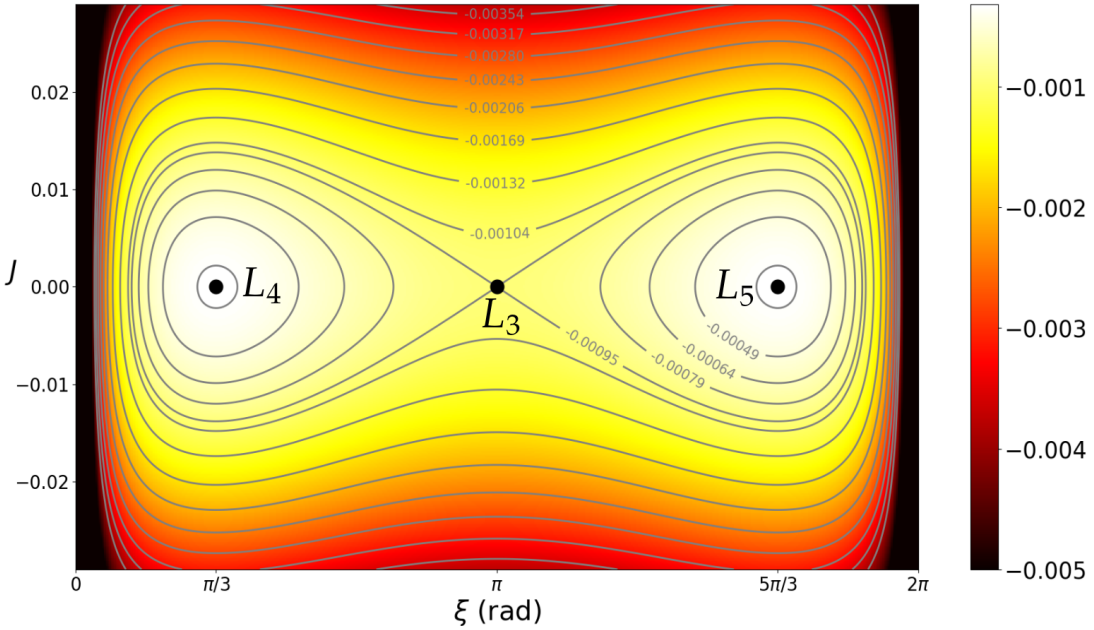

Fig. 3.1 — Phase portrait of the Hamiltonian $\mathcal{H}_K + \mathcal{H}^{(0)}$ with $m_1 = 0.001\, m_0$ and $m_2 = 0.0004\, m_0$. The two elliptic fixed points L_4 and L_5 are energy maximizers, while the hyperbolic fixed point L_3 is a saddle point. Around $L_{4,5}$ are the tadpoles orbits and outside of the separatrix emanating from L_3 are the horseshoe-shaped orbits. The Hamiltonian diverges to minus infinity as $\lambda_1 - \lambda_2 = \xi$ tends to zero.

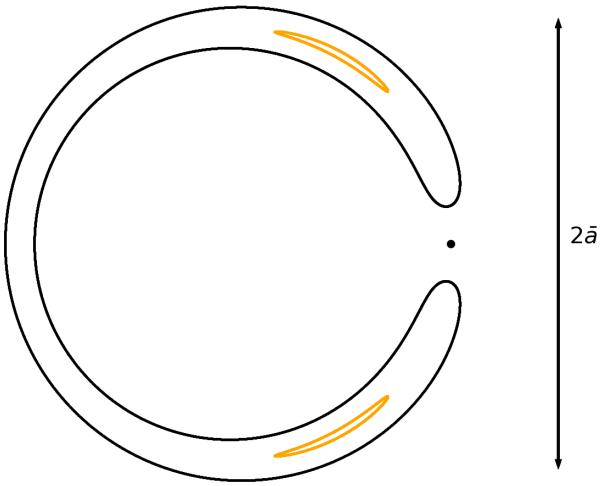

Fig. 3.2 — Relative position of m_1 with respect to m_2 along the trajectories of the Hamiltonian $\mathcal{H}_K + \mathcal{H}^{(0)}$. The trajectories are numerically integrated with a Dormand-Prince method of order 8 using initial conditions $J = 0$ and either $\xi = \pm 45°$ (orange tadpoles) or $\xi = 10°$ (black horseshoe). The curves show the motion of m_1 relative to the black dot m_2; that is, the x and y axes of this figure are $(x, y) = (a_1 \cos\xi - a_2, a_1 \sin\xi)$, the a_j coming from Eq. (3.20) with $J_2 = 0$. The co-orbital masses are $m_2 = 5\,m_1 = 0.001\,m_0$. The period of the motion is here $12.11\,T$ for the black curve and $11.32\,T$ for the orange ones, where $T = 2\pi/\eta$.

splits the phase space in three regions. Around the elliptic fixed points L_4 and L_5 are orbits commonly known as tadpole, while the orbits encircling L_3 are called horseshoe-shaped orbits, due to the shape of the trajectories in the rotating frame (see Fig. 3.2). In our model, the angle $\xi = \lambda_1 - \lambda_2$ is always librating and the exterior of the resonance does not exist. If no expansion in the vicinity of the Keplerian resonance $\Lambda_j = \Lambda_j^\star$ is performed, the phase space contains two more hyperbolic fixed points labeled L_1 and L_2, and the separatrices emanating from them are the boundary of the co-orbital resonance (see Fig. 1 of Robutel and Pousse, 2013). Instead, our phase space features a singular line $\xi = 0$ where the Hamiltonian diverges to $-\infty$, and the model is not valid for very large libration amplitudes.

We show with Eq. (3.16) that the libration frequency of ξ is $\eta\,\mathcal{O}(\iota^{\frac{1}{2}})$. In the vicinity of $L_{4,5}$, we can give an exact expression by linearizing the differential system. We denote $\Delta\xi = \xi - \pi/3$ and in the neighbourhood of L_4 (the dynamics are symmetric in the neighbourhood of L_5), the linearized system reads

$$\frac{d}{dt}\begin{pmatrix}\Delta\xi\\ J\end{pmatrix} = \eta\begin{pmatrix}0 & -3\iota\frac{m_0}{m}\\ \frac{9m}{4m_0} & 0\end{pmatrix}\begin{pmatrix}\Delta\xi\\ J\end{pmatrix}, \tag{3.31}$$

and its eigenvalues are $\pm i\nu$ where

$$\nu = \eta\sqrt{\frac{27\iota}{4}} \tag{3.32}$$

is the libration frequency of ξ in the vicinity of the elliptic Lagrangian equilibria.

For a given trajectory in the phase space, we denote ξ_{ex}, respectively J_{ex}, the extremal value reached by ξ, respectively by J, along that trajectory. When the action is $J = J_{\text{ex}}$, the angle is $\xi = \pi/3$, whereas $\xi = \xi_{\text{ex}}$ implies $J = 0$ (Fig. 3.1). The conservation of

$\mathcal{H}_K + \mathcal{H}^{(0)}$ (Eq. (2.32)) hence gives the relation

$$-\frac{3}{2}\frac{(m_1+m_2)\,m_0}{m_1 m_2} J_{\text{ϵ}}^2 - \frac{1}{2} = \cos\xi_{\text{ϵ}} - (2-2\cos\xi_{\text{ϵ}})^{-1/2}, \tag{3.33}$$

that holds whether the extremum is a minimum or a maximum. The boundary between tadpole and horseshoe-shaped orbits is the separatrix emanating from L_3, and for the largest tadpole orbit (or the the smallest horseshoe-shaped orbit), $\xi_{\text{ϵ}} = \pi$ yields $J_{\text{ϵ}} = \mathcal{O}(\iota^{1/2})$. The boundary between the tadpole and horseshoe domain thus corresponds[7] to $\text{ϙ} = 1/2$, which is the upper bound in Eq. (3.7). For $\text{ϙ} < 1/2$, the system is in the horseshoe domain while it is in the tadpole domain for $\text{ϙ} \geq 1/2$.

For a horseshoe-shaped orbit with a very large libration amplitude, we call $\xi_{\min}$ the minimal value reached by ξ, that is, the minimal angular separation between both co-orbitals. In the following, we compute the value of $\xi_{\min}$ such that the co-orbital planets stay outside of each other Hill's spheres. The closest approach $\mathfrak{d}$ is given by

$$\mathfrak{d} = \bar{a}\xi_{\min}. \tag{3.34}$$

At the closest approach, we perform a Laurent expansion around $\xi_{\min} = 0$ in the right-hand side of Eq. (3.33), retaining only terms of order -1 and 0 in $\xi_{\min}$. This gives

$$\frac{3}{2}\frac{\mathfrak{d}}{\bar{a}}\left(1 + \frac{\iota m_0^2}{m_1 m_2} J_{\text{ϵ}}^2\right) = 1. \tag{3.35}$$

For a large horseshoe-shaped orbit, $\text{ϙ} < 1/2$ implies that $1 \ll \iota m_0^2 J_{\text{ϵ}}^2/m_1 m_2$ and the estimate $J_{\text{ϵ}} = \mathcal{O}(\iota^{\text{ϙ}})$ yields

$$\mathfrak{d} = \mathcal{O}(\iota^{1-2\text{ϙ}})\,\bar{a}. \tag{3.36}$$

Our model is based on a perturbative approach where the planet−planet interactions are assumed to be much smaller than the star−planet interactions. For this approach to make sense, it is necessary that the co-orbital bodies stay well outside of each other Hill's spheres, that is

$$\mathfrak{d} \gg \bar{a}\left(\frac{\iota}{3}\right)^{1/3}, \tag{3.37}$$

or equivalently, using Eq. (3.36)

$$\mathcal{O}(\iota^{2/3-2\text{ϙ}}) \gg 1. \tag{3.38}$$

We retrieve once again the lower bound $1/3 < \text{ϙ}$ given by Niederman *et al.* (2020), showing that this lower bound can be obtained in three different manners. We can either request that

- the remainder $\hat{R}_K^{(2)}$ of the expansion (3.9) around the Keplerian resonance is negligible with respect to the perturbative part H_P of the Hamiltonian, or that
- the remainder $\check{H}^{(2)}$ of the Lie serie expansion (3.17) is negligible with respect to $\check{H}_P$, or that
- the co-orbital planets do not enter each other Hill's spheres.

These three conditions are equivalent to $1/3 < \text{ϙ}$ in Eq. (3.7).

[7] This is due to $J_{\text{ϵ}} = \mathcal{O}(\iota^{\text{ϙ}})$.

3.2.2 Eccentric dynamics

The secular dynamics of the problem is driven by the Hamiltonian $\mathcal{H}_K + \mathcal{H}^{(0)} + \sum_{n\geq 1} \mathcal{H}^{(2n)}$. If we limit the summation to $n = 1$; that is, if we only consider $\mathcal{H} = \mathcal{H}_K + \mathcal{H}^{(0)} + \mathcal{H}^{(2)}$, the equations of motion are linear in X_j (see Eqs. (3.23) & (3.29)), which is convenient to obtain analytical results at low eccentricity. We show in Chap. 6 that tidal dissipation damps the eccentricities to 0, and the analytical insight at low eccentricity allows us to understand most of the dynamics. Hence we only consider $\mathcal{H} = \mathcal{H}_K + \mathcal{H}^{(0)} + \mathcal{H}^{(2)}$ in the rest of this chapter and we will include $\mathcal{H}^{(4)}$ back again in Sect. 6.1.1 when we include tidal dissipation in the analytical model. At this order in eccentricity, the equations of motion read

$$\begin{pmatrix} \dot{X}_1 \\ \dot{X}_2 \end{pmatrix} = -\frac{i\eta}{m_0} \begin{pmatrix} m_2 A_h(\xi(t)) & m_2 \bar{B}_h(\xi(t)) \\ m_1 B_h(\xi(t)) & m_1 A_h(\xi(t)) \end{pmatrix} \begin{pmatrix} X_1 \\ X_2 \end{pmatrix}, \tag{3.39}$$

where $(J(t), \xi(t))$ is a solution of $\mathcal{H}_K + \mathcal{H}^{(0)}$, such as those plotted in Fig. 3.2. The system of Eqs. (3.39) is linear and periodic of time and in general, its stability can be studied, at least numerically, with the Floquet theory. Nevertheless, at one of the Lagrangian equilibria, the solutions of $\mathcal{H}_K + \mathcal{H}^{(0)}$ are constant and system (3.39) becomes both linear and time-independent, and is studied by diagonalisation. The hyperbolic point L_3 is unstable, and we are not interested in its dynamics. Both elliptic equilibria L_4 and L_5 are symmetric by the transformation $\xi \mapsto -\xi$ and it is enough to study one of them only. We study the eccentric dynamics at L_4 and we set $(J, \xi) = (0, \pi/3)$ in Eq. (3.39); that is, we set (see Eq. (3.30))

$$A_h = -\frac{27}{8} \quad \text{and} \quad B_h = \frac{27}{8} e^{-i\pi/3}. \tag{3.40}$$

The matrix

$$\mathcal{M}_0 = -\frac{i\eta}{m_0} \begin{pmatrix} m_2 A_h & m_2 \bar{B}_h \\ m_1 B_h & m_1 A_h \end{pmatrix} \tag{3.41}$$

of the differential system has eigenvalues ig_1 and ig_2 where

$$ig_1 = i\eta \frac{27\iota}{8}, \quad ig_2 = 0, \tag{3.42}$$

with associated eigenvectors

$$V_1 = \begin{pmatrix} m_2 e^{4i\pi/3} \\ m_1 \end{pmatrix} \quad \text{and} \quad V_2 = \begin{pmatrix} e^{i\pi/3} \\ 1 \end{pmatrix}. \tag{3.43}$$

The neutral eigenmode, collinear to V_2, is the so-called Lagrange configuration where

$$\frac{X_1}{X_2} = \exp\left(i\frac{\pi}{3}\right). \tag{3.44}$$

Since the corresponding eigenvalue ig_2 is zero, this configuration corresponds to a family of fixed points parameterized by $J_2 \propto \Lambda_1 + \Lambda_2$, where the eccentricities verify $e_1 = e_2$ and $\varpi_1 - \varpi_2 = \pi/3$. The precessing eigenmode, collinear to V_1, is called anti-Lagrange configuration by Giuppone *et al.* (2010) and verify

$$\frac{X_1}{X_2} = \frac{m_2}{m_1} \exp\left(i\frac{4\pi}{3}\right). \tag{3.45}$$

Along this family of periodic orbits, the eccentricities are constant such that $m_1 e_1 = m_2 e_2$ and the pericentres precess at the same frequency ηg_1 while maintaining the relation $\varpi_1 - \varpi_2 = 4\pi/3$.

For an arbitrary solution $(J(t), \xi(t))$, the differential system (3.39) has a priori to be studied with the Floquet theory, which generally does not allow for analytical expressions[8]. Nevertheless, since $g_1 \ll \nu$, the system (3.39) can be studied by time-averaging over one period of ξ. This is justified mathematically by the existence of a canonical transformation Ψ (Theorem 4.5 of Niederman *et al.*, 2020, second averaging theorem)

$$\Psi(J, \xi) = \left(\dot{J}, \dot{\xi}\right), \tag{3.46}$$

such that the dependency on $\dot{\xi}$ is pushed to the second order in eccentricity, that is

$$\dot{\mathcal{H}}(\dot{J}, \dot{\xi}, X_j, \bar{X}_j) = \mathcal{H}(J, \xi, X_j, \bar{X}_j) = \dot{\mathcal{H}}_K(\dot{J}) + \dot{\mathcal{H}}^{(0)}(\dot{J}) + \dot{\mathcal{H}}^{(2)}(\dot{J}, \dot{\xi}, X_j, \bar{X}_j), \tag{3.47}$$

where $\dot{\mathcal{H}} = \mathcal{H} \circ \Psi^{-1}$. A first-order Lie serie expansion (Sect. 2.2.2) performed on Eq. (3.47) would then allow the dependency on $\dot{\xi}$ to be lost, where $\dot{\mathcal{H}}_K + \dot{\mathcal{H}}^{(0)}$ plays the role of $\mathcal{H}_0$ in Eq. (2.60).

The coefficients of the time average of $\mathcal{M}_0(t)$ cannot be given analytically, but in the horseshoe domain, the symmetry of the orbits allows some analytical insight. The expression of B_h in Eq. (3.30) shows that $\mathfrak{Im}(B_h(2\pi - \xi)) = -\mathfrak{Im}(B_h(\xi))$, and since the trajectories $(J(t), \xi(t))$ are symmetric around $(0, \pi)$ in the horseshoe domain (see Fig. 3.1), the time average of $\mathfrak{Im}\, B_h$ vanishes for horseshoe-shaped orbits. As a consequence, the coefficients of the averaged matrix

$$\underline{\mathcal{M}_0} = \frac{1}{2\pi} \int_0^{2\pi} \mathcal{M}_0(\dot{\xi}) d\dot{\xi} = -\frac{i\eta}{m_0} \begin{pmatrix} m_2 \underline{A_h} & m_2 \underline{B_h} \\ m_1 \underline{B_h} & m_1 \underline{A_h} \end{pmatrix}, \tag{3.48}$$

are pure imaginary. Diagonalising $\underline{\mathcal{M}_0}$ shows that its eigenvectors are such that

$$\arg\left(\frac{X_1}{X_2}\right) = \varpi_1 - \varpi_2 = 0, \tag{3.49}$$

for the Lagrange-like configuration, while

$$\arg\left(\frac{X_1}{X_2}\right) = \varpi_1 - \varpi_2 = \pi, \tag{3.50}$$

for the anti-Lagrange-like configuration. This corresponds to aligned and anti-aligned pericentres. We show in Chap. 6 that for a system initially close to L_4, tidal dissipation induces an exponential increase of the libration amplitude, and the system ends up reaching the horseshoe-shaped orbits. In that case, for a system in the Lagrange configuration (*resp.* in the anti-Lagrange configuration), the difference of the pericentres $\varpi_1 - \varpi_2$ starts at $\pi/3$ (*resp.* $4\pi/3$) and decreases until it reaches 0 (*resp.* π) when the system reaches the horseshoe-shaped orbits. This is very visible in Fig. 6.4

[8] The monodromy matrix cannot be computed analytically.

3.3 Contribution of general relativity

Up to this point, we have studied the point-mass co-orbital resonance 1 : 1 according to the Newtonian laws. In this section, we maintain the point-mass approximation but we now consider that the three bodies interact according to the laws of general relativity. As long as the nominal semimajor axis $\bar{a}$ is large with respect to the Schwarzschild radius

$$r_s = \frac{2\mathcal{G}m_0}{c^2} \tag{3.51}$$

of the star, where c is the speed of light, the general relativity only slightly perturbs the motion as described by the laws of Newton, and we will only consider in this section the first Post-Newtonian corrections of the general relativity.

3.3.1 Some intuition

In the circular case, the dynamics of the co-orbital resonance in the Newtonian, point-mass approximation are described by the one degree of freedom Hamiltonian (Eqs. (3.24) & (3.29))

$$\mathcal{H}_0(J,\xi) = \mathcal{H}_K(J) + \mathcal{H}^{(0)}(J,\xi). \tag{3.52}$$

Since the perturbations due to general relativity can be written in Hamiltonian form (Eq. (3.54)), there exists a Hamiltonian $\mathcal{H}_1(J,\xi)$ such that, in the circular case, the Hamiltonian of the co-orbital resonance in the Post-Newtonian expansion reads

$$\mathcal{H}_0(J,\xi) + \varepsilon\mathcal{H}_1(J,\xi), \tag{3.53}$$

where $\varepsilon = v^2/c^2 \approx r_s/(2\bar{a}) \ll 1$ is written to emphasize the smallness of $\mathcal{H}_1$ with respect to $\mathcal{H}_0$ and $v = \bar{a}\eta$ is the orbital speed of the co-orbitals. The two Lagrangian equilibria of $\mathcal{H}_0$ at $(J,\xi) = (0, \pm\pi/3)$, are elliptic (stable), since the eigenvalues in their vicinity, $\pm i\nu$ (see Eq. (3.32)), are pure imaginary. The eigenvalues of $\mathcal{H}_0 + \varepsilon\mathcal{H}_1$ will be a slight perturbation of $\pm i\nu$, and the Lagrangian equilibria may become unstable under the influence of general relativity if one of the eigenvalues is perturbed to a strictly positive real part (Sect. 2.4.1)

Nevertheless, we proved at the end of Sect. 2.4.3 that one degree of freedom Hamiltonians are protected against destabilization by a Hamiltonian perturbation. This means that the eigenvalues in the vicinity of the Lagrangian equilibria will indeed be perturbed by general relativity, but the perturbations will themselves be pure imaginary, and we know without calculations that the Lagrangian equilibria are stable under the effect of general relativity.

This is at least true at the first post-Newtonian approximation, because at the fifth order in v/c and beyond, the emission of gravitational waves induces a dissipation of the orbital energy and prevents the perturbations due to general relativity to be written in Hamiltonian form. Since the Lagrangian equilibria L_4 and L_5 are energy maximizers (Fig. 3.1), a dissipation of the total orbital energy should in that case make the Lagrangian equilibria unstable.

3.3.2 The Post-Newtonian Hamiltonian

At first order in $\varepsilon = v^2/c^2$, the Hamiltonian of two bodies of masses m_0 and m_j reads (*e.g.* Landau and Lifshitz, 1980, page 366)

$$\begin{aligned}\mathcal{H}_{RG}(\hat{\boldsymbol{r}}_{\boldsymbol{j}}, \boldsymbol{r}_{\boldsymbol{j}}) = \frac{\hat{\boldsymbol{r}}_{\boldsymbol{j}}^{\,2}}{2\beta_j} - \frac{\mathcal{G}m_0m_j}{r_j} - \frac{\hat{r}_j^4}{8c^2}\left(\frac{1}{m_0^3} + \frac{1}{m_j^3}\right) + \frac{\mathcal{G}^2 m_0 m_j\,(m_0+m_j)}{2c^2 r_j^2} \\ - \frac{\mathcal{G}}{2c^2 r_j}\left\{3\hat{\boldsymbol{r}}_{\boldsymbol{j}}^{\,2}\left(\frac{m_j}{m_0} + \frac{m_0}{m_j} + \frac{7}{3}\right) + \left(\hat{\boldsymbol{r}}_{\boldsymbol{j}}.\frac{\boldsymbol{r}_{\boldsymbol{j}}}{r_j}\right)^2\right\},\end{aligned} \tag{3.54}$$

where $\hat{\boldsymbol{r}}_{\boldsymbol{j}}$ and $\boldsymbol{r}_{\boldsymbol{j}}$ are respectively the barycentric momentum and heliocentric position, defined in Sect. 2.1.4. The first two terms give the Hamiltonian of the two-body problem in the Newtonian approximation (see Eq. (2.36)), and we remove them in order to only keep the relativistic perturbations. Due to the low mass of the planets with respect to that of the star, we do not take into account the planet−planet non-Newtonian interactions. Neglecting m_j/m_0 in front of 1, we write the relativistic perturbations to the Hamiltonian of the co-orbital problem as $\varepsilon\mathcal{H}_1 = \mathcal{H}_{RG}^{(1)} + \mathcal{H}_{RG}^{(2)}$, where

$$\mathcal{H}_{RG}^{(j)} = -\frac{\hat{r}_j^4}{8c^2m_j^3} + \frac{\mathcal{G}^2m_0^2m_j}{2c^2r_j^2} - \frac{3}{2}\frac{\mathcal{G}m_0\hat{\boldsymbol{r}}_{\boldsymbol{j}}^{\,2}}{m_jc^2r_j}. \tag{3.55}$$

As in Sect. 3.1.3, we rewrite the Hamiltonian $\mathcal{H}_{RG}^{(j)}$ in the variables $(J, J_2, \xi, \xi_2, X_j, \bar{X}_j)$. We are only interested in the secular (*i.e.* long-term) evolution of the orbits, and we average over the angle ξ_2. Even though the perturbation H_P, due to planet−planet Newtonian interactions, was expanded at the zeroth order (Eq. (3.11)) in the variables Λ_j around the Keplerian resonance (Eq. (3.6)), we keep exact expressions[9] in the Λ_j (that is in J and J_2) for $\mathcal{H}_{RG}^{(j)}$. At second order in eccentricity, the Hamiltonian $\mathcal{H}_{RG}^{(j)}$ reads, after performing the rescaling (3.22)

$$\mathcal{H}_{RG}^{(j)} = -\frac{9}{8}\varepsilon\eta\frac{m_j}{m}\mathcal{R}_j^{-4}\left(1 + \frac{4}{3}\mathcal{R}_j^{-1}X_j\bar{X}_j\right), \tag{3.56}$$

where the quantity $\mathcal{R}_j(J)$ was defined by Eq. (3.20) and $m = \sqrt{m_1m_2}$. The total Hamiltonian that we consider for the planar relativistic co-orbital resonance is then

$$\mathcal{H} = \mathcal{H}_K + \mathcal{H}^{(0)} + \mathcal{H}^{(2)} + \sum_{j\in\{1,2\}}\mathcal{H}_{RG}^{(j)}, \tag{3.57}$$

where $\mathcal{H}_K$ is given by Eq. (3.24) and $\mathcal{H}^{(0)}$ and $\mathcal{H}^{(2)}$ are given by Eq. (3.29). The pair of variables $(X_j, \bar{X}_j)$ is not canonical and the equations of motion are given by Eq. (3.23). We obtain the differential system

$$\begin{aligned}\dot{J} &= -\frac{\partial(\mathcal{H}^{(0)} + \mathcal{H}^{(2)})}{\partial\xi}, \\ \dot{\xi} &= \frac{\partial\mathcal{H}_K}{\partial J} + \frac{9}{2}\eta\varepsilon\left\{\mathcal{R}_1^{-5}\left(1 + \frac{5}{3}\frac{X_1\bar{X}_1}{\mathcal{R}_1}\right) - \mathcal{R}_2^{-5}\left(1 + \frac{5}{3}\frac{X_2\bar{X}_2}{\mathcal{R}_2}\right)\right\}, \\ \dot{X}_j &= -2i\frac{m}{m_j}\frac{\partial\mathcal{H}^{(2)}}{\partial\bar{X}_j} + 3i\eta\varepsilon\mathcal{R}_j^{-5}X_j.\end{aligned} \tag{3.58}$$

[9] A zeroth-order expansion loses all dynamical information in the circular case.

General relativity also introduces a small perturbation on $\dot{\xi}_2$, but since the differential system does not depend on this fast angle, and we are not interested in its dynamics, we ignored the corresponding line in Eq. (3.58).

3.3.3 Equilibria and linearization

Taking into account the contributions of general relativity, the Lagrangian equilibria are the fixed point of the differential system (3.58). They still correspond to $X_j = 0$, and in their vicinity, the degree of freedom (J, ξ) is uncoupled from the two degrees of freedom $(X_j, \bar{X}_j)$. We are once again able to study the circular and the eccentric dynamics separately.

Circular dynamics

We evaluate the differential system (3.58) at $X_j = 0$. Because $\mathcal{R}_1(J = 0) = \mathcal{R}_2(J = 0)$, and since general relativity does not perturb the value of dJ/dt, it is easy to see that the Lagrangian equilibria are not displaced by general relativity. The points L_4 and L_5 are still located at $(J, \xi) = (0, \pm\pi/3)$. The point L_3, located at $(J, \xi) = (0, \pi)$, is hyperbolic without general relativity, and given the considerations stated in Sects. 2.4.3 & 3.3.1, we know that general relativity will not make it elliptic, and we are still not interested in its dynamics.

As in Sect. 3.2.1, we linearize the system (3.58) in the vicinity of L_4. The resulting linear system is a small perturbation of Eq. (3.31). Writing $\Delta\xi = \xi - \pi/3$, we have

$$\frac{d}{dt}\begin{pmatrix}\Delta\xi\\ J\end{pmatrix} = \eta\begin{pmatrix}0 & -3\dfrac{m_1+m_2}{m}\left(1+\dfrac{15}{2}\varepsilon\right)\\ \dfrac{9m}{4m_0} & 0\end{pmatrix}\begin{pmatrix}\Delta\xi\\ J\end{pmatrix}. \tag{3.59}$$

The eigenvalues of this linear system can be computed immediately, as

$$\pm i\nu\left(1+\frac{15}{4}\varepsilon\right), \tag{3.60}$$

where ν, the libration frequency of the co-orbitals without general relativity, is given by Eq. (3.32) and we recall that $v = \bar{a}\eta$. As we guessed in Sect. 3.3.1, the Lagrangian equilibria are still elliptic and general relativity is only able to slightly increase the libration frequency.

Eccentric dynamics

Here, we simply repeat the calculations from Sect. 3.2.2, taking into account corrections due to general relativity. At the Lagrangian point L_4, the eccentricities are governed by the linear differential system

$$\frac{d}{dt}\begin{pmatrix}X_1\\ X_2\end{pmatrix} = \mathcal{M}\begin{pmatrix}X_1\\ X_2\end{pmatrix}, \tag{3.61}$$

where the matrix $\mathcal{M}$ is a perturbation of the matrix $\mathcal{M}_0$ given in Eq. (3.41). It reads

$$\mathcal{M} = \mathcal{M}_0 + 3i\eta\varepsilon\mathbb{I}_2 = \mathcal{M}_0 + \varepsilon\mathcal{M}_1. \tag{3.62}$$

The perturbative approach described in Sect. 2.4.2 allows the eigenvalues of $\mathcal{M}$ to be obtained without any calculation. Indeed, $\mathcal{M}_1$ is proportionnal to identity, so it keeps the same expression in any basis. Since the perturbations to the eigenvalues are given by the diagonal terms of $\mathcal{M}_1$, written in a basis that diagonalizes $\mathcal{M}_0$, we can conclude that the perturbations to the eigenvalues are simply the diagonal terms of $3i\eta\varepsilon\mathbb{I}_2$. Denoting λ_1 and λ_2 the eigenvalues of $\mathcal{M}$, we thus have, at first order in ε (see Eq. (3.42))

$$\lambda_1 = ig_1 + 3i\eta\varepsilon, \quad \lambda_2 = ig_2 + 3i\eta\varepsilon = 3i\eta\varepsilon. \tag{3.63}$$

In particular, after one orbital period, the precession of the pericentres due to general relativity, for both Lagrange and anti-Lagrange eigenmodes, amounts to

$$\delta\varpi = 6\pi\varepsilon = \frac{6\pi\mathcal{G}m_0}{\bar{a}c^2}, \tag{3.64}$$

which is the well-known expression of the pericentre advance in general relativity. The eigenvalues λ_j are both pure imaginary, and even in the eccentric case, general relativity is unable to make the Lagrangian equilibria unstable.

3.4 Conclusion

In this chapter, we built an analytical model to study the planar 1 : 1 mean-motion resonance. We studied the limits of validity of the model by estimating the sizes of the remainders of the expansions that we performed. We showed that near the Lagrangian equilateral equilibria, the circular and eccentric dynamics are uncoupled, which allowed us to study them separately. By linearizing the equations of motions in the neighbourhood of the Lagrangian equilibria, we gave analytical expressions of the fundamental frequencies of the system.

In the last section of the chapter, we included the perturbations due to general relativity, showing that the relativistic effects cannot destabilize the Lagrangian equilibria. These effects are only able to slightly modify the fundamental frequencies of the system, and we analytically computed these changes.

Chapter 4

Co-orbital planets in a planar first-order resonance chain

The results of this chapter were first published in Couturier et al. *(2022).*

4.1 Hamiltonian of the $p : p : p + 1$ resonance chain

It has been shown that, at least around low mass stars, co-orbital planets are often formed within a resonance chain (Leleu *et al.*, 2019). In this chapter, we study an occurrence of the planar four-body problem where a star of mass m_0 is orbited by two co-orbital planets of mass m_1 and m_2, and a third planet of mass m_3 further away from the star and in a first-order mean motion resonance with the pair of co-orbital planets. In other words, we study the planar $p : p : p + 1$ resonance chain, where the co-orbitals have a certain nominal period and the nominal period of the outermost third planet is $(p + 1)/p$ that of the co-orbitals. We perform the calculation for any value of the integer p, but the figures that we show in this chapter and in Chap. 7 are for $p = 1$, that is for the resonance chain $1 : 1 : 2$. We do not take into account effects due to general relativity.

4.1.1 The averaged Hamiltonian

We denote $(\tilde{\Lambda}_j, \tilde{D}_j; \lambda_j, -\varpi_j)$ the Poincaré canonical variables (Eq. (2.49), Sect. 2.1.4), that is, we write

$$\tilde{\Lambda}_j = \beta_j \sqrt{\mu_j a_j} \quad \text{and} \quad \tilde{D}_j = \tilde{\Lambda}_j \left(1 - \sqrt{1 - e_j^2}\right), \tag{4.1}$$

where λ_j and ϖ_j are the mean longitude and longitude of the pericentre (of the j^{th} planet), respectively. As in Chap. 3, we have defined $\beta_j = m_0 m_j / (m_0 + m_j)$ and $\mu_j = \mathcal{G}(m_0 + m_j)$, where $\mathcal{G}$ is the gravitational constant. According to Eq. (2.54), we write the complete Hamiltonian as

$$H = H_K(\tilde{\Lambda}_j) + \iota H_P(\tilde{\Lambda}_j, \lambda_j, \tilde{D}_j, \varpi_j), \tag{4.2}$$

where the Keplerian part, due to star−planet interactions, reads (Eq. (2.55))

$$H_K = -\sum_{j\in\{1,2,3\}} \frac{\beta_j^3 \mu_j^2}{2\tilde{\Lambda}_j^2}, \tag{4.3}$$

and the perturbation H_P, due to planet−planet interaction, has a size relative to H_K of order $\iota = (m_1 + m_2 + m_3)/m_0$. We assume that the system is close to the resonance $p : p : p+1$. This means that the nominal mean motions verify

$$n_1^{(0)} = n_2^{(0)} := \eta = \frac{p+1}{p} n_3^{(0)}, \tag{4.4}$$

while the nominal semi-major axes $a_j^{(0)}$ are related to $n_j^{(0)}$ by the Kepler law ${n_j^{(0)}}^2 {a_j^{(0)}}^3 = \mu_0 = \mathcal{G}m_0$. The a_j are always close to their nominal value $a_j^{(0)}$, and the $\tilde{\Lambda}_j$ stay close to the quantities $\Lambda_j^\star$ defined as (Eq. (3.6))

$$\Lambda_j^\star = m_j \sqrt{\mu_0 a_j^{(0)}}. \tag{4.5}$$

At the exact mean motion resonance (Eq. (4.4)), the semi-major axes do not precisely verify $a_1^{(0)} = a_2^{(0)} = (p/(p+1))^{2/3} a_3^{(0)}$. However, it is still possible to consider that the exact resonance occurs at $\tilde{\Lambda}_j = \Lambda_j^\star$, since Sect. 3.1.1 shows that the subsequent error is negligible with respect to the width of the resonance.

To study the dynamics in the vicinity of the resonance, the Hamiltonian is expanded in the neighbourhood of the $\Lambda_j^\star$. As justified in Sect. 3.1.1, if the expansion of the Keplerian part is pushed up to the second order, then an expansion at order 0 in the perturbative part is enough, and we limit ourselves to

$$\iota H_P(\tilde{\Lambda}_j, \lambda_j, \tilde{D}_j, \varpi_j) = \iota H_P(\Lambda_j^\star, \lambda_j, \tilde{D}_j, \varpi_j). \tag{4.6}$$

A suitable linear change of variables to deal with the $p : p : p+1$ resonance chain is (*e.g.* Delisle, 2017)

$$\begin{pmatrix} \xi \\ \xi_2 \\ \xi_3 \\ \sigma_1 \\ \sigma_2 \\ \sigma_3 \end{pmatrix} = \begin{pmatrix} 1 & -1 & 0 & 0 & 0 & 0 \\ 0 & p & -p & 0 & 0 & 0 \\ 0 & -p & p+1 & 0 & 0 & 0 \\ 0 & -p & p+1 & 1 & 0 & 0 \\ 0 & -p & p+1 & 0 & 1 & 0 \\ 0 & -p & p+1 & 0 & 0 & 1 \end{pmatrix} \begin{pmatrix} \lambda_1 \\ \lambda_2 \\ \lambda_3 \\ -\varpi_1 \\ -\varpi_2 \\ -\varpi_3 \end{pmatrix}, \tag{4.7}$$

which is canonical if we transform the actions according to (Eq. (2.31))

$$\left(\tilde{\Lambda}_1, \tilde{\Lambda}_2, \tilde{\Lambda}_3, \tilde{D}_j\right) \mapsto \left(L', \Gamma', G', D_j'\right) = \left(\tilde{\Lambda}_1, \frac{p+1}{p}\left(\tilde{\Lambda}_1 + \tilde{\Lambda}_2\right) + \tilde{\Lambda}_3, \sum_{j\leq 3}\left(\tilde{\Lambda}_j - \tilde{D}_j\right), \tilde{D}_j\right).$$

Since the total angular momentum G' is a first integral, the Hamiltonian does not depend on the angle ξ_3. Moreover, in the $p : p : p+1$ resonance, the angle ξ_2 is fast circulating and we average over it. As we showed in Sect. 2.2.2, averaging over ξ_2 amounts in performing

a canonical transformation[1] that sends the dependency on ξ_2 in a remainder of order ι^2, that we neglect. The averaged Hamiltonian reads

$$H'\left(L',\Gamma',G',\xi,D'_j,\sigma_j\right) = H'_K\left(L',\Gamma',G',D'_j\right) + \frac{1}{2\pi}\int_0^{2\pi} \iota H'_P\left(\xi,\xi_2,D'_j,\sigma_j\right) d\xi_2, \tag{4.8}$$

where we did not write the neglected remainder. The transformation (4.7), along with the averaging process, allows the two degrees of freedom associated with $(\Gamma',G';\xi_2,\xi_3)$ to be eliminated, and we are left with four degrees of freedom. After the averaging process, the scaling parameter Γ' and the angular momentum G' are both parameters and a rescaling by Γ' reduces the dependency to only one parameter. As we study the effect of tidal dissipation on the dynamics in Chap. 7, it is actually more convenient to normalize by the constant (Eq. (4.5))

$$\Gamma^\star = (p+1)\left(\Lambda_1^\star + \Lambda_2^\star\right)/p + \Lambda_3^\star \tag{4.9}$$

rather than by Γ', which is not constant when dissipation is present. In other words, we perform the canonical[2] transformation

$$\mathcal{H} = \frac{H'}{\Gamma^\star}, \quad L = \frac{L'}{\Gamma^\star}, \quad G = \frac{G'}{\Gamma^\star}, \quad \Gamma = \frac{\Gamma'}{\Gamma^\star}, \quad D_j = \frac{D'_j}{\Gamma^\star}, \quad \Lambda_j = \frac{\tilde{\Lambda}_j}{\Gamma^\star}, \tag{4.10}$$

while the angles are unchanged.

4.1.2 Expansion of the Keplerian part

As we did in Chap. 3, we expand the Keplerian part of the Hamiltonian at second order in the vicinity of the $\Lambda_j^\star$. If we denote $\Delta\tilde{\Lambda}_j = \tilde{\Lambda}_j - \Lambda_j^\star$, the expansion reads

$$H_K = \sum_{j=1}^{3} n_{j,0}\Delta\tilde{\Lambda}_j - \frac{3}{2}\sum_{j=1}^{3}\frac{n_{j,0}}{\Lambda_j^\star}\Delta\tilde{\Lambda}_j^2. \tag{4.11}$$

Substituting $\tilde{\Lambda}_j - \Lambda_j^\star$ for $\Delta\tilde{\Lambda}_j$, we obtain

$$H_K = 4\sum_{j=1}^{3} n_{j,0}\tilde{\Lambda}_j - \frac{3}{2}\sum_{j=1}^{3}\frac{n_{j,0}}{\Lambda_j^\star}\tilde{\Lambda}_j^2 - \frac{5}{2}\sum_{j=1}^{3} n_{j,0}\Lambda_j^\star. \tag{4.12}$$

The third term is constant and can be removed without changing the dynamics. In the variables L, G, Γ and D_j, $\mathcal{H}_K$ takes the form

$$\mathcal{H}_K = -\frac{3}{2}\eta\left\{C_1L^2 + C_2\left(p\left(\Gamma-\Upsilon\right)-L\right)^2 + C_3p\left(p+1\right)\left(\Upsilon - \frac{p\Gamma}{p+1}\right)^2\right\} + \frac{4\eta p\Gamma}{p+1}, \tag{4.13}$$

where we denoted $\Upsilon = G + D_1 + D_2 + D_3 = \sum_j \Lambda_j$ and $C_j = \Gamma^\star/\Lambda_j^\star$, that is

$$\begin{aligned} C_1 &= \left(\frac{p+1}{p}\right)^{1/3}\frac{m_3}{m_1} + \frac{p+1}{p}\left(1+\frac{m_2}{m_1}\right), \\ C_2 &= \frac{m_1}{m_2}C_1, \quad C_3 = 1 + \left(\frac{p+1}{p}\right)^{2/3}\frac{m_1+m_2}{m_3}. \end{aligned} \tag{4.14}$$

[1] For convenience, we do not change the name of the variables.

[2] The Jacobian of this transformation is not symplectic, but the rescaling of the Hamiltonian guarantees that the form of Eq. (2.19) is preserved.

Without dissipation, Γ and G are both integrals of motion. Due to the normalization by the constant $\Gamma^\star$, Γ is close to 1 and we simply evaluate $\mathcal{H}_K$ at $\Gamma = 1$, hence achieving the reduction to only one parameter. The relevant parameter to consider is Γ/G and the variations of Γ are now[3] absorbed by G (Eqs. (4.34) and (4.35)). The last term of Eq. (4.13) is constant and can be removed from the Hamiltonian.

Instead of the variables L, G, and Γ, we can use the variables ΔL, ΔG, and $\Delta\Gamma$ defined by their difference to the Keplerian resonance (4.5). In this case the approximation $\Gamma = 1$ becomes $\Delta\Gamma = 0$ and Eq. (4.11) yields, once normalized,

$$\mathcal{H}_K = -\frac{3}{2}\eta\left\{\left(p^2C_2 + p(p+1)C_3\right)\Delta\Upsilon^2 + 2pC_2\Delta\Upsilon\Delta L + \left(C_1+C_2\right)\Delta L^2\right\}, \tag{4.15}$$

where $\Delta\Upsilon = \Delta G + D_1 + D_2 + D_3 = \sum_j \Delta\Lambda_j$. We find the Hamiltonian (4.15) to be well adapted to the analytical work derived in Sect. 4.3.1, while we use the Hamiltonian (4.13) elsewhere. Moreover, we do not perform the evaluation $\Gamma = 1$ in Chap. 7, where we study the resonance chain $p : p : p+1$ in presence of tidal dissipation, making Γ a variable quantity. Hamiltonians (4.13) & (4.15) both yield the same dynamics and using either is only a matter of preference.

4.1.3 Expansion of the perturbative part

The perturbative part $\iota\mathcal{H}_P$ of the Hamiltonian is expanded in power series of the eccentricities. To this end, we separate the contributions due to the interactions between each pair of planets as

$$\iota\mathcal{H}_P = \mathcal{H}_{1,2} + \mathcal{H}_{1,3} + \mathcal{H}_{2,3}. \tag{4.16}$$

We denote $X_j = \sqrt{2\tilde{D}_j/\tilde{\Lambda}_j}\, e^{i\varpi_j} = e_j e^{i\varpi} + \mathcal{O}\left(e_j^3\right)$. For a pair $(p_1,p_2) \in \{(1,2),(1,3),(2,3)\}$ of planets, the Hamiltonian $\mathcal{H}_{p_1,p_2}$ is given by Eq. (2.58). The d'Alembert rule (2.59), combined with the average over $\xi_2 = p\lambda_2 - p\lambda_3$, implies that $\mathcal{H}_{1,2}$ has no term of odd degree in eccentricity, while $\mathcal{H}_{1,3}$ and $\mathcal{H}_{2,3}$ have no term of degree 0. Since we limit ourselves to the second degree in eccentricity, we write

$$\mathcal{H}_{1,2} = \mathcal{H}^{(0)} + \mathcal{H}^{(2)}_{1,2}, \quad \mathcal{H}_{j,3} = \mathcal{H}^{(1)}_{j,3} + \mathcal{H}^{(2)}_{j,3}, \tag{4.17}$$

where $j \in \{1,2\}$. The superscript refers to the degree in eccentricity, while the subscript refers to the considered pair of planets. The Hamiltonian $\mathcal{H}^{(0)}$ has no subscript since only the co-orbital pair yields terms of degree 0 and no confusion is possible. The part $\mathcal{H}_{1,2}$ of the Hamiltonian was already computed in Chap. 3, and is given by Eq. (3.29). Using the variables D_j and σ_j, and given the normalization (4.10), we can write

$$\begin{aligned}
\mathcal{H}^{(0)} &= \frac{m_1}{m_0}\frac{\eta}{C_2}\left(\cos\xi - \Delta^{-1}\right),\\
\mathcal{H}^{(2)}_{1,2} &= \frac{m_1}{m_0}\frac{\eta}{C_2}\left\{A_h\left(C_1D_1 + C_2D_2\right) + 2\sqrt{C_1C_2D_1D_2}\,\mathfrak{Re}\left(B_h e^{i(\sigma_2-\sigma_1)}\right)\right\},
\end{aligned} \tag{4.18}$$

where $\Delta = \sqrt{2-2\cos\xi}$. The coefficients A_h and B_h are given by Eq. (3.30), and the C_j, that depends only on the planetary masses and on p, were defined by Eq. (4.14).

[3] After the evaluation $\Gamma = 1$, G is in fact G/Γ, but we abusively keep writing G.

Following Laskar and Robutel (1995) and using the algebraic manipulator *Trip* (Gastineau and Laskar, 2011), $\mathcal{H}^{(1)}_{j,3}$ and $\mathcal{H}^{(2)}_{j,3}$ can be written

$$\mathcal{H}^{(1)}_{j,3} = \frac{m_j n_3^{(0)}}{m_0 C_3} \left\{ C^{(1)}_{p,1} \sqrt{2C_j D_j} \cos\left(p\delta_{j,1}\xi - \sigma_j\right) + C^{(1)}_{p,2} \sqrt{2C_3 D_3} \cos\left(p\delta_{j,1}\xi - \sigma_3\right) \right\}, \quad (4.19)$$

and

$$\begin{aligned} \mathcal{H}^{(2)}_{j,3} = \frac{2m_j}{m_0} \frac{n_3^{(0)}}{C_3} \Big\{ & C^{(2)}_{p,1} C_j D_j \cos\left(2p\delta_{j,1}\xi - 2\sigma_j\right) + C^{(2)}_{p,2} C_3 D_3 \cos\left(2p\delta_{j,1}\xi - 2\sigma_3\right) \\ & + C^{(2)}_{p,3} \sqrt{C_j C_3 D_j D_3} \cos\left(2p\delta_{j,1}\xi - \sigma_j - \sigma_3\right) \\ & + C^{(2)}_{p,4} \left(C_j D_j + C_3 D_3\right) + C^{(2)}_{p,5} \sqrt{C_j D_j C_3 D_3} \cos\left(\sigma_j - \sigma_3\right) \Big\}, \end{aligned} \quad (4.20)$$

where $\delta_{j,1} = 1$ if $j = 1$ and zero if $j = 2$. The quantities $C^{(n)}_{p,m}$ depend only on p and can be obtained using the Laplace coefficients. For $p = 1$, their analytical expressions, as well as a numerical evaluation, is given in Eqs. (B.2) & (B.3) of Appendix B. The final Hamiltonian of the model is then

$$\mathcal{H}(L, D_j; \xi, \sigma_j) = \mathcal{H}_K + \mathcal{H}^{(0)} + \mathcal{H}^{(1)}_{1,3} + \mathcal{H}^{(1)}_{2,3} + \mathcal{H}^{(2)}_{1,2} + \mathcal{H}^{(2)}_{1,3} + \mathcal{H}^{(2)}_{2,3}. \quad (4.21)$$

As opposition to the complete Hamiltonian of Eq. (4.2), we refer to Eq. (4.21) as the simplified Hamiltonian, or as the model. We recall the three simplifications that led from Eq. (4.2) to Eq. (4.21)

- Average over the angle $\lambda_2 - \lambda_3$, that is, Lie serie expansion at first order in ι, while ignoring the associated near-identity change of variables (see Sect. 2.2.2).
- Expansion at second order in eccentricity.
- Expansion of the semimajor axes in the neighbourhood of Eq. (4.5), at second order for H_K, and at the zeroth order for ιH_P.

We denote $F_0 : \mathbb{R}^8 \mapsto \mathbb{R}^8$ the vector field derived from Eq. (4.21) by the Hamilton Eqs. (2.18).

4.2 Important theoretical results on resonance chains

4.2.1 From fixed points to *libration centres*

As we will see in Sect. 4.3.2, the model (4.21) has equilibria, that is, points in the phase space where the vector field F_0 vanishes. At a fixed point (or equilibrium) of the model, L and D_j are constant and so are e_j and a_j. Similarly, the angles σ_j and ξ are constant; that is, there exists constants c_j such that

$$\sigma_j = -p\lambda_2 + (p+1)\lambda_3 - \varpi_j = c_j. \quad (4.22)$$

However, the secular angle $\xi_3 = -p\lambda_2 + (p+1)\lambda_3$ and the pericentres ϖ_j are not constant at the equilibria, but they all precess with the same frequency, which we denote ν_3.

Even though the model has equilibria, the complete Hamiltonian (4.2) has none, since no initial condition in the n-body problem leads to the immobility of the system. The canonical change of variable that we ignored, inherent to the Lie serie expansion, explains the inconsistency. Indeed, as is explained in Sect. 2.2.2, the average over the angle ξ_2 in Eq. (4.8) is in fact a near-identity canonical transformation that allows the dependency on that angle to be pushed to the neglected second order in ι. As a consequence, the simplified Hamiltonian $\mathcal{H}$ (Eq. (4.21)) does not depend on $\boldsymbol{x} = {}^t(L, \Gamma, G, D_j; \xi, \xi_2, \xi_3, \sigma_j)$, but rather on $\check{\boldsymbol{x}} = {}^t\left(\check{L}, \check{\Gamma}, \check{G}, \check{D}_j; \check{\xi}, \check{\xi}_2, \check{\xi}_3, \check{\sigma}_j\right)$, where (Eq. (2.63))

$$\check{\boldsymbol{x}} = \Phi_{\iota\chi}(-1, \boldsymbol{x}) = e^{-\iota L_\chi}\boldsymbol{x}. \tag{4.23}$$

Equations. (2.67) to (2.70) show that the transformation $\Phi_{\iota\chi}(-1, \cdot)$ is quasiperiodic with vector of frequencies $\boldsymbol{\omega_0} = \partial\mathcal{H}_K/\partial\boldsymbol{J}$, where $\boldsymbol{J} = {}^t(L, \Gamma, G, D_1, D_2, D_3)$. Furthermore, at an equilibrium of the model, because $\check{\boldsymbol{x}}$ is constant, the Fourier decomposition of χ in Eq. (2.69) only depends on the frequencies ν_2 and ν_3, with

$$\nu_2 = \dot{\xi}_2 = \frac{\partial\mathcal{H}}{\partial\Gamma} \quad \text{and} \quad \nu_3 = \dot{\xi}_3 = \frac{\partial\mathcal{H}}{\partial G} = \frac{\partial\mathcal{H}}{\partial\Upsilon}, \tag{4.24}$$

where these quantities are evaluated at the equilibrium. This means that at an equilibrium of the model (4.21), the transformation $\check{\boldsymbol{x}} \mapsto \boldsymbol{x}$ is quasiperiodic with frequencies ν_2 and ν_3, and so is $\boldsymbol{x}$. More precisely, $\boldsymbol{x}$ is periodic with frequency ν_2, in a frame rotating with the pericentres ϖ_j at frequency ν_3. Furthermore, for a quantity invariant around the axis of total angular momentum, like ξ or the σ_j, the Fourier decomposition does not feature ν_3, and the motion of $\boldsymbol{x}$ in the complete Hamiltonian (4.2) is periodic with frequency ν_2.

In other words, the motion of a quantity z depending on $\boldsymbol{x}$, along the flow of the complete Hamiltonian (Eq. (4.2)), using an equilibrium of the simplified Hamiltonian (Eq. (4.21)) as initial condition, is

- Periodic with frequency ν_2 if z is invariant by the angle translation $(\lambda_j, \varpi_j) \mapsto (\lambda_j + \vartheta, \varpi_j + \vartheta)$, where ϑ is any constant angle.
- Quasiperiodic with frequencies ν_2 and ν_3 if z is not invariant by this angle translation.

Given the general change of variables proposed by Eq. (A.1) of Delisle (2017), it is easy to notice that this result is true for any chain of resonances. In the rest of this work, what is known as a fixed point or equilibrium for the model is referred to as a *libration centre* in the complete system.

4.2.2 An algorithm to find the *libration centres*

According to Sect. 4.2.1, the equilibria of the simplified Hamiltonian (Eq. (4.21)), should correspond to points in the phase space where, along the flow of the complete Hamiltonian (Eq. (4.2)), the motion of a quantity z invariant by rotation and depending on $\boldsymbol{x} = {}^t(L, \Gamma, G, D_j; \xi, \xi_2, \xi_3, \sigma_j)$, is periodic with frequency ν_2. However, due to the expansion of the Hamiltonian in eccentricities and semimajor axes, the *libration centres* of the complete Hamiltonian do not coincide with the equilibria of the model. We develop here an iterative algorithm, similar to that in Couetdic *et al.* (2010), to find a *libration*

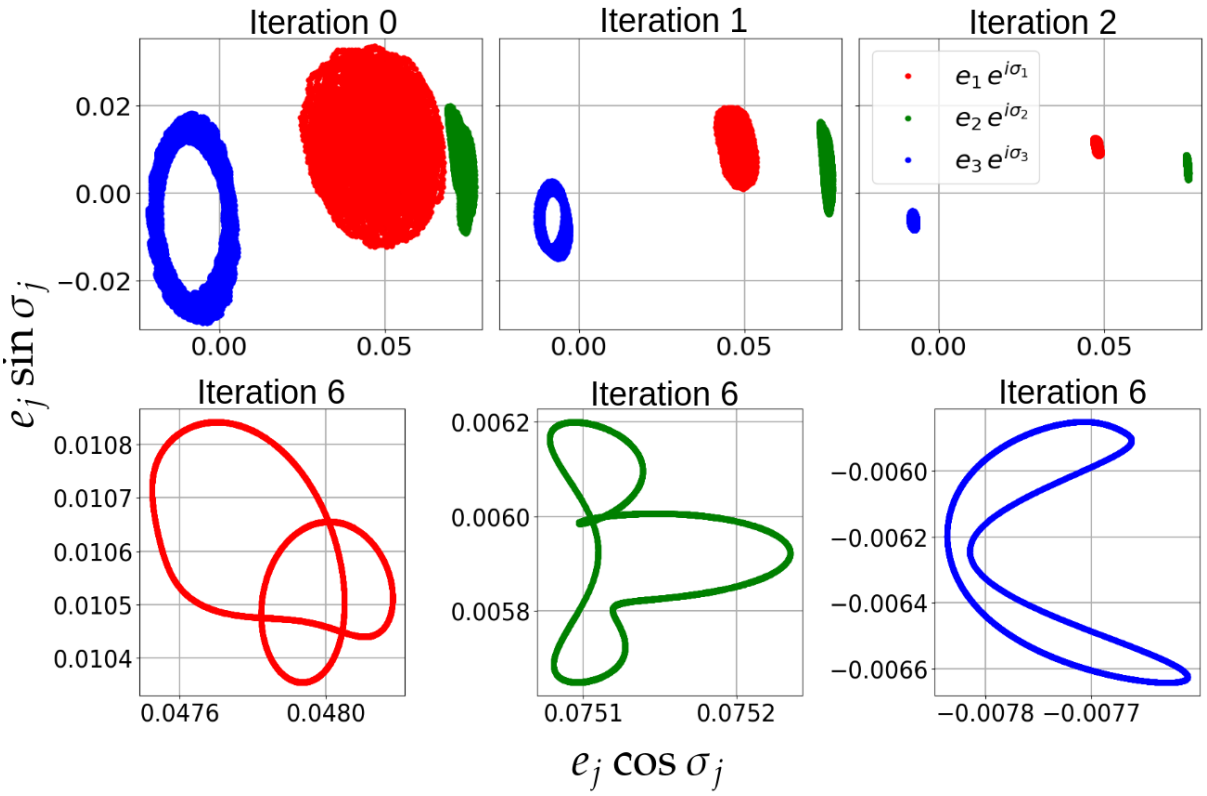

Fig. 4.1 — Trajectories of $e_j e^{i\sigma_j}$ in the complete Hamiltonian (4.2) for the six iterations needed for the algorithm to converge to the *libration centre*. Iteration 0 is an elliptic equilibrium[4] of the simplified Hamiltonian (4.21). It is rather far from the *libration centre* of the complete Hamiltonian (see also Fig. 4.4). After six iterations, the algorithm converges to the *libration centre* and the motion is periodic (hence the closed curves) with frequency ν_2 (Sect. 4.2.1). The planetary masses are those of Fig. 4.2 and the resonance chain is $1:1:2$.

centre of the complete Hamiltonian using an equilibrium of the simplified Hamiltonian as initial condition.

We assume, close enough to a *libration centre* of the complete Hamiltonian (4.2), that the trajectories are quasiperiodic, and we write, for any complex quantity z depending on these trajectories,

$$z\,(t) = \sum_{\boldsymbol{k}\in\mathbb{Z}^6} z_{\boldsymbol{k}} e^{i\boldsymbol{k}\cdot\boldsymbol{\omega}t}, \tag{4.25}$$

where the coordinates of the vector $\boldsymbol{\omega} = {}^t(\nu, \nu_2, \nu_3, g_1, g_2, g_3)$ are the fundamental frequencies of the complete Hamiltonian (4.2). The frequencies ν, ν_2, and ν_3 have approximate values given by Eqs. (4.39), (4.24), and (4.30), respectively. The description of the algorithm is as follows:

- Find the position of an elliptic equilibrium of the simplified Hamiltonian (4.21) with a Newton-Raphson method. Use it as the initial condition to integrate numerically the trajectories of the complete Hamiltonian (4.2).
- For a complex quantity z depending on the trajectories of (4.2), obtain the decomposition (4.25) using a frequency analysis method (*e.g.* Laskar, 1993).

[4] It is the main branch, introduced in Sect. 4.3.1, at $\delta = 5$ (see Eq. (4.34)).

- Identify the terms depending on frequencies other than ν_2 and set to 0 the corresponding coefficient $z_{\boldsymbol{k}}$.
- Proceed similarly for enough quantities z and evaluate them at time $t = 0$ in order to obtain a new initial condition. Restart from the first step using the new initial condition instead of the equilibrium of (4.21).

The process is iterated until a convergence occurs. In Fig. 4.1, we display the trajectories of the quantities $e_j e^{i\sigma_j}$ in the plane $(e_j \cos\sigma_j,\ e_j \sin\sigma_j)$ as the algorithm iterates. Isolating terms featuring frequencies other than ν_2 is difficult, if not impossible, since the frequency analysis gives the scalars $\boldsymbol{k}\cdot\boldsymbol{\omega}$ but not the vector $\boldsymbol{k}$, which cannot be deduced as the vector $\boldsymbol{\omega}$ is unknown for the complete Hamiltonian. We can get around this difficulty because ν_2 is much larger than the other frequencies, hence it is easy to isolate terms that depend on ν_2 from those that do not. The implementation is thus simplified by setting to 0 the coefficients $z_{\boldsymbol{k}}$ of the terms that do not depend on ν_2, instead of setting to 0 the coefficients $z_{\boldsymbol{k}}$ of the terms that depends on frequencies other than ν_2. This does not prevent the algorithm from properly converging.

4.3 Equilibria and linearization

In this section we study the equilibria of the resonance $p : p : p+1$ and the dynamics in their vicinity.

4.3.1 Analytical results

The fixed points of the Hamiltonian (4.21) cannot be given analytically, even if it is truncated at first degree in eccentricity. Similar difficulties were met by Delisle (2017) for resonance chains with first-order resonances between non-consecutive planets. However, we show here that further simplifications allow us to obtain analytical expressions of the equilibria and of the eigenvalues of the linearized system. In this subsection, we consider the Hamiltonian $\mathcal{H} = \mathcal{H}_K + \mathcal{H}^{(0)} + \mathcal{H}^{(1)}$, that is, the Hamiltonian of Eq. (4.21), where the terms of second order in eccentricity (those featuring the superscript (2)) have been removed. The Hamiltonian $\mathcal{H}_K + \mathcal{H}^{(0)} + \mathcal{H}^{(1)}$ is only a small perturbation of the Hamiltonian $\mathcal{H}_K + \mathcal{H}^{(0)}$, studied in Sect. 3.2.1, which has equilibria at $\xi \in \{\pm\pi/3, \pi\}$. The equilibrium at $\xi = \pi$ is unstable and we are not interested in its dynamics. Only the equilibria $\xi = \pm\pi/3$ are interesting to us, and since their dynamics are symmetric, it is enough to only consider $\xi = \pi/3$.

To further simplify the Hamiltonian, we force a decoupling between the degree of freedom $(\xi, \Delta L)$ associated with the libration of the co-orbitals and the three other degrees of freedom (σ_j, D_j). We proceed in two steps :

- We first evaluate $\mathcal{H}^{(1)} = \mathcal{H}^{(1)}_{1,3} + \mathcal{H}^{(1)}_{2,3}$ at $\xi = \pi/3$, meaning that $\mathcal{H}^{(1)}$ loses its dependency on ξ.
- We then replace the variable ΔL by the constant $\Delta L^\star$ in the anti-diagonal term[5] of $\mathcal{H}_K$ in (4.15), where $\Delta L^\star$ is the value of ΔL for which $\partial\mathcal{H}_K/\partial\Delta L$ vanishes, that is

[5]The term proportional to $\Delta L\Delta\Upsilon$

$$\Delta L^\star = -\frac{pC_2}{C_1+C_2}\left(\Delta G + D_{1,0} + D_{2,0} + D_{3,0}\right). \tag{4.26}$$

The $D_{j,0}$ are given by Eq. (4.29). While the evaluation at $\xi = \pi/3$ allows analytical expressions for the position of the fixed points, the evaluation at $\Delta L = \Delta L^\star$ uncouples $(\xi, \Delta L)$ from (σ_j, D_j) and enables analytical expressions of the eigenvalues of the linearized system in the vicinity of the fixed points. The differential system derived from $\mathcal{H}_K + \mathcal{H}^{(0)} + \mathcal{H}^{(1)}$, after these simplifications have been performed, is given in Appendix C. It vanishes when the angles are equal to

$$\xi_0 = \frac{\pi}{3}, \quad \sigma_{1,0} = p\frac{\pi}{3} + \epsilon\pi, \quad \sigma_{2,0} = \epsilon\pi, \quad \sigma_{3,0} = \arctan\frac{m_1 \sin p\xi_0}{m_2 + m_1 \cos p\xi_0} + (1-\epsilon)\,\pi, \tag{4.27}$$

where[6]

$$\epsilon = \begin{cases} 0 & \text{if } \nu_3 < 0, \\ 1 & \text{if } \nu_3 > 0, \end{cases} \tag{4.28}$$

and when the actions are equal to[7]

$$\begin{aligned} &C_1 D_{1,0} = C_2 D_{2,0}, \quad \frac{D_{3,0}}{D_{1,0}} = \frac{C_3 {C_{p,2}^{(1)}}^2 H^2}{C_1 {C_{p,1}^{(1)}}^2}, \quad \Delta L_0 = 0 \quad \text{and} \\ &\frac{C_1 {C_{p,1}^{(1)}}^2 m_1^2 p^2}{2C_3^2 m_0^2 (p+1)^2} = \left(\frac{\nu_3}{\eta}\right)^2 D_{1,0} \end{aligned} \tag{4.29}$$

where the precession frequency of the pericentres is

$$\nu_3 = -\eta K \left(\Delta G + D_{1,0} + D_{2,0} + D_{3,0}\right), \quad K = \frac{3p^2 C_1 C_2}{C_1 + C_2} + 3p\,(p+1)\,C_3, \tag{4.30}$$

and we define the constant H by

$$H = \cos\left(p\xi_0 - \sigma_{3,0}\right) + \frac{m_2}{m_1}\cos\sigma_{3,0}. \tag{4.31}$$

The unknowns quantities of Eq. (4.29) are the $D_{j,0}$, and since the ratios $D_{2,0}/D_{1,0}$ and $D_{3,0}/D_{1,0}$ are known, we are reduced to the unique unknown quantity $D_{1,0}$. The precession frequency of the pericentres, ν_3, depends on $D_{1,0}$ (see Eq. (4.30)). Denoting $C = 1 + D_{2,0}/D_{1,0} + D_{3,0}/D_{1,0}$ and performing the translation $Z = D_{1,0} + 2\Delta G/3C$, we can rewrite Eq. (4.29) as a third-degree polynomial in Z

$$\begin{aligned} &Z^3 - PZ - Q = 0, \\ &\text{where} \quad P = \frac{\Delta G^2}{3C^2} \quad \text{and} \quad Q = \frac{2\Delta G^3}{27C^3} + \frac{C_1 {C_{p,1}^{(1)}}^2 m_1^2 p^2}{2C^2 C_3^2 K^2 m_0^2 (p+1)^2}. \end{aligned} \tag{4.32}$$

The coefficients P and Q of this polynomial depend on the parameter ΔG, that we properly define in Eq. (4.35). There is a bifurcation between 1 and 3 real solutions when $27Q^2 - 4P^3 = 0$ (Cardano, 1545), that is at

$$\Delta G = \Delta G_{\text{bif}} = -\left(\frac{27 C_1 {C_{p,1}^{(1)}}^2 p^2 C m_1^2}{8 C_3^2 K^2 m_0^2 (p+1)^2}\right)^{1/3}. \tag{4.33}$$

[6] An analytical expression for ν_3 is given by Eq. (4.30).

[7] $C_1 D_{1,0} = C_2 D_{2,0}$ yields $e_{1,0} = e_{2,0}$ since $e_j = \sqrt{2C_j D_j}$.

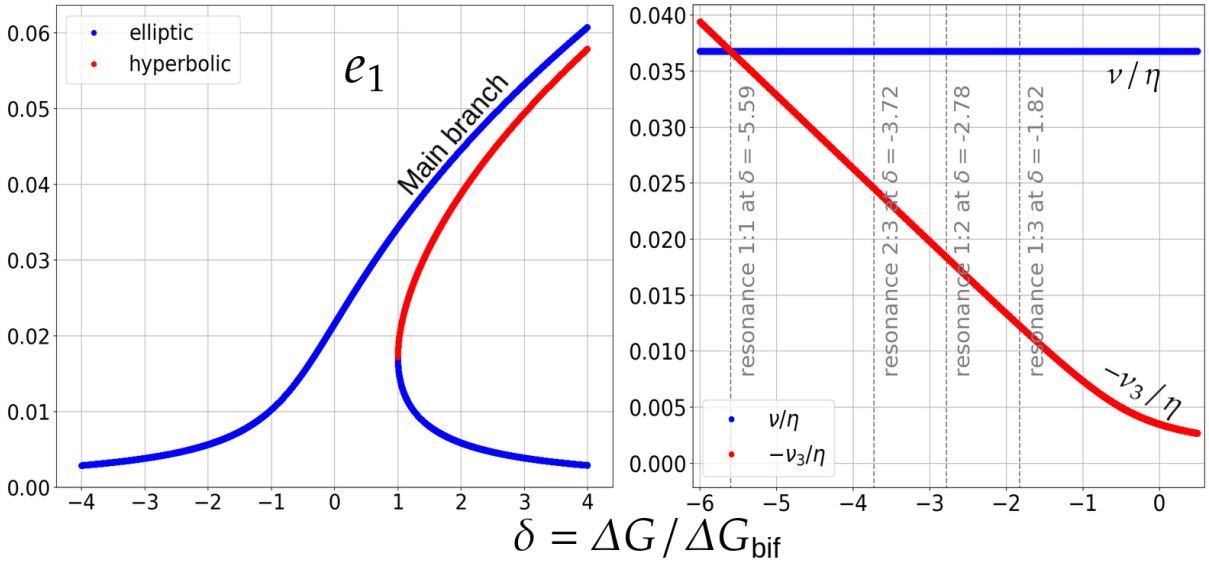

Fig. 4.2 — Values of the eccentricities and fundamental frequencies given by the analytical results. *Left*: Value of e_1 at the fixed points of the resonance chain $1:1:2$ as predicted by Eq. (4.32). *Right*: Values of ν/η and ν_3/η along the main branch as a function of δ, for the same resonance chain, predicted by Eqs. (4.39) and (4.30). In both panels the planetary masses are $(m_1+m_2)/2 = m_3 = 10^{-4}\,m_0$ and $m_2/m_1 = 10$. According to Eq. (4.29), $e_1 = e_2$, and for this choice of masses and resonance chain $e_3/e_1 = 0.5471$. In Table 4.1, which gathers the fixed points at second order in eccentricity, the three branches visible in the left plot are branches 1 (main branch), 2, and 6. The secular resonances between ν and ν_3 are shown on the right, and are also easy to spot in Fig. 4.6.

In the rest of this work we use the parameter

$$\delta = \Delta G / \Delta G_{\rm bif}, \tag{4.34}$$

where

$$\Delta G = \frac{G'}{\Gamma'} - \frac{G^\star}{\Gamma^\star} = \frac{G}{\Gamma} - \frac{\sum_j \Lambda_j^\star}{\Gamma^\star} = \frac{G}{\Gamma} - \sum_{j=1}^{3} C_j^{-1}. \tag{4.35}$$

In this chapter, $\Gamma = \Gamma'/\Gamma^\star \approx 1$ is simply evaluated at 1 and ignored, but not in Chap. 7, where tidal dissipation induces a drift in Γ, hence in δ. The normalisation by $\Delta G_{\rm bif}$ ensures that the bifurcation is at $\delta = 1$, regardless of the planetary masses.

The forced decoupling that we performed to obtain these expressions leads to results that are very similar to the second fundamental model of resonance proposed by Henrard and Lemaitre (1983). The fixed points are given by the roots of the third-degree polynomial in Z (4.32), which has one or three real solutions depending on δ, hence a bifurcation. The solutions of Eq. (4.32) are plotted in Fig. 4.2. For $\delta < 1$, only one elliptic equilibrium exists, called the main branch, while for $\delta \geq 1$ two other fixed points appear, one of them being hyperbolic, hence the presence of separatrices in the phase space and the formal existence of a resonance. These results come from a strong hypothesis, and we see in Sect. 4.3.2 that the topology of the Hamiltonian (4.21) is different (see Table 4.1). However, we show in Fig. 4.3 that these analytical expressions are accurate for low eccentricities.

We now linearize the set of Eqs. (C.1) in the vicinity of the main branch. We make

use of the cartesian coordinates

$$u_j = \sqrt{2D_j}\cos\sigma_j \quad \text{and} \quad v_j = \sqrt{2D_j}\sin\sigma_j, \tag{4.36}$$

and denoting $X = {}^t(u_1, u_2, u_3, v_1, v_2, v_3, \Delta L, \xi)$, the linearized system is

$$\begin{aligned} \frac{d\Delta X}{dt} &= \begin{pmatrix} \mathcal{Q}_6 & 0_{6,2} \\ 0_{2,6} & \mathcal{Q}_2 \end{pmatrix} \Delta X, \quad \text{where} \quad \Delta X = X - X_0, \\ \mathcal{Q}_2 &= \begin{pmatrix} 0 & \dfrac{9m_1}{4m_0}\eta C_2^{-1} \\ -3\eta\,(C_1 + C_2) & 0 \end{pmatrix}, \end{aligned} \tag{4.37}$$

and X_0 is the equilibrium value of X. The matrix $\mathcal{Q}_6$ is given by Eq. C.4. Its characteristic polynomial reads

$$\det\left(\lambda\mathbb{I}_6 - \mathcal{Q}_6\right) = \left(\lambda^2 + \nu_3^2\right)^2 \left(\lambda^2 + \nu_3^2 - 2\nu_3 I \sum_{j=1}^{3} D_{j,0}\right), \tag{4.38}$$

where the constant I is defined in Eq. (C.3). It is interesting to note that the precession frequency of the pericentres, $\pm i\nu_3$, is an eigenvalue of the differential system (4.37). This factorisation was already noted by Pucacco (2021), who studied the resonance chain $1:2:4$ of the Galilean satellites, although it was not attributed to the precession of the pericentres (see their Eq. (109)). The eigenvalues of $\mathcal{Q}_2$ are $\pm i\nu$, where ν is given by Eq. (3.32)

$$\nu = \eta\sqrt{\frac{27}{4}\frac{m_1 + m_2}{m_0}}. \tag{4.39}$$

We recall that ν is the libration frequency of the angle ξ in the neighbourhood of the equilateral Lagrangian configuration. Figures 4.2 and 4.5 show that $\nu_3 < 0$ for the main branch, which ensures that the roots of (4.38) are pure imaginary. Evaluating the eigenvalues $\pm i\nu$ and $\pm i\nu_3$ in the vicinity of the main branch shows that, at $\delta \approx -5.6$ for the planetary masses in Fig. 4.2, all these eigenvalues have roughly the same value, yielding a $1:1$ secular resonance between the libration frequency of the co-orbitals and the precession frequency of the pericentres. Other secular resonances between ν and ν_3 are shown in Fig. 4.2, and are also very visible on the stability map from Fig. 4.6. We show in Sect. 7.2.2 that the secular resonance $1:1$ has important consequences for the tidal stability of the co-orbital pair.

4.3.2 Numerical results

In the previous section, strong approximations allowed the equilibria and eigenvalues of the model to be given analytically. We now develop a Newton–Raphson-based algorithm to numerically and exactly find the equilibria of the Hamiltonian (4.21) and compare them with the analytical approximations elaborated in Sect. 4.3.1.

The Newton–Raphson algorithm finds equilibria by starting from a random initial condition in the phase space, and we discretize it by exploring a grid in the parallelepiped defined by $|u_j| < 0.08$ and $|v_j| < 0.08$ (recall that $e_j^2 = C_j(u_j^2 + v_j^2)$). In order to pretend to have found all possible equilibria, it is necessary that the discretization is thin, or in other

	$100\,e_1$	$100\,e_2$	$100\,e_3$	σ_1 (°)	σ_2 (°)	σ_3 (°)	$L-0.0345$	ξ (°)	nature	domain
1	4.449	7.490	5.878	$\pm$14.433	$\pm$22.572	$\mp$92.014	6.461e−5	$\pm$59.760	elliptic	$\delta \in \mathbb{R}$
2	0.168	0.165	0.093	$\mp$119.18	$\pm$179.92	$\pm$4.6606	19.34e−5	$\pm$60.003	δ-dependent	$\delta > 1.129$
3	5.201	7.645	5.470	$\pm$14.216	$\mp$15.688	$\pm$95.525	6.483e−5	$\pm$59.806	elliptic	$\delta > 5.997$
4	8.344	8.646	0.305	180	0	0	6.501e−5	180	hyperbolic	$\delta \in \mathbb{R}$
5	7.939	7.180	5.922	$\mp$151.76	$\mp$20.944	$\pm$92.729	6.439e−5	$\pm$179.13	hyperbolic	$\delta > 4.195$
6	10.11	6.330	6.246	$\mp$102.00	$\pm$177.92	$\pm$4.3287	7.200e−5	$\pm$62.538	hyperbolic	$\delta > 1.129$
7	6.009	8.721	1.696	$\pm$6.8311	$\mp$1.8178	$\pm$86.449	6.518e−5	$\pm$59.710	hyperbolic	$\delta > 5.999$
8	0.164	0.165	0.079	0	180	0	19.34e−5	180	hyperbolic	$\delta > 1.082$
9	3.708	6.584	6.887	0	180	0	7.157e−5	180	hyperbolic	$\delta > 1.082$

Table 4.1 — The 15 equilibria of the simplified Hamiltonian (4.21). They are found for the resonance chain 1 : 1 : 2 at $\delta = 7$ using a Newton–Raphson method. Values given without decimal places are exact. The planetary masses are as in Fig. 4.2. Branch 2 is hyperbolic only for $5.548 \leq \delta \leq 5.802$ and elliptic elsewhere. The entry value of δ in the formal resonance (here 1.129) weakly depends on the planetary masses because of the normalisation by ΔG_{bif} (It occurs at $\delta = 1$ in the analytical results of Sect. 4.3.1). Branch 1 is the only elliptic branch existing for all values of δ and it is the main branch introduced in Sect. 4.3.1. It corresponds to the only real solution of Eq. (4.32) when $\delta < 1$. Branches 3, 5, and 7 do not exist at first order in eccentricity, while they exist at second order; hence, we cannot exclude that the complete Hamiltonian (4.2) has more *libration centres*, either because we did not discretize the phase space thinly enough to find them or because they do not exist at second order in eccentricity.

words, that the grid is dense. However, since the phase space has eight dimensions, a thin discretization leads to too many initial conditions, and to limit the computational time, we are only able to discretize the axes u_j and v_j with eight points, evenly distributed in the range $[-0.08, 0.08]$. Since the semimajor axes stay close to their Keplerian value, the L-axis is discretized with the unique point $L_0 = L^\star := \Lambda_1^\star/\Gamma^\star$, which corresponds to the value of L at the Keplerian resonance (Eq. (4.5)). Similarly, because the model (4.21) is only a perturbation of $\mathcal{H}_K + \mathcal{H}^{(0)}$, its equilibria are expected to be close to $\xi_0 \in \{\pm\pi/3, \pi\}$ (see Fig. 3.1) and the ξ-axis is discretized with these three points only. The algorithm hence explores a grid composed of 3×8^6 points in the phase space.

For $\delta = 7$, all 786 432 initial conditions of the Newton–Raphson method converged towards 15 distinct equilibria. The vector field F_0 derived from the Hamiltonian (4.21) depends on the choice of the parameter δ (through ΔG), and once a fixed point is found for a particular value of δ, we repeat the Newton-Raphson algorithm for slowly varying values of δ in order to travel along the whole branch. In Table 4.1, we display the 15 found equilibria, their hyperbolic or elliptic nature, and the value of δ that gives birth to the branch. Since the Hamiltonian (4.21) is invariant by the transformation $(\xi, \sigma_j) \mapsto (-\xi, -\sigma_j)$, fixed points with values of the angles different from 0 or π have a symmetric, hence the $\pm$ and $\mp$ signs in Table 4.1 (the upper sign corresponds to a fixed point and the lower sign to its symmetric). This symmetry corresponds to the invariance of the system by a rotation of angle π around an axis normal to the total angular momentum.

As can be seen in Table 4.1, only the branches 1, 2, and 3 of fixed points can be elliptic, and thus we focus only on them in the rest of this work. In Fig. 4.3 we plot these branches for values of δ ranging from -2 to 9. For branches 1 and 2, which are predicted by the first order in eccentricity, we also plot them as given by Eqs. (4.27) and (4.32), for comparison. This section shows how the analytical results are unable

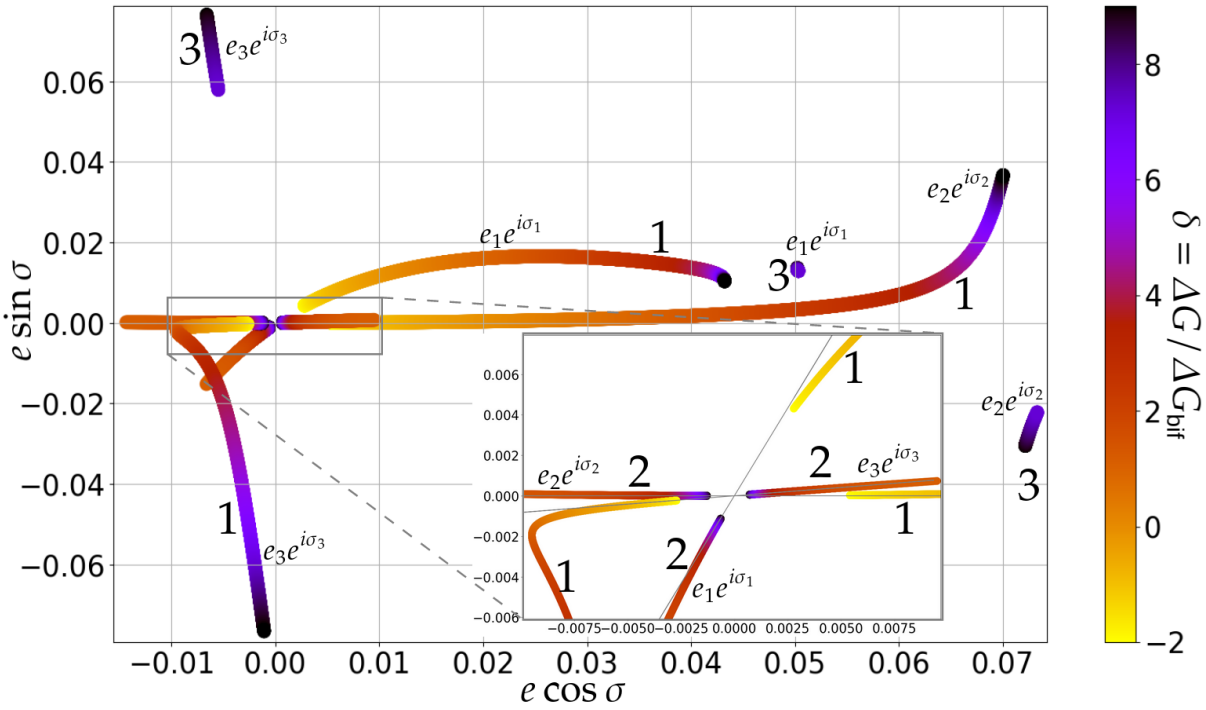

Fig. 4.3 — Position of the elliptic branches 1, 2, and 3 (see Table 4.1) of equilibria of the Hamiltonian (4.21) in the resonance $1:1:2$, for $-2 \leq \delta \leq 9$. For each branch three curves appear, corresponding to $e_j e^{i\sigma_j}$ for $j = 1, 2, 3$. The planetary masses are the same as in Fig. 4.2. A zoomed-in image close to the origin is shown in the inset. In this area, the analytical position of these equilibria, given by Eqs. (4.27) and (4.32), is plotted by thin grey lines. The agreement is good at low values of eccentricity, but quickly worsens further from the origin. In particular, the thin grey lines are straight since σ_j does not depend on δ in Eq. (4.27). Branch 1 exists for all values of δ and has all colours from yellow to dark purple, while branch 3 only exists at $\delta > 5.997$ and thus only has purple.

to locate the equilibria of the model (4.21) for $e_j \gtrsim 0.005$ (see Fig. 4.3) and does not even give its topology for $e_j \gtrsim 0.05$ (branches 3, 5, and 7 do not exist at first order in eccentricity; see Table 4.1). This discrepancy between first and second order in eccentricity was already mentioned by Beaugé *et al.* (2006) in the case of the two-planet $1:2$ mean motion resonance.

4.4 Comparison with the unaveraged system

4.4.1 Fixed points versus *libration centres*

As previously justified, the *libration centres* of the complete Hamiltonian (4.2) (Sect. 4.2.1) do not coincide with the equilibria of the model (4.21). We use the algorithm described in Sect. 4.2.2 to locate the *libration centres* of the complete system and compare them with the equilibria of the model. Since this algorithm is only able to find *libration centres* associated with elliptic fixed points, we locate the branches of *libration centres* associated with branches 1, 2, and 3 of Table 4.1. We confirm the existence of a small hyperbolic zone for branch 2 in the complete Hamiltonian when the algorithm stops converging as it

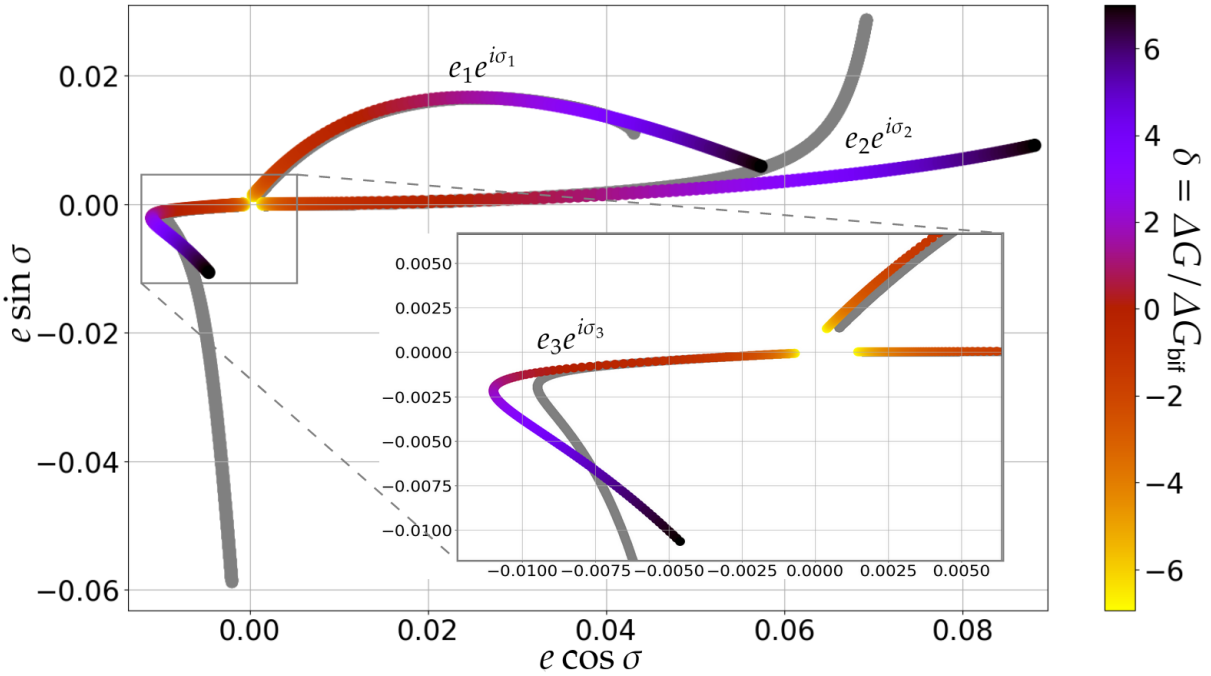

Fig. 4.4 — Position of branch 1 of elliptic *libration centres* of the complete Hamiltonian (4.2) in the resonance $1:1:2$ for $-7 \leq \delta \leq 7$. The planetary masses are the same as in Fig. 4.2. As a comparison, branch 1 of equilibria of the simplified Hamiltonian (4.21) is plotted in grey for the same range in δ. For small enough values of δ the eccentricity is not too high and the agreement is good. Then, the simplified and the complete Hamiltonian diverge when $\delta \to +\infty$.

travels along the branch (by slowly incrementing the value of δ). We plot in Fig. 4.4 the main branch (branch 1) of the *libration centres* of the complete Hamiltonian (4.2) and we compare it with the main branch of equilibria of the simplified Hamiltonian (4.21). In order not to overload the figure, only branch 1 is plotted. It is also the most interesting branch when tidal dissipation is involved (see section 7.2).

In Fig. 4.5 we plot the precession frequency of the pericentres, ν_3, for the main branch of the *libration centres*, and we compare it with the analytical expression (4.30). This figure shows that, for high values of δ, n_1/n_3 tends towards $(p+1)/p$ (which is equal to 2 in this case). For small values of δ though, this ratio diverges from its nominal value and *libration centres* at small values of δ are far from the Keplerian resonance. For branch 1, we now refer to very negative values of δ as far from the resonance and to very positive values of δ as deep in the resonance. The value of ν_3 in the complete Hamiltonian is obtained from the frequency analysis of $e^{i\xi_3}$, once the *libration centre* is known.

4.4.2 A stability map of the $p:p:p+1$ resonance chain

Before taking into account tidal dissipation in the model, we study the stability of the point-mass $p:p:p+1$ resonance chain by constructing a dynamical map using the frequency analysis method to determine the chaoticity of a given orbit (Laskar, 1990). More precisely, we study the stability of the chain along its main branch (see Fig. 4.2) between $\delta = 7$, deep in the resonance, and $\delta = -7$, outside the resonance.

For each value of δ, we compute the position of the exact *libration centre* by means

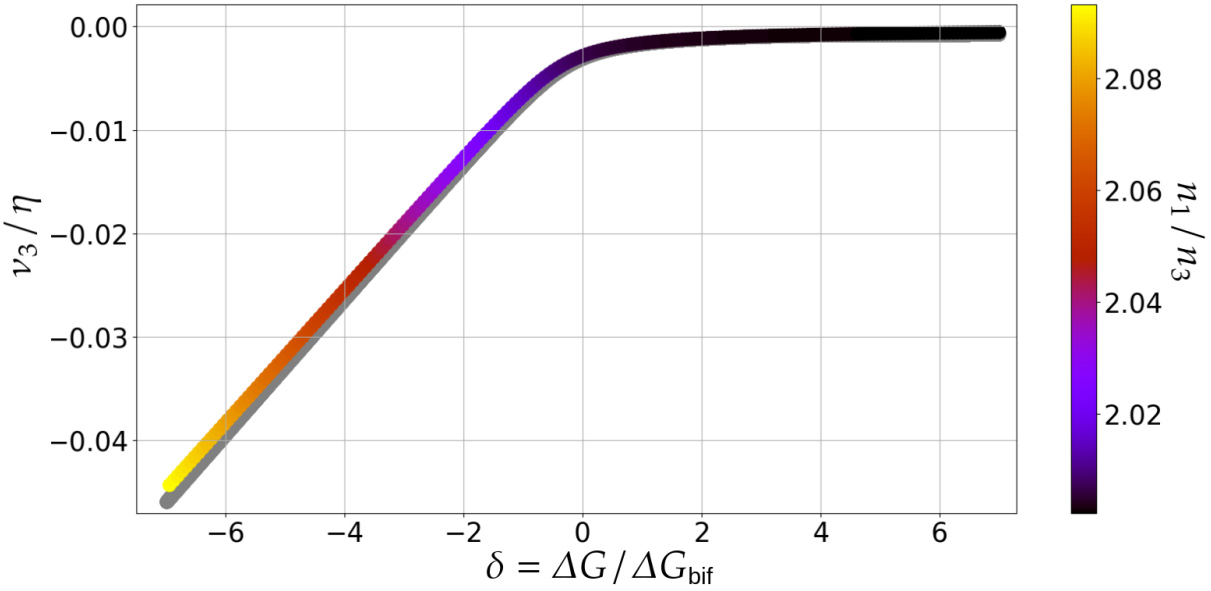

Fig. 4.5 — ν_3/η as a function of δ, in the complete Hamiltonian, for the resonance chain $1:1:2$, along branch 1 of the *libration centres* in Fig. 4.4. The analytical expression (4.30) is plotted in grey for comparison. The colour gives the value of n_1/n_3. As expected from Eqs. (4.30) & (4.34), ν_3 is proportionnal to δ far from the resonance, where the eccentricities are small.

of the algorithm described in Sect. 4.2.2, and we choose an initial value for the angle ξ between its equilibrium value (near 60°) and the value at the boundary between tadpole and horseshoe-shaped orbits (close to 24°, see Robutel and Pousse, 2013). For values of ξ_0 close to 60°, the considered orbit is close to the main branch and it moves away for decreasing values of ξ_0. For all other variables, we choose as the initial condition the value at the *libration centre*. Every trajectory (*i.e.* every choice of δ and ξ_0) is integrated over 80 000 periods of the co-orbital planets, and for each half of the simulation the exact value of the libration frequency ν is extracted from the frequency analysis of $e^{i\xi}$. We obtain two values of ν, namely $\nu^{(1)}$ for the first half of 40 000 periods and $\nu^{(2)}$ for the second half. The diffusion index, defined as (Robutel and Gabern, 2006)

$$\zeta_\nu = \log_{10}\left|\frac{\nu^{(1)} - \nu^{(2)}}{\nu^{(1)}}\right|, \tag{4.40}$$

measures the degree of quasi-periodicity of the orbit. Orbits with $\zeta_\nu < -6$ are considered close to be quasi-periodic (stable), while orbits with $\zeta_\nu > -2$ are very chaotic (unstable). We plot the stability map for the resonance chain $1:1:2$ in Fig. 4.6. Secular resonances between ν and ν_3, already predicted by the analytical results in Fig. 4.2 are visible and induce chaotic motion. Overall, this stability map shows that the chain $p:p:p+1$ is mainly stable.

4.5 Conclusion

In this chapter, we have studied the dynamics of a pair of co-orbital planets in the presence of a first-order mean motion resonance with a third planet orbiting outside the co-orbitals.

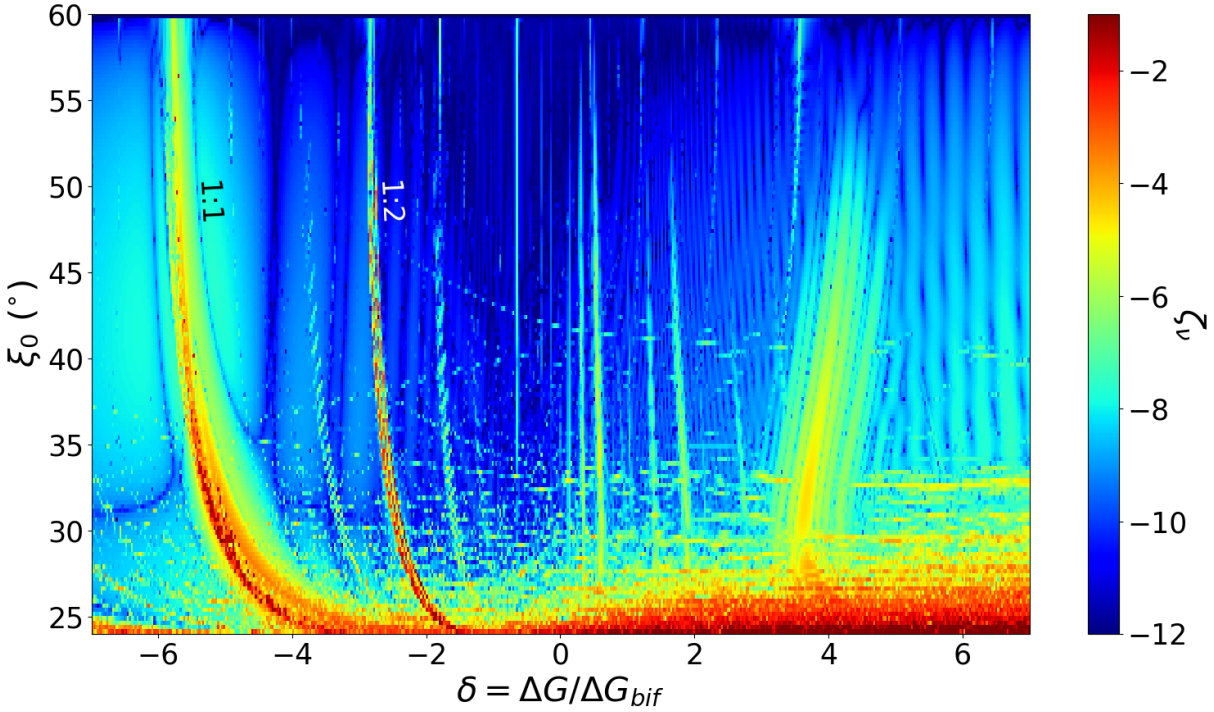

Figure 4.6 — Diffusion index ζ_ν as a function of δ and ξ_0. The planetary masses are as in Fig. 4.2 and the chain is $1:1:2$. The top of the figure, at $\xi_0 \approx 60°$, is the main branch. The blue-to-green regions are almost quasi-periodic (stable), while the red regions are chaotic (unstable). The secular resonances between the libration frequency ν and the precession frequency of the pericentres ν_3, predicted by the analytical results (see Fig. 4.2), are visible, especially the resonance $1:1$, which can lead to chaotic orbits for high enough values of the libration amplitude. The horseshoe-shaped orbits at the bottom are mostly chaotic, as expected, since $m_1 + m_2 = 2 \times 10^{-4}$ is close to the limit 3×10^{-4} of their existence (Leleu *et al.*, 2015). The main branch around the $1:1$ resonance between ν and ν_3 is tidally attractive (see Fig. 7.1). Systems undergoing tides entering this zone can either converge towards the top of the figure or become completely chaotic.

We built an averaged model (Eq. (4.21)) from which we were able to analytically retrieve the equilibria of the system and the eigenvalues in their vicinity. With these analytical results, we showed that the resonance chain $p:p:p+1$ has some similarities with the two-planet second fundamental model of resonance of Henrard and Lemaitre (1983), as well as some other proper characteristics, like the existence of a secular $1:1$ resonance between the libration frequency of the co-orbitals and the precession frequency of the pericentres, that can lead to chaotic orbits.

The analytical expressions came from strong assumptions, and we have compared them with numerical results, obtained after all simplifications were removed. This allowed us to reach the conclusion that the analytical expressions were correct, for eccentricities less than 0.005. We have shown that the resonance chain $p:p:p+1$ possesses many families of equilibria, some of them being stable. We also formally studied the relation between the equilibria of the averaged model and the *libration centres* of the unaveraged, complete problem, and we have checked the ability of our model to predict the location of the *libration centres* of the system, by means of a dedicated algorithm.

Chapter 5

Main theory on tidal dissipation

This chapter aims to establish the main theory of tides, that we use in Chaps. 6 and 7.

5.1 Tidal potentials

Celestial bodies are not perfectly rigid and the differential gravitational interactions between them give rise to inelastic deformations and distortions, leading to dissipation of energy by heating up. This energy loss modifies their spins and orbits and it is important to have a satisfying tidal description to study the long term dynamics of planetary systems. Our current mathematical understanding of tidal mechanisms comes from a very general formulation initiated by Darwin (1880). We consider in this chapter an extended body $\mathbb{B}$ of barycentre $\mathcal{O}$ and mean radius R_0 upon which tides are raised.

5.1.1 The perturbing potential

Tides arise when a celestial body, referred to as perturbing body, orbits in space around $\mathbb{B}$. We note $\tilde{\boldsymbol{r}}$ the position of the perturbing body with respect to $\mathcal{O}$. If $\boldsymbol{r}$ is the position, with respect to $\mathcal{O}$, of a point within $\mathbb{B}$, this point undergoes from the perturbing body the potential per unit mass

$$W(\boldsymbol{r}) = -\frac{\mathcal{G}\tilde{m}}{|\boldsymbol{r}-\tilde{\boldsymbol{r}}|} = -\frac{\mathcal{G}\tilde{m}}{\tilde{r}}\sum_{l=0}^{+\infty}\left(\frac{r}{\tilde{r}}\right)^l P_l(\cos S), \tag{5.1}$$

where $\tilde{m}$ is the mass of the perturbing body, S is the angle between $\boldsymbol{r}$ and $\tilde{\boldsymbol{r}}$ and the P_l are the Legendre polynomials, whose definition is recalled in appendix A. Tides are due to the differential acceleration caused by W within $\mathbb{B}$, which means that the first two terms of the perturbing potential, those corresponding to $l=0$ and $l=1$, do not contribute to the deformation of $\mathbb{B}$. Indeed, their gradient complies with

$$\nabla\left(\frac{\mathcal{G}\tilde{m}}{\tilde{r}}\left(1+\frac{\boldsymbol{r}\cdot\tilde{\boldsymbol{r}}}{\tilde{r}^2}\right)\right) = \frac{\mathcal{G}\tilde{m}\tilde{\boldsymbol{r}}}{\tilde{r}^3}, \tag{5.2}$$

and these terms are merely responsible for the orbital motion of $\mathbb{B}$ around the perturbing body. Hence we redefine the perturbing potential as

$$W(\boldsymbol{r}) = -\frac{\mathcal{G}\tilde{m}}{\tilde{r}} \sum_{l=2}^{+\infty} \left(\frac{r}{\tilde{r}}\right)^l P_l(\cos S). \tag{5.3}$$

In most practical cases, $r \ll \tilde{r}$, and only the term $l = 2$ is retained

$$W(\boldsymbol{r}) = -\frac{\mathcal{G}\tilde{m}r^2}{\tilde{r}^3} P_2(\cos S). \tag{5.4}$$

5.1.2 Perturbed potential and definition of the Love numbers

In order to study the evolution of a planetary system undergoing tidal dissipation, we need to establish a relation between the perturbing potential $W(\boldsymbol{r}, t)$ and the perturbed potential $V(\boldsymbol{r}, t)$, that is, the potential raised by the redistribution of mass inside $\mathbb{B}$. Generally, the auto-gravitation is the main contribution to the equilibrium figure of a body, and tides raised by other bodies of the system act as tiny perturbations. Thus, it is safe to assume that V responds linearly to W and we write $V = K(W)$, where K is a linear operator. Furthermore, $V(\boldsymbol{r}, t)$ should a priori depend on the value of W at any point in space and at any time prior to t. To account for this and for the linearity, we express $V(\boldsymbol{r}, t)$ as the convolution product (Boué *et al.*, 2019)

$$V(\boldsymbol{r}, t) = \int_{-\infty}^{t} \int_{\mathbb{R}^3} k(\boldsymbol{r}, \boldsymbol{r'}, t - t') W(\boldsymbol{r'}, t') d\boldsymbol{r'} dt'. \tag{5.5}$$

The integration over space can be restricted to the volume of $\mathbb{B}$, and in fact, when $\mathbb{B}$ is incompressible, it can even be restricted to any sphere encircling completely the body $\mathbb{B}$[1]. For simplicity, we choose a sphere $\mathbb{S}$, centered on $\mathcal{O}$, and of radius R slightly larger than R_0, as to ensure that $\mathbb{B}$ is entirely inside of $\mathbb{S}$. Thus, we write

$$V(R, \sigma, t) = \int_{-\infty}^{t} \int_{\mathbb{S}} k(R, \sigma, \sigma', t - t') W(R, \sigma', t') d\sigma' dt', \tag{5.6}$$

where $\sigma = (\theta, \varphi)$ are the colatitude and longitude and $d\sigma = \sin\theta \, d\theta \, d\varphi$. We now decompose V and W over the spherical harmonics (Appendix A.1), that is

$$\begin{aligned} V(R, \sigma, t) &= \sum_{l=0}^{+\infty} \sum_{m=-l}^{l} V_{lm}(R, t) Y_{lm}(\sigma), \\ W(R, \sigma', t') &= \sum_{l'=2}^{+\infty} \sum_{m'=-l'}^{l'} W_{l'm'}(R, t') Y_{l'm'}(\sigma'), \end{aligned} \tag{5.7}$$

where l' starts at 2, as in Eq. (5.3). When $\mathbb{B}$ is isotropic, the coefficients of the decomposition verify a relation similar to Eq. (5.6), namely

$$V_{lm}(R, t) = \int_{-\infty}^{t} k_{lm}(R, t - t') W_{lm}(R, t') dt'. \tag{5.8}$$

[1]This comes from the general solution of the Laplace equation in spherical coordinates (Eq. (A.11)), that forces the form of W everywhere inside the sphere, once W is known on the surface of the sphere.

The demonstration of Eq. (5.8) (Boué *et al.*, 2019) is given in appendix A.3, while we recall the definition of Y_{lm} in appendix A.1. In this equation, the Love numbers k_{lm} depend on the arbitrary radius R and we would like to define more general Love numbers. According to the Poisson equation, we have $\Delta V = 0$ everywhere outside of $\mathbb{B}$ and $\Delta W = 0$ everywhere in space (expect inside the body responsible for the tides). Since V and W do not diverge at $\mathcal{O}$ and at infinity, we can deduce, from the general solution of the Laplace equation $\Delta = 0$ in spherical coordinates (Eq. (A.11)), that

$$V_{lm}(R,t) \propto R^{-(l+1)} \quad \text{and} \quad W_{lm}(R,t) \propto R^{l}, \tag{5.9}$$

in the vicinity of $\mathbb{S}$. As a consequence, we have

$$k_{lm}(R,t) \propto R^{-(2l+1)}, \tag{5.10}$$

and we redefine the Love numbers as

$$k_{lm}(t) = \left(\frac{R}{R_0}\right)^{2l+1} k_{lm}(R,t). \tag{5.11}$$

We also redefine the coefficients V_{lm} with an equation similar to (5.8)

$$V_{lm}(t) = \int_{-\infty}^{t} k_{lm}(t-t')W_{lm}(R_0,t')dt', \tag{5.12}$$

which yields, for $r \geq R$

$$V(r,\sigma,t) = \sum_{l=2}^{+\infty} \left(\frac{R_0}{r}\right)^{l+1} \sum_{m=-l}^{l} V_{lm}(t)Y_{lm}(\sigma). \tag{5.13}$$

Equations (5.12) and (5.13) give the final form of the perturbed potential, as a function of the perturbing potential. To give an expression for V, the Love numbers $k_{lm}(t)$ need to be known. Choosing a particular tidal model is equivalent to choosing a particular expression for the $k_{lm}(t)$. The convolution product (5.12) can be conveniently written in the frequency domain

$$\hat{V}_{lm}(\eta) = \hat{k}_{lm}(\eta)\hat{W}_{lm}(R_0,\eta), \tag{5.14}$$

where $\hat{f}$ denotes the Fourier transform of f. In the rest of this manuscript, we drop the hat to denote the Fourier transform. In general, R_0/r is much smaller than unity and the serie (5.13) is truncated at $l = 2$, which means that the knowlegde of $k_{2m}(t)$, for $-2 \leq m \leq 2$, is enough. Furthermore, the dependency on m is artificial, since there exists integers p and q such that $k_{2m}(\eta) = k_{20}(pn + q\omega)$, where ω and n are the rotation rate and mean motion of the perturbed body (around the perturbing body), respectively (*e.g.* Correia and Laskar, 2003, Sect. 2.1). Only the second Love number $k_2(t) := k_{20}(t)$ is thus needed to define a tidal model.

5.2 Simple rheologies and subsequent tidal models

In order to define a tidal model, we need to obtain an expression for the Love number $k_2\,(t)$. The idea is to consider a case where the perturbing potential W and the perturbed

potential V are both independently known and to use Eq. (5.14) to deduce the k_{lm}. Since these numbers depend on the considered body, but not on the choice of potential, this method allows us to determine them in a convenient way.

We consider for W the potential generated by the own rotation of $\mathbb{B}$. This rotation is responsible for an equatorial bulge whose associated potential is V. These potentials are axisymmetric and the coefficients of their decomposition (5.7) will verify $W_{lm} = V_{lm} = 0$ for $m \neq 0$. Hence, the decomposition in the spherical harmonics will conveniently feature only the Legendre polynomials P_l, since $Y_{l0} \propto P_l$ (appendix A). Besides being axisymmetric, V and W are also independent of time, which means that V depends on W only at present time. Given the form of Eq. (5.12), this implies $k_2(t) \propto \delta(t)$ where δ is Dirac's distribution. This choice for the potentials implies a frequency of excitation zero, and we will only retrieve the value of the Love number k_2 at frequency $\eta = 0$. Indeed, $k_2(t) \propto \delta(t)$ yields $k_2(\eta) = \mathrm{C}_{\mathrm{stant}} = k_2(\eta = 0)$. To obtain the true dependency of k_2 on the frequency, potentials more general than V and W need to be chosen. In Sect. 5.2.2, we present the general method to retrieve the dependency on η.

5.2.1 The elastic body

In this section, $\mathbb{B}$ is homogeneous, incompressible and perfectly elastic with a shear modulus μ. We note m and ω the mass and rotation rate of $\mathbb{B}$ and define ω_c as the rotation rate that would compensate gravity at the equator if $\mathbb{B}$ was rigid, that is, $\omega_c^2 = \mathcal{G}m/R_0^3$. We also introduce the small parameter $\iota = \omega^2/\omega_c^2$. With these notations, the centrifugal acceleration in the frame rotating with $\mathbb{B}$ derives from the potential

$$W(r,\theta) = -\frac{1}{2}\iota\omega_c^2 r^2 \sin^2\theta = \frac{1}{3}\iota\omega_c^2 r^2 \left[P_2(\cos\theta) - 1\right]. \tag{5.15}$$

To determine the potential V, We consider that the surface of $\mathbb{B}$ is deformed axisymmetrically under its own rotation (*e.g.* Ragazzo and Ruiz, 2015; Wahr, 1996, Sect. 4.2)

$$\zeta(\theta) = R_0\left[1 + hP_2(\cos\theta)\right], \tag{5.16}$$

where ζ is the altitude of the surface and $|h| \ll 1$. Such a form for the deformation ensures the conservation of volume at first order in h. Following Ragazzo and Ruiz (2015), we assume that the deformation is linear and we define the matrix $\mathcal{A} = \mathbb{I} + \mathcal{E}$ such that the vector position $\boldsymbol{r}$ of a point of $\mathbb{B}$ is displaced at the position $\mathcal{A}\boldsymbol{r}$ by the deformation. If $(\vec{e}_x, \vec{e}_y, \vec{e}_z)$ denotes the orthonormal cartesian basis, with $\vec{e}_z$ pointing towards the north pole of $\mathbb{B}$, then these vectors are clearly eigenvectors of $\mathcal{A}$. Hence, $\mathcal{A}$ is diagonal in the cartesian basis and looking at Eq. (5.16), we have

$$\mathcal{A}_{(\vec{e}_x,\vec{e}_y,\vec{e}_z)} = \mathrm{diag}\left(1 - \frac{h}{2}, 1 - \frac{h}{2}, 1 + h\right). \tag{5.17}$$

The increment in potential energy due to the equatorial bulge reads (*e.g.* Wahr, 1996, Sect. 4.2)

$$V(r,\theta) = -\frac{3}{5}R_0^2\omega_c^2 h\frac{R_0^3}{r^3}P_2(\cos\theta), \tag{5.18}$$

and, from Eqs. (5.12) & (5.13) and using $k_2(t) \propto \delta(t)$, the second Love number k_2 is

$$k_2(\eta) = -\frac{9}{5}\frac{h}{\iota}. \tag{5.19}$$

We need to determine the ratio h/ι. A way to do so is to interpret h as the generalized coordinate of the Lagrangian

$$\mathcal{L} = \mathcal{T}(h) - \mathcal{U}_{\rm g}(h) - \mathcal{U}_{\rm el}(h), \tag{5.20}$$

and to obtain its value from the least action principle. In this Lagrangian, $\mathcal{T}$ is the kinetic energy of rotation of $\mathbb{B}$ while $\mathcal{U}_{\rm g}$ and $\mathcal{U}_{\rm el}$ are the gravitational binding energy and the elastic energy, respectively. For these quantities, we only consider the increment due to the rotation. A direct computation gives

$$\mathcal{T}(h) = \int_0^{2\pi}\int_0^{\pi}\int_{R_0}^{\zeta(\theta)} \frac{1}{2}\rho r^4\omega^2\sin^3\theta dr d\theta d\varphi = -\frac{1}{5}m\omega_c^2\iota h R_0^2, \tag{5.21}$$

where ρ is the density of $\mathbb{B}$. Denoting $\boldsymbol{\sigma}$ the stress tensor of $\mathbb{B}$ and $\boldsymbol{\varepsilon}$ its strain tensor, the elastic energy of deformation of $\mathbb{B}$ is

$$\mathcal{U}_{\rm el} = \frac{1}{2}\int_{\mathbb{B}} \boldsymbol{\sigma}\cdot\boldsymbol{\varepsilon}\, d\boldsymbol{r} = \mu\int_{\mathbb{B}} \boldsymbol{\varepsilon}\cdot\boldsymbol{\varepsilon}\, d\boldsymbol{r}, \tag{5.22}$$

where we used Hooke's law for a perfectly elastic body $\boldsymbol{\sigma} = 2\mu\boldsymbol{\varepsilon}$. The strain tensor is given by (Ragazzo and Ruiz, 2015)

$$\boldsymbol{\varepsilon} = \frac{1}{2}\left(\mathcal{A} + {}^t\mathcal{A}\right) - \mathbb{I} = \mathcal{E}. \tag{5.23}$$

Equation (5.17) yields $\boldsymbol{\varepsilon}\cdot\boldsymbol{\varepsilon} = 3h^2/2$, and by conservation of the volume, we obtain

$$\mathcal{U}_{\rm el}(h) = \frac{3}{2}\mu h^2\int_{\mathbb{B}} d\boldsymbol{r} = 2\pi\mu h^2 R_0^3. \tag{5.24}$$

The gravitational binding energy is the potential energy of auto-gravitation

$$\mathcal{U}_{\rm g} = -\frac{\mathcal{G}\rho^2}{2}\int_{\mathbb{B}}\int_{\mathbb{B}} \frac{d\boldsymbol{r_1}d\boldsymbol{r_2}}{|\boldsymbol{r_1}-\boldsymbol{r_2}|} = -\frac{\mathcal{G}\rho^2}{2}\int_{\mathbb{B}_0}\int_{\mathbb{B}_0} \frac{d\boldsymbol{r_1}d\boldsymbol{r_2}}{|\mathcal{A}\,(\boldsymbol{r_1}-\boldsymbol{r_2})|}, \tag{5.25}$$

where $\mathbb{B}_0$ is the ball of radius R_0 centered at $\mathcal{O}$. Ragazzo and Ruiz (2015) give

$$\mathcal{U}_{\rm g} = -\frac{3m^2\mathcal{G}}{10R_0}\int_0^{+\infty} \frac{d\lambda}{\sqrt{\det(\mathcal{A}^2+\lambda\mathbb{I})}}. \tag{5.26}$$

Given the simple form of $\mathcal{A}$ (Eq. (5.17)), this integral can be computed analytically, and at second order in h, we have

$$\int_0^{+\infty} \frac{d\lambda}{\sqrt{\det\left(\mathcal{A}^2+\lambda\mathbb{I}\right)}} = 2 - \frac{2}{5}h^2. \tag{5.27}$$

The factor 2 gives the gravitational binding energy of a homogeneous ball and we discard it, since we are only interested in the increment due to the deformation. Thus we have

$$\mathcal{U}_{\mathrm{g}}(h) = \frac{3}{25} m\omega_c^2 R_0^2 h^2. \tag{5.28}$$

We normalize the Lagrangian $\mathcal{L}$ by the constant $-m\omega_c^2 R_0^2$ and obtain

$$\mathcal{L} = \frac{1}{5}\iota h + \frac{3}{25}h^2 + \frac{3}{2}\frac{\mu}{\rho g R_0}h^2, \tag{5.29}$$

where $g = \mathcal{G}m/R_0^2$ is the surface gravity of $\mathbb{B}$ when undeformed. The Euler-Lagrange equation (Eq. (2.12)) yields

$$\frac{h}{\iota} = -\frac{5}{6}\left(1 + \frac{25}{2}\frac{\mu}{\rho g R_0}\right)^{-1}, \tag{5.30}$$

and then, using Eq. (5.19) (*e.g.* Roberts and Nimmo, 2008)

$$k_2(\eta) = \frac{3}{2}\left(1 + \frac{25}{2}\frac{\mu}{\rho g R_0}\right)^{-1}. \tag{5.31}$$

In the original computation by Love, the coefficient 25/2 is 19/2 instead. The discrepancy is due to the assumption that the deformation is linear ($\boldsymbol{r} \mapsto \boldsymbol{\mathcal{A}r}$), which induces an overestimation of the elastic energy in this work (Ragazzo and Ruiz, 2015, Appendix 2).

For a perfectly fluid body ($\mu = 0$), we retrieve the known value $k_2(\eta) = 3/2$, or equivalently, $k_2(t) = 3\delta(t)/2$. The energy dissipated into heat due to tidal dissipation is proportional to the imaginary part of the second Love number, written in the frequency domain (Segatz *et al.*, 1988, Eq. (13)). For a perfectly elastic body, $\mathfrak{Im}\, k_2 = 0$ implies the absence of energy dissipation. Such a behaviour is not satisfying because for realistic celestial bodies, the long term evolution of the orbits comes from the dissipation of the mechanical energy.

5.2.2 A simple viscoelastic body : the Maxwell model

Besides having a zero imaginary part, the second Love number in Eq. (5.31) was obtained using time-independent potentials (Eqs. (5.15) & (5.18)) and thus does not depend on the frequency η. Considering time dependent potentials, the form of Eq. (5.31) does not change (Appendix B of Efroimsky, 2012, Appendix A of Correia *et al.*, 2014) and we have

$$k_2(\eta) = \frac{3}{2}\left(1 + \frac{25}{2}\frac{\mu(\eta)}{\rho g R_0}\right)^{-1}. \tag{5.32}$$

The complex shear modulus $\mu(\eta)$ depends on the rheology of $\mathbb{B}$ and we consider, for the Maxwell model, a homogeneous body with a spring-like behaviour of shear modulus μ and a piston-like behaviour of damping coefficient ς, put in serie (Christensen, 1982, Fig. 1.2).

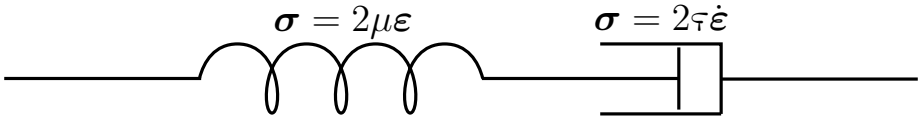

In the time domain, the differential equation verified by this system is $\boldsymbol{\sigma} = 2\mu\boldsymbol{\varepsilon} + 2\varsigma\dot{\boldsymbol{\varepsilon}}$, while it reads $\boldsymbol{\sigma} = 2\mu\left(1 + i\eta\tau\right)\boldsymbol{\varepsilon}$ in the frequency domain, where we defined the Maxwell relaxation time as $\tau = \varsigma/\mu$. Hence we have

$$\mu(\eta) = \mu\left(1 + i\eta\tau\right). \tag{5.33}$$

Other rheologies can be imagined by forming different mechanical systems. In the Kelvin model for instance, the spring and piston are in parallel and $\mu(\eta) = \mu i\eta\tau/\left(1 + i\eta\tau\right)$. The Maxwell model corresponds to a low-pass filter, since $\lim_{\eta\to+\infty} k_2 = 0$. In the time domain, its second Love number reads

$$k_2(t) \propto e^{-t/\tau'} \quad \text{with} \quad \tau' = \tau\left(1 + \frac{2}{25}\frac{\rho g R_0}{\mu}\right)^{-1}, \tag{5.34}$$

which corresponds to an exponentially decreasing memory of the past. Furthermore, $\mathfrak{Im}\, k_2(\eta) \neq 0$ ensures the dissipation of energy.

5.2.3 The constant-Δt model

While the behaviour of the Maxwell model is qualitatively satisfying, the form of Eq. (5.34) makes it impossible to obtain an analytical expression of the perturbed potential V, because of the convolution product (5.12). In the limit when η goes to zero, a first-order Taylor expansion in the vicinity of $\eta = 0$ in $k_2(\eta)$ (Eq. (5.32)) shows that there exists a scalar κ_2 and a time Δt, depending on the rheology of $\mathbb{B}$, such that the second Love number reads[2] $k_2(\eta) = \kappa_2\left(1 - i\eta\Delta t\right) + \mathcal{O}\left(\eta^2\Delta t^2\right)$. The constant-$\Delta t$ model is thus defined as

$$k_2(\eta) = \kappa_2 e^{-i\eta\Delta t} \approx \kappa_2\left(1 - i\eta\Delta t\right), \tag{5.35}$$

or equivalently

$$k_2(t) = \kappa_2\,\delta(t - \Delta t). \tag{5.36}$$

The Dirac distribution in Eq. (5.36) solves the problem that the Maxwell model yields when trying to obtain an analytical expression for the perturbed potential. The constant-Δt model is the limiting behaviour of any tidal model when $\eta \to 0$. In this model, the time Δt corresponds to the memory of $\mathbb{B}$, that is, the time between the stress generated by the perturbing body and the response in the perturbed potential V. In the literature, the dimensionless parameter κ_2 is often referred to as the second Love number.

Due to the Taylor expansion, the constant-Δt model is only valid when $\eta\Delta t \ll 1$. If $\eta\Delta t \gg 1$, W evolves on timescales much shorter than Δt, and looking at Eq. (5.36), this means that $\mathbb{B}$ undergoes deformations on timescales much shorter than Δt . Since Δt represents the time needed by $\mathbb{B}$ to reach hydrostatic equilibrium after a stress, the shape of $\mathbb{B}$ cannot evolve on timescales shorter than Δt. In that case, if W were to suddenly start oscillating at high frequency, then V would not react for a time Δt and then would also suddenly start oscillating at high frequency, with an amplitude κ_2 that of W. This is obviously highly unrealistic. In practice, the constant-Δt model is a good approximation as Δt is at most of the order of a few minutes, while $2\pi/\eta$ generally exceeds one day.

[2] Any realistic tidal model is such that $\eta = 0 \Rightarrow \mathfrak{Im}\, k_2 = 0$, to ensure the absence of energy dissipation in the static case.

5.2.4 Quality factor

The quality factor Q is related to the amount of energy dissipated in a period $T = 2\pi/\eta$, and is defined as (MacDonald, 1964, Eq. (124))

$$Q^{-1} = \frac{1}{2\pi\mathfrak{E}^\star}\int_0^T \frac{d\mathfrak{E}}{dt}dt, \tag{5.37}$$

where $\mathfrak{E}(t)$ is the energy stored inside of $\mathbb{B}$ and $\mathfrak{E}^\star$ is its maximum over the period T, called peak energy and defined as

$$\mathfrak{E}^\star = -\mathfrak{E}(T/4) = -\int_0^{T/4} \frac{d\mathfrak{E}}{dt}dt. \tag{5.38}$$

The stored energy $\mathfrak{E}(t)$ is given by the amount of work done by the perturbing potential W, that is

$$\frac{d\mathfrak{E}}{dt} = \int_{\mathbb{B}} \rho\boldsymbol{v}\cdot\nabla W d\boldsymbol{r}, \tag{5.39}$$

where $\boldsymbol{v}$ is the speed of the elemental volume surrounding $\boldsymbol{r}$, in the frame attached to $\mathbb{B}$. The incompressibility of $\mathbb{B}$ reads $\nabla\cdot\boldsymbol{v} = 0$ and yields $\boldsymbol{v}\cdot\nabla W = \nabla\cdot(W\boldsymbol{v})$. Using Green-Ostrogradsky theorem and neglecting the tangential contributions of $\boldsymbol{v}$, Eq. (5.39) can be rewritten

$$\frac{d\mathfrak{E}}{dt} = \int_{\partial\mathbb{B}} \rho W(R_0,\sigma,t)\frac{\partial\zeta(\sigma,t)}{\partial t}d\sigma, \tag{5.40}$$

where $\partial\mathbb{B}$ is the surface of $\mathbb{B}$, ζ its altitude (Eq. (5.16)), $\sigma = (\theta,\varphi)$ and $d\sigma = \sin\theta d\varphi d\theta$. If $\mathbb{B}$ is excited with a frequency η, that is

$$W(r,\sigma,t) = W_0(r,\sigma)\cos\eta t, \tag{5.41}$$

then, there exists a phase lag δ, accounting for the delay in the response due to the non-elasticity of $\mathbb{B}$, such that the altitude of the surface takes the form

$$\zeta(\sigma,t) = \zeta_0(\sigma)\cos(\eta t-\delta). \tag{5.42}$$

Equation (5.40) yields $d\mathfrak{E}/dt = -\eta\rho\mho\cos\eta t\sin(\eta t-\delta)$, where $\mho = \int_{\partial\mathbb{B}} W_0(R_0,\sigma)\zeta_0(\sigma)d\sigma$. The energy dissipated over one period and the peak energy then read

$$\int_0^T \frac{d\mathfrak{E}}{dt}dt = \pi\rho\mho\sin\delta \quad\text{and}\quad \mathfrak{E}^\star = \frac{\rho\mho}{2}\cos\delta. \tag{5.43}$$

Posing $\delta = \eta\Delta t$ and using Eq. (5.37), we finally have for Q (MacDonald, 1964, Eq. (130))

$$Q^{-1} = \tan\delta = \tan\eta\Delta t \approx \eta\Delta t. \tag{5.44}$$

In the literature, it is often assumed that Q is constant, instead of Δt (*e.g.* Lainey *et al.*, 2012, Fig. 2). In the rest of this manuscript, we adopt the constant-Q model[3] and make use of the parameters κ_2 and Q. The timescales of orbital decay due to tides do not depend on both κ_2 and Q, but rather on the ratio κ_2/Q (see Eq. (6.29)). We give this ratio in Table 5.1 for some bodies of the Solar System.

[3]With a unique frequency of excitation η, the constant-Δt and constant-Q models are identical.

	Earth	Moon	Mars	Jupiter	Io	Saturn	Uranus	Sun
$10^4\,\kappa_2/Q$	11	6.4	17	0.11	150	1.6	> 2	0.001

Table 5.1 — Value of κ_2/Q for eight bodies in the Solar System. For the planets and satellites the values are constrained by astrometric measurements (Lainey, 2016). For the Sun, we used $\kappa_2 = 0.02$ (Claret and Cunha, 1997, Fig. 3) and $Q = 2 \times 10^5$ (Barker, 2020, Fig. 8).

5.3 The pseudo-Hamiltonian formalism

Combining together Eqs. (5.4), (5.12), (5.13) and (5.36), the final form for the perturbed potential due to the tidal bulge raised upon $\mathbb{B}$ is

$$V(\boldsymbol{r}) = -\kappa_2 \frac{\mathcal{G}\tilde{m}}{r} \left(\frac{R_0}{r}\right)^2 \left(\frac{R_0}{r^\star}\right)^3 P_2(\cos S^\star), \tag{5.45}$$

where $\boldsymbol{r}^\star = \tilde{\boldsymbol{r}}(t - \Delta t)$ and $S^\star$ is the angle between $\boldsymbol{r}$ and $\boldsymbol{r}^\star$. Studying a dynamical system with tidal dissipation, we write the Hamiltonian of the problem as

$$\mathcal{H} = \mathcal{H}_K(\boldsymbol{p}) + \iota_1 \mathcal{H}_P(\boldsymbol{p}, \boldsymbol{q}) + \iota_2 \mathcal{U}(\boldsymbol{p}, \boldsymbol{q}, \boldsymbol{p}^\star, \boldsymbol{q}^\star) + \mathcal{T}(\boldsymbol{p}), \tag{5.46}$$

where the tidal potential $\mathcal{U}$ contains every tidal contribution and $\mathcal{T}$ is the sum of the kinetic energies of rotation of the non point-mass bodies. The Hamiltonians $\mathcal{H}_K$ and $\mathcal{H}_P$ are the Keplerian and perturbative contributions of the point-mass Hamiltonian, while the vector $\boldsymbol{p}$ contains the momenta conjugated to the generalised coordinates $\boldsymbol{q}$. The order of magnitude of the parameter ι_1 is the planet-to-star mass ratio, or the satellite-to-planet mass ratio, depending on the system, while ι_2 is generally much smaller than ι_1, due to the factor R_0^5/r^5 in Eq. (5.45). In the N-body problem, the tidal potential $\mathcal{U}$ is the sum of $N\,(N-1)^2$ contributions[4] like in Eq. (5.45), but suitable simplifications allow most of them to be discarded, as we show in Sect. 6.1.1.

The equations of motion are obtained from $\mathcal{H}$ using the Hamilton Eqs. (2.18), considering that the quantities $\boldsymbol{p}^\star$ and $\boldsymbol{q}^\star$ are constant parameters; that is, we do not derive with respect to the starred variables. The subsequent vector field then depends on the parameters $\boldsymbol{p}^\star$ and $\boldsymbol{q}^\star$, and the dependency is removed with the first-order Taylor expansion

$$\boldsymbol{p}^\star = \boldsymbol{p} - \Delta t\, \dot{\boldsymbol{p}}, \quad \boldsymbol{q}^\star = \boldsymbol{q} - \Delta t\, \dot{\boldsymbol{q}}, \tag{5.47}$$

in the vector field. The Hamilton equations are used again in Eq. (5.47) to compute $\dot{\boldsymbol{p}}$ and $\dot{\boldsymbol{q}}$. To prevent an implicit relation, only the main contributions of the Hamiltonian are considered. In other words, we assume $\iota_1 = \iota_2 = 0$ to compute the time-derivatives in Eq. (5.47), that is

$$\boldsymbol{p}^\star = \boldsymbol{p} \;\text{ and }\; \boldsymbol{q}^\star = \boldsymbol{q} - \Delta t \frac{\partial\,(\mathcal{H}_K + \mathcal{T})}{\partial \boldsymbol{p}}. \tag{5.48}$$

[4] Each of the N bodies raises $N-1$ bulges, and every bulge affects the orbit of $N-1$ bodies.

Chapter 6

Tides in the planar three-body co-orbital problem

Most results of this chapter were first published in Couturier et al. *(2021), except those of Sect. 6.4, which are original.*

6.1 Pseudo-Hamiltonian and equations of motion

This chapter extends Chap. 3 by adding tidal dissipation to the analytical model. We will add terms to the conservative Hamiltonian $\mathcal{H}_K + \mathcal{H}^{(0)} + \mathcal{H}^{(2)} + \mathcal{H}^{(4)}$ (Eqs. (3.24) & (3.29)) to account for tidal effects, using the results from Chap. 5. In this chapter, like in Chap. 3, ι denotes $(m_1 + m_2)/m_0$. The central body and two co-orbitals have radii R_0, R_1 and R_2, respectively. We showed in Sect. 5.2.3 that in order to have simple analytical expressions for the tidal perturbations, we need to consider the constant-Δt model. We adopt this model in this chapter and the rheology of the bodies is hence characterized by their second Love number κ_2 (Eqs. (5.35) & (5.36)) and their quality factor Q (Sect. 5.2.4).

6.1.1 Expression of the pseudo-Hamiltonian

We want to build a tidal pseudo-Hamiltonian by adding to the conservative Hamiltonian contributions of the form (5.45). However, each of the three bodies can be a perturbing body, a perturbed body, or an interacting one, and taking into account every single tidal contribution will generate 12 new terms like in Eq. (5.45) (Sect. 5.3). In order to prevent a gruesome expression for the tidal pseudo-Hamiltonian, we show that for a star−planet−planet system, 10 out of 12 of these contributions can be neglected.

Indeed, tides raised by a planet on a planet, as well as tides raised by the star on a planet, and interacted with by the other planet, can readily be discarded due to the low masses and radii of the planets, with respect to that of the star. Hence, only six contributions remain. Two of these correspond to tides raised by the star on each planet

and interacted with by the star, and four correspond to tides raised by a planet on the star and interacted with by each planet. The four latter have an order of magnitude $\kappa_2^{(0)}/Q_0(\iota m_0)^2(R_0/\bar{a})^5$, while the two former have an order of magnitude $\kappa_2^{(j)}/Q_j m_0^2(R_j/\bar{a})^5$, where $j \in \{1,2\}$. Assuming a similar density for all the bodies, we have $R_j \propto m_j^{1/3}$, and then (Table 5.1)

$$\frac{\kappa_2^{(0)}(\iota m_0)^2 R_0^5/Q_0}{\kappa_2^{(j)} m_0^2 R_j^5/Q_j} = \iota^{1/3}\frac{\kappa_2^{(0)}/Q_0}{\kappa_2^{(j)}/Q_j} \ll 1. \tag{6.1}$$

Tides raised by the planets on the star can be discarded too and we only consider the two contributions due to tides raised by the star on each planet and interacted with by the star. In the case of satellites co-orbiting a planet, we stress that tides raised on the central body cannot be neglected, because the κ_2/Q of planet is not smaller than that of satellites, and the ratio (6.1) could be close to unity. We will treat this case in Sect. 6.4. For now, we write the perturbation to the conservative Hamiltonian, due to tides, as

$$H_t = U_t^{(1)} + U_t^{(2)} + T_1 + T_2, \tag{6.2}$$

where T_j is the kinetic energy of rotation of planet j and $U_t^{(j)}$ is the contribution due to tides raised by the star on planet j and interacted with by the star. In the heliocentric reference frame, we have (Eq. (5.45))

$$U_t^{(j)} = -\kappa_2^{(j)}\mathcal{G}m_0^2\frac{R_j^5}{r_j^3 r_j^{\star 3}}P_2\left(\cos S\right) \quad \text{and} \quad T_j = \frac{\Theta_j'^2}{2\mathcal{C}_j}, \tag{6.3}$$

with

$$S = \lambda_j - \lambda_j^\star - \left(\theta_j - \theta_j^\star\right), \tag{6.4}$$

where θ_j is the angle of rotation of body j, $\Theta_j' = \mathcal{C}_j\omega_j'$ is the conjugated momentum of θ_j, $\mathcal{C}_j = \alpha_j m_j R_j^2$ is the moment of inertia of body j, $\omega_j' = d\theta_j/dt$ is its rotation rate, and α_j is a dimensionless structure constant depending on the state equation of body j ($\alpha_j = 2/5$ for an homogeneous body). For any quantity z appearing in $U_t^{(j)}$, we denote

$$z^\star = z(t - \Delta t_j), \tag{6.5}$$

while for any angular quantity ς appearing in $U_t^{(j)}$, we define

$$\Delta\varsigma = \varsigma - \varsigma^\star = \varsigma(t) - \varsigma(t - \Delta t_j). \tag{6.6}$$

We write the tidal Hamiltonian H_t in the variables $(J, J_2, X_j; \xi, \xi_2, \bar{X}_j)$ introduced in Sect. 3.1.2 and we define $\Theta_j = \Theta_j'/(m\bar{a}^2\eta)$ in order to normalize the action variable Θ_j' (see Eq. (3.18)). We showed in Sect. 3.1.1 that it is enough to expand the Hamiltonian ιH_P at order 0 (Eq. (3.11)) in the vicinity of the Keplerian resonance given by Eq. (3.6). However, we show after giving the equations of motions with tides (Eqs. (6.15)), that expanding $U_t^{(j)}$ at order 0 in the neighbourhood of the Keplerian resonance loses almost all tidally relevant dynamics, and we have to keep a dependency on the variables J and J_2 in $U_t^{(j)}$. We thus keep exact expressions in theses variables. In order to only consider the secular (*i.e.* long-term) dynamics, we average $U_t^{(j)}$ over λ_j and $U_t^{(j)}$ depends on this angle through $\Delta\lambda_j$ only. Similarly, $U_t^{(j)}$ depends on θ_j through $\Delta\theta_j$ only, in virtue of Eq. (6.4). Since ιH_P was expanded up to the fourth degree in eccentricity, we also expand

$U_t^{(j)}$ up to that order. The expansion is achieved using the results of Laskar and Robutel (1995), viewing $\boldsymbol{r_j}$ and $\boldsymbol{r_j^\star}$ as two distinct bodies. We define the quantities

$$q_j = \kappa_2^{(j)} \varrho_j^5, \quad \text{and} \quad \varrho_j = \frac{R_j}{\bar{a}}, \tag{6.7}$$

and performing the rescaling (3.22), we get for $\mathcal{H}_t = H_t/(m\bar{a}^2\eta)$ the expression[1]

$$\begin{aligned} \mathcal{U}_t^{(j)} &= -q_j \eta \frac{m_0}{m} \mathcal{R}_j^{-6} \mathcal{R}_j^{\star -6} \left\{ A_t^{(j)} + \mathfrak{D}_2^{(j)} + \mathfrak{D}_4^{(j)} \right\} = \frac{U_t^{(j)}}{m\bar{a}^2\eta}, \\ \mathcal{T}_j &= \frac{\eta}{2\alpha_j} \frac{m}{m_j} \frac{\Theta_j^2}{\varrho_j^2} = \frac{T_j}{m\bar{a}^2\eta}, \end{aligned} \tag{6.8}$$

where

$$\mathfrak{D}_2^{(j)} = B_t^{(j)} \left(\mathcal{R}_j^{-1} X_j \bar{X}_j + \mathcal{R}_j^{\star -1} X_j^\star \bar{X}_j^\star \right) + \left(\mathcal{R}_j \mathcal{R}_j^\star \right)^{-1/2} \left(C_t^{(j)} X_j \bar{X}_j^\star + \bar{C}_t^{(j)} X_j^\star \bar{X}_j \right), \tag{6.9}$$

and

$$\begin{aligned} A_t^{(j)} &= \frac{1}{4} + \frac{3}{4} \cos\left[2\left(\Delta\lambda_j - \Delta\theta_j\right)\right], \\ B_t^{(j)} &= \frac{3}{8} - \frac{15}{8} \cos\left[2\left(\Delta\lambda_j - \Delta\theta_j\right)\right], \\ C_t^{(j)} &= \frac{3}{32} e^{i(\Delta\lambda_j - 2\Delta\theta_j)} + \frac{9}{16} e^{-i\Delta\lambda_j} + \frac{147}{32} e^{-i(3\Delta\lambda_j - 2\Delta\theta_j)}. \end{aligned} \tag{6.10}$$

The term $\mathfrak{D}_4^{(j)}$ contains the fourth order in eccentricity and is given in Appendix B.3. The pseudo-Hamiltonian that we consider for the model is then

$$\mathcal{H} = \mathcal{H}_K(J, J_2) + \iota \mathcal{H}_P(\xi, X_1, X_2, \bar{X}_1, \bar{X}_2) + \mathcal{H}_t, \tag{6.11}$$

where

$$\mathcal{H}_K = -\frac{3}{2}\eta \frac{m_1 + m_2}{m} J^2 - \frac{3}{2}\eta \frac{m}{m_1 + m_2} J_2^2 + \eta J_2, \tag{6.12}$$

the perturbation $\iota\mathcal{H}_P = \mathcal{H}^{(0)} + \mathcal{H}^{(2)} + \mathcal{H}^{(4)}$ is given by Eq. (3.29), and

$$\mathcal{H}_t = \sum_{j \in \{1,2\}} \mathcal{U}_t^{(j)}(J, J_2, J^\star, J_2^\star, \Delta\xi, \Delta\xi_2, \Delta\theta_j, X_j, X_j^\star, \bar{X}_j, \bar{X}_j^\star) + \sum_{j \in \{1,2\}} \mathcal{T}_j(\Theta_j). \tag{6.13}$$

6.1.2 Equations of motions in the presence of tides

The equations of motion are derived from the pseudo-Hamiltonian (6.11), following the procedure described in Sect. 5.3 and using Eq. (3.23). Denoting

$$\vartheta_j = 1 - \frac{\omega_j'}{\eta}, \tag{6.14}$$

[1] $\mathcal{R}_j(J, J_2)$ is defined by Eq. (3.20) and $m = \sqrt{m_1 m_2}$.

The differential system describing the motion of two planar co-orbital planets, undergoing tides, reads[2]

$$\begin{aligned}
\dot{\vartheta}_j &= -3\eta\alpha_j^{-1}\frac{m_0}{m_j}\varrho_j^{-2}\frac{q_j}{Q_j}\mathcal{R}_j^{-12}\left\{\vartheta_j + 3\left(1-\mathcal{R}_j\right) + h_2^{(j)}\mathcal{R}_j^{-1}X_j\bar{X}_j + h_4^{(j)}\mathcal{R}_j^{-2}X_j^2\bar{X}_j^2\right\},\\
\dot{J} &= -\frac{\partial\mathcal{H}_P}{\partial\xi} + \left(1-\delta\right)\dot{J}_2^{(1)} - \delta\dot{J}_2^{(2)},\\
\dot{J}_2 &= \dot{J}_2^{(1)} + \dot{J}_2^{(2)},\\
\dot{\xi} &= \frac{\partial\mathcal{H}_K}{\partial J} + 6\eta q_1\frac{m_0}{m_1}\mathcal{R}_1^{-13}\mathfrak{Q}_2\left(\mathcal{R}_1^{-1}X_1\bar{X}_1\right) - 6\eta q_2\frac{m_0}{m_2}\mathcal{R}_2^{-13}\mathfrak{Q}_2\left(\mathcal{R}_2^{-1}X_2\bar{X}_2\right),\\
\dot{X}_j &= -2i\frac{m}{m_j}\frac{\partial\left(\mathcal{H}^{(2)}+\mathcal{H}^{(4)}\right)}{\partial\bar{X}_j} - 3\eta\frac{q_j}{Q_j}\frac{m_0}{m_j}\mathcal{R}_j^{-13}X_j\left\{p_2^{(j)} - \frac{5}{2}iQ_j + \frac{X_j\bar{X}_j}{\mathcal{R}_j}\left(p_4^{(j)} - \frac{65}{4}iQ_j\right)\right\},
\end{aligned} \tag{6.15}$$

where

$$\begin{aligned}
\dot{J}_2^{(j)} &= -3\eta\frac{q_j}{Q_j}\frac{m_0}{m}\mathcal{R}_j^{-12}\left\{\vartheta_j + 3\left(1-\mathcal{R}_j\right) + k_2^{(j)}\mathcal{R}_j^{-1}X_j\bar{X}_j + k_4^{(j)}\mathcal{R}_j^{-2}X_j^2\bar{X}_j^2\right\},\\
h_2^{(j)} &= \frac{93}{2} + \frac{15}{2}\vartheta_j - \frac{81}{2}\mathcal{R}_j, & h_4^{(j)} &= \frac{1989}{8} + \frac{195}{8}\vartheta_j - \frac{819}{4}\mathcal{R}_j,\\
k_2^{(j)} &= \frac{157}{2} + \frac{27}{2}\vartheta_j - 69\mathcal{R}_j, & k_4^{(j)} &= \frac{2515}{4} + \frac{273}{4}\vartheta_j - \frac{2091}{4}\mathcal{R}_j,\\
p_2^{(j)} &= 32 + 6\,\vartheta_j - \frac{57}{2}\mathcal{R}_j, & p_4^{(j)} &= \frac{3041}{8} + \frac{351}{8}\vartheta_j - 318\mathcal{R}_j,\\
\mathfrak{Q}_2\left(Z\right) &= 1 + \frac{65}{8}Z + \frac{455}{16}Z^2.
\end{aligned} \tag{6.16}$$

The set of Eqs. (6.15) does not depend on the angle ξ_2. Since we are not interested in the dynamics of this angle, we discarded the line $\dot{\xi}_2$ from the differential system. If the Hamiltonian $\mathcal{H}_t$ had been expanded at order 0 in the vicinity of the Keplerian resonance (3.6) (*i.e.* at order 0 in the variables J and J_2), then the subsequent differential system would be the set of Eqs. (6.15), with the substitution $\mathcal{R}_j = 1$. Let us study the circular dynamics in that case, that we treated in the point-mass approximation in Sect. 3.2.1. We show in Sect. 6.2.2 that the rotation rates ω_j are damped by tides in a timescale much smaller than the other tidal timescales, so we also perform the substitution $\vartheta_j = 0$ in Eqs. (6.15) to consider the dynamics after reaching the spin-orbit synchronization. In the circular case, we substitute X_j by 0 and we obtain, for the librating angle ξ, the differential equation

$$\ddot{\xi} = -3\eta^2\iota\sin\xi\left(1 - \left(2-2\cos\xi\right)^{-3/2}\right). \tag{6.17}$$

All tidal contributions have disappeared and we end up with the differential equation describing the motion of ξ in the point-mass approximation (Yoder *et al.*, 1983, Eq. (9)). This equation predicts a periodic motion for ξ and no long-term effects due to tides are described. It is thus necessary to keep a dependency in J and J_2 in the tidal Hamiltonian to have a satisfying description of the tidal dynamics of the co-orbital motion.

[2] δ was defined by Eq. (3.14).

6.1.3 Conservation of the total angular momentum with tides

While tides do not preserve the total energy of the system because of the dissipation, the total angular momentum of the system star−planet−planet has to be conserved, even with tides, since the system is closed. We can show that the differential system (6.15) is indeed consistent with the conservation of the total angular momentum. The normalized[3] total angular momentum $\mathfrak{C}$ reads (Robutel and Pousse, 2013, Eq. (6))

$$\mathfrak{C} = \sum_j \frac{m_j}{m}\mathcal{R}_j - \frac{1}{2}\sum_j \frac{m_j}{m} X_j \bar{X}_j + \sum_j \alpha_j \frac{m_j}{m}\wp_j^2 \left(1 - \vartheta_j\right). \tag{6.18}$$

From (6.15) we get

$$\dot{\mathcal{C}} = \sum_{j=1}^{2} 3\eta \frac{q_j}{Q_j}\frac{m_0}{m}\mathcal{R}_j^{-13} X_j \bar{X}_j \left\{h_2^{(j)} - k_2^{(j)} + p_2^{(j)} + \mathcal{R}_j^{-1} X_j \bar{X}_j \left(h_4^{(j)} - k_4^{(j)} + p_4^{(j)}\right)\right\}, \tag{6.19}$$

and the total angular momentum is conserved since we have (Eq. (6.16))

$$\begin{aligned} h_2^{(j)} - k_2^{(j)} + p_2^{(j)} &= 0 \quad \text{and} \\ h_4^{(j)} - k_4^{(j)} + p_4^{(j)} &= 0. \end{aligned} \tag{6.20}$$

6.2 Equilibria and linearization

In this section, we compute the equilibria of the differential system (6.15) and the eigenvalues in their vicinity, in order to infer the stability of the system, using the results of Sect. 2.4.1.

6.2.1 The eigenvalues

Since the system (6.15) is a perturbation of the Hamiltonian system derived from $\mathcal{H}_K + \iota\mathcal{H}_P$, its fixed points are a perturbation of the Lagrangian equilibria. Only the tidal contributions of first order in $\iota^{-1}(q_1 + q_2)$ appear in (6.15), and it is enough to restrict to the first order to compute the position of the fixed points. We find, for $j \in \{1, 2\}$,

$$\begin{aligned} \vartheta_j &= 0, \\ \xi - \frac{\pi}{3} &= 0, \\ -3\frac{m_1 + m_2}{m} J + 6q_1\frac{m_0}{m_1} - 6q_2\frac{m_0}{m_2} &= 0, \\ X_j &= 0. \end{aligned} \tag{6.21}$$

Note that this choice for the fixed points does not make the right hand side of system (6.15) to be exactly zero, but rather a quantity of second order in $\iota^{-1}(q_1 + q_2)$. Infinitely many choices are possible for Eq. (6.21) that make the right-hand side of (6.15) a quantity of second order in $\iota^{-1}(q_1 + q_2)$, and we choose one of them. This choice is the most natural

[3] Normalized by $m\bar{a}^2\eta$.

because it guarantees that the fixed points correspond to a solid rotation of the whole system ($\vartheta_j = 0$). Equations (6.21) only provide 6 independent equations for 7 variables[4]. In order to have a unique fixed point in the neighbourhood of which to linearize the system, we arbitrarily choose

$$f_1 + f_2 = 0, \tag{6.22}$$

where the f_j are defined by Eq. (3.21). At first order in $\iota^{-1}(q_1 + q_2)$, the linearized system does not depend on the choice of Eqs. (6.21) & (6.22).

Before we linearize the differential system, we show that our model allows us to recover a well known result, called pseudo-synchronization. We fix to 0 the value of $\dot{\vartheta}_j$ in (6.15). If we place ourselves at the Keplerian resonance; that is, at $a_j = \bar{a}$ (or equivalently $\mathcal{R}_j = 1$), we find[5] for the equilibrium value of the rotation rate of planet j

$$\frac{\omega'_j}{\eta} = 1 + 6e_j^2 + \frac{3}{8}e_j^4 + \mathcal{O}\left(e_j^6\right). \tag{6.23}$$

This is the pseudo-synchronization of the rotation rates. At non-zero eccentricities, the rotation rates ω'_j are not synchronized with $\dot{\lambda}_j$, but rather slightly super-synchronous. The same result can be reached by equating to zero the right-hand side of Eq. (3) in Correia and Laskar (2004). Equation (6.23) and Sect. 6.1.3 provide two independent verifications of the set of Eqs. (6.15).

Let $\mathfrak{X}_0 = {}^t(\vartheta_{1,0}, \vartheta_{2,0}, \xi_0, J_0, J_{2,0}, X_{1,0}, X_{2,0})$ be the unique solution of Eqs. (6.21) & (6.22), that is, the equilibrium value of $\mathfrak{X} = {}^t(\vartheta_1, \vartheta_2, \xi, J, J_2, X_1, X_2)$. Once linearized in the vicinity of $\mathfrak{X}_0$, the differential system (6.15) reads

$$\frac{d}{dt}\Delta\mathfrak{X} = (\mathcal{Q}_0 + \mathcal{Q}_1)\,\Delta\mathfrak{X}, \tag{6.24}$$

where $\Delta\mathfrak{X} = \mathfrak{X} - \mathfrak{X}_0$. The matrix $\mathcal{Q}_0$ derives from the conservative Hamiltonian $\mathcal{H}_K + \iota\mathcal{H}_P$, while $\mathcal{Q}_1$ corresponds to the tidal contribution $\mathcal{H}_t$. The 7×7 matrix $\mathcal{Q}_0 + \mathcal{Q}_1$ is block diagonal with a 5×5 block corresponding to $(\vartheta_1, \vartheta_2, \xi, J, J_2)$, and 2×2 block, corresponding to X_1 and X_2. This shows that, even in the presence of tides, the circular and eccentric dynamics are uncoupled near the Lagrangian equilibria $L_{4,5}$. A detailed expression of theses matrices is given in appendix C.3. The set of eigenvalues of $\mathcal{Q}_0$ is

$$\{0, 0, 0, i\nu, -i\nu, ig_1, ig_2\}, \tag{6.25}$$

where (Eqs. (3.32) & (3.42))

$$\nu = \eta\sqrt{\frac{27\iota}{4}}, \qquad g_1 = \eta\frac{27\iota}{8}, \qquad g_2 = 0. \tag{6.26}$$

Among the first three 0 eigenvalues, two correspond to the constant rotation rate of the planets and another to the conservation of the total angular momentum (constancy of J_2). The $\pm i\nu$ eigenvalues give the libration frequency of the resonant angle $\xi = \lambda_1 - \lambda_2$ around the Lagrangian equilibria $L_{4,5}$ (Sect. 3.2.1), and the last two eigenvalues give the precession frequency of the pericentres in the eigenmodes anti-Lagrange for g_1 and Lagrange for g_2

[4] This is due to the conservation of the total angular momentum of the system.
[5] Using $X_j\bar{X}_j = 2\left(1 - \sqrt{1 - e_j^2}\right) = e_j^2 + e_j^4/4 + \mathcal{O}(e_j^6)$.

(Sect. 3.2.2). In particular, all seven eigenvalues of $\mathcal{Q}_0$ are pure imaginary and without the contribution of tides, the trajectories of the linearized system are quasiperiodic.

The matrix $\mathcal{Q}_0 + \mathcal{Q}_1$ is too gruesome for its eigenvalues to be computed by finding the roots of its characteristic polynomial. Instead, since $\mathcal{Q}_1$ is a small perturbation of $\mathcal{Q}_0$, and because we can easily find a diagonal basis of $\mathcal{Q}_0$, we use the perturbative approach described in Sect. 2.4.2 to find the eigenvalues of $\mathcal{Q}_0 + \mathcal{Q}_1$ at first order in $\iota^{-1}(q_1 + q_2)$. The computations are performed with the algebraic manipulator *Maxima* and the set of eigenvalues of $\mathcal{Q}_0 + \mathcal{Q}_1$ is

$$\left\{\text{ϡ}_1, \text{ϡ}_2, 0, \lambda, \bar{\lambda}, \lambda_{\mathrm{AL}}, \lambda_{\mathrm{L}}\right\}, \tag{6.27}$$

with

$$\begin{aligned}
\text{ϡ}_j &= \boxed{-3\eta\alpha_j^{-1}\frac{q_j}{Q_j}\text{ϒ}_j^{-2}\frac{m_0}{m_j} + 9\eta\iota^{-1}\frac{q_j}{Q_j}} < 0,\\
\lambda &= \boxed{\frac{9}{2}\eta\iota^{-1}\left(\frac{m_1}{m_2}\frac{q_2}{Q_2} + \frac{m_2}{m_1}\frac{q_1}{Q_1}\right)} + i\nu\left[1 + 13\iota^{-1}\left(\frac{m_1}{m_2}q_2 + \frac{m_2}{m_1}q_1\right)\right],\\
\lambda_{\mathrm{AL}} &= \boxed{-\frac{21}{2}\eta\iota^{-1}\left(\frac{m_1}{m_2}\frac{q_2}{Q_2} + \frac{m_2}{m_1}\frac{q_1}{Q_1}\right)} + ig_1\left[1 + \frac{20}{9}\iota^{-2}\left(\frac{m_1}{m_2}q_2 + \frac{m_2}{m_1}q_1\right)\right],\\
\lambda_{\mathrm{L}} &= \boxed{-\frac{21}{2}\eta\iota^{-1}\left(\frac{q_1}{Q_1} + \frac{q_2}{Q_2}\right)} + \frac{15}{2}i\eta\iota^{-1}(q_1 + q_2).
\end{aligned} \tag{6.28}$$

We note that the eigenvalues are no longer pure imaginary and we boxed the real parts for a better visualization. The real parts are proportional to the inverse quality factors Q_j^{-1}, while the perturbations to the imaginary parts are not. As a consequence, elastic tides, for which $Q_j = \infty$ (or equivalently, $\Delta t_j = 0$, see Eq. (5.44)), do not yield dissipation but only change slightly the fundamental frequencies of the system. We computed the eigenvectors of the linearized system and we show in appendix C.3 how the eigenmodes Lagrange and anti-Lagrange are slightly modified by tides.

The matrix $\mathcal{Q}_0 + \mathcal{Q}_1$ is singular, and one of its eigenvalues is zero, corresponding to the conservation of the total angular momentum (Sect. 6.1.3). As a result of tidal dissipation, the eigenvalues λ_{AL} and λ_{L}, perturbations of ig_1 and ig_2, respectively, have non-zero negative real parts. Therefore, both eccentric eigenmodes Lagrange and anti-Lagrange are damped to zero. Similarly, $\text{ϡ}_j < 0$, and the rotation rates of both planets are also damped. On the contrary, the real part of λ and $\bar{\lambda}$, perturbations of $i\nu$ and $-i\nu$, are strictly positive, which leads to an exponential increase of the libration amplitude of ξ when the system is close to the Lagrangian equilibria L_4 or L_5.

The fact that $\mathfrak{Re}\,\lambda$ is strictly positive is not a surprise. Indeed, L_4 and L_5 are maxima of energy in the phase space (Fig. 3.1), and since tides are responsible for a decrease in the orbital energy, we expect the system to be driven away from the Lagrangian equilibria by tides, hence the positivity of $\mathfrak{Re}\,\lambda$. The fact that L_4 and L_5 are maxima of energy is not a surprise either, as Moeckel (2017) proved that a system of $N \geq 3$ rigid bodies rotating rigidly and uniformly around their axis of total angular momentum cannot be an energy minimizer of the space phase. Therefore, we could have expected without calculation that the elliptic Lagrangian equilibria are energy maximizers[6], and as a consequence, that

[6]They must be critical points, in order to be equilibria of the averaged model, and they cannot be

dissipative tides make them unstable.

6.2.2 The timescales of tidal evolution

We define here the characteristic timescale of a given proper mode of the system (6.24) as the time needed for its amplitude to be multiplied (or divided, if the corresponding real part is negative) by a factor exp(1). According to the eigenvalues (6.28), these times are

$$\begin{aligned}
\tau_{\mathrm{rot}}^{(j)} &= \frac{1}{6\pi}\alpha_j \mathfrak{P}_j^2 \frac{m_j}{m_0}\frac{Q_j}{q_j}\left[1+\frac{3m_j}{m_1+m_2}\mathfrak{P}_j^2\alpha_j\right]T,\\
\tau_{\mathrm{L}} &= \frac{\iota}{21\pi}\left(\frac{q_1}{Q_1}+\frac{q_2}{Q_2}\right)^{-1}T,\\
\tau_{\mathrm{AL}} &= \frac{\iota}{21\pi}\left(\frac{m_2}{m_1}\frac{q_1}{Q_1}+\frac{m_1}{m_2}\frac{q_2}{Q_2}\right)^{-1}T,\\
\tau_{\mathrm{lib}} &= \frac{7}{3}\tau_{\mathrm{AL}},
\end{aligned} \tag{6.29}$$

where $T = 2\pi/\eta$ is the orbital period. We note that the times $\tau_{\mathrm{rot}}^{(j)}$ are much smaller than the three other characteristic timescales, due to the presence of the factor $\mathfrak{P}_j^2 \ll 1$. That is, regardless of the parameters and initial conditions, the rotations of the planets are damped to their equilibrium value (6.23) in a timescale such that the eccentricities and the libration angle do not undergo significant damping or excitation. We know from the analysis of the eigenvalues (6.28) that the two eccentric eigenmodes Lagrange and anti-Lagrange are damped to zero, while the libration amplitude of the resonant angle ξ exponentially increases. We now compare the timescales τ_{AL}, τ_{L} and τ_{lib} to determine which proper mode amplitude evolves faster. Even though both eccentric eigenmodes are damped, the damping times may be different. By comparing them, we can find if the system favours the Lagrange or the anti-Lagrange configuration. Indeed if

- $\dfrac{\tau_{\mathrm{AL}}}{\tau_{\mathrm{L}}} < 1$, then the system settles in Lagrange, whereas if
- $\dfrac{\tau_{\mathrm{AL}}}{\tau_{\mathrm{L}}} > 1$, then the system settles in anti-Lagrange.

Moreover, comparing the time τ_{lib} with the eccentric times τ_{AL} and τ_{L} allows us to determine if the system is still eccentric or already nearly circular when the libration amplitude has significantly increased. We have

$$\tau_{\mathrm{lib}} = \frac{\iota}{9\pi\Omega}\frac{\tau_{\mathrm{AL}}}{\tau_{\mathrm{L}}}T, \tag{6.30}$$

where we defined $\Omega = q_1/Q_1 + q_2/Q_2$ the sum of the dissipation rates. Equation (6.30) shows that, for a given sum of the planetary masses, ι, and sum of the dissipation rates, Ω, the system moves away from $L_{4,5}$ faster if it favours Lagrange, and slower if it favours anti-Lagrange.

These results are a priori valid only in a small neighboorhoud of $L_{4,5}$, but in fact, the simulations from Sect. 6.3 show that the behaviour of the system near $L_{4,5}$ is valid

saddle points, or they would be hyperbolic.

even at high libration amplitudes. This means that the exponential increase in libration amplitude is unbounded. Once the libration amplitude of ξ increased too much, Eq. (3.37) is not verified anymore, the co-orbitals enter each other's Hill sphere and planet−planet interactions disrupt the system. The planets either get ejected from the co-orbital resonance, or they collide. The disruption time depends on $\tau_{\rm lib}$, and so, Lagrange-like systems have a short life expectancy, while anti-Lagrange-like systems have a long life expectancy (for a given ι and Ω). Moreover, a Lagrange-like system is eccentric when old[7] (as long as it was eccentric when young), while an anti-Lagrange-like system is always circular when old. Indeed, for an anti-Lagrange-like system, the characteristic time $\tau_{\rm e}$ of eccentricity damping is given by $\tau_{\rm AL}$ and then, $\tau_{\rm lib} = 7\tau_{\rm e}/3 \sim \tau_{\rm e}$ ensures that the eccentricity is damped when the libration amplitude has significantly increased. On the other hand, for a Lagrange-like system, $\tau_{\rm e} = \tau_{\rm L}$ and then, $\tau_{\rm lib} \ll \tau_{\rm e}$ ensures that the system is still eccentric when the libration amplitude has significantly increased.

Although it is clear that $\tau_{\rm lib}$ depends on the semi-major axis $\bar{a}$, Eq. (6.30) does not explicitly show it, since the dependency on $\bar{a}$ is hidden in q_j, Q_j and T. We have

$$\tau_{\rm lib} \propto \frac{\tau_{\rm AL}}{\tau_{\rm L}} \bar{a}^{\beta}, \tag{6.31}$$

where β is 8 for the constant-Δt model and 6.5 for the constant-Q model. Thus, for a large $\bar{a}$ or a strong anti-Lagrange tendency, co-orbital planetary systems may survive for the entire life-time of the star in the main sequence.

Interestingly, the ratio between the two eccentric damping timescales depends only on the ratio between the planetary masses and the ratio between the dissipation rates inside the planets. That is, denoting

$$x = \frac{m_1}{m_2} \quad \text{and} \quad y = \frac{q_2/Q_2}{q_1/Q_1} = \frac{\kappa_2^{(2)} \wp_2^5 / Q_2}{\kappa_2^{(1)} \wp_1^5 / Q_1}, \tag{6.32}$$

we have

$$\frac{\tau_{\rm AL}}{\tau_{\rm L}} = \frac{x\,(1+y)}{1+yx^2}. \tag{6.33}$$

The equality between the eccentric damping timescales ($\tau_{\rm AL} = \tau_{\rm L}$) occurs at $x = 1$ and $xy = 1$, plotted by black lines in Fig. 6.1, where we also show the ratio $\tau_{\rm AL}/\tau_{\rm L}$ as a function of x and y. We clearly observe two regions, corresponding to Lagrange-like and anti-Lagrange-like systems.

Let us assume that the quality factor Q_j is mass independent. We then deduce from $\wp_j \propto m_j^{1/3}$ and Eq. (6.32) that

$$y \propto x^{-5/3}. \tag{6.34}$$

The blue line in Fig. 6.1 plots $y = x^{-5/3}$. It shows the path followed by a system with two initially identical planets (white spot) when we change the mass repartition between them. We conclude that for a given sum of the planetary masses ι, and sum of the dissipation rates Ω, the expectancy of life of the system is at its shortest for $m_1 = m_2 = \iota m_0/2$ (orange area) and it tends towards infinity if either m_1 or m_2 tends towards ιm_0, or towards zero (yellow/white area).

[7] Old means that its age is significant with respect to its expectancy of life.

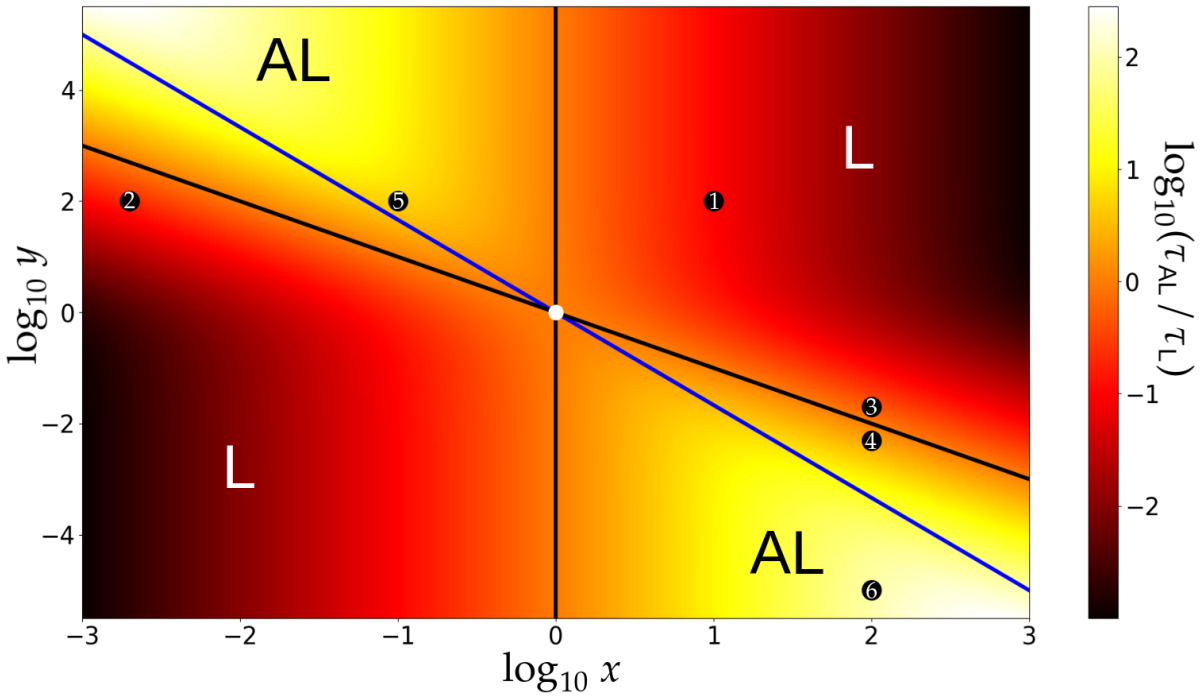

Fig. 6.1 — Value of $\tau_{\rm AL}/\tau_{\rm L}$ in colorscale. The black straight lines are the locations of the points where $\tau_{\rm AL} = \tau_{\rm L}$. The blue line is the path followed by a system of variable mass repartition. The black spots are the positions of the numerical simulations of Sect. 6.3. The white dot $(x = 1, y = 1)$ is where Rodríguez *et al.* (2013) performed all of their simulations. It complies with $\tau_{\rm AL} = \tau_{\rm L}$, explaining why they did not see any hierarchy between the eccentric eigenmodes. Systems in the red-black regions settle into Lagrange, have a short life expectancy and are eccentric when old, while systems in the yellow-white regions settle into anti-Lagrange, have a long life expectancy and are circular when old.

Combining Eqs. (6.30) & (6.33), the characteristic timescale for the increase of the libration amplitude reads

$$\tau_{\rm lib} = \frac{\iota}{9\pi\Omega}\frac{x\,(1+y)}{1+yx^2}T. \tag{6.35}$$

In the case of identical co-orbital planets (same mass, radius and tidal parameters), we derive for the characteristic timescale of destruction the simple expression

$$\tau_{\rm lib} = \frac{m_j Q_j T}{9\pi m_0 q_j} = 0.565\ {\rm Gyr}\left(\frac{m_j}{M_\oplus}\right)\left(\frac{M_\odot}{m_0}\right)^{3/2}\left(\frac{\bar{a}}{0.04\,{\rm AU}}\right)^{6.5}\left(\frac{R_\oplus}{R_j}\right)^{5}\left(\frac{0.0011}{\kappa_2^{(j)}/Q_j}\right), \tag{6.36}$$

where we considered two co-orbital Earth-like planets for the numerical evaluation in Eq. (6.36). The value of κ_2/Q for the Earth is given in Table 5.1.

6.2.3 Looking for co-orbital exoplanets

We can use the results from Sect. 6.2.2 to estimate whether or not an already discovered exoplanet may have an undetected co-orbital companion. For a co-orbital system, we denote $\tau_{\rm hs}$ and $\tau_{\rm dest}$ the time needed to reach the horseshoe-shaped orbits (that is, to cross the separatrix emanating from L_3), and the time needed for close encounters to disrupt

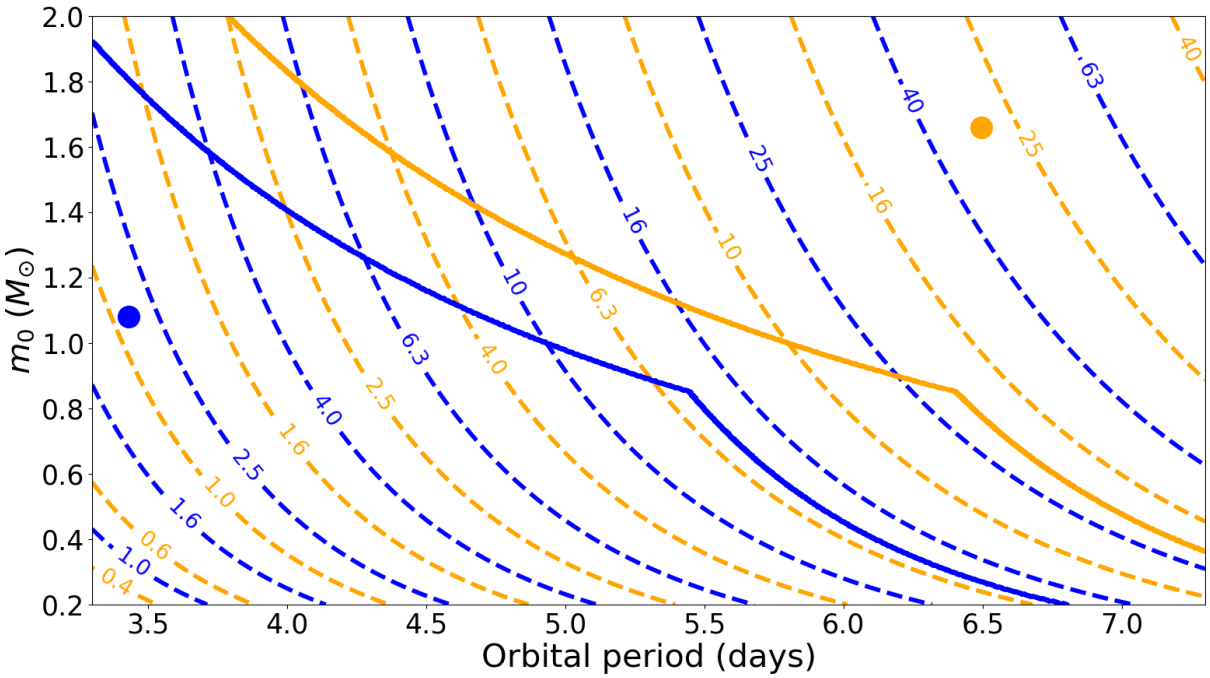

Fig. 6.2 — Disruption time (Gyr) of an hypothetical co-orbital system as a function of the orbital period of the observed planet and of the mass of the host star. The couple Saturn+Earth is plotted in orange while the couple Earth+Earth is plotted in blue. The solid lines plot the minimum of the main sequence duration and of the age of the universe for both couples. Systems below these lines may have been already destroyed at the time of observation, but systems above outlive either their host star or the age of the universe. The blue and orange dots correspond to HD 158259 c and HD 102956 b, respectively. Note that, for a given orbital period, co-orbital systems live longer around a massive host star because they have a larger semi-major axis.

the co-orbital resonance, respectively. In the rest of this section, we use the accessible observational parameters to approximate $\tau_{\rm dest}$ and then discard cases such that $\tau_{\rm dest}$ is too small.

The libration amplitude $\Delta\xi = \max(\xi - 60°)$ is defined as the angular distance to L_4. If $\Delta\xi_0$ is the initial libration amplitude of the system and if $\Delta\xi$ is a small libration amplitude greater than $\Delta\xi_0$, then, by definition of $\tau_{\rm lib}$, the time τ_ξ needed to reach the libration amplitude $\Delta\xi$ is given by

$$\tau_\xi = \ln\left(\frac{\Delta\xi}{\Delta\xi_0}\right)\tau_{\rm lib}. \tag{6.37}$$

Equation (6.37) cannot be used, a priori, to predict the time $\tau_{\rm hs}$, since the separatrix emanating from L_3 is far from the fixed point L_4. Nevertheless, by performing numerical simulations of the set of Eqs. (6.15) with arbitrary parameters and initial conditions, we verify that the expression

$$\tau_{\rm hs} \approx \ln\left(\frac{60°}{\Delta\xi_0}\right)\tau_{\rm lib}, \tag{6.38}$$

is always a good approximation as long as $\Delta\xi_0 \leq 15°$, where $\Delta\xi_0$ is in arc degrees. Although $\tau_{\rm hs}/\tau_{\rm lib}$ only depends on $\Delta\xi_0$, we expect that $\tau_{\rm dest}/\tau_{\rm lib}$ also depends on ι, since this parameter controls the maximum libration amplitude before the system becomes

Co-orbital pair	$\tau_{\rm hs}$ (Gyr)	Co-orbital pair	$\tau_{\rm hs}$ (Gyr)	Co-orbital pair	$\tau_{\rm hs}$ (Gyr)
Earth & Earth	3.612	Moon & Mars	28.48	Mars & Saturn	5.000
Earth & Moon	43.81	Moon & Jupiter	50.63	Jupiter & Jupiter	0.7214
Earth & Mars	5.552	Moon & Io	4.374	Jupiter & Io	2.072
Earth & Jupiter	3.567	Moon & Saturn	43.13	Jupiter & Saturn	0.04741
Earth & Io	2.085	Mars & Mars	5.892	Io & Io	2.072
Earth & Saturn	1.803	Mars & Jupiter	5.878	Io & Saturn	2.054
Moon & Moon	50.76	Mars & Io	2.250	Saturn & Saturn	0.03704

Table 6.1 — Time to horseshoe-shaped orbits $\tau_{\rm hs}$ for a variety of co-orbital systems, computed with Eq. (6.40). The tidal parameters are those of Table 5.1 and only the six bodies for which κ_2/Q is well constrained are included. In general, $\tau_{\rm dest}$ is close to $\tau_{\rm hs}$.

unstable (Eq. (3.37)). The smaller ι is, the larger the maximum libration amplitude is. Since $\iota = 3 \times 10^{-4}$ is the highest value allowing horseshoe-shaped orbits (Leleu *et al.*, 2015, Fig. 4), the equality $\tau_{\rm dest} = \tau_{\rm hs}$ occurs at this value. If we take $\Delta\xi_0 = 10°$, we have

$$1/2\,\tau_{\rm hs} \leq \tau_{\rm dest} \leq 2\,\tau_{\rm hs} \;\Leftrightarrow\; 10^{-9} \lesssim \iota \lesssim 0.005, \tag{6.39}$$

and so, $\tau_{\rm hs}$ and $\tau_{\rm dest}$ do not differ by more than a factor 2 for a wide range of ι. We thus consider $\tau_{\rm dest} \approx \tau_{\rm hs}$ in this range and Eqs. (6.35) & (6.38) can be used to predict $\tau_{\rm dest}$.

Figure 6.2 shows the disruption times of a Saturn-Earth co-orbital system (in orange), and of a system of two Earth-like planets (in blue), with $\Delta\xi_0 = 10°$. The tidal parameters adopted for these systems are given in Table 5.1. The solid line plots $\min(\tau_{\rm ms}, \tau_{\rm u})$ where $\tau_{\rm ms} = 10^{10}\,{\rm yr}\,(m_0/M_\odot)^{-2}$ is the duration of the main-sequence of the host star and $\tau_{\rm u} = 13.77$ Gyr is the age of the Universe. Assuming that the Earth and Saturn are representative of the average rocky planet and gas giant, Fig. 6.2 tells us if an already detected gas giant may have a companion (orange lines), or if an already detected rocky planet may have a companion (blue lines). The detected exoplanet is located in Fig. 6.2 using its orbital period and the mass of the host star. If it is below its associated solid line (orange for a gas giant, blue for a rocky planet), then its companion was already ejected, if it ever existed. On the contrary, if it is above this line, the hypothetical pair of co-orbital outlives either the host star or the age of the Universe and it is worth looking for the companion. As an example, it is very unlikely to find a co-orbital companion for the rocky planet HD 158259 c (Hara *et al.*, 2020), plotted with a blue dot in Fig. 6.2, but we cannot rule out that the gas giant HD 102956 b (Luhn *et al.*, 2019), plotted with an orange dot in Fig. 6.2, has a co-orbital companion.

Combining Eqs. (6.35) & (6.38), the time $\tau_{\rm hs}$ to reach the horseshoe-shaped orbits takes the form

$$\tau_{\rm hs} = \frac{\iota}{9\pi\Omega}\frac{x\,(1+y)}{1+yx^2}\ln\left(\frac{60°}{\Delta\xi_0}\right)T. \tag{6.40}$$

We can use the tidal parameters given by Table 5.1 to compute this time for a large variety of co-orbital systems. We give in Table 6.1 the time $\tau_{\rm hs}$ for hypothetical co-orbital pairs of exoplanets made up of Solar System bodies. The semimajor axis is $\bar{a} = 0.04$ AU and the mass of the host star is $m_0 = M_\odot$, but $\tau_{\rm hs}$ can easily be deduced for other values using the exponents of Eq. (6.36), that are still valid for different co-orbitals. We choose

$\Delta\xi_0 = 0.1°$, and again, it is straightforward to extend the results to another choice of $\Delta\xi_0$ using Eq. (6.38).

6.3 Numerical simulations

In this section, in order to verify the analytical results of Sect. 6.2, we perform some numerical simulations of planetary systems representative of the different dynamical regimes of co-orbital planets undergoing tidal interactions with the star, such as those described in Sect. 6.2.

6.3.1 Procedure

We numerically integrate the six systems that correspond to the black dots on Fig. 6.1. For all of them we choose the initial conditions and parameters[8]

$$\begin{aligned} &\iota = 2\times10^{-4}, \quad \Omega = 4\times10^{-13}, && m_0 = M_\odot, && \alpha_1 = \alpha_2 = 0.33, \\ &\rho_2 = 4\rho_1 = 2000\,\mathrm{kg/m^3}, && e_{2,0} = 2e_{1,0} = 0.04, && \varpi_{1,0} = \varpi_{2,0} = 0, \\ &a_{1,0} = a_{2,0} = \bar{a} = 0.02\,\mathrm{AU}, && \vartheta_{1,0} = \vartheta_{2,0} = 0, && \xi_0 = 62°, \end{aligned} \tag{6.41}$$

that is, the systems are initially 2° away from L_4. Since the total planetary masses ι and the total dissipation rate $\Omega = q_1/Q_1 + q_2/Q_2$ are the same for all systems, their positions can all be plotted in Fig. 6.1 and their tidal timescales are entirely determined by the values of the mass ratio x and the dissipation rate ratio y (see Eq. (6.32)), which are the only variable parameters between the systems (see Table 6.2). According to Eq. (6.30), we expect that the systems that are in the yellow regions of Fig. 6.1 live longer than those in the red regions. This choice for the initial eccentricities and longitude of the pericentres guarantees that the systems are not initially collinear to the Lagrange or anti-Lagrange configuration, and their evolution allows us to determine if they are Lagrange-like or anti-Lagrange-like. The timescales of the six systems, in number of orbital periods and deduced from Sect. 6.2.2, are given in Table 6.2. The time τ_{lib} is the characteristic timescale of libration amplitude excitation given by Eqs. (6.35), while $\tau_{\mathrm{lib}}^{(\mathrm{num})}$ is directly computed from the numerical value of $\mathcal{Z}_0 + \mathcal{Z}_1$ (given in appendix C.3), without using the perturbative method of Sect. 2.4.2.

[8]The variable ρ_j is the density of planet j.

#	color	x	y	τ_{lib}	$\tau_{\mathrm{lib}}^{(\mathrm{num})}$	τ_{AL}	τ_{L}
1	blue	10	100	1 785 893	1 845 021	765 382	7 578 807
2	green	1/500	100	3 570 716	4 198 710	1 530 306	7 578 807
3	red	100	1/50	8 973 910	9 161 859	3 845 961	7 578 807
4	purple	100	1/200	34 847 651	34 893 952	14 934 707	7 578 807
5	yellow	1/10	100	89 303 607	89 304 263	38 272 974	7 578 807
6	black	100	10^{-5}	1 607 641 764	1 607 642 323	688 989 327	7 578 807

Table 6.2 — Values of x, y and of the corresponding timescales of the systems. The timescales are given in number of orbital periods, that is, in units of $2\pi/\eta$.

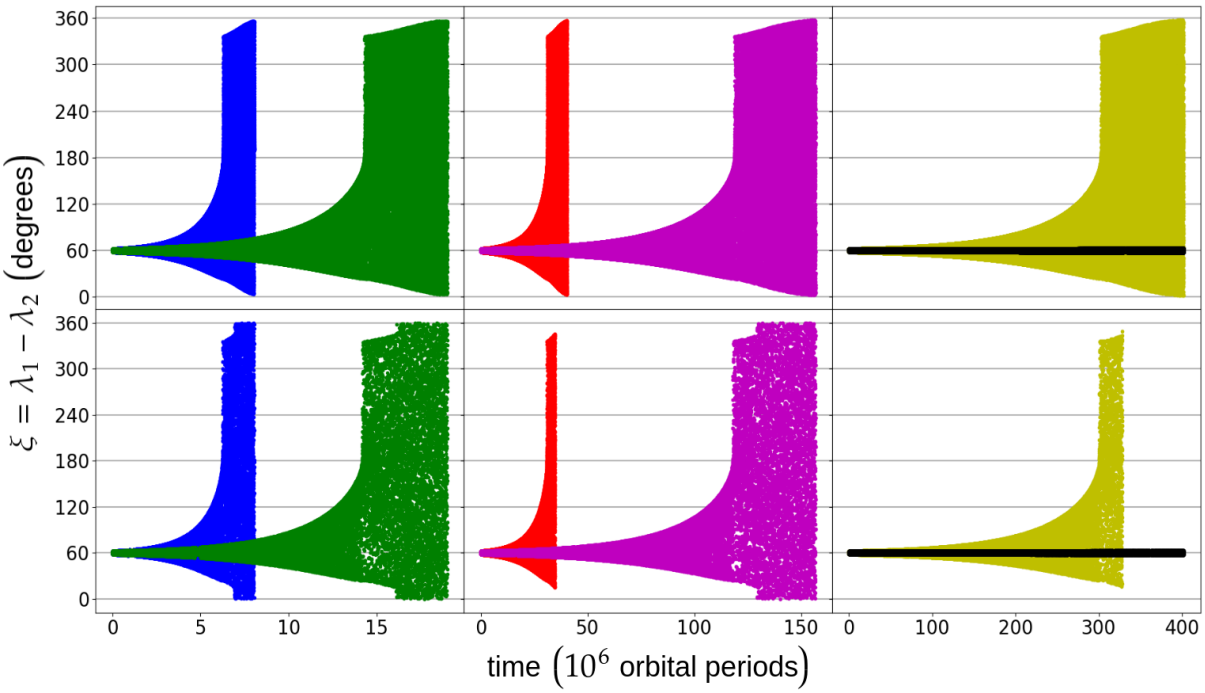

Fig. 6.3 — Value of the libration angle $\xi = \lambda_1 - \lambda_2$ against time, integrated with Eqs. (6.15) (*top*) and Eqs. (C.13) (*bottom*). The switching from tadpole to horseshoe-shaped orbits (crossing of the separatrix emanating from L_3) is very visible, as the libration amplitude suddenly increases, giving this boot-shape to the plots. As expected from Fig. 6.1 and Table 6.2, systems 4, 5 and 6 live longer than systems 1, 2 and 3.

For some systems, especially system 2, there is a slight difference between $\tau_{\rm lib}^{\rm (num)}$ and $\tau_{\rm lib}$. For these systems, the values of $\mathfrak{a}_1$ and $\mathfrak{a}_2$ in the matrix $\mathcal{Z}_1$ (appendix C.3) are much larger than the other entries of the matrix, and are such that $\mathfrak{a}_j \sim \nu$, which means that the condition $|\lambda_i - \lambda_j| \gg \varepsilon$ in Eq. (2.88) of Sect. 2.4.2 is poorly respected. A smaller value for the sum of the dissipation rates Ω provides a perfect agreement between $\tau_{\rm lib}^{\rm (num)}$ and $\tau_{\rm lib}$ for all six systems, but it also leads to much longer simulations. Here, we purposefully choose a large value for Ω in order to have quick simulations. On the other hand, there is no disagreement between the analytical values of $\tau_{\rm AL}$ and $\tau_{\rm L}$ given by Eq. (6.29) and their numerical counterparts, since the eccentricities are uncoupled from the rest of the variables in the linearized system and the entries of $\mathcal{M}_1$ in appendix C.3 respect the condition of Eq. (2.88) for all six systems.

Each system is numerically integrated using two different sets of equations. In the first set, we use the secular Eqs. (6.15) derived in Sect. 6.1.2. In the second set, we use a n-body unaveraged and unexpanded model in the regular position-speed coordinates, with the constant-Δt model. The second set is given by Eq. (C.13) of appendix C.4. The results are displayed in Figs. 6.3, 6.4 and 6.5. In each figure, the top panels correspond to the set of Eqs. (6.15) while the bottom panels correspond to the set of Eqs. (C.13). All systems except system 6 are integrated long enough for the co-orbital configuration to be destroyed.

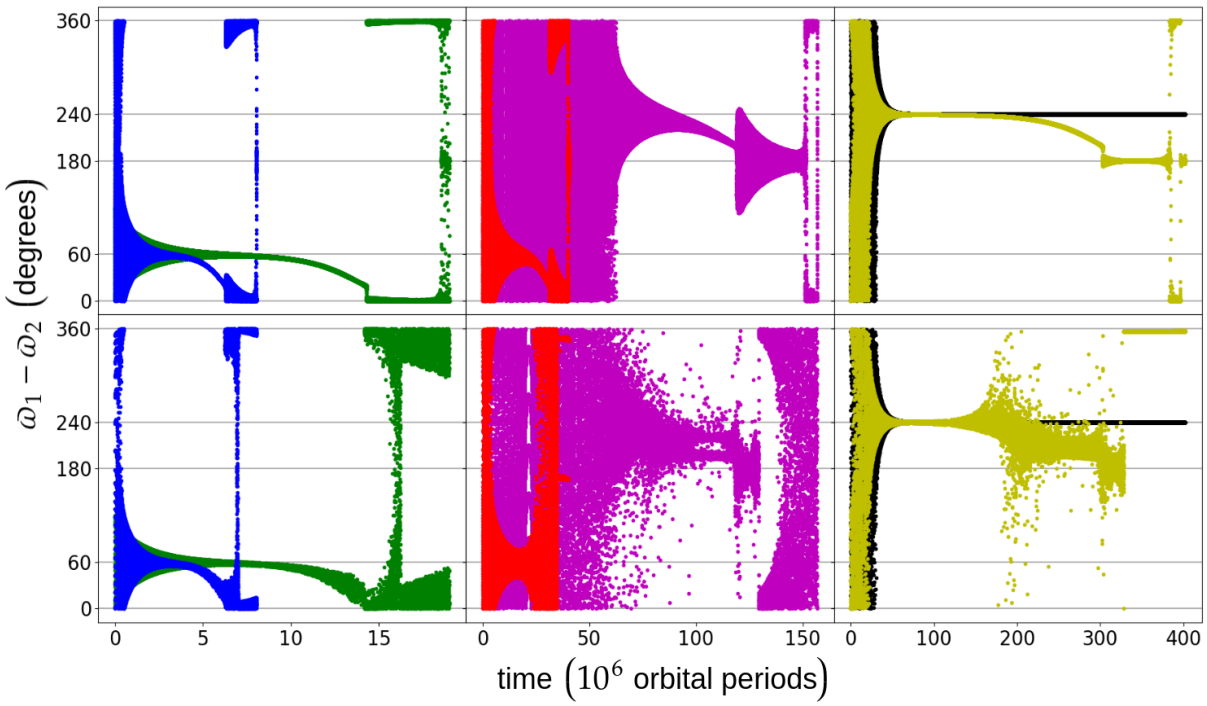

Fig. 6.4 — Value of $\varpi_1 - \varpi_2$ against time, integrated with Eqs. (6.15) (*top*) and Eqs. (C.13) (*bottom*). Blue, green and red systems settle into the Lagrange configuration and have a short life while purple, yellow and black systems settle into the anti-Lagrange configuration and live long. This is in agreement with what we deduce from the analytical results, especially Fig. 6.1 and Table 6.2.

6.3.2 Comparison between the model and the complete system

We observe that there is always a very good agreement between Eqs. (6.15) and Eqs. (C.13), except when the libration amplitude is near 360°. Indeed, as the libration amplitude increases, close encounters between the planets mean that planet−planet interactions are no longer perturbations of the Keplerian motion and Eq. (3.37) is not verified anymore. On the top plot of Fig. 6.3, the amplitude of ξ tends towards 360° as time goes to infinity but never reaches it, while on the bottom plot, there exists a finite time when ξ reaches 360°, meaning it is a circulating angle and the planets either collide or get ejected off the co-orbital resonance. All simulations confirm the destruction of the co-orbital resonance. We also note that for small eccentricities, the averaged Eqs. (6.15) (plotted on top) differ from the complete Eqs. (C.13) (plotted at the bottom). We believe that this is due to short period influences that were averaged out in our model. Indeed, while the manifold $(X_1 = X_2 = 0)$ is stable by the flow of the averaged Hamiltonian, it is not stable by the flow of the complete Hamiltonian. This may explain the differences between both plots at low eccentricities. This does not discredit though the theoretical results obtained in Sect. 6.2.

Let $\tau_{\mathrm{hs}}^{(\mathrm{a})}$, $\tau_{\mathrm{hs}}^{(\mathrm{s})}$ and $\tau_{\mathrm{hs}}^{(\mathrm{c})}$ be the times needed to reach the horseshoe-shaped orbits according to the analytical expression[9] (6.38), the simulation of the secular Eqs. (6.15) and the

[9]Due to tides being too strong (Ω is too large) for systems 1 and 2, we considered $\tau_{\mathrm{lib}}^{(\mathrm{num})}$ instead of τ_{lib}. With weaker tides, there is no difference between these two timescales.

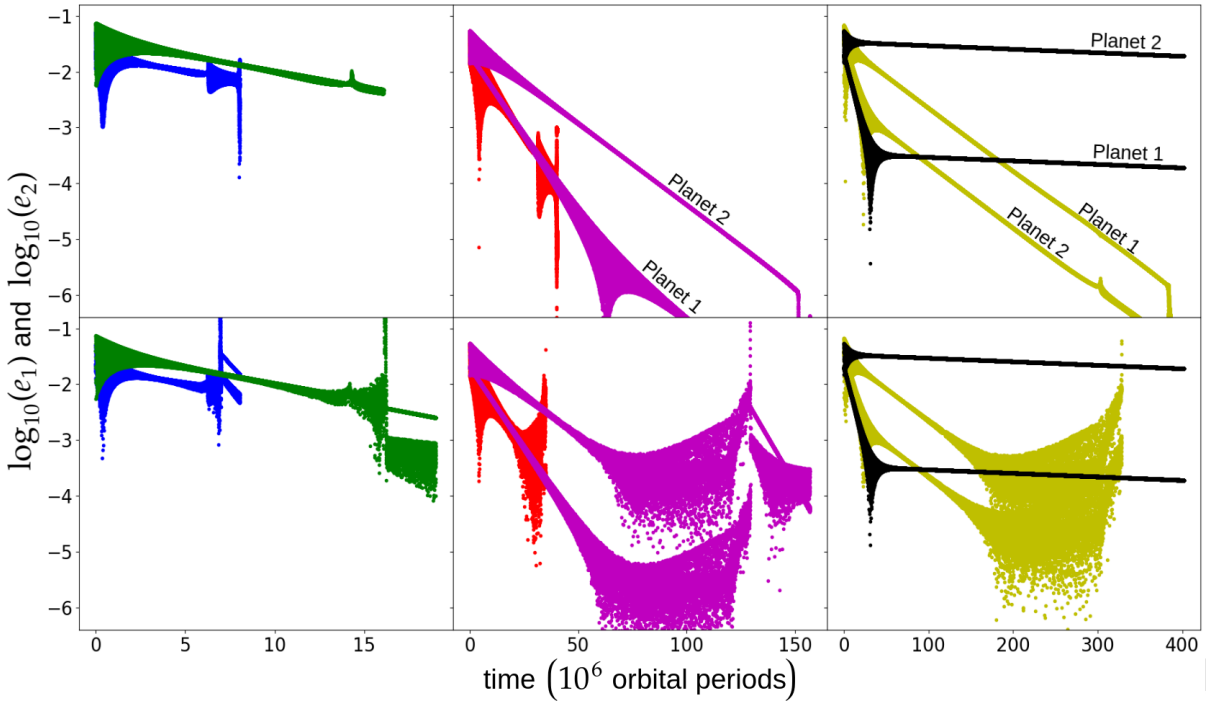

Fig. 6.5 — Eccentricities of both planets against time, integrated with Eqs. (6.15) (*top*) and Eqs. (C.13) (*bottom*). For a same system, e_1 and e_2 are plotted with the same color. Anti-Lagrange-like systems comply with $m_1 e_1 = m_2 e_2$ and both plots are easily distinguished while for Lagrange-like system, such that $e_1 = e_2$, both plots are almost overlaid. This is in agreement with what we deduce from Fig. 6.1 and Table 6.2.

simulation of the complete Eqs. (C.13), respectively. We give these times in Table 6.3, for reference. In our model, the exterior of the co-orbital resonance does not exist (Fig. 3.1), and only the simulation of the complete Eqs. (C.13) allows $\tau_{\rm dest}$, the time before destruction of the co-orbital pair, to be known. We also give this time in Table 6.3. The relative error between the three times $\tau_{\rm hs}$ is consistently smaller than 1%, and the model is reliable on the whole tadpole region. For this choice of ι, we have, for the first 5 systems, $\tau_{\rm hs}/\tau_{\rm dest} \approx 1.1$, which allowed us to predict the destruction time for system 6.

As expected from the values of $\tau_{\rm AL}$ and $\tau_{\rm L}$ given in Table 6.2, the three shortest simulations correspond to Lagrange-like systems, while the three longest correspond to anti-Lagrange like systems. This is particularly clear in Fig. 6.4, which displays the

#	$\tau_{\rm hs}^{\rm (a)}$	$\tau_{\rm hs}^{\rm (s)}$	$\tau_{\rm hs}^{\rm (c)}$	$\lvert\tau_{\rm hs}^{\rm (a)} - \tau_{\rm hs}^{\rm (s)}\rvert/\tau_{\rm hs}^{\rm (s)}$	$\lvert\tau_{\rm hs}^{\rm (s)} - \tau_{\rm hs}^{\rm (c)}\rvert/\tau_{\rm hs}^{\rm (c)}$	$\tau_{\rm dest}$
1	6.2753	6.2856	6.2427	0.001639	0.00683	6.9202
2	14.281	14.306	14.178	0.001748	0.00894	16.146
3	31.161	31.272	31.054	0.003550	0.00695	34.841
4	118.68	118.98	118.15	0.002521	0.00693	129.36
5	303.74	302.79	300.44	0.003137	0.00777	328.04
6	5467.9					$\sim 6\,010$

Table 6.3 — Times to reach horseshoe-shaped orbits and until destruction, in millions of periods.

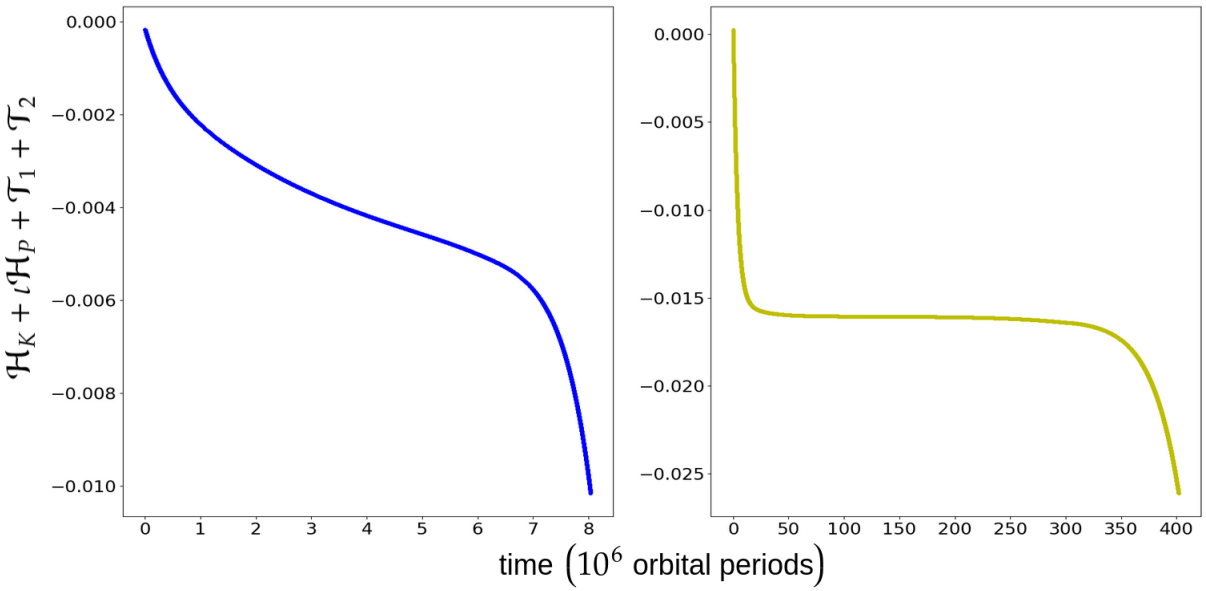

Fig. 6.6 — Total normalized energy of system 1 (*left*) and system 5 (*right*). The very anti-Lagrange-like system 5 features a pronounced plateau in its energy decrease and lives long while the very Lagrange-like system 1 does not show any marked plateau and has a short life.

value of $\varpi_1 - \varpi_2$. For the short-lived systems (blue, green and red), the difference of the longitude of pericentres first settles around $60° = \pi/3$ at low libration amplitude, before it moves to 0°, when in horseshoe orbit. For the long-lived systems (yellow, black and purple), the difference of the longitude of pericentres first settles around $240° = 4\pi/3$ at low libration amplitude, before it moves to $180° = \pi$, when in horseshoe orbit. This is in total agreement with Eqs. (3.44), (3.45), (3.49) & (3.50).

Figure 6.5 also confirms the Lagrange-like behaviour of short-lived systems, since $e_1 = e_2$ for these systems, while $m_1 e_1 = m_2 e_2$ for long-lived simulations, characteristic of their anti-Lagrange-like behaviour (Eqs. (3.44) & (3.45), Sect. 3.2.2). As also expected from the theoretical results, Lagrange-like system are still eccentric when they are old (*e.g.* the green and blue plots), while anti-Lagrange-like system are circular when they are at the end of their life (yellow plot).

6.3.3 A plateau in the energy decrease

In Fig. 6.6, we show the total energy $\mathcal{H}_K + \iota\mathcal{H}_P + \mathcal{T}_1 + \mathcal{T}_2$ of system 1 and system 5. The energy of the anti-Lagrange-like system 5 (yellow) features two steep decrease and a broad plateau. At the beginning of the simulation, the eccentricities of the planets are still significant, meaning that $\dot{w}_j$, the time derivative of their true longitude, is not constant. This prevents a solid rotation around the star, although the equilibrium rotation is already reached (small $\tau_{\text{rot}}^{(j)}$), and ensures dissipation: it is the first steep decrease. Then, the eccentricities are almost damped while the libration amplitude did not significantly increase yet. The motion around the star is almost a solid rotation and very few energy is dissipated into heat: it is the plateau. Finally, the high libration amplitude of ξ reached in late tadpole and horseshoe-shaped orbits ensures the non-constancy of $\dot{w}_j$ and energy dissipation: it is the second steep decrease.

For almost restricted systems, very anti-Lagrange-like, the amplitude of libration has to be very high for the least massive planet to significantly perturb the solid rotation of the most massive one. Thus, these systems have very broad plateau and a very high life expectancy. On the other hand, the energy of the Lagrange-like system 1 (blue), does not feature such a marked plateau, because the eccentricities are always nonzero even at high libration amplitude, and hence its life is far shorter.

6.4 Tides raised on the central body

In the previous sections of this chapter, we discarded tides raised on the central body, because we showed that for a system star−planet−planet, the ratio of Eq. (6.1) is much smaller than unity. In this section, we show that such tides have to be taken into account for a system planet−satellite−satellite and we establish the corresponding tidal timescales.

6.4.1 Orders of magnitude

In Sect. 6.1.1, we only retained two out of the 12 tidal potentials of the form of Eq. (5.45), namely those corresponding to tides raised by the star on each planet and interacted with by the star. In this section, the central body is a planet, while the co-orbitals are satellites. Four additional contributions have hence to be taken into account, corresponding to tides raised by both satellites on the planet and interacted with by both satellites. Indeed, the ratio of Eq. (6.1) in that case can be of the order of unity.

The best example of such system is the pair Janus and Epimetheus orbiting Saturn. For this system, we have $\iota^{1/3} = 0.00163$ and according to Table 5.1, the κ_2/Q of Saturn is $\kappa_2^{(0)}/Q_0 = 1.6 \times 10^{-4}$ (Lainey, 2016). The κ_2/Q of Janus and Epimetheus are unknown, but we can estimate them. We first estimate the value of κ_2 with Eq. (5.31). For icy satellites made up of intact ice, it is common to take $\mu = 4$ GPa (Quillen *et al.*, 2017), but fractures and pores reduce this value. According to Nimmo and Schenk (2006), the porous or fractured nature of the satellites is unlikely to decrease the value of μ by more than one order of magnitude (see their Fig. 6), so we consider 0.4 GPa $\leq \mu \leq 4$ GPa for both satellites and Eq. (5.31) yields[10] $1.12 \times 10^{-5} \leq \kappa_2 \leq 1.12 \times 10^{-4}$ for Epimetheus and $2.74 \times 10^{-5} \leq \kappa_2 \leq 2.74 \times 10^{-4}$ for Janus. These values are rough approximations and we consider, for both satellites, $\kappa_2 = 10^{-4}$ if $\mu = 0.4$ GPa and $\kappa_2 = 10^{-5}$ if $\mu = 4$ GPa.

We now give a minimal value for the quality factor Q. According to the considerations stated in the last paragraph of Sect. 5.2.3, the time-lag Δt cannot exceed the time needed for a seismic wave to travel through the satellite[11]. Calling K the bulk modulus, the speed of sound is given by $c_s = \left(\left(K + 4\mu/3\right)/\rho\right)^{1/2}$. Assuming $K \sim \mu$, the time lag Δt is majored by $\Delta t \leq R_j/c_s = R_j(3\rho/(7\mu))^{1/2}$ and the quality factor Q complies with (Eq. (5.44))

$$Q \geq \eta^{-1} R_j^{-1} \sqrt{\frac{7\mu}{3\rho}}. \tag{6.42}$$

[10] Using $\rho = 618$ kg/m^3, $R_j = 58.1$ km and $g = 0.0104$ m/s^2 for Epimetheus and $\rho = 646$ kg/m^3, $R_j = 89.5$ km and $g = 0.0158$ m/s^2 for Janus.

[11] In practice, Δt is much smaller than that.

Assuming a typical frequency of excitation $\eta \sim 2$ rad/day, $\mu = 0.4$ GPa gives $Q \geq 914$ for Epimetheus and $Q \geq 580$ for Janus, while $\mu = 4$ GPa yields $Q \geq 2890$ for Epimetheus and $Q \geq 1835$ for Janus. These are once again very rough estimates and we consider for both satellites $Q \geq 1000$ if $\mu = 0.4$ GPa and $Q \geq 3000$ if $\mu = 4$ GPa. We thus have for Janus and Epimetheus, and more generally for any satellite far from the hydrostatic equilibrium

$$\frac{\kappa_2^{(j)}}{Q_j} \leq \begin{cases} 10^{-7} & \text{if } \mu = 0.4 \text{ GPa}, \\ 0.3 \times 10^{-8} & \text{if } \mu = 4 \text{ GPa}. \end{cases} \tag{6.43}$$

In the case of the system Saturn−Janus−Epimetheus, the ratio of Eq. (6.1) verifies

$$\iota^{1/3} \frac{\kappa_2^{(0)}/Q_0}{\kappa_2^{(j)}/Q_j} \geq \begin{cases} 2.6 & \text{if } \mu = 0.4 \text{ GPa}, \\ 87 & \text{if } \mu = 4 \text{ GPa}. \end{cases} \tag{6.44}$$

and tides raised on the central planet cannot be discarded since this ratio is not much smaller than 1. It is unclear if it is much larger than 1 for this system, so we cannot say if the two tidal contributions that we considered in the previous sections of this chapter (tides raised on the orbiting bodies by the central body and interacted with by the central body) can be discarded in this section. If they cannot, then the real parts given by Eqs. (6.28) have to be added to the real parts given by Eqs. (6.61) in order to get to total tidal contribution.

For a system composed of two large satellites (like the Galilean satellites) orbiting a gas giant, $\kappa_2^{(j)}/Q_j$ is of the order of 0.015 (see the value for Io in Table 5.1), while $\kappa_2^{(0)}/Q_0$ is rather of the order of 10^{-5} to 10^{-4} (see the values for Jupiter and Saturn in Table 5.1). The ratio (6.1) is hence much smaller than 1 and tides raised on the central planet can be discarded again, as if it was a star−planet−planet system, meaning that the results of Sects. 6.2 & 6.3 apply.

6.4.2 Expression of the pseudo-Hamiltonian

As in Sect. 6.1.1, we write the tidal perturbation of the pseudo-Hamiltonian as

$$H_t = U_t^{(11)} + U_t^{(22)} + U_t^{(12)} + U_t^{(21)} + T, \tag{6.45}$$

where $U_t^{(jk)}$ is the contribution of tides raised by the satellite k on the planet and interacted with by the satellite j, and T is the kinetic energy of rotation of the planet. We denote R_0 the radius of the planet and its rheology is characterized by its second Love number $\kappa_2^{(0)}$ (Eqs. (5.35) & (5.36)) and its quality factor Q_0 (Sect. 5.2.4). We have (Eq. (5.45))

$$U_t^{(jk)} = -\kappa_2^{(0)} \mathcal{G} m_j m_k \frac{R_0^5}{r_j^3 r_k^{\star 3}} P_2(\cos S), \quad T = \frac{\Theta'^2}{2\mathcal{C}_0} \tag{6.46}$$

with

$$S = \lambda_j - \lambda_k^\star - (\theta - \theta^\star), \tag{6.47}$$

where θ is the rotation angle of the planet, $\Theta' = \mathcal{C}_0 \omega$ is the conjugated momentum of θ, $\mathcal{C}_0 = \alpha_0 m_0 R_0^2$ is the moment of inertia of the planet, $\omega = d\theta/dt$ is its rotation rate, and

α_0 is a dimensionless structure constant depending on the state equation of the planet ($\alpha_j = 2/5$ if it is homogeneous). Like in Sect. 6.1.1, we denote

$$z^\star = z(t - \Delta t_0) \tag{6.48}$$

for any quantity z. We repeat the calculations from Sect. 6.1.1 and we write the tidal Hamiltonian H_t in the variables $(J, J_2, \xi, \xi_2, X_j, \bar{X}_j)$. We define $\Theta = \Theta'/(m\bar{a}^2\eta)$ in order to normalise Θ' (see Eq. (3.18)). We average $U_t^{(jk)}$ over λ_j and λ_k and $U_t^{(jk)}$ depends on these angles through $\Delta\lambda^{(jk)}$ only, where

$$\Delta\lambda^{(jk)} = \lambda_j - \lambda_k^\star \quad \text{and} \quad \Delta\theta = \theta - \theta^\star. \tag{6.49}$$

In virtue of Eq. (6.47), $U_t^{(jk)}$ depends on θ through $\Delta\theta$ only. We define the quantities

$$q_0 = \kappa_2^{(0)} \wp_0^5, \quad \text{and} \quad \wp_0 = \frac{R_0}{\bar{a}}, \tag{6.50}$$

and performing the rescaling (3.22), we get for $\mathcal{H}_t = H_t/(m\bar{a}^2\eta)$ the expression[12]

$$\begin{aligned} \mathcal{U}_t^{(jk)} &= -q_0\eta \frac{m_j m_k}{m_0 m} \mathcal{R}_j^{-6} \mathcal{R}_k^{\star -6} \left\{ A_t^{(jk)} + \mathfrak{D}_2^{(jk)} + \mathfrak{D}_4^{(jk)} \right\} = \frac{U_t^{(jk)}}{m\bar{a}^2\eta}, \\ \mathcal{T} &= \frac{\eta}{2\alpha_0} \frac{m}{m_0} \frac{\Theta^2}{\wp_0^2} = \frac{T}{m\bar{a}^2\eta}, \end{aligned} \tag{6.51}$$

where (Eq. (6.9))

$$\mathfrak{D}_2^{(jk)} = B_t^{(jk)} \left(\mathcal{R}_j^{-1} X_j \bar{X}_j + \mathcal{R}_k^{\star -1} X_k^\star \bar{X}_k^\star \right) + (\mathcal{R}_j \mathcal{R}_k^\star)^{-1/2} \left(C_t^{(jk)} X_j \bar{X}_k^\star + \bar{C}_t^{(jk)} X_k^\star \bar{X}_j \right), \tag{6.52}$$

and the coefficients $A_t^{(jk)}$, $B_t^{(jk)}$ and $C_t^{(jk)}$ are given by Eq. (6.10), substituting $\Delta\lambda^{(jk)}$ for $\Delta\lambda_j$ and $\Delta\theta$ for $\Delta\theta_j$. The coefficient $\mathfrak{D}_4^{(jk)}$ contains the fourth order in eccentricity and is given in appendix B.3, with the same substitution. As in Sect. 6.1.1, the pseudo-Hamiltonian that we consider for the model is

$$\mathcal{H} = \mathcal{H}_K(J, J_2) + \iota \mathcal{H}_P(\xi, X_1, X_2, \bar{X}_1, \bar{X}_2) + \mathcal{H}_t, \tag{6.53}$$

where $\mathcal{H}_K$ is given by Eq. (6.12), the perturbation $\iota\mathcal{H}_P = \mathcal{H}^{(0)} + \mathcal{H}^{(2)} + \mathcal{H}^{(4)}$ is given by Eq. (3.29) and

$$\mathcal{H}_t = \sum_{j=1}^{2} \sum_{k=1}^{2} \mathcal{U}_t^{(jk)}(J, J_2, J^\star, J_2^\star, \xi, \Delta\xi, \Delta\xi_2, \Delta\theta, \boldsymbol{X}, \boldsymbol{X}^\star, \bar{\boldsymbol{X}}, \bar{\boldsymbol{X}}^\star) + \mathcal{T}(\Theta), \tag{6.54}$$

where $\boldsymbol{X} = (X_1, X_2)$, $\Delta\xi = \xi - \xi^\star$ and $\Delta\xi_2 = \xi_2 - \xi_2^\star$.

6.4.3 Equilibria and eigenvalues

As in Sect. 6.1.2, we derive the equations of motion from the pseudo-Hamiltonian (6.53), following the procedure described in Sect. 5.3 and using Eq. (3.23). The major difference with Sect. 6.1 is the existence of crossed tides. While the Hamiltonian $\mathcal{H}_t$ depends only

[12] $\mathcal{R}_j(J, J_2)$ is defined by Eq. (3.20) and $m = \sqrt{m_1 m_2}$.

on $\lambda_j - \lambda_j^\star$ in Sect. 6.1, we now also have a dependency on $\lambda_j - \lambda_k^\star$, where $j \neq k$. As a consequence, $\mathcal{H}_t$ depends on ξ in Eq. (6.54), whereas it did not depend on ξ in Eq. (6.13). This new dependency complexifies immensely the differential system derived from the pseudo-Hamiltonian, and while we were able to give it in a compact form in Eq. (6.15), it is no longer possible to write the differential system in a readable form. Instead, we merely linearize it in the vicinity of its equilibria.

Due to the conservation of the total angular momentum, the differential system derived from the pseudo-Hamiltonian (6.53) only provides five independent equations for six variables to locate the equilibria, and in order to have one unique equilibrium in the vicinity of which we linearize the differential system, we again choose the arbitrary Eq. (6.22). As explained in Sect. 6.2.1, the linearized system does not depend on the choice of Eq. (6.22) at first order in ιq_0. We define $\vartheta = 1 - \omega/\eta$ and the Lagrangian equilibrium L_4 is located at[13]

$$\begin{aligned} \vartheta_0 &= X_{1,0} = X_{2,0} = 0, \\ \xi_0 &= \frac{\pi}{3} + \frac{q_0}{\sqrt{3}}, \\ a_{1,0} &= \bar{a}\left(1 + 2q_0\frac{m_1 - m_2}{m_0}\right), \\ a_{2,0} &= \bar{a}\left(1 + 2q_0\frac{m_2 - m_1}{m_0}\right). \end{aligned} \tag{6.55}$$

Let $\mathfrak{X}_0 = {}^t(J_{2,0}, \vartheta_0, J_0, \xi_0, X_{1,0}, X_{2,0})$ and $\mathfrak{X} = {}^t(J_2, \vartheta, J, \xi, X_1, X_2)$. Linearized in the vicinity of the Lagrangian equilibrium L_4, the differential system derived from the pseudo-Hamiltonian (6.53) reads

$$\frac{d}{dt}\Delta\mathfrak{X} = (\mathcal{Q}_0' + \mathcal{Q}_1')\,\Delta\mathfrak{X}, \tag{6.56}$$

where $\Delta\mathfrak{X} = \mathfrak{X} - \mathfrak{X}_0$. The matrix $\mathcal{Q}_0'$ derives from the conservative Hamiltonian $\mathcal{H}_K + \iota\mathcal{H}_P$, while $\mathcal{Q}_1'$ corresponds to the tidal contribution $\mathcal{H}_t$. Because the dynamics of X_1 and X_2 is uncoupled from the dynamics of the other variables, the matrices $\mathcal{Q}_0'$ and $\mathcal{Q}_1'$ are block diagonal and take the form

$$\mathcal{Q}_0' = \begin{pmatrix} \mathcal{Z}_0' & 0_{4\times2} \\ 0_{2\times4} & \mathcal{M}_0' \end{pmatrix} \quad \text{and} \quad \mathcal{Q}_1' = \begin{pmatrix} \mathcal{Z}_1' & 0_{4\times2} \\ 0_{2\times4} & \mathcal{M}_1' \end{pmatrix}, \tag{6.57}$$

where $\mathcal{Z}_0'$, $\mathcal{M}_0'$, $\mathcal{Z}_1'$ and $\mathcal{M}_1'$ are given in this Maxima worksheet. The set of eigenvalues of $\mathcal{Q}_0$ is (Eq. (6.25))

$$\{0, 0, i\nu, -i\nu, ig_1, ig_2\}, \tag{6.58}$$

where ν (Eq. (3.32)) is the libration frequency of ξ around L_4 while g_1 and g_2 (Eq. (3.42)) are the precession frequencies of the pericentres in the eccentric eigenmodes anti-Lagrange and Lagrange, respectively. The first 0 eigenvalue corresponds to the constancy of J_2 (conservation of the total angular momentum), while the second one corresponds to the constant rotation rate of the planet. Like in Sect. 6.2.1, all six eigenvalues of $\mathcal{Q}_0'$ are pure imaginary and the linearized system is quasiperiodic without tides.

[13] Or equivalently, $J_0 = \frac{9}{4}q_0\frac{m\,(m_1 - m_2)}{m_0\,(m_1 + m_2)}$ and $J_{2,0} = \frac{9}{8}q_0\frac{(m_1 - m_2)^2}{m_0 m}$.

We use the perturbative approach described in Sect. 2.4.2 to find the eigenvalues of $\mathcal{Q}'_0 + \mathcal{Q}'_1$ at first order in ιq_0. In order to alleviate the expression of the eigenvalues, it is convenient to define, for integers p and q, the quantity

$$\aleph_p^q = \frac{p\,(m_1 - m_2)^2 + q m_1 m_2}{m_0\,(m_1 + m_2)}. \tag{6.59}$$

The set of eigenvalues of $\mathcal{Q}'_0 + \mathcal{Q}'_1$ is

$$\left\{\nleftarrow, 0, \lambda, \bar{\lambda}, \lambda_{\mathrm{AL}}, \lambda_{\mathrm{L}}\right\}, \tag{6.60}$$

with

$$\begin{aligned}
\nleftarrow &= \boxed{3\eta \frac{q_0}{Q_0} \aleph_1^1 \left(3 - \alpha_0^{-1} \varsigma_0^{-2} \iota\right)}, \\
\lambda &= \boxed{\frac{27}{2} \eta \frac{q_0}{Q_0} \aleph_0^1} + i\nu - i\nu \frac{q_0}{8} \aleph_7^{-206} - \frac{45}{16} i \eta^2 \nu^{-1} q_0 \iota, \\
\lambda_{\mathrm{AL}} &= \boxed{-\frac{225}{8} \eta \frac{q_0}{Q_0} \aleph_0^1} + i g_1 + \frac{3}{8} i \eta q_0 \aleph_7^{45}, \\
\lambda_{\mathrm{L}} &= \boxed{-\frac{3}{8} \eta \frac{q_0}{Q_0} \aleph_{28}^{37}} + i g_2 + \frac{15}{8} i \eta q_0 \aleph_4^7.
\end{aligned} \tag{6.61}$$

The eigenvalues are no longer pure imaginary and we boxed the real parts. They are proportional to the inverse quality factor Q_0^{-1} and as in Sect. 6.2.1, elastic tides do not contribute to the real parts but only change slightly the fundamental frequencies. Due to the conservation of the total angular momentum, the matrix $\mathcal{Q}'_0 + \mathcal{Q}'_1$ is singular and one of its eigenvalues is zero. The eigenvalues λ_{AL} and λ_{L}, perturbations of ig_1 and ig_2, respectively, have non-zero negative real parts and both eccentric eigenmodes Lagrange and anti-Lagrange are damped to zero, as with the tides raised on the co-orbitals. Similarly, the real part of λ and $\bar{\lambda}$, perturbations of $i\nu$ and $-i\nu$, are strictly positive, which once again leads to an exponential increase of the libration amplitude of ξ when the system is close to the Lagrangian equilibria L_4 or L_5.

A notable difference with Sect. 6.2.1 resides in the eigenvalue $\nleftarrow$, associated with the rotation of the central planet. While $\nleftarrow_1$ and $\nleftarrow_2$ were large negative in Sect. 6.2.1 (Eq. (6.28)), leading to a quick damping of the rotation rates of the co-orbitals, $\nleftarrow$ is not necessarily negative, and can be of the same order of magnitude as the other eigenvalues' real parts. As a consequence, the rotation of the central planet does not necessarily evolve on timescales much smaller than the timescale of eccentricity damping and libration amplitude pumping. If $\nleftarrow < 0$, then the system converges towards the spin-orbit synchronization[14], while $\nleftarrow > 0$ means that the system diverges away from the spin-orbit synchronization. There exists a critical semimajor axis $\bar{a}_c$ beyond which (*resp.* below which) $\nleftarrow < 0$ and the system is stable (*resp.* $\nleftarrow > 0$ and the system is unstable). According to the value of $\nleftarrow$ in Eq. (6.61), such critical semimajor axis is given by

$$\bar{a}_c = \sqrt{3\alpha_0 \iota^{-1}} R_0. \tag{6.62}$$

[14]Or towards the spin-orbit pseudo-synchronization at non-zero eccentricity.

This result was reached in a completely different manner by Hut (1980). Hut studied a binary system and showed that the Hessian of the Hamiltonian at the equilibrium (circularity, coplanarity and spin-orbit synchronization) is positive-definite if, and only if, $\bar{a} \geq \bar{a}_c$, hence the result[15]. Hut's result can be reformulated equivalently by saying that the spin-orbit synchronization is stable if, and only if, the central planet contains in its rotation at most 1/4 of the system's total angular momentum. In the case of tides raised on the co-orbitals, the eigenvalues λ_1 and λ_2 in Eq. (6.28) are always negative because the co-orbitals, due to their low masses and radii, can never contain in their rotations more than 1/4 of the total angular momentum.

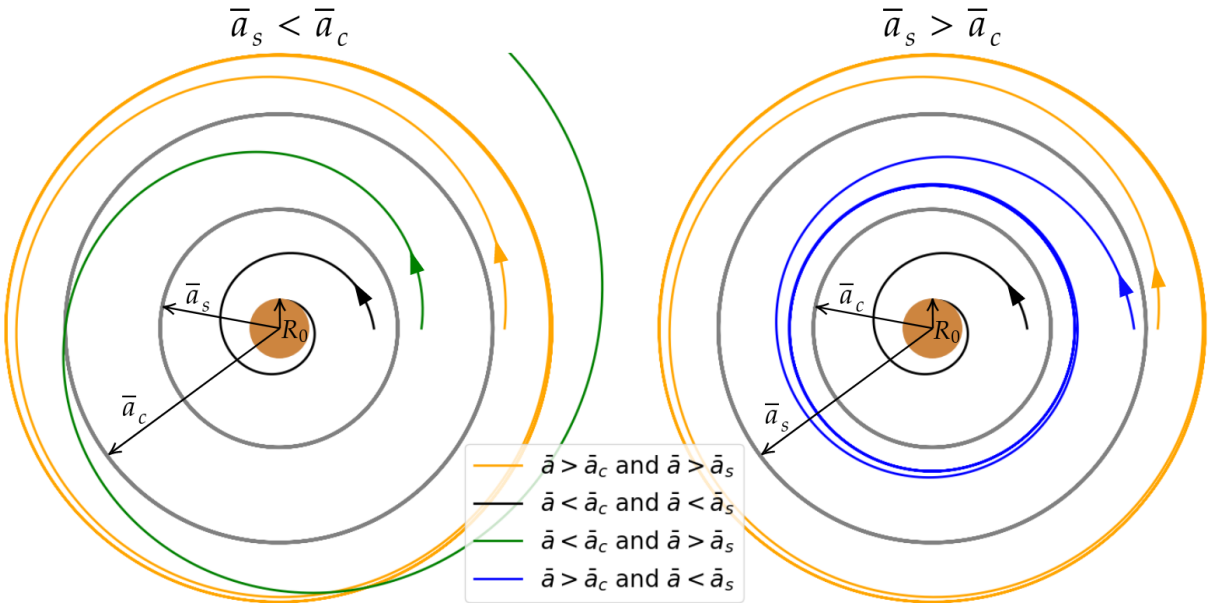

Fig. 6.7 — Schematic representation of the trajectories of the co-orbital satellites in the case of a non-synchronized planet. We distinguish the cases $\bar{a}_s < \bar{a}_c$ (*left*) and $\bar{a}_s > \bar{a}_c$ (*right*). For visibility, the spiraling motion is largely exaggerated and only one co-orbital satellite is represented.

When the ratio ω/η is below 1, then the co-orbitals are in advance (by an angle $(\eta - \omega)\,\Delta t_0$) with respect to the tidal bulges they raise on the central planet. The subsequent torque increases ω and, by conservation of the total angular momentum, decreases the semimajor axes. When $\omega/\eta > 1$, ω decreases while the semimajor axes increase. The ratio ω/η is below 1 (*resp.* above 1) if $\bar{a}$ is smaller (*resp.* greater) than the synchronous semimajor axis $\bar{a}_s$, given by

$$\bar{a}_s = \left(\frac{\mathcal{G} m_0}{\omega^2}\right)^{1/3}. \tag{6.63}$$

Four cases are possible :

- $\bar{a} \leq \bar{a}_c$ and $\bar{a} \leq \bar{a}_s$. The planet's rotation rate is sub-synchronous and $\lambda > 0$: The co-orbitals fall onto the planet.

[15] In Hut's work, the expression of $\bar{a}_c$ features m_0/m_1 instead of $\iota^{-1} = m_0/(m_1 + m_2)$.

- $\bar{a} \leq \bar{a}_c$ and $\bar{a} \geq \bar{a}_s$. The planet's rotation rate is super-synchronous and $\gothic{n} > 0$: The co-orbitals go to infinity.
- $\bar{a} \geq \bar{a}_c$ and $\bar{a} \leq \bar{a}_s$. The planet's rotation rate is sub-synchronous and $\gothic{n} < 0$: The co-orbitals' semimajor axes decrease and stabilize.
- $\bar{a} \geq \bar{a}_c$ and $\bar{a} \geq \bar{a}_s$. The planet's rotation rate is super-synchronous and $\gothic{n} < 0$: The co-orbitals' semimajor axes increase and stabilize.

The situation is illustrated in Fig. 6.7. For the system Saturn−Janus−Epimetheus, we consider $\alpha_0 = 0.22$ (Fortney *et al.*, 2018, Sect. 3.4.2) and a numerical evaluation yields $\bar{a}_c = 1.2 \times 10^4\, R_0$. The critical semimajor axis $\bar{a}_c$ is larger than 12000 Saturn's radii and Janus and Epimetheus are largely below (The rotation of Saturn contains 99.999992 % of the total angular momentum of the system Saturn−Janus−Epimetheus). Since Saturn is super-synchronous ($\omega/\eta = 1.5813$), we expect Janus and Epimetheus' semimajor axes to diverge to infinity under the influence of the tides they raise on Saturn (green plot in Fig. 6.7). Deimos around Mars is also in the green case while Phobos is in the black case and the Moon around the Earth is in the orange case[16].

6.4.4 Characteristic timescales

If, for the considered co-orbital system, the ratio (6.44) is found much larger than unity, then the eigenvalues are given by Eq. (6.61) only. If it is of the order of unity, the eigenvalues given by Eq. (6.28) have to be added to the eigenvalues given by Eq. (6.61). Finally, if the ratio (6.44) is much smaller than 1, only the contributions of Eq. (6.28) need to be considered and the timescales are given by Eq. (6.29). Once the eigenvalues are established, the timescales, defined as the times needed for the associated eigenmodes to be damped or pumped by a factor exp(1), are given by

$$\tau_{\rm lib} = \frac{T}{2\pi\,|\Re\mathfrak{e}\,\lambda|}, \quad \tau_{\rm AL} = \frac{T}{2\pi\,|\Re\mathfrak{e}\,\lambda_{\rm AL}|}, \quad \tau_{\rm L} = \frac{T}{2\pi\,|\Re\mathfrak{e}\,\lambda_{\rm L}|}, \quad \tau_{\rm rot} = \frac{T}{2\pi\,|\Re\mathfrak{e}\,\gothic{n}|}. \tag{6.64}$$

We have $\tau_{\rm lib} = 25\tau_{\rm AL}/12$ and as in Sect. 6.2.2, $\tau_{\rm lib}$ is always of the same order as $\tau_{\rm AL}$ and anti-Lagrange-like system are nearly circular when old. While the ratio $\tau_{\rm AL}/\tau_{\rm L}$ depends on $x = m_1/m_2$ and $y = q_2Q_1/(q_1Q_2)$ in Sect. 6.2.2, where tides were raised on the co-orbitals, it now depends on x alone and reads

$$\frac{\tau_{\rm AL}}{\tau_{\rm L}} = \frac{37}{75} + \frac{28}{75}\frac{(1-x)^2}{x}. \tag{6.65}$$

In Fig. 6.8, we plot the ratio $\tau_{\rm AL}/\tau_{\rm L}$. The equation $\tau_{\rm AL} = \tau_{\rm L}$ has roots $\{x_1, x_2\} = \left\{(47 \pm 5\sqrt{57})/28\right\} \approx \{0.3304, 3.0268\}$. Between the roots, $\tau_{\rm AL} \leq \tau_{\rm L}$ and the system is Lagrange-like, while it is anti-Lagrange-like outside the roots (Sect. 3.2.2). In Sect. 6.2.2, there exists values of x and y such that $\tau_{\rm AL} \ll \tau_{\rm L}$ (red-black regions in Fig. 6.1), and the associated systems are very Lagrange-like and short-lived. Here, the ratio $\tau_{\rm AL}/\tau_{\rm L}$ is never smaller than $37/75 \approx 1/2$ and co-orbital systems are never very Lagrange-like when tides are raised on the central body.

[16] Because of the Sun's perturbations, the Moon will still leave the Earth's Hill sphere.

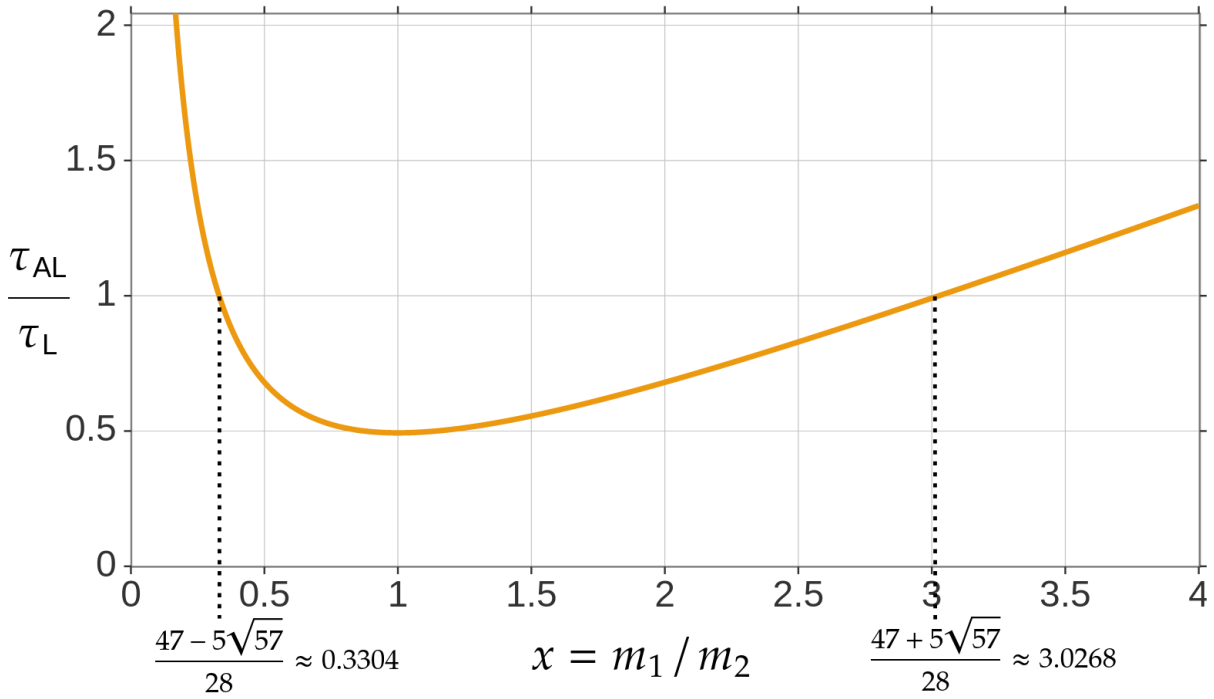

Fig. 6.8 — Value of the ratio τ_{AL}/τ_L as a function of $x = m_1/m_2$. Between (*resp.* outside) the roots of $\tau_{AL}/\tau_L = 1$, the system settles in the Lagrange (*resp.* anti-Lagrange) configuration.

Given the value of $\nleftarrow$ in Eq. (6.61) from Sect. 6.4.3, the timescale τ_{rot} of convergence to, or divergence away from, the spin-orbit synchronization is

- Of the same order of magnitude as the other tidal timescales if $\bar{a} \ll \bar{a}_c$.
- Much larger than the other tidal timescales if $\bar{a} \approx \bar{a}_c$.
- Much smaller than the other tidal timescales if $\bar{a} \gg \bar{a}_c$.

6.5 Conclusion

In this chapter, we extended the work of Chap. 3 by considering tidal dissipation in our model. We first proved that for a co-orbital system star−planet−planet, it is enough to only consider tides raised by the star on the planets and interacted with by the star. We built the pseudo-Hamiltonian of the co-orbital dynamics, including these types of tides, and we gave the complete expression of the averaged equations of motion, at fourth order in eccentricity. We provided three independent verifications of the differential system (6.15), namely, the conservation of the total angular momentum (Sect. 6.1.3), the pseudo-synchronization (Eq. 6.23) and the numerical simulations (Sect. 6.3).

We analytically computed the eigenvalues of the system in the vicinity of the Lagrangian equilibria and we showed that these equilibria are made unstable by tides, leading to the systematic destruction of the system by close encounters. The tidal evolution is essentially dominated by three characteristics timescales. Two of them are responsible for damping the proper modes of the eccentricity and the third one for pumping the libration amplitude of the resonant angle $\lambda_1 - \lambda_2$. The lifetime of the system depends on the

masses, radii, tidal parameters and semimajor axes, and we provided a precise analytical expression that we applied to hypothetical cases in Table 6.1 and to the detection of co-orbital exoplanets in Sect. 6.2.3. From the computation of the eigenvalues, we also concluded that, depending on the parameters, the system can settle along the Lagrange configuration, or along the anti-Lagrange one. The latter configuration is associated with a long lifetime, while the former configuration is associated with a short lifetime.

The validity of the analytical work was established in Sect. 6.3, where we performed numerical simulations of targeted systems, using our model as well as the complete equations of motion of the N-body problem. These simulations show the great reliability of the model, and due to the average over the mean motions, it is η/ν times faster to integrate than the complete equations with similar CPU performances (27 times faster with $\iota = 2 \times 10^{-4}$), while also generating less oscillating curves.

The main achievement of this chapter was to provide an analytical proof of the instability of the Lagrangian equilibria under tides and to give the timescale of destruction. Recently, Dobrovolskis and Lissauer (2022) gave another proof with another model. They consider a restricted problem where one of the co-orbitals, the only one where tides are raised, is massless and point-mass. Although this approach does not allow them to provide a destruction timescale and is limited to the restricted case, it allows them to prove the instability of the Lagrangian equilibria without average over the mean longitudes nor expansion in series of the eccentricities or around the Keplerian resonance.

Finally, we dedicated Sect. 6.4 to the case where tides raised by the co-orbitals on the central body cannot be discarded, as it is the case with a system planet−satellite−satellite made up of small satellites. We provided a complete discussion that allowed us to determine which types of tides need to be taken into account, depending on the type of system. We computed the eigenvalues in the vicinity of the Lagrangian equilibria in the case of tides raised on the central body, and we inferred the associated timescales of tidal evolution. We showed that these tides have a lot of similarities with those raised on the orbiting bodies, as well as some proper characteristics, like the existence of a critical semimajor axis that decides whether or not the spin-orbit synchronization is stable. This last section is important to understand the stability of the co-orbital satellites of Saturn and it will be explored in more details in a forthcoming study.

Chapter 7

Tides in the planar four-body $p : p : p + 1$ resonance chain

Most results of this chapter were first published in Couturier et al. *(2022).*

7.1 Pseudo-Hamiltonian and equations of motion

In this chapter, we push further the work of Chap. 4 on the planar resonance chain $p : p : p + 1$ by removing the point-mass approximation. Tidal dissipation due to the distortion of the extended bodies is hence responsible for long-term changes on the dynamics of the chain. We want here to investigate the effects of tides following the same procedure that we used in Chap. 6, where we studied tides in the resonance chain $1 : 1$. More precisely, we want to

- Establish the pseudo-Hamiltonian of the averaged problem,
- Derive the equations of motion from the pseudo-Hamiltonian,
- Locate the equilibria of the averaged problem and linearize in their vicinity,
- Obtain stability and timescales results from the eigenvalues,
- Check the results given by the eigenvalues with numerical simulations.

The star and three planets have radii R_0 to R_3, respectively, and we use the same notations as in Chaps. 4 & 6.

7.1.1 Pseudo-Hamiltonian

We study a four-body system star−planet−planet−planet and as we justified in Sect. 6.1.1, among the $4\,(4-1)^2 = 36$ tidal contributions as given by Eq. (5.45), only three

of them need to be retained. We thus write the perturbation to the Hamiltonian due to tides as (Eq. (6.2))

$$H_t = \sum_{j=1}^{3} U_t^{(j)} + \sum_{j=1}^{3} T_j, \tag{7.1}$$

where the tidal potential $U_t^{(j)}$ and the kinetic energy of rotation T_j of planet j are given by Eq. (6.3), conserving the same notations[1]. In particular, we reuse the notations $z^\star = z(t-\Delta t_j)$ and $\Delta\varsigma = \varsigma - \varsigma^\star$ defined by Eqs. (6.5) & (6.6). We also denote (Eq. (6.7)) $q_j = \kappa_2^j \wp_j^5$ and in this chapter we have

$$\wp_j = \frac{R_j}{a_j^{(0)}}, \tag{7.2}$$

which coincides with the definition of Chap. 6, $\wp_j = R_j/\bar{a}$, for $j = 1, 2$. We define $\mathcal{R}_j$ similarly as in Eq. (3.20), that is

$$\mathcal{R}_j = \left(\frac{a_j}{a_j^{(0)}}\right)^{1/2} = \frac{\tilde{\Lambda}_j}{\Lambda_j^\star} = C_j \Lambda_j, \tag{7.3}$$

where C_j is defined by Eq. (4.14), $\Lambda_j^\star$ by[2] Eq. (4.5) and Λ_j by Eq. (4.10). In Sect. 6.1.1, we wrote the tidal Hamiltonian H_t in the variables $(J, J_2, X_j; \xi, \xi_2, \bar{X}_j)$, but to be consistent with the work of Chap. 4, we write it here in the variables $(D_j, L, \Gamma, G; \sigma_j, \xi, \xi_2, \xi_3)$, introduced in Sect. 4.1.1. As in Sect. 6.1.1, we normalize the action variable Θ_j' by writing $\Theta_j = \Theta_j'/\Gamma^\star$, where the constant $\Gamma^\star$ is given by Eq. (4.9). In order to only consider the secular (*i.e.* long-term) dynamics, we average $U_t^{(j)}$ over λ_j and $U_t^{(j)}$ depends on this angle through $\Delta\lambda_j$ only. Similarly, $U_t^{(j)}$ depends on θ_j through $\Delta\theta_j$ only. We perform the rescaling given by Eq. (4.10) and at second order in eccentricity, the tidal Hamiltonian $\mathcal{H}_t = H_t/\Gamma^\star$ reads

$$\begin{aligned} \mathcal{U}_t^{(j)} &= -q_j \frac{m_0}{m_j} n_j^{(0)} C_j^{-1} \mathcal{R}_j^{-6} \mathcal{R}_j^{\star -6} \left(A_t^{(j)} + \mathfrak{D}_2^{(j)}\right) = \frac{U_t^{(j)}}{\Gamma^\star}, \\ \mathcal{T}_j &= \frac{C_j n_j^{(0)} \Theta_j^2}{2\alpha_j \wp_j^2} = \frac{T_j}{\Gamma^\star}, \end{aligned} \tag{7.4}$$

where (Eq. (6.9))

$$\mathfrak{D}_2^{(j)} = B_t^{(j)} \left(\mathcal{R}_j^{-1} D_j + \mathcal{R}_j^{\star -1} D_j^\star\right) + \left(\mathcal{R}_j \mathcal{R}_j^\star\right)^{-1/2} \mathfrak{Re}\left(C_t^{(j)} \sqrt{D_j D_j^\star} e^{i\Delta\varpi_j}\right), \tag{7.5}$$

and the coefficient $A_t^{(j)}$, $B_t^{(j)}$ and $C_t^{(j)}$ are given by Eq. (6.10). The total pseudo-Hamiltonian that we consider for the model is then (Eq. (6.11))

$$\mathcal{H} = \mathcal{H}_K(D_j, L, \Gamma, G) + \iota \mathcal{H}_P(D_j, \sigma_j, \xi) + \mathcal{H}_t, \tag{7.6}$$

[1] Do not confuse $\mathcal{C}_j$, defined below Eq. (6.4), with C_j, defined by Eq. (4.14).

[2] For the variables $\Lambda_j^\star$ and $\Gamma^\star$, the superscripted star does not denote the evaluation at time $t - \Delta t_j$ but the value at the Keplerian resonance given by Eq. (4.5).

where $\mathcal{H}_K$ is given by Eq. (4.13), the perturbation $\iota\mathcal{H}_P = \mathcal{H}^{(0)} + \mathcal{H}^{(1)}_{1,3} + \mathcal{H}^{(1)}_{2,3} + \mathcal{H}^{(2)}_{1,2} + \mathcal{H}^{(2)}_{1,3} + \mathcal{H}^{(2)}_{2,3}$ by Eqs. (4.18), (4.19) & (4.20) and (Eq. (6.13))

$$\mathcal{H}_t = \sum_{j=1}^{3} \mathcal{U}_t^{(j)}(\mathcal{R}_j, \mathcal{R}_j^\star, \Delta\xi, \Delta\xi_2, \Delta\xi_3, \Delta\sigma_j, \Delta\theta_j) + \sum_{j=1}^{3} \mathcal{T}_j(\Theta_j). \tag{7.7}$$

The quantity $\mathcal{R}_j$ depends on Λ_j, that is on L, Γ, G and the D_j.

7.1.2 Equations of motion

The equations of motion are derived from the pseudo-Hamiltonian (7.6) using the Hamilton Eqs. (2.18), following the procedure described in Sect. 5.3. The perturbation to the vector field F_0 (derived from the conservative Hamiltonian of Eq. (4.21)), due to tides and at second order in eccentricity, reads

$$\begin{aligned}
\dot{D}_j &= 3n_j^{(0)} D_j \frac{m_0}{m_j} \mathcal{R}_j^{-13} \frac{q_j}{Q_j} \left(12\omega_j + 57\mathcal{R}_j - 76\right), \\
\dot{L} &= 3\eta \frac{m_0}{m_1} \mathcal{R}_1^{-13} \frac{q_1}{Q_1} \left\{\omega_1 \left(\Lambda_1 + 27D_1\right) + \left(3\mathcal{R}_1 - 4\right)\left(\Lambda_1 + 46D_1\right)\right\}, \\
\dot{\sigma}_j &= -\frac{15}{2} n_j^{(0)} \frac{m_0}{m_j} q_j \mathcal{R}_j^{-13}, \\
\dot{\xi} &= \frac{3}{2}\eta \frac{m_0}{m_1} q_1 \mathcal{R}_1^{-13} \frac{4\Lambda_1 + 65D_1}{\Lambda_1} - \frac{3}{2}\eta \frac{m_0}{m_2} q_2 \mathcal{R}_2^{-13} \frac{4\Lambda_2 + 65D_2}{\Lambda_2}, \\
\dot{\Gamma} &= \sum_{j=1}^{3} 3 \frac{n_j^{(0)}}{n_3^{(0)}} n_j^{(0)} \frac{m_0}{m_j} \mathcal{R}_j^{-13} \frac{q_j}{Q_j} \left\{\omega_j \left(\Lambda_j + 27D_j\right) + \left(3\mathcal{R}_j - 4\right)\left(\Lambda_j + 46D_j\right)\right\}, \\
\dot{G} &= \sum_{j=1}^{3} 3n_j^{(0)} \frac{m_0}{m_j} \mathcal{R}_j^{-13} \frac{q_j}{Q_j} \left\{\omega_j \left(\Lambda_j + 15D_j\right) + \left(3\mathcal{R}_j - 4\right)\left(\Lambda_j + 27D_j\right)\right\}, \\
\dot{\omega}_j &= -3n_j^{(0)} C_j \alpha_j^{-1} \wp_j^{-2} \frac{m_0}{m_j} \mathcal{R}_j^{-13} \frac{q_j}{Q_j} \left\{\omega_j \left(\Lambda_j + 15D_j\right) + \left(3\mathcal{R}_j - 4\right)\left(\Lambda_j + 27D_j\right)\right\},
\end{aligned} \tag{7.8}$$

where we posed $\omega_j = \omega_j'/n_j^{(0)}$. Since the differential system does not depend on ξ_2 and ξ_3 and as the dynamics of these fast-circulating angles are of no interest to us, the lines $\dot{\xi}_2$ and $\dot{\xi}_3$ are absent from the differential system (7.8). The system (7.8) only contains the tidal perturbations, and the total differential system that we consider for our model is the one derived from the Hamiltonian (4.21), F_0, to which we add the tidal perturbations (7.8). We denote it $F : \mathbb{R}^{13} \mapsto \mathbb{R}^{13}$.

7.2 Pseudo-equilibria and linearization

7.2.1 The eigenvalues

As explained at the beginning of this section, we want to find the equilibria of F and to study the linearized dynamics in their vicinity. However, although F_0 has many equilibria (Table 4.1), we show that F has none. The last five lines of Eqs. (7.8), those corresponding

to $\dot{\Gamma}$, $\dot{G}$, $\dot{\omega}_1$, $\dot{\omega}_2$ and $\dot{\omega}_3$, cannot all vanish if $D_j \neq 0$. Indeed, if the planets are all synchronized, that is, if the $\dot{\omega}_j$ all vanish[3], then $\dot{\Gamma} < 0$ and

$$\dot{\Gamma} \approx -\sum_{j=1}^{3} 21 \frac{n_{j,0}}{n_{3,0}} n_{j,0} \frac{m_0}{m_j} \frac{q_j}{Q_j} D_j \propto -\sum_{j=1}^{3} \frac{m_0}{m_j} \frac{q_j}{Q_j} e_j^2. \tag{7.9}$$

However, F_0 has no equilibria at $D_j = 0$ (Table 4.1) and does not contribute to these five lines. We thus conclude that F has no equilibria. This result contrasts with the case of co-orbitals without companion, studied in Chap. 6. Indeed, the differential system (6.15), that governs the averaged dynamics of the resonance chain $1:1$ under tidal dissipation, does have equilibria. This is because the conservative part of the differential system (6.15), derived from the Hamiltonian $\mathcal{H}_K + \iota\mathcal{H}_P$ in Eq. (6.11), has equilibria at zero eccentricity, that is, at $D_j = 0$, whereas all the equilibria of F_0 are at non-zero eccentricity.

We call pseudo-equilibrium of F, or pseudo-fixed point of F, a point $\mathfrak{X} \in \mathbb{R}^{13}$ such that $F(\mathfrak{X}) = {}^t\big(0,0,0,0,0,0,0,0,\dot{\Gamma}(\mathfrak{X}),0,0,0,0\big)$. Even though it does not have equilibria, F has pseudo-equilibria, and we find them using an extension of the Newton–Raphson-based algorithm that we developed for Sect. 4.3.2. In the case of the resonance chain $p:p:p+1$, the variable Γ, that many authors refer to as scaling parameter (Michtchenko *et al.*, 2008; Delisle, 2017; Petit *et al.*, 2020), drifts along the branches of pseudo-equilibria of F. In the case of the co-orbital resonance $1:1$ however, the scaling parameter is[4] J_2, and while this quantity drifts at a random point of the phase space, it does not drift along the branches of equilibria of the differential system (6.15).

Equation (7.9) shows that, on a branch of pseudo equilibria of F, the parameter Γ (and thus the parameter δ, see Eq. (4.35)) drifts at a speed proportionnal to the square of the eccentricities. This means that, with tides, the system travels along the main branch from right to left in Fig. 4.2 (Delisle *et al.*, 2014) much more quickly when $\delta > 0$ than when $\delta < 0$ (due to high eccentricities for positive δ). As the system travels, whether or not it stays close to the main branch or moves away depends on the linear stability of the differential system F in the vicinity of the branch. That is, it depends on the real parts of the eigenvalues of the linear system associated with F (Sect. 2.4.1). Since Γ is not constant at the pseudo-fixed points, but drifts at a speed given by Eq. (7.9), computing the eigenvalues of the linearized system makes sense only if Γ drifts slowly enough, that is, only if

$$\left|\dot{\Gamma}\right| \ll \max_{1\leq k\leq 13} \left|\mathfrak{Re}\,\lambda_k\right|, \tag{7.10}$$

where the λ_k are the eigenvalues of the linearized system. Indeed, $|\dot{\Gamma}|^{-1}$ is the timescale of evolution of Γ, while $(\max_{k\leq 13} |\mathfrak{Re}\,\lambda_k|)^{-1}$ is the timescale of tidal evolution. When the criterion (7.10) is fulfilled, Γ can be considered constant on the timescale of tidal evolution, and the real parts of the linearized system have physical meaning.

Branch 3 always has high eccentricities (see Fig. 4.3) and exists only for $\delta > 5.997$. The drift in δ towards negative values is fast at high eccentricity (see Eq. (7.9)), and so branch 3 is tidally very unstable and uninteresting to us. Branch 2 has low values of the eccentricities at large δ, but the existence of a hyperbolic zone at $5.55 \leq \delta \leq 5.80$ (see Table 4.1) makes it uninteresting as well since the drift ensures that this zone is reached. Hence, we limit the study of tidal dissipation to the main branch (branch 1).

[3]Then, $\dot{G}$ also vanishes, since $\dot{G} + \sum_j \alpha_j \mathfrak{P}_j^2 C_j^{-1} \dot{\omega}_j = 0$ by conservation of the total angular momentum.

[4]In a resonance chain, the scaling parameter is the momentum associated with the averaged fast angle.

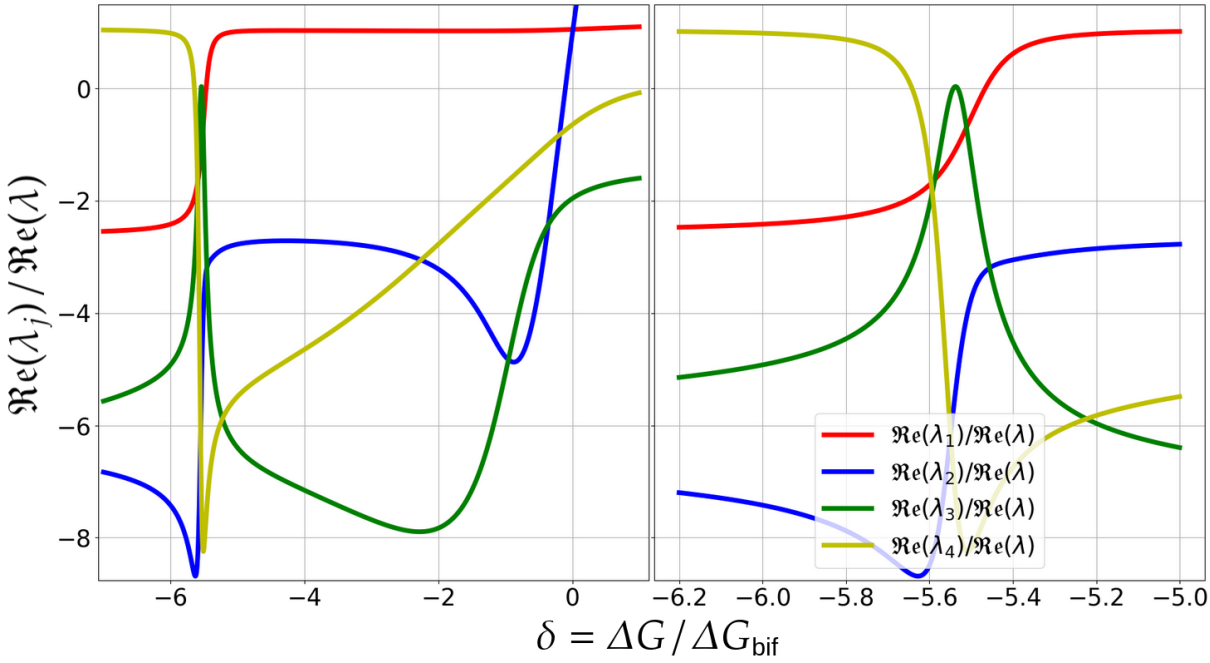

Fig. 7.1 — Real parts of the eigenvalues of the linearized system associated with F in the vicinity of its main branch of pseudo-equilibria, for $-7 \leq \delta \leq 1$ (left) and $-6.2 \leq \delta \leq -5$ (right). The planetary masses are as in Fig. 4.2, the resonance chain is $1:1:2$ and the tidal parameters are those of system 1 in Table 7.1. Only the four eigenvalues (actually eight, counting their complex conjugated) associated with the four degrees of freedom of the conservative system are represented. The five other eigenvalues, associated with the three rotation rates ω_j, with the total angular momentum, and with Γ, are of no interest. The real parts behave erratically at the $1:1$ secular resonance between ν and ν_3 (see Fig. 4.2), in such a way that all of them are negative for $-5.64 \leq \delta \leq -5.47$, yielding a linear stability in this region (Sect. 2.4.1). In the region $\delta \leq 1$ we have $|\dot{\Gamma}|/\Re e\,\lambda \leq 0.012$, and the criterion (7.10) is very well respected. Similar figures with other planetary masses are available in Sect. 7.3.4.

7.2.2 The *linearly stable region*

As explained in Sect. 4.3.1, it is not possible to give analytically the equilibria of F_0, and so a fortiori, it is not possible to give the equilibria of F. Consequently, it is clear that the eigenvalues of the differential system F, linearized in the vicinity of the main branch, cannot be given analytically. In particular, the perturbative approach described in Sect. 2.4.2 is of no help here, since we do not have an analytical expression of a diagonal basis of $\mathcal{M}_0$ in Eq. (2.82). This is a notable difference with the case of the co-orbital resonance $1:1$ for which we were able to give analytical expressions of the eigenvalues with tides (Eq. (6.28)).

We work numerically instead, and in Fig. 7.1 we plot the real parts of the eigenvalues of the linearized system associated with F, along its main branch of pseudo equilibria, which is a little perturbation of the main branch of equilibria of (4.21). To guarantee that the condition (7.10) is well respected, we limit ourselves to $\delta < 1$. This is not really a restriction since tides ensure that this region is quickly reached. Only the eigenvalues that are the extension of Eqs. (4.38) & (3.32) are plotted. In the absence of a third planet, we showed with Eq. (6.28) that the eigenvalue responsible for the exponential increase in the

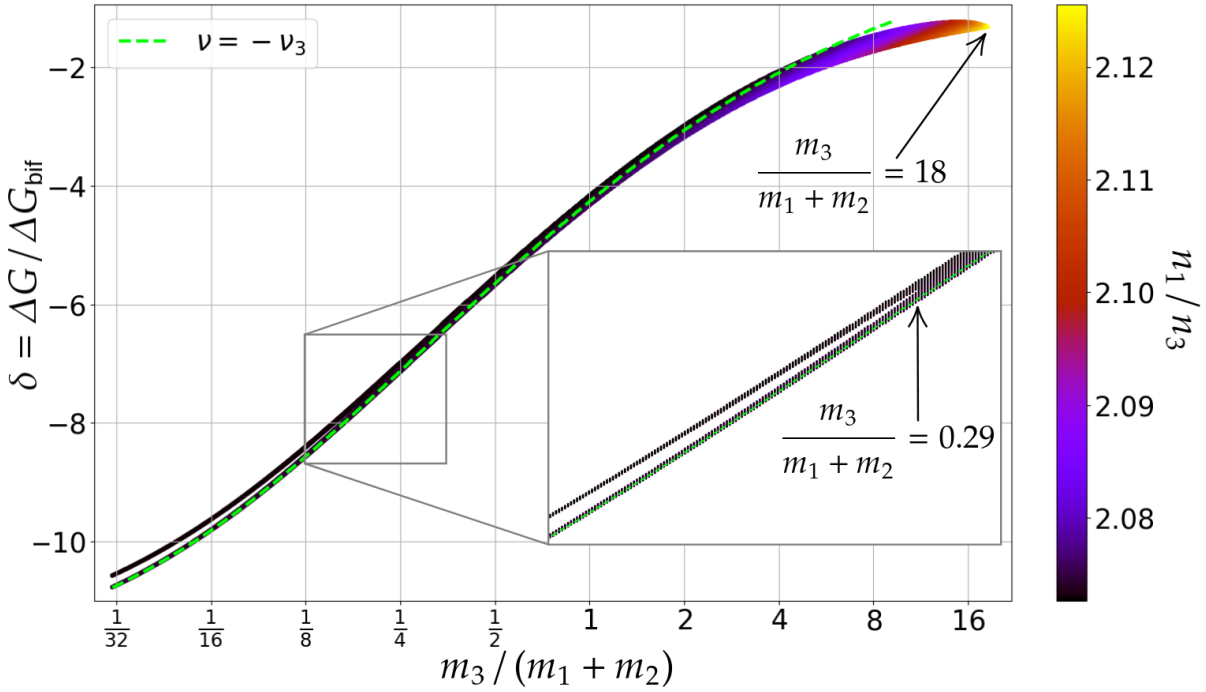

Fig. 7.2 — Position of the *linearly stable region* for the resonance chain $1:1:2$ in the plane (m_3, δ). For every point in this plane the eigenvalues of the linearized system associated with the vector field F are computed, and the point is plotted only if all the real parts are negative (actually, if they all are less than $0.05\,\mathfrak{Re}\,\lambda$). The co-orbital masses are $m_1 = m_2 = 10^{-4}$ and the tidal parameters are those of the system 0 in Table 7.1. The position of the *linearly stable region* weakly depends on m_1/m_2 and on the tidal parameters. The colour gives n_1/n_3 and shows that the chain stabilizes the dynamics far from the Keplerian resonance (for which $n_1/n_3 = 2$). The dashed yellow line plots the secular $1:1$ resonance between ν and ν_3, computed with Eqs. (4.39) and (4.30), respectively. For $m_3 > 18\,(m_1 + m_2)$, the *linearly stable region* disappears, while for $m_3 < 0.29\,(m_1 + m_2)$, two distinct *linearly stable regions* exist, whose widths tend to 0 with m_3.

libration amplitude of ξ, and thus for the destruction of the co-orbital motion, has a real part

$$\mathfrak{Re}\,\lambda = \frac{9}{2}\eta\frac{m_0}{m_1+m_2}\left(\frac{m_1}{m_2}\frac{q_2}{Q_2} + \frac{m_2}{m_1}\frac{q_1}{Q_1}\right), \tag{7.11}$$

and so we normalize by this quantity in Fig. 7.1 and Sect. 7.3.4. The region within $-5.64 \leq \delta \leq -5.47$, at the $1:1$ secular resonance between ν and ν_3 (*i.e.* between the libration frequency of the co-orbitals and the frequency of all the pericentres at the pseudo-equilibria), is such that all the eigenvalues of the system have negative real parts, and we thus expect this region to be linearly stable[5] (Sect. 2.4.1). We show in Sect. 7.3.2 that this is indeed the case. The linear stability is only temporary though, since the drift in δ ensures that this region is eventually left. We call it the *linearly stable region* in the remainder of this work. The range in δ corresponding to the *linearly stable region* strongly depends on the ratio $m_3/(m_1 + m_2)$. In Fig. 7.2 we display its position in the plane (m_3, δ).

[5]Even though it is slightly chaotic far from the main branch, according to the map in Fig. 4.6.

7.3 Numerical simulations

In this section we investigate the ability of our model to predict the behaviour of a system in the $p : p : p+1$ resonance under tidal dissipation. We especially check the results drawn in Sect. 7.2.2 on the linearized dynamics in the vicinity of the main branch and the existence of a *linearly stable region*. In Sect. 7.3.4, we investigate the influence of m_3 on the co-orbital dynamics.

7.3.1 Procedure

We numerically integrate two different sets of equations. The first set, our model, is the differential system F, that is, the vector field F_0 derived from the conservative Hamiltonian (4.21), to which we add the tidal perturbations given by Eqs. (7.8). The second set is a n-body unaveraged and unexpanded model in the regular position-speed coordinates, with the constant-Δt model, given by Eq. (C.13) of appendix C.4.

When the third planet is absent, we showed in Sect. 6.2.2 that the relevant parameters to consider to predict the destruction time of a system of two co-orbital planets are (Eq. (6.2.2))

$$\Omega = \frac{q_1}{Q_1} + \frac{q_2}{Q_2}, \quad x = \frac{m_1}{m_2}, \quad y = \frac{q_2 Q_1}{q_1 Q_2}, \quad \text{and} \quad \iota = \frac{m_1 + m_2}{m_0}, \tag{7.12}$$

namely the total dissipation rate, the co-orbital mass ratio, the dissipation rate ratio, and the planet-to-star mass ratio. Since we are interested in comparing the lifetimes of the co-orbitals when they are inside the resonance chain $1 : 1 : 2$ with their lifetimes when they are alone, we make use of these parameters. As explained in Sect. 7.2.2, we do not have analytical expressions depending on the parameters of the lifetime of the system, and trying to draw a complete picture would require a very large number of simulations. Instead, we are interested in performing a small number of simulations with parameters that we judge interesting. Thus, in order to check the semi-analytical results obtained in Sect. 7.2.2, we only show the evolution of two systems for the chain $1 : 1 : 2$, whose parameters are given in Table 7.1. Nevertheless, we performed additional simulations with different choices for the planetary masses and the initial δ. The most interesting ones are presented in Sect. 7.3.4, where we thoroughly discuss the influence of larger or smaller values for m_3.

For the systems listed in Table 7.1, the chosen value of δ is such that the beginning of the simulations is at the rightmost point of the *linearly stable region*; these regions

#	Ω	x	y	ι	δ
0	4×10^{-12}	1	1	2×10^{-4}	-5.51
1	4×10^{-12}	1/10	100	2×10^{-4}	-5.46

Table 7.1 — Parameters of the two numerical simulations of Figs. 7.3 & 7.4. In this table, the chosen value of δ is that of the maximum of the region where all the real parts are negative, ensuring that the system crosses the whole *linearly stable region*. The rotations rates ω_j are initially synchronized and both sets of parameters verify $m_3/m_0 = 10^{-4}$, $\kappa_2^{(3)} = 0$ and $\bar{a} = 0.02$ AU. System 1 is the system that was used for all the figures in Chap. 4 and Sect. 7.2.

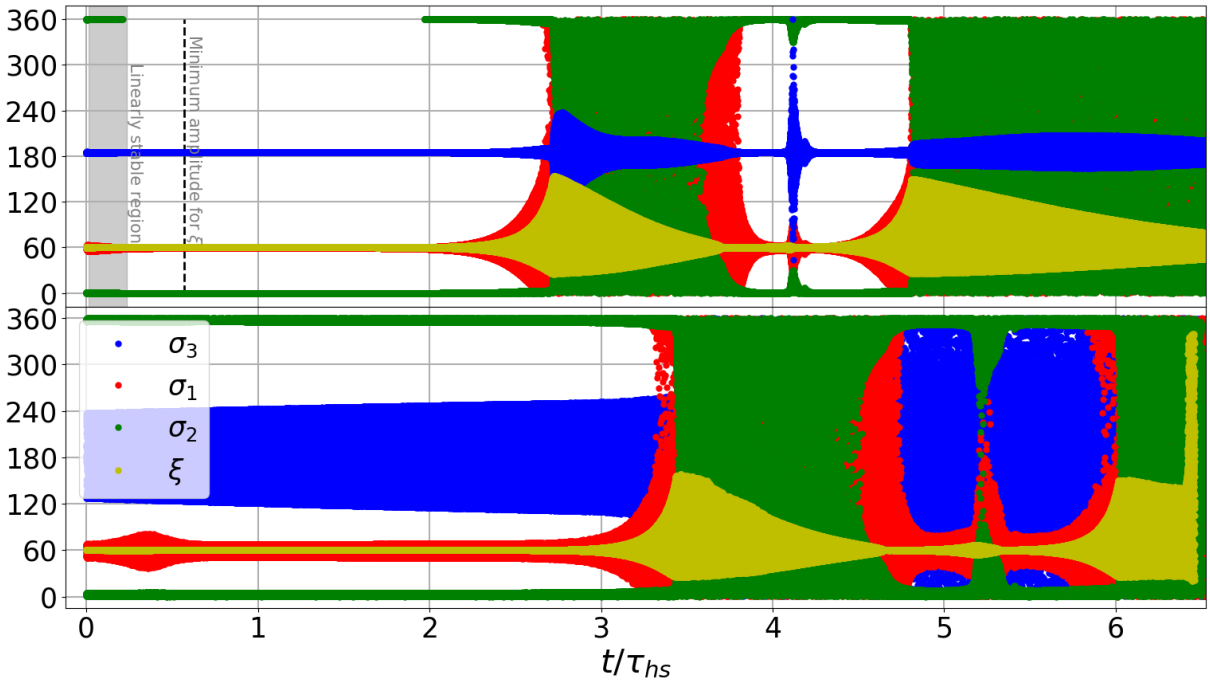

Fig. 7.3 — Evolution of ξ and the σ_j (in arc degrees) as a function of time for system 1 (see Table 7.1) as integrated by the simplified model F (Eqs. (4.21) & (7.8)) (*top*) and the direct n-body simulation (C.13) (*bottom*). In the direct simulation horseshoe-shaped orbits are reached after $6.42\,\tau_{\rm hs}$, and the co-orbital motion is destroyed shortly after that (chaoticity in Fig. 4.6). The model reaches the horseshoe-shaped orbits at $t = 13.1\,\tau_{\rm hs}$. Here, the presence of the chain increases the lifetime of the co-orbitals by a factor of 6.42. The thickness of the lines in the bottom plot (*e.g.* σ_3) is due to the short-period oscillations that were averaged out in the model. The grey-shaded area is the *linearly stable region*, that the system leaves at $t = 0.2\,\tau_{\rm hs}$.

are $-5.67 \leq \delta \leq -5.52$ for system 0 and $-5.64 \leq \delta \leq -5.47$ for system 1 (see Fig. 7.1). These systems are thus expected to be initially very stable until they leave this region (due to the drift in δ, see Sect. 7.2.1).

To integrate the two systems with the simplified model F (Eqs. (4.21) & (7.8)), we find, for the given value of δ and the planetary masses, the position of the fixed point of F_0 along the main branch, and use it as initial condition for the integration, with a shift $\Delta\xi = 0.1°$ in ξ, in order to not start exactly at the fixed point. The pseudo-fixed point of F is very close to the fixed point of F_0, and we ignore the difference. To integrate the system with the complete n-body set of Eqs. (C.13), we find, for the given value of δ and the planetary masses, the position of the *libration centre* along the main branch with the algorithm described in Sect. 4.2.2, and use it as the initial condition for the integration, again with the shift $\Delta\xi = 0.1°$.

7.3.2 Increased co-orbital life inside the resonance chain

When the co-orbital planets are alone, the positivity of $\mathfrak{Re}\,\lambda$ in Eqs. (7.11) & (6.28) ensures that the system systematically reaches the horseshoe-shaped orbits and is destroyed by close encounters (Fig. 6.3). In this case the time $\tau_{\rm hs}$ needed to reach the horseshoe-shaped orbits is given by Eq. (6.40), while the time $\tau_{\rm dest}$ until destruction is close to $\tau_{\rm hs}$ for a

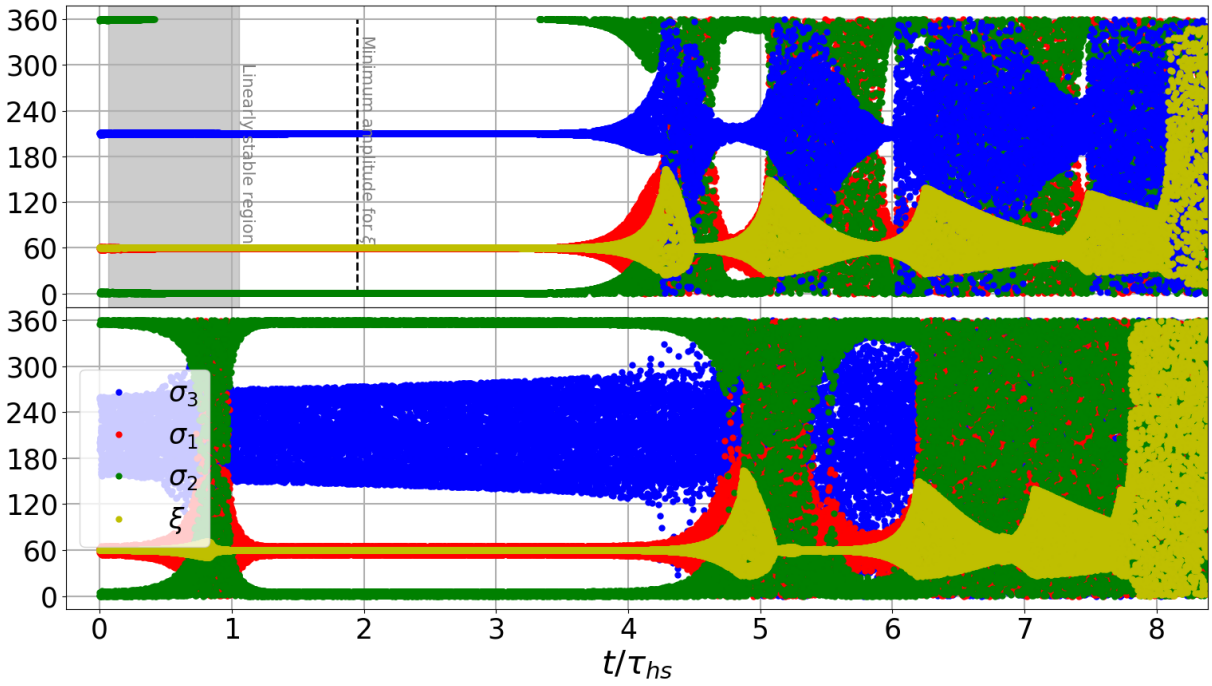

Fig. 7.4 — Evolution of ξ and the σ_j (in arc degrees) as a function of time for system 0 as integrated by the simplified model F (Eqs. (4.21) & (7.8)) (*top*) and by the direct n-body simulation (C.13) (*bottom*). In the direct simulation the horseshoe-shaped orbits are reached after $7.8\,\tau_{\rm hs}$, and the co-orbital motion is destroyed shortly after that (chaoticity in Fig. 4.6). The model reaches horseshoe-shaped orbits at $8.1\,\tau_{\rm hs}$. The grey-shaded area is the *linearly stable region*, that the system leaves at $t = 1.05\,\tau_{\rm hs}$.

large range in ι (Sect. 6.2.3), and we approximate $\tau_{\rm hs} \sim \tau_{\rm dest}$. In order to better compare the co-orbital lifetime inside and outside the chain $p : p : p+1$, we normalize the time by $\tau_{\rm hs}$ in Figs. 7.3, 7.4, 7.5, and in Sect. 7.3.4.

In Figs. 7.3 and 7.4 we plot the angles ξ and σ_j as a function of time. The system spends a large amount of time close to the main branch of equilibria, which allows the co-orbitals to live notably longer with the presence of the third planet. This can be seen from the destruction occurring at a time $t > \tau_{\rm hs}$. When the system crosses the *linearly stable region*, the libration amplitude of ξ decreases instead of increasing exponentially, since the real parts of all the eigenvalues of the linearized system associated with F are negative. When the system leaves this region due to the drift in δ and the real part of one eigenvalue becomes positive again, the libration amplitude of ξ is much smaller than it was before entering the *linearly stable region*. As a result, the system needs more time to reach large libration amplitudes and settle in horseshoe-shaped orbits, which delays the co-orbital destruction; in other words, crossing the *linearly stable region* while being sufficiently close to the main branch (so that the linear dynamics dominate) guarantees a co-orbital lifetime longer than without the third planet.

In Fig. 7.3, the negative real parts of all the eigenvalues in the *linearly stable region* allow the libration amplitude of ξ to reach values as small as 1.8 arcseconds at $t = 0.57\,\tau_{\rm hs}$. This minimum happens after the *linearly stable region* is left since the proper mode associated with the newly positive real part (in yellow in Fig. 7.1) has been completely damped by the *linearly stable region* and some time is needed to pump it noticeably.

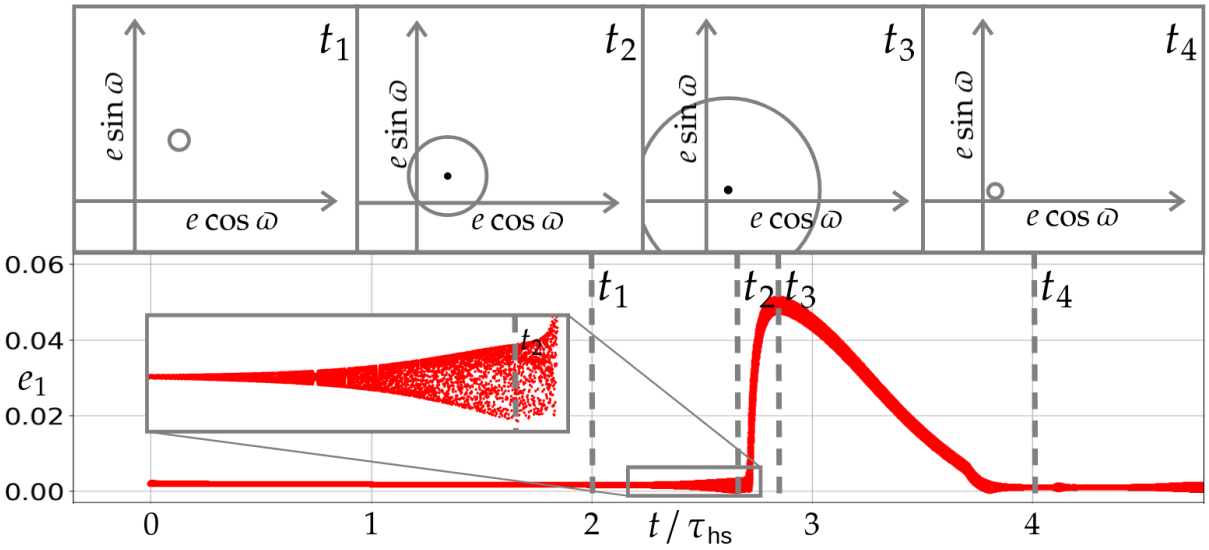

Fig. 7.5 — Value of e_1 as a function of time for system 1 in Table 7.1, as integrated by the simplified model F (Eqs. (4.21) & (7.8)) (*bottom*), and a schematic representation of the eccentricity vector $e_1 e^{i\varpi_1}$, for four particular times (*top*). The schema explains the different stages of the *eccentricity damping stabilization* mechanism. The drift in δ brings the centre of the circle drawn by $e_1 e^{i\varpi_1}$ (equilibrium value of e_1 along the main branch) closer to the origin (see Fig. 4.2).

Similarly, in Fig. 7.4, 3.5 arcseconds of libration amplitude are reached at $t = 1.95\,\tau_{\mathrm{hs}}$. In the bottom panel of Fig. 7.7 from Sect. 7.3.4, we display the important damping of ξ. The early augmentation of the libration amplitude of the angles in the bottom plot is due to the fact that in the complete simulation (C.13), the *linearly stable region* is not exactly at the same values of δ as in the simplified model.

7.3.3 The *eccentricity damping stabilization* mechanism

The *linearly stable region* is not the only reason why co-orbitals in resonant chains can live longer. Another phenomenon, which we refer to as *eccentricity damping stabilization* in the rest of this work, allows the libration amplitude to not cross the separatrix leading to horseshoe-shaped orbits. After an exponential increase in the libration amplitudes of ξ and σ_j, due to at least one eigenvalue with a strictly positive real part, the amplitudes suddenly decrease and the system returns close to the equilibria. This stabilization of ξ, due to eccentricity damping (see Fig. 7.5), can happen several times before horseshoe-shaped orbits are finally reached, and the system is destroyed (see Fig 7.4).

The explanation of the *eccentricity damping stabilization* relies on the behaviour of the eccentricities. In Fig. 7.5, we plot the eccentricity e_1 of planet 1 as a function of time, together with a schema of its behaviour in the plane $(e\cos\varpi, e\sin\varpi)$. At time $t = t_1$ the system is still close to the fixed points, hence the quantity $e_1 e^{i\varpi_1}$ (or any of the two other eccentricities) describes a circle of small radius. Outside the *linearly stable region*, the eigenvalues of the linearized systems have one positive real part, and as time evolves the radius of the circle grows, while its centre, the equilibrium position of $e_1 e^{i\sigma_1}$, gets closer to the origin due to the drift in δ (the eccentricities are smaller on the main branch at

small δ-values, see Fig. 4.2). At time $t > t_2$ the circle $e_1 e^{i\varpi_1}$ surrounds the origin and keeps growing, as predicted by the eigenvalues, which triggers a jump in the eccentricity. On the one hand, the linearized system predicts that the circle drawn by $e_1 e^{i\varpi_1}$ grows to infinity; on the other hand, tides impose an exponential decay of the eccentricities. Indeed, the first line of Eqs. (7.8) yields (Correia, 2009)

$$\dot{e}_j = -\frac{e_j}{\tau_j}, \qquad \tau_j = \frac{2}{21}\frac{m_j}{m_0}\frac{Q_j}{q_j}\frac{1}{n_j^{(0)}}, \tag{7.13}$$

and so, at time $t = t_3$, the circle reaches its maximum radius, the system is now far from its equilibrium, and tides, through non-linear contributions of the vector field F, force the eccentricities to decrease. At $t = t_4$, the system has returned into the vicinity of the main branch, where the libration amplitude of the σ_j, but also of ξ, is small. In Figs. 7.3 and 7.4, several occurrences of the *eccentricity damping stabilization* prevent the angle ξ from reaching the horseshoe-shaped orbits and increase the lifetime of the co-orbital planets.

While the stability induced by the *linearly stable region* comes from linear contributions of the vector field F, the *eccentricity damping stabilization* comes from non-linear contributions. This latter mechanism works thanks to a strong coupling between the eccentricities $(D_j; \sigma_j)$ and the co-orbital angle $(L; \xi)$. In the region $\delta < 0$ (tidally interesting), at most one eigenvalue has a positive real part (see Fig. 7.1), but due to the coupling, it allows an exponential growth of the libration angle ξ, as well as the eccentricities, which makes the *eccentricity damping stabilization* possible. When the time $t = t_3$ is reached, the coupling ensures that the eccentricity damping also induces a damping of the libration angle ξ, hence the stabilization of the co-orbital motion. In the absence of the third planet, we showed in Sect. 6.2.1 that the eccentricities are uncoupled from the co-orbital angle ξ (the matrix $\mathcal{Q}_0 + \mathcal{Q}_1$ is block diagonal). This means that the positive real part $\mathfrak{Re}\,\lambda$ (Eqs. (7.11) & (6.28)) associated with $(L; \xi)$ does not induce an exponential growth of the eccentricities, which are on the contrary damped to 0 due to the negative real parts of their eigenvalues. In this case, because of the decoupling, even if some other mechanism increases the eccentricities, the eccentricity damping predicted by Eq. (7.13) still occurs, but it does not induce a stabilization of ξ.

The occurrence of the *eccentricity damping stabilization* is not systematic. It occurs only if the time $t = t_3$ happens before the co-orbital planets reach horseshoe-shaped orbits. If not, the co-orbital configuration is destroyed before the exponential decrease in the eccentricities can save it. Figures 7.8 & 7.9 from Sect. 7.3.4 give examples of systems where the *eccentricity damping stabilization* fails (systems 3, 4 and 6 in Table 7.2). Deciding whether or not a given system will be saved by the *eccentricity damping stabilization* requires to know the proper modes of the linearized system associated with F and how $(L; \xi)$ and the $(D_j; \sigma_j)$ are written in the corresponding diagonal basis. Only a numerical work is possible, and we did not undertake it since it is much easier to simply run the corresponding numerical simulation.

If a larger initial δ-value is chosen in these simulations, the system initially has at least one positive real part and moves away from the fixed point at exponential speed. If the *eccentricity damping stabilization* works, or if the initial δ-value is small enough, the *linearly stable region* is reached. However, if the system reaches the *linearly stable region* when it is too far from the equilibria, the non-linear contributions of F, combined with the chaotic motion induced by the $1:1$ secular resonance between ν and ν_3 (see

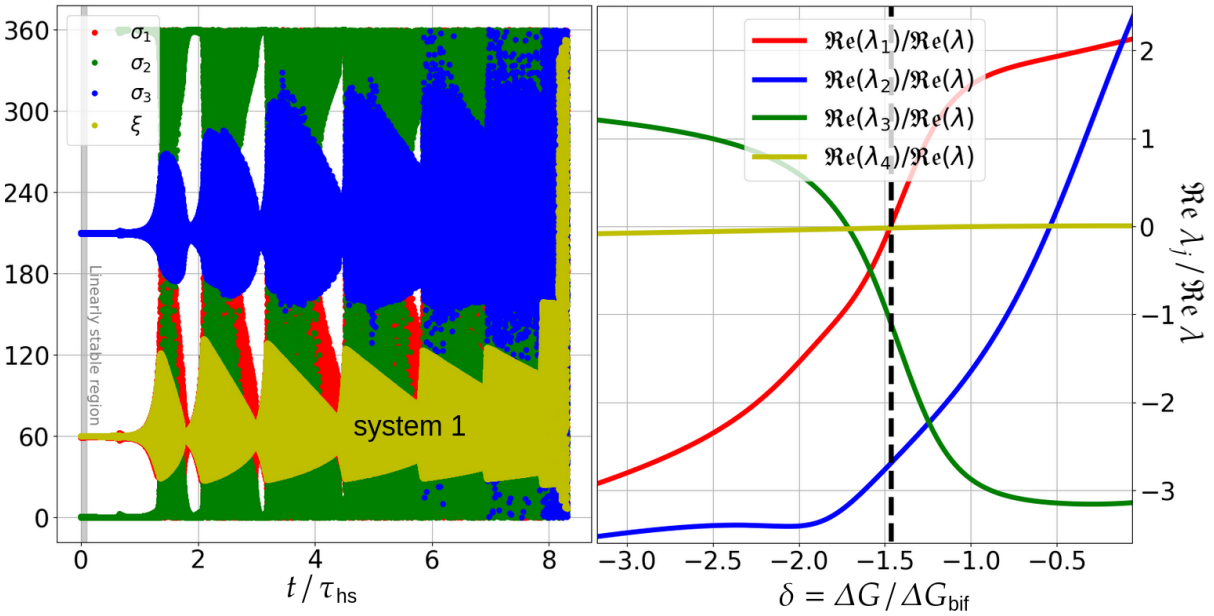

Fig. 7.6 — Evolution of ξ and the σ_j for $m_3 = 8\,(m_1 + m_2)$ (*left*) and real parts of the eigenvalues in the vicinity of the main branch (*right*).

the stability map in Fig. 4.6), can lead to peculiar orbits (*e.g.* switching between the Lagrangian equilibria L_4 and L_5, that is, a permutation of the co-orbitals). Entering the *linearly stable region* while still close enough to the equilibria ensures a convergence towards the main branch, and thus an increased stability.

It can be seen in Fig. 4.5 that for $\delta = -5.46$ the system is already far from the exact resonance. For system 1 at $\delta = -5.46$, we have $n_1/n_3 = 2.072$. As time goes by, δ drifts towards more negative values, and at $t = 6.42\,\tau_{\rm hs}$, when it is about to reach horseshoe-shaped orbits and be destroyed, system 1 verifies $\delta = -13.77$ and $n_1/n_3 = 2.186$. Similar considerations are valid for system 0, which means that the system is already outside the resonance, but it is still influenced by the chain. As the system leaves the resonance due to the drift in δ, the coupling between the eccentricities and ξ becomes weaker, meaning that the *eccentricity damping stabilization* ends up failing, although it can still work for values of n_1/n_3 as high as 2.6. This prevents the co-orbitals from living forever. Only positive values of δ allow for n_1/n_3 a value close to $(p+1)/p = 2$ (see Fig. 4.5). When a positive value of δ is chosen at $t = 0$, the quick drift in δ due to the high values of the eccentricities (Eq. (7.9)) forces the system to reach the region $\delta < 0$ on a timescale generally shorter than $1/\mathfrak{Re}\,\lambda$, where it can be saved by the *linearly stable region*. For systems on the main branch, this means that tides favour for the ratio n_1/n_3 values above their Keplerian value. This result was shown by Delisle *et al.* (2014) for a two-planet chain and is confirmed by the observations of the Kepler mission, where a large number of exoplanets were discovered with a mean motion ratio slightly higher than $(p+1)/p$ (*e.g.* Delisle and Laskar, 2014).

This section shows that our averaged model (Eqs. (4.21) & (7.8)) is able to satisfyingly predict the tidal evolution of a resonance chain of the form $p : p : p+1$, at least qualitatively, since a precise quantitative description can only be achieved by running the simulation of the complete set of Eqs. (C.13). This contrasts with the 1 : 1 mean motion resonance

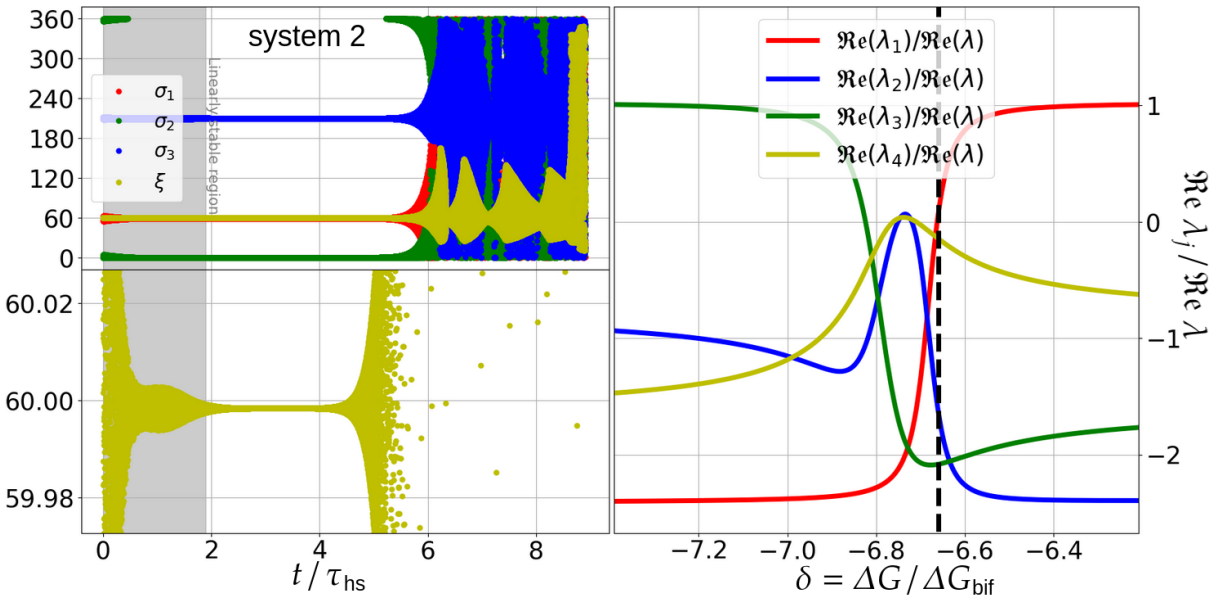

Fig. 7.7 — Evolution of ξ and the σ_j for $m_3 = 0.29\,(m_1 + m_2)$ (*left*) and real parts of the eigenvalues in the vicinity of the main branch (*right*).

alone, that we studied in Chap. 6, where the secular model is able to quantitatively predict the outcome of the complete simulations of the unaveraged system with less than 1% relative error (Fig. 6.3 & Table 6.3).

7.3.4 Influence of the mass of the third planet

In this section, we present the six most interesting simulations that were not shown earlier in Sect. 7.3. We particularly focus on the influence of the mass m_3 on the co-orbital dynamics. All the simulations comply with $m_1 = m_2 = 10^{-4}\,m_0$, and their tidal parameters are those of system 0 in Table 7.1. We only integrate here the simplified model F (Eqs. (4.21) & (7.8)), defined at the end of Sect. 7.1.2.

For each simulation, the real parts of the eigenvalues of the linearized system associated with F are shown alongside the time evolution of the angles ξ and σ_j. In the figures of the real parts, a dashed vertical black line shows the starting value of δ of the corresponding simulation. In the figures of the angles, a grey-shaded area shows the *linearly stable region*, when relevant. Choosing other tidal parameters does not significantly modify the figures shown here, since we normalize the real parts by $\mathfrak{Re}\,\lambda$ (Eqs. (7.11) & (6.28)) and the times by $\tau_{\rm hs}$ (Eq. (6.40)), which is the time to reach horseshoe-shaped orbits (close to the destruction time) in the absence of a third planet (Sect. 6.2.3). The mass of the third planet, m_3, and the value of δ at $t = 0$, denoted by δ_0, are the only two varying parameters between the different simulations, and these two quantities are also the axes of Fig. 7.2 that displays the *linearly stable region*. The parameters m_3 and δ_0 of the six systems integrated here are given in Table 7.2. For each δ_0 and m_3, the simulation starts at the corresponding point of the main branch, with a shift $\Delta\xi = 0.1°$ to ξ, in order not to start exactly at the equilibrium.

In Fig. 7.6, we have $m_3 = 8\,(m_1 + m_2)$, which corresponds to the value yielding the largest *linearly stable region* (Fig. 7.2). However, for this choice of m_3, the *linearly stable*

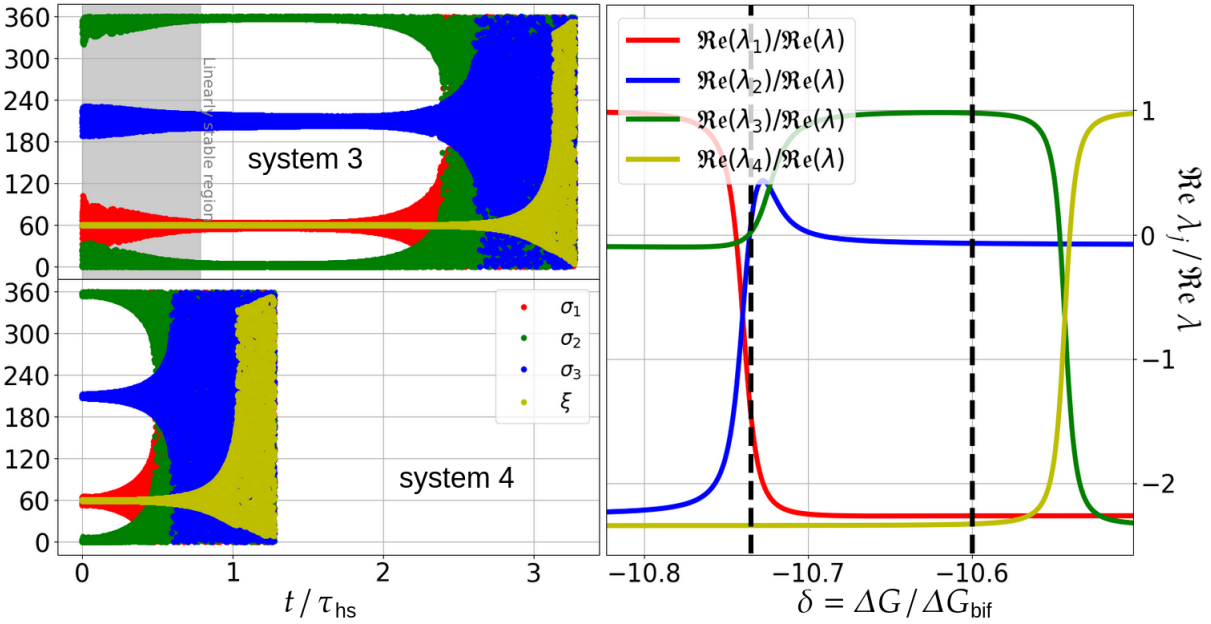

Fig. 7.8 — Evolution of ξ and the σ_j for $m_3 = (m_1+m_2)/32$ (*left*) and real parts of the eigenvalues in the vicinity of the main branch (*right*).

region is located at larger values of δ, which then drifts quickly (Sect. 7.2.1). Furthermore, Eq. (7.9) shows that the drift in δ is proportional to $\sum_j m_j^{2/3}$, and so, a rather large m_3-value is responsible for a quicker drift. Despite the *linearly stable region* being thickest for this value of m_3, system 1 leaves it after less than $0.1\,\tau_{hs}$, much more quickly than in Fig. 7.7, where m_3 is smaller. The amplitude of libration of ξ, $\Delta\xi = \max(\xi - \xi_{eq})$, reaches 0.07° at its lowest, not significantly smaller than its initial value of 0.1°. However, for this choice of m_3, the *eccentricity damping stabilization* is very efficient and occurs seven times, yielding a co-orbital lifetime of $8\,\tau_{hs}$.

In Fig. 7.7, we have $m_3 = 0.29\,(m_1+m_2)$, which is the best compromise between the width of the *linearly stable region* and the speed of the drift in δ. System 2 stays in this region for nearly $2\,\tau_{hs}$, 20 times longer than system 1 in Fig. 7.6. The *linearly stable region* is so efficient that at $t = 3.2\,\tau_{hs}$, the libration amplitude of ξ reaches $\Delta\xi = 4$ milliarcseconds, gaining a factor $\sim 80\,000$ from the initial $\Delta\xi = 0.1°$. The system stays close to the main branch for $6\,\tau_{hs}$, which is longer than any other simulation that we performed. We also display in Fig. 7.7 a zoomed-in view of ξ close to the main branch to better visualize the damping of its libration amplitude. At time $t \sim 1\,\tau_{hs}$, $\Delta\xi$ temporarily stops decreasing and even slightly increases. Indeed, for this value of m_3, the *linearly stable region* splits into two distinct strips (Fig. 7.2), and in the middle of the region, the

	1	2	3	4	5	6
$m_3/(m_1+m_2)$	8	0.29	1/32	1/32	22	22
δ_0	−1.466	−6.66	−10.735	−10.6	−1.3	−7.4

Table 7.2 — Parameters of the six systems integrated in Sect. 7.3.4. All six systems verify $m_1 = m_2 = 10^{-4}\,m_0$, and their tidal parameters are those of system 0 in Table 7.1.

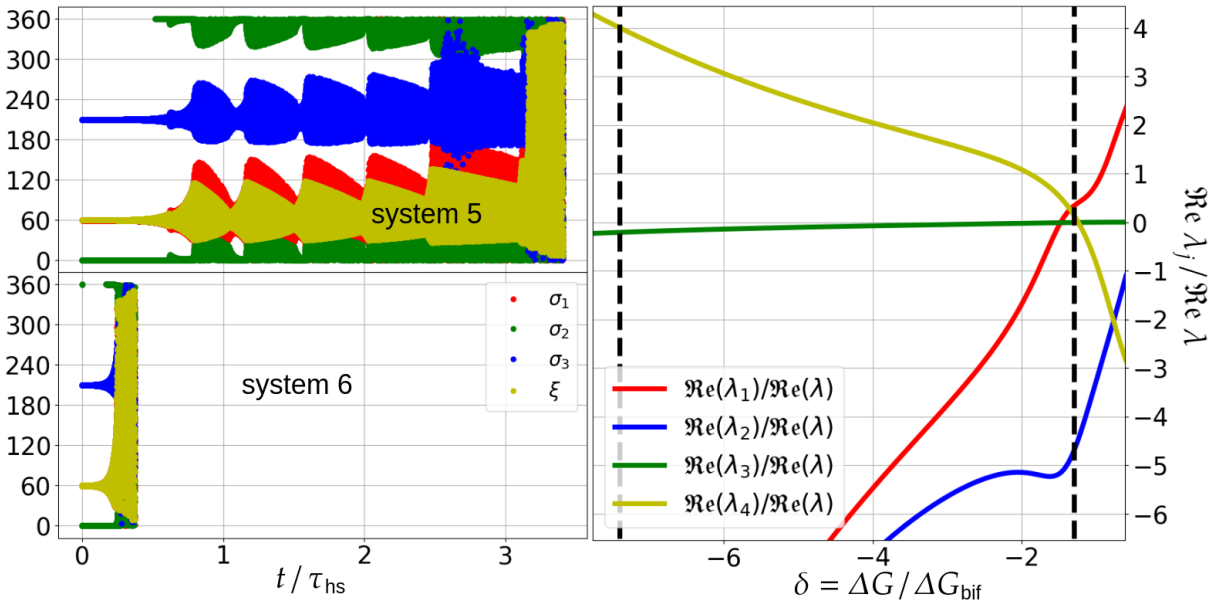

Fig. 7.9 — Evolution of ξ and the σ_j for $m_3 = 22\,(m_1 + m_2)$ (*left*) and real parts of the eigenvalues in the vicinity of the main branch (*right*).

real part of λ_2 (the blue eigenvalue in Fig. 7.7) temporarily becomes slightly positive and reaches $0.067\,\mathfrak{Re}\,\lambda$. This is in perfect agreement with the slight increase observed for $\Delta\xi$. The *eccentricity damping stabilization* is not as efficient as it was for system 1, but still allows the system to reach $8.5\,\tau_{\rm hs}$ before the destruction of the co-orbital motion.

In Fig. 7.8, we have $m_3 = (m_1 + m_2)\,/32$. With such a low mass for the third planet, the two *linearly stable regions* are extremely narrow, and the linear stability occurs only if the system is exactly at the $1:1$ secular resonance between ν, the libration frequency of ξ (Eq. (3.32)), and ν_3, the precession frequency of the ϖ_j (Eq. (4.30)). With such a tiny difference on δ_0, the initial conditions between system 3 and system 4 are very close, but the outcomes are completely different, as system 3 lives three times longer than system 4. Outside the $1:1$ secular resonance between ν and ν_3, the unique positive real part is equal to $\mathfrak{Re}\,\lambda$ and the horseshoe-shaped orbits are reached at $\tau_{\rm hs}$ exactly, as in the absence of the third planet. This is consistent with the small value of m_3. The *eccentricity damping stabilization* fails for both systems.

In Fig. 7.9, the third planet has a mass $m_3 = 22\,(m_1 + m_2)$ and the *linearly stable region* does not exist (Fig. 7.2). We perform a simulation at the $1:1$ secular resonance between ν and ν_3, where it would have been if it existed. In this region the positive real parts are not greater than $\mathfrak{Re}\,\lambda$, and with the action of the *eccentricity damping stabilization*, system 5 is destroyed after more than $3\,\tau_{\rm hs}$. However, system 6 is very far from the Keplerian resonance and λ_4 (the yellow eigenvalue in Fig. 7.9) has a real part $4\,\mathfrak{Re}\,\lambda$. This means that this system reaches the horseshoe-shaped orbits after a time $\tau_{\rm hs}/4$ only. Furthermore, since (L, ξ) and (D_j, σ_j) are weakly coupled far from the Keplerian resonance, the *eccentricity damping stabilization* fails, leading to a very premature destruction of the co-orbital motion (the co-orbitals would have lived four times longer without the third planet). Choosing a smaller δ or a larger m_3 leads to an even quicker destruction.

In this subsection, we showed that the *linearly stable region* is most efficient in

preventing the destruction of the co-orbitals at low to intermediate values of m_3, while the *eccentricity damping stabilization* works best at moderately large values of m_3, especially if the system is not too far from the Keplerian resonance (δ not too negative). Generally, a first-order mean-motion resonance with an outward third planet either increases or does not change the co-orbital lifetime. The third planet can nevertheless lead to a premature destruction if it is much more massive than the co-orbitals and far from the mean-motion resonance.

7.4 Discussion and conclusion

In this chapter we pushed further the study of the resonance chain $p:p:p+1$, started in Chap. 4, where an outer third planet is in a first-order mean motion resonance with the pair of co-orbital planets. We took into account dissipation due to tides and we built the pseudo-Hamiltonian of the problem, from which we derived the complete expression of the averaged equations of motion, at second order in eccentricity.

In the conservative case, the secular $1:1$ resonance between the libration frequency of the co-orbital angle and the precession frequency of the pericentres tends to destabilize the chain by chaoticity. When tidal dissipation is involved though, we showed that this secular resonance greatly stabilizes the chain by making negative the real part of the eigenvalues in the vicinity of the main branch of equilibria. This negativity of the real part is responsible for the existence of a value for n_1/n_3, close to the secular resonance, around which the libration amplitude of the co-orbital angle $\lambda_1 - \lambda_2$ is damped to zero. As a consequence, the lifetime of the co-orbital pair is noticeably longer with the presence of the third planet. For the chain $1:1:2$, this linear stability generally occurs near $n_1/n_3 \sim 2.07$. Another stabilization mechanism, due to eccentricity damping, is presented and explained. The model that we built is able to predict the position of the *libration centres* of the complete system. When tides are involved, the model reliably gives the qualitative behaviour of the system and, to a certain extent, its quantitative behaviour. This work shows that when tidal dissipation is included, co-orbital systems are more stable if they are inside a resonance chain of the form $p:p:p+1$, rather than alone, which increases the chances of a future detection of a co-orbital pair of exoplanets.

One important contribution of the work done in Chaps. 4 & 7 is the discovery of the $1:1$ secular resonance between the libration of $\lambda_1 - \lambda_2$ and the precession of the pericentres, as well as the inherent dynamical consequences (Figs. 4.6 & 7.1). *Libration centres* correspond to periodic orbits of the unaveraged problem that generalize the equilibria of the averaged model. They are such that all the pericentres precess at the same frequency in their vicinity, a result that holds true for every resonance chain of any number of planets. We thus expect, for other resonance chains, the existence of similar secular resonances, for example between $\xi = \lambda_1 - 4\lambda_2 + 3\lambda_3$ and the ϖ_j for the chain $1:2:3$.

We proved that tides are responsible for the system traveling towards the left of the main branch in Fig. 4.2. In our model, we only considered the secular contributions due to the resonance $p:p+1$ (Eqs. (4.19) & (4.20)), which means that the main branch is asymptotic to the horizontal axis and goes up to $\delta = -\infty$. However, Malhotra (2022) showed than the main branch of the resonance $p:p+1$ is connected to the branch 2

(the other elliptic branch of Fig. 4.2) of the resonance $p-1:p$. Under the action of the *linearly stable region* (Sect. 7.2.2) and the *eccentricity damping stabilization* (Sect. 7.3.3), it is possible, with some choices of the parameters, that before the destruction of the co-orbital configuration, tides allow the system to reach the branch 2 of the $p:p:p+1$ resonance, while traveling from the main branch of the $p+1:p+1:p+2$ resonance. We did not investigate this scenario here.

Chapter 8

Conclusions

8.1 Overview

In this thesis manuscript, we studied the dynamics of the co-orbital motion with a particular focus on the secular perturbations due to tides and mean-motion resonance with a third planet. As our work makes heavy use of the mathematical theory of celestial mechanics, we recalled the main parts of this theory in Chap. 2. We rederived in Chap. 3 the important analytical results describing the point-mass $1:1$ mean-motion resonance. In particular, we studied there the circular and eccentric dynamics of the co-orbital pair, which allowed us to define and explain notions that were essential later in the manuscript. Chapter 3 also contains work original to this thesis and in particular, we showed how perturbations due to general relativity cannot perturb the co-orbital motion in the same way as tides do.

We considered once again the point-mass approximation in Chap. 4, where we switched from a three-body problem to a four-body problem by adding a third planet to the planetary system. We chose to put the third planet in a first order mean-motion resonance with the co-orbital pair in order to study the dynamics of a co-orbital pair perturbed by a resonance chain. As the third planet was exterior to the co-orbital pair, we studied a resonance chain of the form $p:p:p+1$, for any integer p. Chapter 4 showed us that on certain aspects, the dynamics of the point-mass $1:1$ resonance is similarly to that of the $p:p:p+1$ resonance chain, as simplifications allow the dynamics of the librating angle $\lambda_1 - \lambda_2$ to be uncoupled from the rest of the dynamics. Nevertheless, we also discovered specificities inherent the the chain $p:p:p+1$, like the existence of a secular $1:1$ resonance between the precession frequency of the pericentres and the libration frequency of the angle $\lambda_1 - \lambda_2$. The vicinity of this secular resonance can make the trajectories of the system chaotic and we suspect that it exists for other resonance chains.

In order to properly deal with tidal dissipation, we dedicated the entire Chap. 5 to revise the main theory on tides. We redefined there important tidal quantities like the Love numbers and the quality factor, and we studied the tidal models associated with

different rheologies. In particular, we showed how the choice of the constant-Δt tidal model allows the equations of motions to be derived from a pseudo-Hamiltonian, as if tides were a conservative perturbation.

In Chaps. 6 & 7, we included tides in the analytical models built in Chaps. 3 & 4, respectively. In Chap. 6, we linearized the equations of motion in the vicinity of the Lagrangian stable equilibria and an analysis of the real parts of the eigenvalues showed us that they are made unstable by tides, whatever are the masses, radii and tidal parameters of the co-orbitals. The instability is due to an exponential increase of the libration amplitude of the angle $\lambda_1 - \lambda_2$, that eventually leads to close encounters between the co-orbitals and the destruction of the system. The amplitude of the real parts gave us informations on the timescale of instability and we were able to give an analytical expression for the lifetime of the co-orbital pair in Eq. (6.40). We explain in Sect. 6.2.3 how this work can be applied to an intelligent search for co-orbital pairs of exoplanets. The analysis of the real part of the eigenvalues is not limited to the obtention of the timescale of destruction but also shows how the eccentric proper modes Lagrange and anti-Lagrange, discovered numerically by Giuppone *et al.* (2010) and analytically by Robutel and Pousse (2013) are perturbed by tides. We reached the conclusion that the most stable co-orbital pairs settle in the anti-Lagrange configuration. We showed how for a system star−planet−planet, it is enough to consider tides raised on the co-orbitals only, but we also considered in Sect. 6.4 tides raised on the central body to treat the case of a system planet−satellite−satellite made up of small satellites.

In Chap. 7, we included tides in the $p : p : p + 1$ resonance chain. We linearized the equations of motions in the vicinity of the equilibria of the system, and we showed that close to the secular $1 : 1$ resonance between the precession of the pericentres and the libration of $\lambda_1 - \lambda_2$, all the real part are negative and the equilibria are made asymptotically stable by tides. For the chain $1 : 1 : 2$, such secular resonance occurs near $n_3/n_1 \approx 2.07$, outside the Keplerian resonance, and in this region, the libration amplitude of $\lambda_1 - \lambda_2$, instead of increasing exponentially, decreases exponentially. For this reason, the third planet has the ability to greatly extend the lifetime of the co-orbital pair, although it cannot save it from the destruction, as the system always leaves this region of asymptotic stability. We thoroughly studied the influence of the mass of the third planet and we showed that it generally increases the lifetime of the co-orbital pair, although in some few cases, the third planet can lead to a premature destruction of the co-orbital pair.

8.2 Consequences

This work, although it shows the systematic destruction of the co-orbital motion, does not entirely explain the absence of detection of co-orbital pair of exoplanets. Indeed, the timescale of destruction is heavily dependent on the semimajor axis (Eq. (6.36)), and co-orbital exoplanets located more than ~ 0.08 AU away from their host star can be considered immune to tides. As of September 2, 2022, 52.4 % of the 5159 detected exoplanets had a semimajor axis larger than that[1] and were undergoing from their host star negligible tidal effects. It is thus likely that the challenge that a co-orbital detection represents constitutes the main explanation to the absence of co-orbital exoplanet discovery.

[1] exoplanet.eu, considering a sample of 2841 exoplanets with known semimajor axis.

The disruption due to tidal dissipation constitutes another satisfying explanation. It is also possible that the current formation models overestimate their formation, and co-orbital exoplanets could be rarer than we believe. The results of this work hence cannot be interpreted as a reason to abandon the search for co-orbital exoplanet, and further endeavours will most likely lead to their detection.

In order to prove the unavoidable destruction of the co-orbital motion, this work assumes a very simple tidal model. However, any tidal model leads to the loss of orbital energy, and according to the results of Moeckel (2017) (last paragraph of Sect. 6.2.1), considering a more subtle model could change the timescale of destruction, but it will not save the co-orbital pair. Three more assumptions of our model, namely the expansion in semi-major axis (Eqs. (3.9) & (3.11)), the expansion in eccentricities (Eq. (3.29)), and the averaging process (Eq. (3.17)) were shown to be perfectly valid in Sect. 6.3. The fifth and last approximation that we made is the planar state of the system. In other words, we assumed that a small mutual inclination between the co-orbitals is not pumped by tides like the libration amplitude of the angle $\lambda_1 - \lambda_2$. While we did not check this hypothesis, Dobrovolskis and Lissauer (2022) showed that, at least in the restricted case, the mutual inclination between the co-orbital bodies is damped by tides, which validates our last assumption. In the absence of more planets in the planetary system, it is therefore legitimate to consider that our work closes the question of tides raised on co-orbital planets.

8.3 Perspectives

While the question of tides in the the $1:1$ mean motion resonance is closed, the work performed in this thesis only briefly explores the case of larger resonance chains. We restricted ourselves to the chain $p:p:p+1$, for which we showed that whereas the co-orbital lifetime was generally enhanced by the third planet, the destruction was still unavoidable. It is possible that other resonance chains could make the co-orbital motion stable over arbitrarily large timescales, or even indefinitely. In particular, we did not investigate the dynamics of the chain $p:p+1:p+1$, for which the third planet is innermost. It is not absurd to believe that it could have dynamical features completely different from those of the chain $p:p:p+1$, since such phenomenon has already been observed, even for a two-planet system. Indeed, Beaugé *et al.* (2006) showed that in the $1:2$ mean motion resonance, the second fundamental model of resonance of Henrard and Lemaitre (1983) ceases to be valid at large eccentricities if the most massive planet is innermost, while it stays valid if the most massive planet is outermost. Something similar is not to be excluded between the chains $p:p:p+1$ and $p:p+1:p+1$, which is a perspective worth exploring.

Another interesting direction to explore is the scenario mentioned in the last paragraph of Sect. 7.4. As proven by Malhotra (2022), there exist continuous connections between the branches of equilibria of consecutive first-order mean-motion resonances. It would be interesting to build a secular model that takes into account effects of both the $p:p:p+1$ and $p+1:p+1:p+2$ resonance chains, to check if tides, through *linearly stable regions* (Sect. 7.2.2) and *eccentricity damping stabilization* mechanisms (Sect. 7.3.3), could be responsible for the system traveling from the resonance $p+1:p+1:p+2$ to the resonance

$p : p : p + 1$.

The case of a system planet−satellite−satellite requires tides raised on the central planet to be taken into account (Sect. 6.4.1). We studied these types of tides in Sect. 6.4, but we limited ourselved to the obtention of analytical expressions of the timescales of evolution. We did not check these analytical results with numerical simulations. Furthermore, for such a system, other effects, like the oblateness of the central stars, or the presence of a non-resonant, much more massive satellite (*e.g.* the system Saturn−Janus−Epimetheus−Titan) need to be taken into account in order to build a reliable model. We plan to look in this direction in the future.

Finally, the subject of resonance chains is very broad, and for four or more planets, their dynamics are poorly understood, even in the point-mass case. Indeed, adding planets to the chain quickly increases the number of degrees of freedom of the system, and analytical models soon become untractable. Choosing a resonance chain that features a co-orbital pair is a way to reduce the complexity of the model by means of uncoupling simplifications like those explained in Sect. 4.3.1. Furthermore, the presence of a co-orbital pair induces the existence of a fundamental frequency independent of the distance to the Keplerian resonance, namely the libration frequency of the co-orbital angle. The precession frequency of the pericentres, however, depends on the distance to the Keplerian resonance. The presence of a co-orbital pair hence increases the chance of encountering a $1 : 1$ secular resonance at a certain distance from the Keplerian resonance, like the one that exists at $n_1/n_3 \approx 2.07$ for the chain $1 : 1 : 2$. As an example, the four-planet chain $p : p : p+1 : p+1$ could be comparatively easier to study than other four-planet resonance chains, while being very rich due to two $1 : 1$ secular resonances, the first one between $\lambda_1 - \lambda_2$ and the pericentres, and the second one between $\lambda_3 - \lambda_4$ and the pericentres.

Appendix A

Spherical harmonics and demonstration of Eq. (5.8)

A.1 Framework

In this appendix, in order to have more compact notations, we denote

$$\int_{\mathbb{S}} := \int_0^{\pi}\int_0^{2\pi} \sin\theta d\varphi d\theta, \quad \text{or similarly} \quad \int_{\mathbb{S}'} := \int_0^{\pi}\int_0^{2\pi} \sin\theta' d\varphi' d\theta'. \tag{A.1}$$

We use the spherical harmonics defined by

$$Y_{lm}(\theta,\varphi) = P_{lm}(\cos\theta)e^{im\varphi}, \tag{A.2}$$

where the P_{lm} are the associated Legendre polynomials, related to the Legendre polynomials by

$$P_{lm}(X) = (-1)^m \left(1-X^2\right)^{m/2} \frac{d^m}{dX^m} P_l(X). \tag{A.3}$$

The Legendre polynomials can be defined in many ways, for example as the coefficients of the serie expansion (5.1), but their most compact definition is Rodrigues' formula

$$P_l(X) = \frac{1}{2^l l!}\frac{d^l}{dX^l}\left(X^2-1\right)^l. \tag{A.4}$$

For two functions $f(\theta,\varphi)$ and $g(\theta,\varphi)$ on the sphere $\mathbb{S}$, we define the dot product

$$f\cdot g = \int_{\mathbb{S}} f(\theta,\varphi)\,\bar{g}(\theta,\varphi), \tag{A.5}$$

where the upper bar is the complex conjugated. With this dot product, the spherical harmonics are orthogonal, that is

$$Y_{lm}\cdot Y_{l'm'} = c_{lm}^{-1}\delta_{ll'}\delta_{mm'}, \quad \text{with} \quad c_{lm} = \frac{(2l+1)\,(l-m)!}{4\pi\,(l+m)!}. \tag{A.6}$$

The spherical harmonics defined above form an orthogonal basis of the Hilbert space $\mathcal{L}^2_{\mathbb{C}}(\mathbb{S})$ of square integrable functions from $\mathbb{S}$ to $\mathbb{C}$. A given function $f : \mathbb{S} \to \mathbb{C}$ can be decomposed in a unique[1] way as a linear combination of the Y_{lm}

$$f(\theta, \varphi) = \sum_{l=0}^{+\infty} \sum_{m=-l}^{l} f_{lm} Y_{lm}(\theta, \varphi), \tag{A.7}$$

where the coefficients f_{lm} are given by the projection[2] of f onto Y_{lm}

$$f_{lm} = c_{lm}\, f \cdot Y_{lm} = c_{lm} \int_{\mathbb{S}} f(\theta, \varphi) \bar{Y}_{lm}(\theta, \varphi). \tag{A.8}$$

A.2 Laplace equation in spherical coordinates

The Laplace equation reads $\Delta = 0$. Using the spherical coordinates $\boldsymbol{r} = (r, \theta, \varphi)$, where θ and φ are the colatitude and longitude, the Laplace operator reads

$$\Delta = \frac{1}{r^2} \frac{\partial}{\partial r} \left(r^2 \frac{\partial}{\partial r} \right) + \frac{1}{r^2 \sin\theta} \frac{\partial}{\partial \theta} \left(\sin\theta \frac{\partial}{\partial \theta} \right) + \frac{1}{r^2 \sin^2\theta} \frac{\partial^2}{\partial \varphi^2}. \tag{A.9}$$

Assuming the separation of variables, that is

$$F(r, \theta, \varphi) = f(r) g(\theta) h(\varphi), \tag{A.10}$$

the equation $\Delta F = 0$ yields

$$f(r) = r^\beta, \quad g(\theta) = P_{lm}(\cos\theta), \quad h(\varphi) = e^{\pm i m \varphi}, \tag{A.11}$$

where l is a positive integer, β is either l or $-l-1$ and $-l \leq m \leq l$.

A.3 Demonstration of Eq. (5.8)

Here we show Eq. (5.8) from Eqs. (5.6) & (5.7). As in Chap. 5, σ stands for (θ, φ) and $\mathbb{S}$ denotes the sphere of radius R centered on $\mathcal{O}$, the barycentre of the body $\mathbb{B}$. The Love number $k(R, \sigma, \sigma', t - t')$, appearing in Eq. (5.6), is decomposed over the spherical harmonics

$$\begin{aligned} k(R, \sigma, \sigma', t - t') &= \sum_{l=0}^{+\infty} \sum_{m=-l}^{l} \mathfrak{k}_l^m(R, \sigma', t - t') Y_{lm}(\sigma) \\ &= \sum_{l=0}^{+\infty} \sum_{m=-l}^{l} \left(\sum_{l'=0}^{+\infty} \sum_{m'=-l'}^{l'} \mathfrak{k}_{ll'}^{mm'}(R, t - t') \bar{Y}_{l'm'}(\sigma') \right) Y_{lm}(\sigma). \end{aligned} \tag{A.12}$$

[1] $\bar{Y}_{lm}$ can be written in Eq. (A.7) instead of Y_{lm}, in which case $f_{lm} = c_{lm}\, f \cdot \bar{Y}_{lm}$.

[2] The coefficient c_{lm} is due to the fact that the Y_{lm} do not form an orthonormal basis of $\mathcal{L}^2_{\mathbb{C}}(\mathbb{S})$, but rather an orthogonal basis.

This allows Eq. (5.6) to be rewritten as

$$V(R,\sigma,t) = \int_{-\infty}^{t}\int_{\mathbb{S}'}\sum_{l=0}^{+\infty}\sum_{m=-l}^{l}\left(\sum_{l'=0}^{+\infty}\sum_{m'=-l'}^{l'}\mathfrak{k}_{ll'}^{mm'}(R,t-t')\bar{Y}_{l'm'}(\sigma')\right)Y_{lm}(\sigma)W(R,\sigma',t')dt'$$
$$= \sum_{l=0}^{+\infty}\sum_{m=-l}^{l}\int_{-\infty}^{t}\int_{\mathbb{S}'}\sum_{l'=0}^{+\infty}\sum_{m'=-l'}^{l'}\mathfrak{k}_{ll'}^{mm'}(R,t-t')\bar{Y}_{l'm'}(\sigma')W(R,\sigma',t')dt'\,Y_{lm}(\sigma). \tag{A.13}$$

A term-wise identification between Eq. (5.7) and Eq. (A.13) yields, by uniqueness of the decomposition

$$V_{lm}(R,t) = \int_{-\infty}^{t}\int_{\mathbb{S}'}\sum_{l'=0}^{+\infty}\sum_{m'=-l'}^{l'}\mathfrak{k}_{ll'}^{mm'}(R,t-t')\bar{Y}_{l'm'}(\sigma')W(R,\sigma',t')dt'. \tag{A.14}$$

If $\mathbb{B}$ is isotropic at rest, the coefficients $\mathfrak{k}_{ll'}^{mm'}$ do not depend on the reference frame attached to $\mathbb{B}$, and there exist functions $\mathfrak{k}_l(R,t)$ such that (see Boué *et al.*, 2019)

$$\mathfrak{k}_{ll'}^{mm'}(R,t-t') = \delta_{ll'}\delta_{mm'}\mathfrak{k}_l(R,t-t'). \tag{A.15}$$

Equation (A.14) hence reduces to

$$V_{lm}(R,t) = \int_{-\infty}^{t}\mathfrak{k}_l(R,t-t')\int_{\mathbb{S}'}\bar{Y}_{lm}(\sigma')W(R,\sigma',t')dt'. \tag{A.16}$$

Substituting Eq. (A.8) into the last equation and defining $k_{lm}(R,t) = c_{lm}^{-1}\mathfrak{k}_l(R,t)$ yields

$$V_{lm}(R,t) = \int_{-\infty}^{t}k_{lm}(R,t-t')W_{lm}(R,t')dt', \tag{A.17}$$

which is Eq. (5.8).

Appendix B

Coefficients of $\mathcal{H}^{(4)}$, $\mathcal{U}_t^{(j)}$, $\mathcal{H}_{j,3}^{(1)}$ and $\mathcal{H}_{j,3}^{(2)}$

B.1 Coefficients of $\mathcal{H}^{(4)}$

The coefficients appearing in the Hamiltonian $\mathcal{H}^{(4)}$ defined in Eq. (3.29) are given by[1]

$$\begin{aligned}
D_h &= \frac{7}{16}\cos\xi + \frac{1}{4\Delta^9}\left(-\frac{3951}{32} + 115\cos\xi + \frac{293}{8}\cos 2\xi - 27\cos 3\xi - \frac{37}{32}\cos 4\xi\right),\\
G_h &= \cos\xi + \Delta^{-9}\left(-\frac{4491}{32} + 139\cos\xi + \frac{233}{8}\cos 2\xi - 27\cos 3\xi - \frac{25}{32}\cos 4\xi\right),\\
E_h &= \frac{1}{32}\left(e^{-i\xi} + 81e^{-3i\xi}\right) + \frac{e^{-6i\xi}}{32\Delta^9}P_E(e^{i\xi}),\\
F_h &= -\frac{7}{4}e^{2i\xi} + \frac{e^{-3i\xi}}{4\Delta^9}P_F(e^{i\xi}),
\end{aligned} \tag{B.1}$$

where P_E and P_F are polynomials given by

$$\begin{aligned}
P_E(X) &= -\frac{9}{8} + 15X - \frac{349}{2}X^2 + 171X^3 + \frac{2889}{4}X^4 - 1571X^5 + \frac{2007}{2}X^6 - 87X^7 - \frac{625}{8}X^8,\\
P_F(X) &= \frac{207}{32} + \frac{303}{8}X - \frac{577}{4}X^2 + \frac{603}{8}X^3 + \frac{2511}{16}X^4 - \frac{1475}{8}X^5 + 45X^6 + \frac{57}{8}X^7 - \frac{5}{32}X^8.
\end{aligned}$$

B.2 Coefficients of $\mathcal{H}_{j,3}^{(1)}$ and $\mathcal{H}_{j,3}^{(2)}$

We give here the expressions of the coefficients appearing in Eqs. (4.19) & (4.20) of Sect. 4.1.3. They depend on the Laplace coefficients $b_{n/2}^m(\alpha)$ (defined by Eq. (2.75)), and to improve readability, we denote $b_n^m = b_{n/2}^m(\alpha)$, where $\alpha = \bar{a}/a_{3,0}$. For the resonance $1:1:2$

[1] Recall that $\Delta = \sqrt{2 - 2\cos\xi}$.

we have[2]

$$\begin{aligned} C_{1,1}^{(1)} &= -\alpha b_3^1\left(\frac{7}{6}+\frac{2}{3}\alpha^{-2}+\frac{5}{3}\alpha^2\right)+b_3^0\left(1+\frac{5}{2}\alpha^2\right)\approx 1.1904937,\\ C_{1,2}^{(1)} &= b_3^1\left(1+\frac{3}{2}\alpha^2\right)-\frac{5}{2}\alpha b_3^0+\frac{1}{\sqrt{\alpha}}\approx -0.4283898, \end{aligned} \tag{B.2}$$

for the first degree in eccentricity and

$$\begin{aligned} C_{1,1}^{(2)} &= \alpha b_3^1\left(\frac{263}{168}+\frac{16}{35}\alpha^{-4}+\frac{89}{105}\alpha^{-2}+\frac{341}{105}\alpha^2+\frac{184}{35}\alpha^4\right)\\ &\quad -b_3^0\left(\frac{71}{70}+\frac{24}{35}\alpha^{-2}+\frac{67}{35}\alpha^2+\frac{276}{35}\alpha^4\right)\approx -1.6957266,\\ C_{1,2}^{(2)} &= \alpha b_3^1\left(\frac{65}{24}+\frac{4}{3}\alpha^{-2}+\frac{13}{3}\alpha^2\right)-b_3^0\left(2+\frac{13}{2}\alpha^2\right)\approx -3.5937942,\\ C_{1,3}^{(2)} &= -b_3^1\left(\frac{29}{10}+\frac{8}{5}\alpha^{-2}+\frac{59}{10}\alpha^2+\frac{48}{5}\alpha^4\right)+\alpha b_3^0\left(\frac{69}{20}+\frac{12}{5}\alpha^{-2}+\frac{72}{5}\alpha^2\right)\approx 4.9668470,\\ C_{1,4}^{(2)} &= -\frac{1}{8}\alpha b_3^1\approx -0.3876274,\\ C_{1,5}^{(2)} &= \frac{1}{2}b_3^1\left(1+\alpha^2\right)-\frac{3}{4}\alpha b_3^0\approx 0.5756950, \end{aligned} \tag{B.3}$$

for the second degree.

B.3 Coefficients of $\mathcal{U}_t^{(j)}$

We give here the the complete expression of the fourth order in eccentricity of the tidal perturbation $\mathcal{U}_t^{(j)}$ to the Hamiltonian, introduced by Eq. (6.8). The term $\mathfrak{D}_4^{(j)}$ appearing in this equation reads

$$\begin{aligned} \mathfrak{D}_4^{(j)} &= D_t^{(j)}\left(\mathcal{R}_j^{-2}X_j^2\bar{X}_j^2+\mathcal{R}_j^{\star-2}X_j^{\star2}\bar{X}_j^{\star2}\right)+\left(\mathcal{R}_j\mathcal{R}_j^\star\right)^{-1}\left(E_t^{(j)}X_j^2\bar{X}_j^{\star2}+\bar{E}_t^{(j)}X_j^{\star2}\bar{X}_j^2\right)\\ &\quad+\left(\mathcal{R}_j\mathcal{R}_j^\star\right)^{-1}G_t^{(j)}X_jX_j^\star\bar{X}_j\bar{X}_j^\star+\mathcal{R}_j^{-3/2}\mathcal{R}_j^{\star-1/2}\left(F_t^{(j)}X_jX_j^\star\bar{X}_j^2+\bar{F}_t^{(j)}X_j^2\bar{X}_j\bar{X}_j^\star\right)\\ &\quad+\mathcal{R}_j^{-1/2}\mathcal{R}_j^{\star-3/2}\left(F_t^{(j)}X_j^{\star2}\bar{X}_j\bar{X}_j^\star+\bar{F}_t^{(j)}X_jX_j^\star\bar{X}_j^{\star2}\right), \end{aligned} \tag{B.4}$$

where

$$\begin{aligned} D_t^{(j)} &= \frac{3}{8}+\frac{69}{64}\cos\left[2\left(\Delta\lambda_j-\Delta\theta_j\right)\right],\\ G_t^{(j)} &= \frac{9}{16}+\frac{75}{16}\cos\left[2\left(\Delta\lambda_j-\Delta\theta_j\right)\right],\\ E_t^{(j)} &= \frac{81}{64}e^{-2i\Delta\lambda_j}+\frac{867}{32}e^{-2i(2\Delta\lambda_j-\Delta\theta_j)},\\ F_t^{(j)} &= \frac{9}{16}e^{i\Delta\lambda_j}-\frac{3}{128}e^{-i(\Delta\lambda_j-2\Delta\theta_j)}-\frac{1365}{128}e^{i(3\Delta\lambda_j-2\Delta\theta_j)}, \end{aligned} \tag{B.5}$$

with $\Delta\lambda_j=\lambda_j-\lambda_j^\star$ and $\Delta\theta_j=\theta_j-\theta_j^\star$.

[2]Note that these analytical expressions are only valid for $p=1$, that is, for the resonance chain $1:1:2$.

Appendix C

Matrices and differential systems

C.1 Simplified differential system

We give here the expression of the differential system used to obtain the analytical results of Sect. 4.3.1. It is derived from Eq. (2.18) with the Hamiltonian $\mathcal{H}_K + \mathcal{H}^{(0)} + \mathcal{H}^{(1)}$, that is, the Hamiltonian (4.21) truncated at first order in eccentricity, after the degree of freedom $(L;\xi)$ have been uncoupled from the degrees of freedom $(D_j;\sigma_j)$, as explained in Sect. 4.3.1. We have

$$\begin{aligned}
\dot{D}_1 &= -\frac{C_{p,1}^{(1)}\sqrt{2C_1D_1}m_1n_{3,0}}{m_0C_3}\sin\left(p\frac{\pi}{3}-\sigma_1\right),\\
\dot{D}_2 &= -\frac{C_{p,1}^{(1)}\sqrt{2C_2D_2}m_2n_{3,0}}{m_0C_3}\sin\sigma_2,\\
\dot{D}_3 &= -\frac{\sqrt{2C_3D_3}C_{p,2}^{(1)}n_{3,0}}{m_0C_3}\left(m_1\sin\left(p\frac{\pi}{3}-\sigma_3\right)-m_2\sin\sigma_3\right),\\
\dot{\Delta L} &= \eta\frac{m_2\sin\xi}{m_0C_1}\left(1-\frac{1}{\Delta^3}\right),\\
\dot{\sigma}_1 &= \frac{\partial\mathcal{H}_K}{\partial\Delta\Upsilon}+\frac{C_1C_{p,1}^{(1)}m_1n_{3,0}}{C_3\sqrt{2C_1D_1}m_0}\cos\left(p\frac{\pi}{3}-\sigma_1\right),\\
\dot{\sigma}_2 &= \frac{\partial\mathcal{H}_K}{\partial\Delta\Upsilon}+\frac{C_2C_{p,1}^{(1)}m_2n_{3,0}}{C_3\sqrt{2C_2D_2}m_0}\cos\sigma_2,\\
\dot{\sigma}_3 &= \frac{\partial\mathcal{H}_K}{\partial\Delta\Upsilon}+\frac{C_{p,2}^{(1)}n_{3,0}}{m_0\sqrt{2C_3D_3}}\left(m_1\cos\left(p\frac{\pi}{3}-\sigma_3\right)+m_2\cos\sigma_3\right),\\
\dot{\xi} &= -3\eta\left(C_1+C_2\right)\Delta L,
\end{aligned} \tag{C.1}$$

where $\Delta L = L - L^\star$ and[1]

$$\frac{\partial\mathcal{H}_K}{\partial\Delta\Upsilon} = -3\eta\left\{\left(p^2C_2+p\left(p+1\right)C_3\right)\Delta\Upsilon+pC_2\Delta L^\star\right\}. \tag{C.2}$$

[1] $\Delta L^\star$ is defined by Eq. (4.26).

C.2 Expression of the matrix $\mathcal{Q}_6$

We give here the matrix $\mathcal{Q}_6$ that appears in Eq. (4.37). We denote

$$\begin{aligned} &r_j = \sqrt{2D_j}, \quad c_3 = \cos\sigma_3, \quad s_3 = \sin\sigma_3, \quad s = \sin\frac{p\pi}{3}, \\ &c = \cos\frac{p\pi}{3}, \quad I = 3\eta p\left(C_3 + p\left(C_2 + C_3\right)\right), \end{aligned} \tag{C.3}$$

and obtain $\mathcal{Q}_6 =$

$$\begin{pmatrix} Icsr_1{}^2 & Isr_1r_2 & c_3Isr_1r_3 & Is^2r_1{}^2-\nu_3 & 0 & Is_3sr_1r_3 \\ 0 & 0 & 0 & 0 & -\nu_3 & 0 \\ Is_3cr_1r_3 & Is_3r_2r_3 & c_3Is_3r_3{}^2 & Is_3sr_1r_3 & 0 & Is_3{}^2r_3{}^2-\nu_3 \\ -Ic^2r_1{}^2+\nu_3 & -Icr_1r_2 & -c_3Icr_1r_3 & -Icsr_1{}^2 & 0 & -Is_3cr_1r_3 \\ -Icr_1r_2 & -Ir_2{}^2+\nu_3 & -c_3Ir_2r_3 & -Isr_1r_2 & 0 & -Is_3r_2r_3 \\ -c_3Icr_1r_3 & -c_3Ir_2r_3 & -c_3{}^2Ir_3{}^2+\nu_3 & -c_3Isr_1r_3 & 0 & -c_3Is_3r_3{}^2 \end{pmatrix}. \tag{C.4}$$

C.3 Expression of the matrix $\mathcal{Q}_0 + \mathcal{Q}_1$

We give here the complete expression of the matrix $\mathcal{Q}_0 + \mathcal{Q}_1$ of the linearized system (6.24). We have

$$\mathcal{Q}_0 = \begin{pmatrix} \mathcal{Z}_0 & 0_{5\times 2} \\ 0_{2\times 5} & \mathcal{M}_0 \end{pmatrix} \quad \text{and} \quad \mathcal{Q}_1 = \begin{pmatrix} \mathcal{Z}_1 & 0_{5\times 2} \\ 0_{2\times 5} & \mathcal{M}_1 \end{pmatrix}, \tag{C.5}$$

where

$$\mathcal{M}_0 = \frac{27}{8}i\eta \begin{pmatrix} \frac{m_2}{m_0} & -\frac{m_2}{m_0}e^{i\pi/3} \\ -\frac{m_1}{m_0}e^{-i\pi/3} & \frac{m_1}{m_0} \end{pmatrix}, \tag{C.6}$$

$$\mathcal{M}_1 = -\frac{21}{2}\eta\,\mathrm{diag}\left\{\frac{q_1}{Q_1}\frac{m_0}{m_1}\left(1-\frac{5}{7}iQ_1\right), \frac{q_2}{Q_2}\frac{m_0}{m_2}\left(1-\frac{5}{7}iQ_2\right)\right\}, \tag{C.7}$$

$$\mathcal{Z}_0 = \begin{pmatrix} 0 & 0 & 0 & 0 & 0 \\ 0 & 0 & 0 & 0 & 0 \\ 0 & 0 & 0 & -3\gamma\eta & 0 \\ 0 & 0 & 9\iota\eta\gamma^{-1}/4 & 0 & 0 \\ 0 & 0 & 0 & 0 & 0 \end{pmatrix}, \tag{C.8}$$

$$\mathcal{Z}_1 = \begin{pmatrix} -\mathfrak{a}_1 & 0 & 0 & 3\gamma^{-1}\delta^{-1}\mathfrak{a}_1 & 3\gamma^{-1}\mathfrak{a}_1 \\ 0 & -\mathfrak{a}_2 & 0 & -3\gamma\delta\mathfrak{a}_2 & 3\gamma^{-1}\mathfrak{a}_2 \\ 0 & 0 & 0 & -\gamma\left[\delta\mathfrak{c}_2+(1-\delta)\,\mathfrak{c}_1\right] & \gamma^{-1}\left(\mathfrak{c}_2-\mathfrak{c}_1\right) \\ -(1-\delta)\,\mathfrak{b}_1 & \delta\mathfrak{b}_2 & 0 & 3\gamma\left[\delta^2\mathfrak{b}_2+(1-\delta)^2\,\mathfrak{b}_1\right] & 3\gamma^{-1}\left[(1-\delta)\,\mathfrak{b}_1-\delta\mathfrak{b}_2\right] \\ -\mathfrak{b}_1 & -\mathfrak{b}_2 & 0 & 3\gamma^{-1}\delta^{-1}\mathfrak{b}_1-3\gamma\delta\mathfrak{b}_2 & 3\gamma^{-1}\left(\mathfrak{b}_1+\mathfrak{b}_2\right) \end{pmatrix}, \tag{C.9}$$

with

$$\begin{aligned} &\delta = \frac{m_1}{m_1+m_2}, && \gamma = \frac{m_1+m_2}{m}, && \iota = \frac{m_1+m_2}{m_0} \\ &\mathfrak{a}_j = \frac{3\eta}{\alpha_j}\frac{q_j}{Q_j}\varsigma_j^{-2}\frac{m_0}{m_j}, && \mathfrak{b}_j = 3\eta\frac{q_j}{Q_j}\frac{m_0}{m}, && \mathfrak{c}_j = 78\eta q_j\frac{m_0}{m_j}. \end{aligned} \tag{C.10}$$

Near $L_{4,5}$, the eigenvectors of $\mathcal{M}_0 + \mathcal{M}_1$, computed using results from Sect. 2.4.2, reveal that the Lagrange configuration corresponds to

$$\begin{aligned} \varpi_1 - \varpi_2 &= \frac{\pi}{3} + \frac{28}{9}\frac{m_0^2\left(m_1 q_2/Q_2 + m_2 q_1/Q_1\right)}{m_1 m_2\left(m_1+m_2\right)}, \\ \frac{e_1}{e_2} &= 1 + \frac{20}{9}\frac{m_0^2\left(q_2 m_1 - q_1 m_2\right)}{m_1 m_2\left(m_1+m_2\right)}, \end{aligned} \tag{C.11}$$

while the anti-Lagrange configuration complies with

$$\begin{aligned} \varpi_1 - \varpi_2 &= \frac{4\pi}{3} - \frac{28}{9}\frac{m_0^2\left(m_1 q_2/Q_2 + m_2 q_1/Q_1\right)}{m_1 m_2\left(m_1+m_2\right)}, \\ \frac{e_1}{e_2} &= \frac{m_2}{m_1}\left(1 - \frac{20}{9}\frac{m_0^2\left(q_2 m_1 - q_1 m_2\right)}{m_1 m_2\left(m_1+m_2\right)}\right). \end{aligned} \tag{C.12}$$

These last two equations are a perturbation due to tides of Eqs (3.44) & (3.45).

C.4 Complete model for tidal interactions

The complete equations of motion governing the tidal evolution of a planar $(N+1)$-body system in a heliocentric reference frame, using a linear constant time-lag tidal model, are given, for $1 \leq j \leq N$, by (Mignard, 1979)

$$\begin{aligned} \ddot{\boldsymbol{r}}_j &= -\frac{\mu_j}{r_j^3}\boldsymbol{r}_j + \sum_{k\neq j}\mathcal{G}m_k\left(\frac{\boldsymbol{r}_k - \boldsymbol{r}_j}{\left|\boldsymbol{r}_k - \boldsymbol{r}_j\right|^3} - \frac{\boldsymbol{r}_k}{r_k^3}\right) + \frac{\boldsymbol{f}_j}{\beta_j} + \sum_{k\neq j}\frac{\boldsymbol{f}_k}{m_0}, \\ \ddot{\theta}_j &= -3\Delta t_j \frac{\kappa_2^{(j)}\mathcal{G}m_0^2 R_j^3}{\alpha_j m_j r_j^8}\left[\dot{\theta}\, r_j^2 - \left(\boldsymbol{r}_j \times \dot{\boldsymbol{r}}_j\right)\cdot\boldsymbol{k}\right], \end{aligned} \tag{C.13}$$

where $\boldsymbol{r}_j$ is the heliocentric position vector, θ_j the rotation angle of the planet j, $\boldsymbol{k}$ is the unit vector normal to the orbital plane, and $\boldsymbol{f}_j$ is the force arising from the tidal potential energy created by the deformation of planet j (Eq. (6.3))

$$\boldsymbol{f}_j = -3\frac{\kappa_2^{(j)}\mathcal{G}m_0^2 R_j^5}{r_j^8}\boldsymbol{r}_j - 3\frac{\kappa_2^{(j)}\mathcal{G}m_0^2 R_j^5}{r_j^{10}}\Delta t_j\left[2\left(\boldsymbol{r}_j\cdot\dot{\boldsymbol{r}}_j\right)\boldsymbol{r}_j + r_j^2\left(\dot{\theta}\,\boldsymbol{r}_j\times\boldsymbol{k} + \dot{\boldsymbol{r}}_j\right)\right]. \tag{C.14}$$

Bibliography

Adams, F. C. and Bloch, A. M. (2015). On the Stability of Extrasolar Planetary Systems and Other Closely Orbiting Pairs. *Monthly Notices of the Royal Astronomical Society*, 446, pp. 3676–3686.

Andoyer, H. (1923). *Cours de Mecanique Celeste*. Gauthier-Villars et Cie.

Barker, A. J. (2020). Tidal Dissipation in Evolving Low-Mass and Solar-Type Stars with Predictions for Planetary Orbital Decay. *Monthly Notices of the Royal Astronomical Society*, 498, pp. 2270–2294.

Beaugé, C., Michtchenko, T. A. and Ferraz-Mello, S. (2006). Planetary Migration and Extrasolar Planets in the 2/1 Mean-Motion Resonance. *Monthly Notices of the Royal Astronomical Society*, 365, pp. 1160–1170.

Beaugé, C. *et al.* (2007). Co-Orbital Terrestrial Planets in Exoplanetary Systems: A Formation Scenario. *Astronomy and Astrophysics, Volume 463, Issue 1, February III 2007, pp.359-367*, 463.1, p. 359.

Boué, G., Correia, A. C. M. and Laskar, J. (2019). On Tidal Theories and the Rotation of Viscous Bodies. 82, pp. 91–98.

Cardano, G. (1545). *Ars Magna*.

Christensen, R. M. (1982). *Theory of Viscoelasticity : An Introduction*. Second edition, United Kingdom edition. Academic press.

Claret, A. and Cunha, N. C. S. (1997). Circularization and Synchronization Times in Main-Sequence of Detached Eclipsing Binaries II. Using the Formalisms by Zahn. *Astronomy and Astrophysics, v.318, p.187-197*, 318, p. 187.

Correia, A. C. M., Bourrier, V. and Delisle, J.-B. (2020). Why Do Warm Neptunes Present Nonzero Eccentricity? *Astronomy & Astrophysics, Volume 635, id.A37*, 635, A37.

Correia, A. C. M. and Laskar, J. (2010). *Tidal Evolution of Exoplanets*. University of Arizona Press, Tucson, pp. 239–266.

Correia, A. C. M. (2009). Secular Evolution of a Satellite by Tidal Effect: Application to Triton. *The Astrophysical Journal*, 704, pp. L1–L4.

Correia, A. C. M. and Laskar, J. (2003). Different Tidal Torques on a Planet with a Dense Atmosphere and Consequences to the Spin Dynamics. *Journal of Geophysical Research (Planets)*, 108, p. 5123.

Correia, A. C. M. and Laskar, J. (2004). Mercury's Capture into the 3/2 Spin-Orbit Resonance as a Result of Its Chaotic Dynamics. *Nature*, 429, pp. 848–850.

Correia, A. C. M. *et al.* (2014). Deformation and Tidal Evolution of Close-in Planets and Satellites Using a Maxwell Viscoelastic Rheology. *Astronomy & Astrophysics, Volume 571, id.A50*, 571, A50.

Couetdic, J. *et al.* (2010). Dynamical Stability Analysis of the HD 202206 System and Constraints to the Planetary Orbits. *Astronomy and Astrophysics, Volume 519, id.A10*, 519, A10.

Couturier, J., Robutel, P. and Correia, A. C. M. (2022). Dynamics of Co-Orbital Exoplanets in a First-Order Resonance Chain with Tidal Dissipation. *Astronomy & Astrophysics*, 664, A1.

Couturier, J., Robutel, P. and Correia, A. C. M. (2021). An Analytical Model for Tidal Evolution in Co-Orbital Systems. I. Application to Exoplanets. *Celestial Mechanics and Dynamical Astronomy*, 133.8, p. 37.

Cresswell, P. and Nelson, R. P. (2008). Three-Dimensional Simulations of Multiple Protoplanets Embedded in a Protostellar Disc. *Astronomy and Astrophysics, Volume 482, Issue 2, 2008, pp.677-690*, 482.2, p. 677.

Darwin, G. H. (1880). On the Secular Changes in the Elements of the Orbit of a Satellite Revolving about a Tidally Distorted Planet. *Philosophical Transactions of the Royal Society of London Series I*, 171, pp. 713–891.

Delaunay, M. (1861). Théorie Du Mouvement de La Lune. *Monthly Notices of the Royal Astronomical Society*, 21, p. 80.

Delisle, J.-B. (2017). Analytical Model of Multi-Planetary Resonant Chains and Constraints on Migration Scenarios. *Astronomy & Astrophysics, Volume 605, id.A96*, 605, A96.

Delisle, J.-B. and Laskar, J. (2014). Tidal Dissipation and the Formation of Kepler Near-Resonant Planets. *Astronomy & Astrophysics, Volume 570, id.L7*, 570, p. L7.

Delisle, J.-B., Laskar, J. and Correia, A. C. M. (2014). Resonance Breaking Due to Dissipation in Planar Planetary Systems. *Astronomy & Astrophysics, Volume 566, id.A137*, 566, A137.

Dobrovolskis, A. R. and Lissauer, J. J. (2022). Do Tides Destabilize Trojan Exoplanets? *Icarus*, 385, p. 115087.

Efroimsky, M. (2012). Bodily Tides near Spin-Orbit Resonances. *Celestial Mechanics and Dynamical Astronomy*, 112, pp. 283–330.

Euler (1764). Considerationes de Motu Corporum Coelestium. Novi Commentarii Academiae Scientiarum Petropolitanae. *Berlin Acad*, 10, pp. 544–558.

Ford, E. B. and Gaudi, B. S. (2006). Observational Constraints on Trojans of Transiting Extrasolar Planets. *The Astrophysical Journal*, 652, pp. L137–L140.

Fortney, J. J. *et al.* (2018). *The Interior of Saturn*. Cambridge University Press, pp. 44–68.

Gascheau (1843). Examen d'une Classe d'équations Différentielles et Application à Un Cas Particulier Du Problème Des Trois Corps. *C. R. Acad. Sci. Paris*, 16.

Gastineau, M. and Laskar, J. (2011). TRIP: A Computer Algebra System Dedicated to Celestial Mechanics and Perturbation Series. *ACM Communications in Computer Algebra*, 44, pp. 194–197.

Giuppone, C. A., Benítez-Llambay, P. and Beaugé, C. (2012). Origin and Detectability of Co-Orbital Planets from Radial Velocity Data. *Monthly Notices of the Royal Astronomical Society*, 421, pp. 356–368.

Giuppone, C. A. *et al.* (2010). Dynamics of Two Planets in Co-Orbital Motion. *Monthly Notices of the Royal Astronomical Society*, 407, pp. 390–398.

Hara, N. C. *et al.* (2020). The SOPHIE Search for Northern Extrasolar Planets. XVI. HD 158259: A Compact Planetary System in a near-3:2 Mean Motion Resonance Chain. *Astronomy and Astrophysics*, 636, p. L6.

Henrard, J. and Lemaitre, A. (1983). A Second Fundamental Model for Resonance. *Celestial Mechanics*, 30, pp. 197–218.

Hill, G. W. (1913). Motion of a System of Material Points under the Action of Gravitation. *The Astronomical Journal*, 27, pp. 171–182.

Hut, P. (1980). Stability of Tidal Equilibrium. *Astronomy and Astrophysics, vol. 92, no. 1-2, Dec. 1980, p. 167-170.*, 92.1-2, p. 167.

Lagrange (1772). Œuvres Complètes. *Gauthier-Villars*,

Lainey, V. (2016). Quantification of Tidal Parameters from Solar System Data. *Celestial Mechanics and Dynamical Astronomy*, 126, pp. 145–156.

Lainey, V. *et al.* (2012). Strong Tidal Dissipation in Saturn and Constraints on Enceladus' Thermal State from Astrometry. *The Astrophysical Journal*, 752, p. 14.

Landau and Lifshitz (1980). *The Classical Theory of Fields*. Fourth. Vol. 2. Butterworth-Heinemann.

Laskar, J. (1990). The Chaotic Motion of the Solar System: A Numerical Estimate of the Size of the Chaotic Zones. *Icarus*, 88, pp. 266–291.

Laskar, J. (2000). On the Spacing of Planetary Systems. *Physical Review Letters*, 84, pp. 3240–3243.

Laskar, J., Boué, G. and Correia, A. C. M. (2012). Tidal Dissipation in Multi-Planet Systems and Constraints on Orbit Fitting. *Astronomy and Astrophysics*, 538, A105.

Laskar, J. (1993). Frequency Analysis for Multi-Dimensional Systems. Global Dynamics and Diffusion. *Physica D Nonlinear Phenomena*, 67, pp. 257–281.

Laskar, J. (2005). Note on the Generalized Hansen and Laplace Coefficients. *Celestial Mechanics and Dynamical Astronomy*, 91, pp. 351–356.

Laskar, J. (2017). Andoyer Construction for Hill and Delaunay Variables. *Celestial Mechanics and Dynamical Astronomy*, 128, pp. 475–482.

Laskar, J. and Robutel, P. (1995). Stability of the Planetary Three-Body Problem. I. Expansion of the Planetary Hamiltonian. *Celestial Mechanics and Dynamical Astronomy*, 62, pp. 193–217.

Laughlin, G. and Chambers, J. E. (2002). Extrasolar Trojans: The Viability and Detectability of Planets in the 1:1 Resonance. *The Astronomical Journal*, 124, pp. 592–600.

Leleu, A., Robutel, P. and Correia, A. C. M. (2018). On the Coplanar Eccentric Non-Restricted Co-Orbital Dynamics. *Celestial Mechanics and Dynamical Astronomy*, 130, p. 24.

Leleu, A. *et al.* (2017). Detection of Co-Orbital Planets by Combining Transit and Radial-Velocity Measurements. *Astronomy & Astrophysics, Volume 599, id.L7*, 599, p. L7.

Leleu, A. *et al.* (2021). Alleviating the Transit Timing Variation Bias in Transit Surveys. I. RIVERS: Method and Detection of a Pair of Resonant Super-Earths around Kepler-1705. *Astronomy & Astrophysics, Volume 655, id.A66*, 655, A66.

Leleu, A. *et al.* (2022). Alleviating the Transit Timing Variation Bias in Transit Surveys. II. RIVERS: Twin Resonant Earth-sized Planets around Kepler-1972 Recovered from a Kepler False Positive. *Astronomy & Astrophysics, Volume 661, id.A141*, 661, A141.

Leleu, A., Coleman, G. A. L. and Ataiee, S. (2019). Stability of the Co-Orbital Resonance under Dissipation. Application to Its Evolution in Protoplanetary Discs. *Astronomy and Astrophysics*, 631, A6.

Leleu, A., Robutel, P. and Correia, A. C. M. (2015). Detectability of Quasi-Circular Co-Orbital Planets. Application to the Radial Velocity Technique. *Astronomy and Astrophysics*, 581, A128.

Lillo-Box, J. *et al.* (2018). The TROY Project: Searching for Co-Orbital Bodies to Known Planets. I. Project Goals and First Results from Archival Radial Velocity. *Astronomy & Astrophysics, Volume 609, id.A96*, 609, A96.

Luhn, J. K. *et al.* (2019). Retired A Stars and Their Companions. VIII. 15 New Planetary Signals around Subgiants and Transit Parameters for California Planet Search Planets with Subgiant Hosts. *The Astronomical Journal*, 157, p. 149.

Lyra, W. *et al.* (2009). Standing on the Shoulders of Giants. Trojan Earths and Vortex Trapping in Low Mass Self-Gravitating Protoplanetary Disks of Gas and Solids. *Astronomy and Astrophysics, Volume 493, Issue 3, 2009, pp.1125-1139*, 493.3, p. 1125.

MacDonald, G. J. F. (1964). Tidal Friction. *Reviews of Geophysics and Space Physics*, 2, pp. 467–541.

Malhotra, R. (2022). New Results on Orbital Resonances. *IAU Symposium*, 364, pp. 85–101.

Meyer, K. R. and Hall, G. R. (2009). *Introduction to Hamiltonian Dynamical Systems and the N-Body Problem*. Second edition. Vol. 90. Springer.

Michtchenko, T. A., Beaugé, C. and Ferraz-Mello, S. (2008). Dynamic Portrait of the Planetary 2/1 Mean-Motion Resonance - I. Systems with a More Massive Outer Planet. *Monthly Notices of the Royal Astronomical Society*, 387, pp. 747–758.

Mignard, F. (1979). The Evolution of the Lunar Orbit Revisited. I. *Moon and Planets*, 20, pp. 301–315.

Moeckel, R. (2017). Minimal Energy Configurations of Gravitationally Interacting Rigid Bodies. *Celestial Mechanics and Dynamical Astronomy*, 128, pp. 3–18.

Morbidelli, A. (2002). *Modern Celestial Mechanics : Aspects of Solar System Dynamics*.

Namouni, F. (1999). Secular Interactions of Coorbiting Objects. *Icarus*, 137, pp. 293–314.

Niederman, L., Pousse, A. and Robutel, P. (2020). On the Co-orbital Motion in the Three-Body Problem: Existence of Quasi-periodic Horseshoe-Shaped Orbits. *Communications in Mathematical Physics*, 377, pp. 551–612.

Nimmo, F. and Schenk, P. (2006). Normal Faulting on Europa: Implications for Ice Shell Properties. *Journal of Structural Geology*, 28, pp. 2194–2203.

Petit, A. C. *et al.* (2020). The Path to Instability in Compact Multi-Planetary Systems. *Astronomy & Astrophysics, Volume 641, id.A176*, 641, A176.

Pierens, A. and Raymond, S. N. (2014). Disruption of Co-Orbital (1:1) Planetary Resonances during Gas-Driven Orbital Migration. *Monthly Notices of the Royal Astronomical Society*, 442, pp. 2296–2303.

Pousse, A., Robutel, P. and Vienne, A. (2017). On the Co-Orbital Motion in the Planar Restricted Three-Body Problem: The Quasi-Satellite Motion Revisited. *Celestial Mechanics and Dynamical Astronomy*, 128, pp. 383–407.

Pucacco, G. (2021). Normal Forms for the Laplace Resonance. *Celestial Mechanics and Dynamical Astronomy*, 133, p. 11.

Quillen, A. C. *et al.* (2017). Obliquity Evolution of the Minor Satellites of Pluto and Charon. *Icarus*, 293, pp. 94–113.

Ragazzo, C. and Ruiz, L. S. (2015). Dynamics of an Isolated, Viscoelastic, Self-Gravitating Body. *Celestial Mechanics and Dynamical Astronomy*, 122, pp. 303–332.

Roberts, J. H. and Nimmo, F. (2008). Tidal Heating and the Long-Term Stability of a Subsurface Ocean on Enceladus. *Icarus*, 194, pp. 675–689.

Robutel, P. and Gabern, F. (2006). The Resonant Structure of Jupiter's Trojan Asteroids - I. Long-term Stability and Diffusion. *Monthly Notices of the Royal Astronomical Society*, 372, pp. 1463–1482.

Robutel, P. and Pousse, A. (2013). On the Co-Orbital Motion of Two Planets in Quasi-Circular Orbits. *Celestial Mechanics and Dynamical Astronomy*, 117, pp. 17–40.

Rodríguez, A., Giuppone, C. A. and Michtchenko, T. A. (2013). Tidal Evolution of Close-in Exoplanets in Co-Orbital Configurations. *Celestial Mechanics and Dynamical Astronomy*, 117, pp. 59–74.

Segatz, M. *et al.* (1988). Tidal Dissipation, Surface Heat Flow, and Figure of Viscoelastic Models of Io. *Icarus*, 75, pp. 187–206.

Vokrouhlický, D. and Nesvorný, D. (2014). Transit Timing Variations for Planets Co-orbiting in the Horseshoe Regime. *The Astrophysical Journal*, 791, p. 6.

Wahr, J. (1996). *Geodesy and Gravity*. Samizdat Press.

Yoder, C. F. *et al.* (1983). Theory of Motion of Saturn's Coorbiting Satellites. *Icarus*, 53, pp. 431–443.

RÉSUMÉ

Les systèmes planétaires peuvent adopter des configurations remarquables. L'une d'elles, dite co-orbitale, se produit lorsque deux planètes ont la même période orbitale autour de leur étoile, c'est à dire, quand elles sont en résonance de moyen mouvement $1:1$. Même au sein de la résonance co-orbitale, de nombreuses trajectoires sont possibles. Les plus simples sont connues depuis le 18ème siècle, comme deux corps co-orbitaux sur des orbites planes et circulaires formant avec leur étoile un triangle équilatéral tournant. Cependant, certaines configurations plus subtiles n'ont été découvertes que récemment. Dans le cas de deux points matériels à faibles excentricités et inclinaisons, les aspects analytiques de la dynamique sont bien compris. Cependant, de grandes excentricités ou inclinaisons sont responsables de changements topologiques dans l'espace des phases, tandis que des corps étendus peuvent engendrer la dissipation de l'énergie mécanique, et la dynamique dans ces cas a encore des zones d'ombre.
Aucune des huit planètes du système Solaire ne co-orbitent ensemble le Soleil, bien que des corps co-orbitaux existent dans le système Solaire, soit entre deux objets mineurs (orbitant une planète), soit entre une planète et un objet mineur (orbitant le Soleil). Cette absence de planètes co-orbitales n'est a priori pas la norme dans les systèmes exoplanétaires, puisque les modèles de formation prédisent leur existence. Pourtant, en dépit de milliers de détections d'exoplanètes, aucune paire de planètes co-orbitales n'a été détectée à ce jour. Bien que cela puisse s'expliquer par des biais observationnels, nous montrons dans ce manuscrit que les forces de marées sont responsables de la destruction des paires de planètes co-orbitales. Nous construisons un modèle analytique de marées du système plan étoile−planète−planète, basé sur une extension, avec dissipation de marées, du formalisme Hamiltonien. Le modèle fournit une expression analytique précise de la durée de vie de la paire, dépendant des paramètres, et qui permet de prédire quelles exoplanètes déjà découvertes pourraient avoir un compagnon co-orbital non détecté.
Les modèles de formation prédisent aussi qu'un nombre important de planètes co-orbitales sont formées au sein d'une chaîne de résonance. Ainsi, nous étendons l'étude précédente au cas où la paire est au sein d'une chaîne de résonance. Plus précisement, nous construisons un modèle Hamiltonien de la chaîne de résonance $p:p:p+1$ où la paire de co-orbitaux est en résonance de moyen mouvement du premier ordre $p:p+1$ avec une troisième planète externe, p étant un petit entier. Après comparaison des familles d'équilibres du modèle avec les familles d'orbites quasipériodiques correspondantes dans le système complet, nous ajoutons la dissipation de marées au modèle à l'aide d'un formalisme pseudo-Hamiltonien. Nous montrons que cette chaîne de résonance met en scène une résonance séculaire $1:1$ entre la libration de l'angle co-orbital et la précession des péricentres, et en analysant les valeurs propres du système différentiel linéarisé au voisinage des familles d'équilibres, nous montrons comment les marées stabilisent le système aux alentours de cette résonance séculaire, rendant la paire de planètes co-orbitales bien plus stable quand elle est dans la chaîne de résonance $p:p:p+1$.

MOTS CLÉS

Mécanique Céleste ∘ Marées ∘ Problème des Trois & Quatre Corps ∘ Résonance ∘ Co-orbital

ABSTRACT

Planetary systems can adopt remarkable configurations. One of them, said co-orbital, occurs when two planets share the same orbital period around their star, that is, when they are in a $1:1$ mean motion resonance. Even within the co-orbital motion, many trajectories are possible. The simplest ones are known since the 18^{th} century, like two co-orbital bodies on planar and circular orbits forming with the star a rotating equilateral triangle. However, some more subtle configurations were not discovered until recently. In the case of point mass bodies with small eccentricities and inclinations, the analytical features of the dynamics are well understood. However, large eccentricities and inclinations are responsible for topological changes in the phase space, while extended bodies can lead to dissipation of the orbital energy, and the dynamics in these cases still has grey areas.
None of the eight planets of the Solar system are in co-orbital motion together, although co-orbital bodies exist in the Solar system, either between two minor objects (orbiting a planet) or between a planet and a minor object (orbiting the Sun). This absence of planet−planet co-orbital motion should not be the norm in exoplanetary systems, as the formation models predict their existence. Nevertheless, despite thousands of exoplanets detection, no pair of co-orbital planets has been detected so far. While this may be in part explained by detection bias, we show in this manuscript that tidal effects are responsible for the disruption of co-orbital pairs of planets. We build an analytical tidal model of the planar system star-planet-planet, based on an extension of the point-mass Hamiltonian formalism with tidal dissipation. The model provides an accurate analytical expression for the lifetime of the pair depending on the parameters, allowing to predict which already discovered exoplanets might have an undetected co-orbital companion.
Formation models also predict that a significant number of co-orbital planets are formed within a resonance chain. Therefore, we extend the previous study to the case where the pair is within a resonance chain. More precisely, we build a Hamiltonian model of the resonance chain $p:p:p+1$ where the co-orbital pair is in a first-order mean motion resonance $p:p+1$ with an outermost third planet, p being a small integer. After comparing the families of equilibria of the model with the associated families of periodic orbits of the complete system, we add tidal dissipation to the model using a pseudo-Hamiltonian formalism. We show that this resonance chain features a $1:1$ secular resonance between the libration of the co-orbital angle and the precession of the pericentres, and by analizing the eigenvalues of the linearized system in the vicinity of the families of equilibria, we show how tides stabilize the system around this secular resonance, making co-orbital pairs of exoplanets much more stable while inside the $p:p:p+1$ resonance chain.

KEYWORDS

Celestial Mechanics ∘ Tides ∘ Three & Four Body Problem ∘ Resonance ∘ Co-orbital